Spin Structure of ^{3}He and the Neutron at Low Q^2; A Measurement of the Extended GDH Integral and the Burkhardt–Cottingham Sum Rule

---

A Dissertation
Submitted to
the Temple University Graduate Board

by

Karl J. Slifer

In Partial Fulfillment
of the Requirements for the Degree
DOCTOR OF PHILOSOPHY

August, 2004

Dedicated to my parents Harry and Dolores

ABSTRACT

Spin Structure of ^{3}He and the Neutron at Low Q^2; A Measurement of the Extended GDH Integral and the Burkhardt–Cottingham Sum Rule

Karl J. Slifer
DOCTOR OF PHILOSOPHY
Temple University, 2004
Advisor: Dr. Zein-Eddine Meziani

Experiment 94-010 investigated the spin structure of the neutron and ^{3}He at Jefferson Laboratory in Newport News, VA. Longitudinally polarized electrons of incident energy from 0.9 GeV to 5.0 GeV were scattered from a high pressure polarized ^{3}He target in experimental Hall A. ^{3}He was used as an effective neutron target, taking advantage of the approximate cancellation of the two spin-paired protons in the ^{3}He ground state. Longitudinal and transverse target polarizations were maintained, allowing a precision determination of both spin structure functions $g_1(x,Q^2)$ and $g_2(x,Q^2)$. The structure functions were extracted from an inclusive polarized cross section measurement at low momentum transfer ($0.1<Q^2<0.9$ GeV^2) in the threshold, quasielastic, and resonance regions.

The goal of this experiment has been to test our grasp of Quantum Chromodynamics (QCD), the fundamental theory of the strong interaction, in the non-perturbative region. QCD has been verified impressively in the high energy region of asymptotic freedom, that is, when the magnitude of the force between quarks is relatively small. However, experimentally verifiable predictions at low Q^2 have been harder to achieve due to the complexity of the interactions between constituents. Definite predictions do exist however, for the first (and higher) moments of the spin structure functions in the form of the various QCD sum rules. The Burkhardt–Cottingham sum rule is a Q^2–dependent relation which implies the vanishing of the first moment of the g_2 structure function, while the Bjorken and extended GDH sum rules follow directly from QCD and govern the behaviour of the g_1 structure function. These integrals are investigated for a ^{3}He (neutron) target at low momentum transfer.

ACKNOWLEDGEMENTS

First and foremost, I'd like to thank my advisor Dr. Zein-Eddine Meziani for his support and guidance, and for introducing me to this exciting field. I was fortunate to have two other extremely talented spokesmen running my thesis experiment: Jian-Ping Chen and Gordon Cates, and I learned alot from their professional example. I also appreciate the input of the members of my thesis committee who have spent so much time ensuring the quality of this document.

The E94-010 collaboration was a great group to work with. The three month run now only brings back good memories, even though I was sure it would kill me at the time. In particular I will remember the 'RTD squad': Alex, Pibero, Ionis, and Stephen. I'd like to also mention Wang Zu, Feng Xiong, Enkeleida Lakuriqi, Emma Goldberg and Mark Jones. Thanks to Alexandre for many nice conversations on physics and politics over the years and for commenting on this thesis.

Our post-docs were as good as those of any collaboration and I'm certain this experiment could not have succeeded without the intense effort of Sebatien Incerti during the run and the long months of preparation beforehand. E94-010 is particularly indebted to Seonho Choi who was the backbone of the analysis team, and produced so many of the nice neutron results that we all presented at various conferences. I am grateful for his answering countless questions over the years, and am still waiting for the first "I don't know" response.

Xiaodong Jiang provided the necessary monte-carlo analysis for E94-010 and brought good humor to the numerous other tasks he performed. Nilanga Liyanage provided the optics analysis and was always happy to answer my questions no matter how inane. Todd Averett gave some really useful analysis tutoring early on when I seriously had no clue what I was doing. Thanks also to Yves Roblin, Kathy McCormick and Ron Gilman for their considerable contributions. Dave Pripstein introduced some much needed laughter to a high pressure environment. He and Tim Black made the experiment a lot more enjoyable. Thanks to the Kentucky group, Wolfgang and Piotr two of the nicect people I've encountered at JLab. I appreciate the hard work of Eugene Chudakov and the Møller group, and Bob Michaels' efforts to keep the DAQ running at all hours of the night. Also thanks to

Kees de Jager for his support of the ^{3}He program in general. I am grateful to all the JLab staff for their contributions to E94-010. In particular, I would like to thank Ed Folts, Jack Segal, Al Gavalya, Joyce Miller and Susan Esp for their intense efforts.

Thanks to Jian-Ping Chen for carefully reviewing this manuscript and for his tireless efforts to ensure E94-010's success. I've been very lucky to have such an excellent on-site advisor while so far away from my home university. Before E94-010 it never occurred to me how much back-breaking manual labor goes into a large experiment. J.P. will always have my respect for working as hard as, and many times even harder than the graduate students on the nuts and bolts of E94-010.

I am grateful to Wally Melnitchouk for several theoretical discussions and to Jacek Golak, and Sergio Scopetta for providing their Q.E. calculations.

There are a few exceptional teachers who I hold in high regard and merit mentioning: Ms. Margaret Recupido, who taught world history and the finer points of law and debating. Dr. Dieter Forster whose enthusiasm and skill converted me from a calculus-fearing English major into an eventual PhD. candidate. Dr. Theodore Burkhardt for many interesting graduate classes and for pointing out the coolest thing I learned in graduate school: the ubiquity of the principle of least action in so many branches of physics.

I'd like to thank Ed Kaczanowicz for schooling me the black arts of machining and drafting. Any competence I have working with my hands is mostly due to Ed's patient teaching over countless hours in the shop. The Temple physics department is certainly lucky to have such a jack of all trades on hand.

Thanks to Jaideep and Al for some excellent drinking time at UVA, and for many good conversations. Thanks to my long time friends Anthony and John for many adventures and for cracking me up so many times over the years. I am also thankful for the time I had with Justin and Pete, two good friends who I miss to this day.

My family will always be my favorite collaboration. I have the somewhat biased opinion that my parents did a great job raising me, despite the fact that it was quite difficult at times. Lorie, Lesa, Karen, Harry, and Kath: simply a terrific group of good people. Each helped me in some significant way. A few even made the ultimate sacrifice and took in a somewhat grumpy physicist as a temporary roommate. I would never be able to repay the kindness and selflessness you have shown me. Instead, I hope to 'pay it forward' as the saying goes.

Finally, thanks to Patricia for all the wonderful times we've shared, and for putting up with me as I wrote this document.

TABLE OF CONTENTS

ABSTRACT v

ACKNOWLEDGEMENTS vii

LIST OF TABLES xiii

LIST OF FIGURES xv

1 SPIN, STRUCTURE AND THE GDH SUM RULE 1

2 INCLUSIVE ELECTRON SCATTERING 4
- 2.1 Kinematic Variables 4
- 2.2 Form Factors and Structure Functions 5
  - 2.2.1 Elastic Scattering 7
  - 2.2.2 Resonance Production 8
  - 2.2.3 Deep Inelastic Scattering 9
  - 2.2.4 Nuclei 10
- 2.3 Tensor Formulation 11
- 2.4 Physical Meaning of the Structure Functions 13
- 2.5 Virtual Photon Cross Sections 14
- 2.6 Compton Scattering 17

3 THEORETICAL TOOLBOX 19
- 3.1 Chiral Perturbation Theory 19
- 3.2 Lattice Gauge Theory 20
- 3.3 The Operator Product Expansion 20
  - 3.3.1 Wandzura–Wilczek Relation 22
  - 3.3.2 d_2 and Higher Twists 23
  - 3.3.3 Higher Twist Effects in g_1 23
  - 3.3.4 Quark-Hadron Duality 24
- 3.4 Phenomenological Model Predictions 27
  - 3.4.1 MAID 27
  - 3.4.2 Burkert and Ioffe 27
  - 3.4.3 Soffer and Teryaev 28

4 SUM RULES AND MOMENTS 30
4.1 The GDH Sum Rule 30
4.2 Experimental Generalization of the GDH Sum 32
4.3 Dispersive Sum Rules at Arbitrary Q^2 36
    4.3.1 The GDH Sum 37
    4.3.2 The Bjorken Sum Rule 38
    4.3.3 The g_1 Sum Rule 39
    4.3.4 The Burkhardt–Cottingham Sum Rule 41
4.4 Summary 43

5 THE EXPERIMENT 45
5.1 The Accelerator 47
5.2 Hall A Beamline 48
    5.2.1 Beam Current Monitors 48
    5.2.2 Raster 51
    5.2.3 Beam Position Monitors 51
    5.2.4 Beam Polarization 52
    5.2.5 Incident Beam Energy 55
5.3 The Spectrometers 58
    5.3.1 Magnets 59
    5.3.2 Collimator 59
    5.3.3 Spectrometer Survey 60
5.4 Detector Package 62
    5.4.1 Vertical Drift Chamber 62
    5.4.2 Hodoscopes 67
    5.4.3 Čerenkov Radiation 69
    5.4.4 Lead Glass Shower Detector 70

6 THE POLARIZED ^{3}HE TARGET 73
6.1 Thermal Distribution of ^{3}He Polarization 74
6.2 Optical Pumping of Rubidium 75
6.3 Spin Exchange 76
6.4 Rate of Polarization 78
6.5 Relaxation Mechanisms 79
6.6 Experimental Setup 80
6.7 Electron Paramagnetic Resonance Polarimetry 82
6.8 Nuclear Magnetic Resonance Polarimetry 83
    6.8.1 Classical Description 83
    6.8.2 Quantum Mechanical Description 84
    6.8.3 Experimental Method 84

6.9 E94-010 Target Characteristics 85

7 ANALYSIS 88
7.1 Data Acquisition 88
7.2 From Tape to Histogram 89
7.3 Physics Analysis Overview 90
7.4 Detector Calibrations and Efficiencies 92
    7.4.1 Scintillators 92
    7.4.2 VDC 93
    7.4.3 Čerenkov 94
    7.4.4 HRS-L Lead Glass Calorimeter 98
    7.4.5 HRS-R Lead Glass Shower Detector 101
7.5 Particle ID Cuts 103
7.6 Spectrometer Optics 104
    7.6.1 Target Coordinate System 104
    7.6.2 Detector Coordinate System 105
    7.6.3 Transport Tensor 107
7.7 Spectrometer Acceptance 108
7.8 Acceptance Cuts 109
7.9 Good Run Selection 110

8 ^{3}HE UNPOLARIZED CROSS SECTIONS 112
8.1 Raw Cross Sections 112
    8.1.1 Raw Cross Section Systematic 114
    8.1.2 Tail Subtraction and Nitrogen Dilution 118
    8.1.3 Cross Section Errors before Radiative Corrections . . . 119
8.2 Radiative Corrections 121
8.3 Finite Acceptance Correction 128
8.4 Final Systematic Error 128
8.5 Cross Section Evaluation 129
    8.5.1 Radiative Corrections Check 129
    8.5.2 Comparison to Existing ^{3}He Data 129
    8.5.3 Theoretical Calculations and Models 132
    8.5.4 Conclusion 134

9 ^{3}HE POLARIZED QUANTITIES 145
9.1 Asymmetries 145
9.2 Polarized Cross Sections 146
9.3 Interpolation and Extrapolation 156
9.4 Polarized Structure Functions 158

9.5 The Transverse-Transverse Cross Section σ'_{TT} 162
9.6 The Longitudinal–Transverse Cross Section σ'_{LT} 163

10 STRUCTURE FUNCTION MOMENTS 166
10.1 Plot Quantities 166
10.2 The First Moment of g_1 167
10.3 The First Moment of g_2 172
10.4 Extended GDH sum 173

11 CONCLUSION AND DISCUSSION 175

APPENDIX A — NEUTRON RESULTS 178

APPENDIX B — GDH SUM RULE DERIVATION 188

APPENDIX C — RADIATIVE CORRECTIONS 192

APPENDIX D — RADIATION LENGTHS 201

APPENDIX E — INTEGRAL RELATIONS 209

APPENDIX F — PROCESSING OF CROSS SECTIONS 212

APPENDIX G — CROSS SECTION TABLES 215

REFERENCES 243

LIST OF TABLES

5.1 Incident energies in MeV 58

5.2 Characteristics of the HRS 60

5.3 Survey results for E94-010. 61

5.4 HRS mispointing 61

6.1 Average target polarization. 86

6.2 Target density in amagats. 86

8.1 Raw cross section systematics. 116

8.2 Cross section cuts 116

8.3 More cross section systematics 116

8.4 Peaking approximation vs. exact results. E_s=1 GeV 120

8.5 Peaking approximation vs. exact results. E_s=5 GeV 120

8.6 Contributions to the cross section systematic uncertainty . . 120

9.1 False asymmetry 146

10.1 $\overline{\Gamma}_1(Q^2)$ 169

10.2 $\Gamma_2(Q^2)$ 170

10.3 $I_A(Q^2)$ 174

D.1 Pre-target material radiation lengths 203

D.2 Pre-target material radiation lengths 203

D.3 Target cell entrance window thickness. 203

D.4 Exit window, HRS-L side 204

D.5 Exit window, HRS-R side 205

D.6 The thickness of the ^{3}He gas before scattering. 206

D.7 The thickness of the ^{3}He gas after scattering. 206

D.8 Total thickness before scattering. 207

D.9 Total thickness after scattering (HRS-L side) 207

D.10 Total thickness after scattering (HRS-R side) 207

D.11 Comparison to previous analysis, before scattering 208

D.12 Comparison to previous analysis, (HRS-L) after scattering . . 208

D.13 Comparison to previous analysis, (HRS-R) after scattering . . 208

G.1 E94-010 unpolarized ^{3}He cross sections 215

LIST OF FIGURES

2.1 First order scattering diagram. 5
2.2 Helicity projection for $\sigma_{3/2}$ and $\sigma_{1/2}$. 16
2.3 Compton scattering. 17
3.1 Color electric and magnetic fields 25
3.2 Duality in the F_2 structure function. 26
4.1 Kinematic spectrum 33
4.2 MAID prediction for the extended GDH sum 35
4.3 Model of Burkert and Ioffe for $\overline{\Gamma}_1(Q^2)$. 40
4.4 Connecting the partonic and hadronic descriptions. 43
5.1 Kinematic Coverage of E94-010 46
5.2 Energy level diagram for doped GaAs. 47
5.3 CEBAF machine configuration. 48
5.4 JLab experimental Hall A. 49
5.5 Schematic of Beam Current Monitor apparatus 50
5.6 Projection of raster pattern on horizontal and vertical axis . . 52
5.7 Antennae within the beam position monitors 53
5.8 Møller polarimeter schematic 54
5.9 Beam polarimetry measurements. 55
5.10 Configuration of the Arc. 56
5.11 Schematic of *ep* energy measurement setup. 57
5.12 Carbon foil placement 62
5.13 HRS-L carbon foil data,15.503°. 63
5.14 HRS-L carbon foil data,15.495°. 63
5.15 HRS-R carbon foil data, 15.528°. 64
5.16 HRS-R carbon foil data, 15.508°. 64
5.17 Detector package for HRS-L and HRS-R 65
5.18 Vertical Drift Chambers 66
5.19 VDC Drift cell geometry 67
5.20 Čerenkov radiation 69
5.21 HRS-L Čerenkov detector schematic 71
5.22 HRS-L preshower lead glass detector. 72
5.23 HRS-L shower lead glass detector. 72
6.1 Energy level diagram for ^{85}Rb, I=5/2 77
6.2 Temperature dependence of rubidium density 78
6.3 The polarized ^{3}He target. 81
6.4 EPR spectrum 83

6.5 Energy level splitting. 85
6.6 Target polarization vs. run number 86
7.1 Analysis flow diagram. 92
7.2 HRS-L scintillator performance vs. run number. 93
7.3 HRS-L raw Čerenkov ADC for each individual mirror. 95
7.4 HRS-L calibrated Čerenkov ADC for each individual mirror. 96
7.5 Čerenkov single photo-electron peak vs momentum 97
7.6 E/p for properly calibrated shower 99
7.7 Calibrated output for HRS-L calorimeter 100
7.8 Energy deposition in HRS-L calorimeter 101
7.9 Calibrated shower output for HRS-R 102
7.10 Effect of particle ID Cut on π/e ratio (HRS-L). 103
7.11 Effect of particle ID Cut on π/e ratio (HRS-R). 104
7.12 Target coordinate system 105
7.13 Detector coordinate system, top view 106
7.14 Detector coordinate system, side view. 106
7.15 Hall A coordinate system 107
7.16 Spectrometer sieve slit collimator 108
7.17 ^{3}He data target variables y_t & ϕ_t with final cut 110
7.18 ^{3}He data target variables δ_P & θ_t with final cut 111
8.1 HRS acceptance 113
8.2 Variation of the density with pumping chamber temperature 115
8.3 $E_0 =$ 862 MeV cross section 122
8.4 $E_0 =$ 1717 MeV cross section. 123
8.5 $E_0 =$ 2581 MeV cross section. 124
8.6 $E_0 =$ 3382 MeV cross section. 125
8.7 $E_0 =$ 4239 MeV cross section. 126
8.8 $E_0 =$ 5058 MeV cross section. 127
8.9 $E_0 =$ 862 MeV. Radiative corrections check 130
8.10 $E_0 =$ 1717 MeV. Radiative corrections check 130
8.11 Kinematic coverage of Bates and Saclay L-T separation . . . 131
8.12 E94-010 unfolded cross sections. 136
8.13 $E_0 =$ 862 MeV Born cross section in the Q.E. region. 137
8.14 $E_0 =$ 1717 MeV Born cross section in the Q.E. region. 138
8.15 $E_0 =$ 2581 MeV Born cross section in the Q.E. region. 139
8.16 $E_0 =$ 3382 MeV Born cross section in the Q.E. region. 140
8.17 $E_0 =$ 4239 MeV Born cross section in the Q.E. region. 141
8.18 $E_0 =$ 862 MeV Born cross section. 142
8.19 $E_0 =$ 1717 MeV Born cross section. 142
8.20 $E_0 =$ 2581 MeV Born cross section. 143

8.21 $E_0 = 3381$ MeV Born cross section. 143
8.22 $E_0 = 4238$ MeV Born cross section. 144
8.23 $E_0 = 5058$ MeV Born cross section. 144
9.1 E94-010 asymmetries. 147
9.2 $E_0 = 862$ MeV. Polarized cross section 150
9.3 $E_0 = 1717$ MeV. Polarized cross section 151
9.4 $E_0 = 2581$ MeV. Polarized cross section 152
9.5 $E_0 = 3382$ MeV. Polarized cross section 153
9.6 $E_0 = 4239$ MeV. Polarized cross section 154
9.7 Interpolation and extrapolation 155
9.8 Fit of $g_2^{^3\mathrm{He}}$ as a function of W 156
9.9 Fit of $g_1^{^3\mathrm{He}}$ as a function of W 157
9.10 Fit of $g_1^{^3\mathrm{He}}$ as a function of Z_{g_1} 157
9.11 $g_1^{^3\mathrm{He}}$ as a function of Q^2. 159
9.12 Polarized structure functions, constant energy 160
9.13 Polarized structure functions, constant Q^2 161
9.14 $g_1^{^3\mathrm{He}}$ as a function of Nachtman variable ξ 162
9.15 GDH integrand, constant energy 163
9.16 GDH integrand, constant Q^2 164
9.17 σ'_{LT}, constant energy 165
10.1 $\overline{\Gamma}_1$, the first moment of $g_1^{^3He}$ 168
10.2 Γ_2, the first moment of $g_2^{^3He}$ 171
10.3 The extended GDH sum for ^{3}He 173
A.1 $\overline{\Gamma}_1$: Effective polarization approximation 180
A.2 $\overline{\Gamma}_2$: Effective polarization approximation 181
A.3 $\bar{d}_2$: Effective polarization approximation 182
A.4 $\overline{\Gamma}_1$: Comparison of published results to parallel analysis 184
A.5 $\overline{\Gamma}_2$: Comparison of published results to parallel analysis 185
A.6 $\bar{d}_2$: Comparison of published results to parallel analysis 186
A.7 I_A : Comparison of published results to parallel analysis 187
C.1 Next to leading order internal radiative corrections. 193
C.2 Kinematic region that contributes to the radiative corrections. 193
C.3 Schematic of radiative corrections. 196
C.4 $E_0 = 862$ MeV. Polarized cross section difference 200
D.1 Schematic of material thicknesses 202
E.1 $\overline{\Gamma}_1^{^3\mathrm{He}}$ for $W < M_\pi$. 211
F.1 HRS-L raw cross section for $E_0 = 862$ MeV. 213
F.2 Target variables for HRS-R. $E_0 = 862$ MeV. 214

A is A

Ayn Rand, Atlas Shrugged

Serves you right, I said to myself that other evening. Now here you are waiting for what will happen under Foucault's pendulum.

Umberto Eco, Foucault's Pendulum

CHAPTER 1

SPIN, STRUCTURE AND THE GDH SUM

The investigation of spin began with the novel experiments of Stern and Gerlach. In the early 1920's, they performed the first measurement of the electron's magnetic moment by passing a molecular beam of silver atoms through an inhomogeneous magnetic field. They observed that the emerging particles were detected at two highly localized points, which could not be understood in terms of the classical picture of the electron. Uhlenbeck and Goudsmit introduced the concept of *spin* in order to explain Stern and Gerlach's results and other puzzling experimental findings such as the hyperfine splitting in atomic spectral lines.

So, what is spin? Experimentally, we find that an electron placed in a magnetic field will behave like a tiny magnet with a north and south pole, aligning itself along the field lines. Classically, we could understand the magnetic moment of the electron as arising from the angular momentum of the charged electron rotating on its axis and creating its own small magnetic field. However, the electron appears to be point-like, that is without dimension, from all empirical evidence to date. This makes an interpretation in terms of a tiny spinning orb unfeasible, since the rotation would need to be infinitely fast. Instead, Uhlenbeck and Goudsmit interpreted the magnetic moment as arising from an intrinsic property of the electron. The spin appears in every way like an angular momentum, except that it is unrelated to any spatial motion of the particle. In this sense it is a basic characteristic like mass or charge.

In 1928 Dirac published his famous relativistic wave equation governing the behaviour of fundamental point-like particles. In this approach spin emerged as a natural consequence of the formalism. The magnetic moment of a structureless spin-1/2 particle was predicted by Dirac to be:

$$\mu = \frac{e}{2M}$$

in agreement with the experimentally measured electron value*.

---

*Here e represents the charge and M is the mass.

By 1933, Stern had improved his apparatus sufficiently to determine the proton's much smaller magnetic moment. He and his collaborators performed the measurement [1] and obtained a result that disagreed with the Dirac prediction by 150%! This *anomolous* magnetic moment was a clear sign that the proton was not point-like, but instead possessed a complicated internal structure. Of course, in the case of the uncharged neutron any magnetic moment at all would be anomolous.

The measurements of the magnetic moments were the first concrete demonstration of the nucleon's internal structure. Many decades later, experiments at powerful accelerators provided independent confirmation of the nucleon's internal structure. These high energy scattering experiments also enabled us for the first time to examine the constituents of the nucleons, now referred to as quarks and gluons, and to begin to answer the question of how these constituents interact to produce the spin and other global properties of the nucleon.

So, an anomolous magnetic moment serves as a clear signature of complicated internal structure. And any particle with an internal structure must necessarily have an excitation spectrum. The sum rule of Gerasimov, Drell and Hearn (GDH) nicely quantifies this relationship by linking the helicity-dependent cross sections measured in photon scattering to the anomolous magnetic moment of a hadronic target. This sum rule for real photon scattering has provided a foundation for a powerful approach to interpreting the experimental results of electron scattering experiments. In this thesis, we will examine generalizations of the GDH sum and related integrals as applied to the study of the neutron and ^{3}He spin structure.

An ultimate goal of this endeavor is to test Quantum Chromodynamics or QCD, the fundamental theory of the strong interaction (one of only four known forces in nature). In the high energy region, QCD has been verified impressively following decades of experimental results which have been compared to perturbative solutions of the QCD Lagrangian. In the low energy region, an effective field theory approach known as chiral perturbation theory has been implemented. But there is a small intermediate region where neither of these approaches is expected to be applicable. There is good reason to expect that the calculational techniques of lattice gauge theory can soon be applied, but no matter what the eventual theoretical approach, experimental data will be necessary to provide calculational benchmarks. The goal of E94-010 was to provide precise data in this intriguing intermediate region and to test several sum rule predictions.

This thesis is organized as follows. Chapters 2, 3 and 4 present the theoretical formalism. Chapter 5 discusses the JLab accelerator and the

Hall A experimental setup. Chapter 6 gives an overview of the polarized ^{3}He target, while chapter 7 explains the data analysis. Final results and conclusions are presented in chapters 8 to 11.

CHAPTER 2

INCLUSIVE ELECTRON SCATTERING

The modern era of electron scattering can trace its roots to Rutherford's classic experiments in 1911 scattering positively charged alpha-particles from thin metal foils. From these experiments, a crude but essentially correct picture of the atomic nucleus emerged, with an atom possessing a massive, positively charged nucleus with a radius of approximately $10^{-15} - 10^{-14}$m. Experiments that are essentially extensions of Rutherford's early work at more and more powerful accelerators have revealed the nucleus to be composed of nucleons (positively charged protons and uncharged neutrons) which themselves appear to have a rich substructure of quarks and gluons.

In this section we will start from Rutherford's basic formula, and gradually add on the pieces necessary (in a somewhat Frankensteinish fashion) to make it applicable to the electron scattering performed at JLab. Many of the corrections were phenomenological in nature when they were first introduced, and it is in this way that we present them in order to help understand their physical meaning. Later we will see how these formula are a natural relativistic consequence of Lorentz and gauge invariance, together with parity conservation.

2.1 Kinematic Variables

The first order Born approximation for inclusive scattering of electrons from a hadronic target is shown in figure 2.1. In this scenario, an electron with four momentum $\mathrm{p}^{\mu} = (E, \vec{p})$ interacts with a hadronic target of four momentum $\mathrm{P}^{\mu} = (\epsilon, \vec{P})$ via the exchange of a single virtual photon. The final hadronic system with four momentum $\mathrm{P}'^{\mu} = (\epsilon', \vec{P'})$ goes unobserved, while the electron is detected at an angle θ with four momentum $p'^{\mu} = (E', \vec{p})$. The virtual photon is off its mass shell, so the four momentum $\mathrm{q}^{\mu} = (\nu, \vec{q})$ satisfies $q^2 \neq 0$. For a space-like virtual photon $q^2 < 0$, so typically the variable $Q^2 = -q^2$ is used instead.

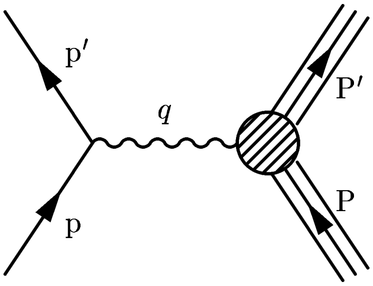

Figure 2.1: First order scattering diagram.

In the process, an energy $\nu = \frac{P \cdot q}{M}$ and momentum $\vec{q} = \vec{p} - \vec{p'}$ are transferred to the target. In the inclusive reaction, only the final scattered electron is detected, so we will often make use of the invariant mass of the residual hadronic system: $W = \sqrt{(P+q)^2}$. We also introduce here two scalar invariants $x = \frac{Q^2}{2P \cdot q}$ and $y = \frac{P \cdot q}{P \cdot p}$, which are utilized frequently in the study of deep inelastic scattering (DIS).

In the laboratory system, where $\mathrm{P}^\mu = (M, 0)$, we find the following useful kinematic relations [2]*:

$$\nu = E - E' = \epsilon - \epsilon' \tag{2.1}$$

$$Q^2 = 4EE' \sin\frac{\theta}{2} \tag{2.2}$$

$$W^2 = M^2 + 2M\nu - Q^2 \tag{2.3}$$

$$x = \frac{Q^2}{2M\nu} \tag{2.4}$$

$$y = \frac{\nu}{E} \tag{2.5}$$

2.2 Form Factors and Structure Functions

The **Rutherford differential cross section** [3] describes scattering of an electron of incident energy E from an atomic nucleus of charge Ze, into a solid angle dΩ:

$$\left(\frac{d\sigma}{d\Omega}\right)_{\mathrm{Ruth}} = \frac{4Z^2\alpha^2E'^2}{|\vec{q}|^4} \tag{2.6}$$

---

[*] We set $\hbar = c = 1$, and neglect the small mass m_e of the electron.

Here, $\vec{q}$ is the vector momentum transfer, α is the fine structure constant and E' is the scattered electron energy. This formula is applicable for heavy nuclei and low energy electrons. In Rutherford scattering the target recoil $E - E'$ is ignored. That is, $E = E'$ and $|\vec{p}| = |\vec{p'}|$. Notice that the result is non-relativistic, and ignores any possible target internal structure. Polarization degrees of freedom are also neglected.

Including electron spin modifies the cross section to:

$$\left(\frac{d\sigma}{d\Omega}\right)^*_{\text{Mott}} = \left(\frac{d\sigma}{d\Omega}\right)_{\text{Ruth}} \cos^2\frac{\theta}{2} \tag{2.7}$$

The factor $\cos^2\frac{\theta}{2}$ prevents scattering at 180° from a spinless target, thus conserving helicity. The * indicates that we are still ignoring target recoil due to the heavy nuclei mass.

The nucleon's spatial extent is around 1 Fermi so the projectile energy must be at least several hundred MeV in order for the electron's de Broglie wavelength to resolve any structure. The mass of a single nucleon is comparable to this energy, so the target recoil can no longer be neglected. We include a recoil factor $\frac{E'}{E}$ and must now use the relativistic four-vector momentum transfer Q^2. The resulting **Mott cross section** is:

$$\left(\frac{d\sigma}{d\Omega}\right)_{\text{Mott}} = \frac{\alpha^2}{4E^2}\left(\frac{\cos^2\frac{\theta}{2}}{\sin^4\frac{\theta}{2}}\right)\frac{E'}{E} \tag{2.8}$$

The Mott formulae represents the expected result for a point-like infinitely heavy target with no internal structure. Taking into account the spatial extent of the nuclei gives:

$$\left(\frac{d\sigma}{d\Omega}\right)_{\text{exp}} = \left(\frac{d\sigma}{d\Omega}\right)^*_{\text{Mott}} \times |F(\vec{q^2})|^2 \tag{2.9}$$

where $\mathrm{F}(\vec{q^2})$ is the nuclear form factor and measures the deviation of the target nucleus from point like behaviour. For a point charge, the form factor would be a constant (unity).

The electron charge interacts with the target charge, but the electric current will also interact with the nucleon's magnetic moment. The magnetic interaction is associated with a flip of the spin of the nucleon, and leads to the following result for a point target:

$$\left(\frac{d\sigma}{d\Omega}\right)_{\text{point}} = \left(\frac{d\sigma}{d\Omega}\right)_{\text{Mott}} \left[1 + 2\tau\tan^2\frac{\theta}{2}\right] \tag{2.10}$$

where[†] $\tau = Q^2/4M^2$. The magnetic term is significant whenever Q^2 or the scattering angle becomes large. This causes the cross section to fall off less strongly than would otherwise be expected.

2.2.1 Elastic Scattering

When electrons are scattered elastically, the energy and scattering angle are constrained by energy and momentum conservation to the following relation:

$$E' = \frac{E}{1 + \frac{2E}{M_T}\sin^2\frac{\theta}{2}} \tag{2.11}$$

where M_T is the mass of the target, and θ is the scattering angle.

Now we generalize equation 2.10 by taking the target's spatial distribution into consideration. Two form factors are necessary to characterise both the electric and magnetic distributions. The cross section for the elastic scattering of an electron from a hadronic target is described by the **Rosenbluth formula** [4]:

$$\left(\frac{d\sigma}{d\Omega}\right) = \left(\frac{d\sigma}{d\Omega}\right)_{\text{Mott}} \times \left\{\frac{G_E^2(Q^2) + \tau G_M^2(Q^2)}{1+\tau} + 2\tau G_M^2(Q^2)\tan^2\frac{\theta}{2}\right\} \tag{2.12}$$

$G_E^2(Q^2)$ and $G_M^2(Q^2)$ are the electromagnetic Sachs form factors. For the nucleons, they are normalized at $Q^2 = 0$ to

$$\begin{aligned} G_E^{p(n)}(0) &= 1(0) \qquad (2.13)\\ G_M^{p(n)}(0) &= \mu_{p(n)} \qquad (2.14)\end{aligned}$$

where p and n refer to the proton and neutron respectively.

At low $Q^2(Q^2 \leq 2\ \text{GeV}^2)$, the electromagnetic form factors can be described quite well by the dipole fit [3]:

$$\begin{aligned} G_E^p(Q^2) &= G_D(Q^2) \qquad (2.15)\\ \frac{G_M^p(Q^2)}{\mu_p} &= G_D(Q^2) \qquad (2.16)\\ \frac{G_M^n(Q^2)}{\mu_n} &= G_D(Q^2) \qquad (2.17)\end{aligned}$$

[†] The τ factor arises from the interaction with the magnetic dipole which is proportional to e/M.

where:

$$G_D(Q^2) = \frac{1}{\left(1 + \frac{Q^2}{0.71\mathrm{GeV}^2}\right)^2} \tag{2.18}$$

The dipole parameterization[‡] shows that the elastic cross sections fall off as Q^{-8} as the momentum transfer increases. Recall that the form factor of a point charge is completely independent of Q^2. The strong Q^2 dependence of the form factors provided the first confirmation from scattering experiments of the nucleon's internal structure.

2.2.2 Resonance Production

When the energy transferred to the target is increased, inelastic scattering becomes possible. For inelastic scattering, excitations of the nucleon known as nucleon resonances can be observed. The existence of these excited states clearly demonstrates that the nucleon is a composite system. The invariant mass of these states is $W^2 = M^2 + 2M\nu - Q^2$. Recall that for elastic scattering $W = M$ so

$$2M\nu - Q^2 = 0$$

while in inelastic processes W>M, and

$$2M\nu - Q^2 > 0$$

This suggests the introduction of a dimensionless parameter

$$x = \frac{Q^2}{2M\nu} \tag{2.19}$$

known as the Bjorken variable[§] which measures the inelasticity of the process. For elastic processes $x = 1$ while for all other processes, $0 < x < 1$.

The first resonant state (and the only one we will examine explicitly) is the Δ or $P_{33}(1232)$.[¶] It is the only resonance that does not significantly overlap any other states. In terms of a multipole expansion [7], it is known to

---

[‡] At larger Q^2, significant deviations from the dipole form have been observed. See for example [5, 6]

[§] Section 2.4 describes x in further detail.

[¶] We follow the standard nomenclature L_{2I2J}, where, in spectroscopic notation, $L = S, P, D, \ldots$ represents orbital angular momentum of $0, 1, 2, \ldots$, I is the isospin, and J represents the total angular momentum.

be dominantly a magnetic dipole transition M_{1+}, with only a small electric quadrupole component, E_{1+}. At first approximation, it represents a single-quark spin flip, and the transition to the P_{33} can be described by a magnetic form factor G_M^Δ alone.

The following has been found to be a good empirical fit [7, 8] to data:

$$\sigma_\Delta = \frac{4\pi\alpha}{\Gamma} \cdot \frac{|\vec{q}|^2}{W(W^2 - M^2)} \cdot \left(|G_M^\Delta|^2 + 3|G_E^\Delta|^2\right) \tag{2.20}$$

with

$$\begin{aligned} G_M^\Delta(Q^2) &= G_M^\Delta(0)\; G_D(Q^2) e^{-0.2Q^2} && (2.21) \\ G_E^\Delta(Q^2) &= 0 && (2.22) \end{aligned}$$

where G_D is the previously introduced dipole form factor. From equation 2.21 we can expect the dipole resonance to die off fairly rapidly with increasing Q^2.

2.2.3 Deep Inelastic Scattering

Above an invariant mass of about 2 GeV, the individual resonance peaks become indistinguishable, and the scattering becomes an incoherent sum over the nucleon's constituents. The **Rosenbluth formulae** for inelastic scattering is:

$$\left(\frac{d\sigma}{d^2\Omega dE'}\right) = \left(\frac{d\sigma}{d\Omega}\right)^*_{\text{Mott}} \left[W_2(\nu, Q^2) + 2W_1(\nu, Q^2)\tan^2\frac{\theta}{2}\right] \tag{2.23}$$

which represents a generalization of equation 2.10. W_1 and W_2 are known as structure functions and parameterise all information concerning the target's unknown internal structure. The second term contains the magnetic interaction. W_1 and W_2 are often replaced by the two dimensionless structure functions

$$\begin{aligned} F_1(x, Q^2) &= MW_1(\nu, Q^2) && (2.24) \\ F_2(x, Q^2) &= \nu W_2(\nu, Q^2) && (2.25) \end{aligned}$$

If one extracts $F_1(x,Q^2)$, and $F_2(x,Q^2)$ at large Q^2, one observes that at fixed values of x the structure functions depend only very weakly on Q^2. This is in clear contrast to elastic and resonant states behaviour. The fact that the structure functions are independent of Q^2 indicates that the electrons are scattered off a point charge. Since nucleons are extended objects, it follows that the proton and neutron have a sub-structure made up of point-like constituents.

The experimentally measured DIS structure functions have been shown to exhibit the following behaviour:

$$2xF_1(x) = F_2(x) \tag{2.26}$$

which is known as the Callan-Gross [9] relation and is predicted to hold for Dirac spin-1/2 particles, which gives us another piece of information regarding the nature of the nucleon's constituents.

2.2.4 Nuclei

If the scattering center is a nuclear targets, such as ^{3}He, there are several additional reaction channels to be considered that do not occur in pure electron-nucleon scattering. A schematic showing the relative positions of the various reaction channels is shown in figure 4.1.

The simplest reaction we can consider is again elastic scattering. From equation 2.19 it is clear that coherent scattering off of a nuclear target occurs at:

$$\nu_{el} = \frac{Q^2}{2M_T} \tag{2.27}$$

The elastic Rosenbluth formulae is applicable as long as the electric and magnetic form factors of the nucleus are substituted for the nucleonic form factors in equation 2.12.

The ^{3}He system can be broken into a deuteron-proton pair when the energy of the incoming photon is larger than the binding energy of the nucleus. This **two body breakup** requires approximately 5.5 MeV. Complete breakup occurs at 7.7 MeV.

Quasielastic Scattering

Quasielastic scattering can be understood in the impulse approximation (IA) as the elastic scattering of the incoming electron from an individual nucleon within the target nucleus. As such, the reaction occurs at a recoil $\nu = E - E'$ given by equation 2.11, but with the peak shifted slightly due to the nuclear binding energy and broadened significantly by the Fermi motion of the nucleons within the nucleus.

The Rosenbluth formula is generalized to the form:

$$\left(\frac{d^2\sigma}{d\Omega dE'}\right) = \left(\frac{d\sigma}{d\Omega}\right)_{\text{Mott}} \left\{ \left(\frac{Q^2}{\vec{q}^{\,2}}\right)^2 R_L + \left[\frac{1}{2}\left(\frac{Q^2}{\vec{q}^{\,2}}\right)^2 + \tan^2\frac{\theta}{2}\right] R_T \right\} \tag{2.28}$$

where $\mathrm{R}_L(\nu, Q^2)$ and $\mathrm{R}_T(\nu, Q^2)$ parametrize the response to longitudinally and transversely polarized virtual photons.

2.3 Tensor Formulation

The various scattering formulae introduced thus far are, in fact, a natural consequence of relativistic Lorentz invariance. The tensor formulation presented in this section also provides a natural way to introduce target and beam spin degrees of freedom.

We consider the doubly-polarized inclusive reaction

$$\vec{e}(p) + \vec{N}(P) \rightarrow e(p') + X \tag{2.29}$$

This represents the inelastic scattering of electrons on hadrons (nucleons or nuclei) without detection of the final hadronic state X.

The differential cross section can be expressed as a product of hadronic and leptonic tensors [2]:

$$\frac{d^2\sigma}{d\Omega dE'} = \frac{\alpha^2}{Q^4}\frac{E'}{E}\ell_{\mu\nu}W^{\mu\nu} \tag{2.30}$$

The lepton tensor is exactly calculable in QED and is given by

$$\ell_{\mu\nu} \;=\; \sum_{s'} \overline{u}_s(p)\gamma_\mu u_{s'}(p')\gamma_\nu u_s(p) \tag{2.31}$$

where the u represent the lepton Dirac spinors and γ_μ is one of the Dirac matrices. Neglecting the small electron rest mass, the tensor can be expressed

$$\ell_{\mu\nu} \;=\; 2\left[p_\mu p'_\nu + p'_\mu p_\nu - g_{\mu\nu} p\cdot p' + i\epsilon_{\mu\nu\alpha\beta}\mathrm{s}^\alpha q^\beta\right] \tag{2.32}$$

where $\mathrm{s}_\mu = \overline{u}\gamma_\mu\gamma_5 u$ defines the lepton spin vector, $g_{\mu\nu}$ is the metric tensor, and the Levi-Cevita tensor has the property $\epsilon_{0123} = +1$. For an unpolarized incident beam the anti-symmetric part of 2.32 vanishes when averaged over the initial spin.

The hadron tensor, on the other hand, is not yet calculable from first principles. It parameterises our lack of knowledge of the hadronic vertex in figure 2.1. If we consider all possible transitions from the normalized hadronic ground state $|N_s(P)\rangle$ (where s is the spin of the target) to any excited state $|X(P')\rangle$, the tensor takes the form

$$\begin{aligned} W_{\mu\nu} &= \frac{2\pi^2}{2M}\sum_X \langle N_s(P)|J_\mu(0)|X(P')\rangle\langle X(P')|J_\nu(0)|N_s(P)\rangle \\ &\qquad \cdot\,\delta(q+P-P') \end{aligned} \tag{2.33}$$

where J^μ is the electromagnetic current operator and the delta function ensures conservation of energy and momentum.

Using the completeness of states $|X\rangle$ gives

$$W_{\mu\nu} = \frac{1}{4\pi}\int d^4\xi\; e^{iq\cdot\xi}\langle N_s(P)|J_\mu(\xi)J_\nu(0)|N_s(P)\rangle \tag{2.34}$$

where ξ is the spatial four-vector. The hadronic tensor can be decomposed into a symmetric and antisymmetric part $W_{\mu\nu} = W^S_{\mu\nu} + W^A_{\mu\nu}$, which are necessarily linear combinations of all possible Lorentz-covariant tensors. Taking into account parity and time reversal invariance, the most general expressions involving the relevant tensors are:

$$\begin{aligned} W^S_{\mu\nu} &= W_1(\nu,Q^2)\left(\frac{q_\mu q_\nu}{q^2} - g_{\mu\nu}\right) \\ &\quad + W_2(\nu,Q^2)\frac{1}{M^2}\left(P_\mu - \frac{P\cdot q}{q^2}q_\mu\right)\left(P_\nu - \frac{P\cdot q}{q^2}q_\nu\right) \end{aligned} \tag{2.35}$$

and

$$W^A_{\mu\nu} = -i\epsilon^{\mu\nu\alpha\beta}q_\alpha\Big[\; S_\beta G_1(\nu,Q^2) + (M\nu S_\beta - S\cdot qP_\beta)G_2(\nu,Q^2)\;\Big] \tag{2.36}$$

where

$$\mathrm{S}^\mu = \frac{\overline{u}(P)\gamma^\mu\gamma_5 u(P)}{2M} \tag{2.37}$$

represents the hadronic spin vector which reduces to $\mathrm{S}^\mu = (0, \chi_s^\dagger\vec{\sigma}\chi_s)$ for a target at rest, and χ_s are the two component Pauli spinors.

Notice the introduction here of two additional structure functions G_1 and G_2 that are necessary to describe the interaction when polarization degrees of freedom are accounted for. As in the case of the unpolarized structure functions (see equation 2.24), G_1 and G_2 are often replaced by the corresponding dimensionless quantities factors[||]:

$$g_1(x, Q^2) = M\nu G_1(\nu, Q^2) \tag{2.38}$$

$$g_2(x, Q^2) = \nu^2 G_2(\nu, Q^2) \tag{2.39}$$

If we average over target and projectile spin, we can recover the Rosenbluth formulae of equation 2.23 for unpolarized scattering. In the case of elastic scattering the structure functions W_1 and W_2 are expressed in terms of the electromagnetic form factors

$$W_1(\nu, Q^2) = \delta\left(\nu - \frac{Q^2}{2M}\right) \frac{Q^2}{4M^2} G_M^2(Q^2) \tag{2.40}$$

$$W_2(\nu, Q^2) = \delta\left(\nu - \frac{Q^2}{2M}\right) \frac{G_E^2(Q^2) + \frac{Q^2}{4M^2} G_M^2(Q^2)}{1 + \frac{Q^2}{4M^2}} \tag{2.41}$$

Insertion of these relations into 2.23 leads back to the elastic scattering relation of equation 2.12.

2.4 Physical Meaning of the Structure Functions

To facilitate the interpretation of the structure functions, Feynman [11] and Bjorken [12] introduced the parton model: In a fast moving reference frame, the transverse momenta and rest mass of the nucleon's constituents can be neglected, so the structure can be described in a first approximation by the longitudinal momenta of the constituents or "partons". Today, the charged partons are associated with quarks, and the neutral partons with gluons. The quarks are further categorized between the 'valence' quarks which are responsible for the quantum numbers of the nucleon and the 'sea' quarks, which are quark-antiquark pairs created spontaneously from the vacuum.

Scattering is viewed as an incoherent sum of the interactions with each individual parton. If the interaction time is short enough, the scattering can be viewed in the impulse approximation (IA) as the elastic scattering from an individual parton and the parton-parton interactions can be ignored. This is expected to be valid in DIS where $Q^2 \gg M^2$ and the partons are asymptotically free.

The parton model provides an interpretation of the Bjorken variable x in the following manner [2]: The partons each carry some fraction of the

---

[||] Unfortunately there are several different choices possible for G_1, G_2, depending on the initial normalization of the hadronic tensor. We follow the convention used in ref. [10].

nucleon momentum which we will call ξ. Since parton masses are neglected, we find

$$(\xi P + q)^2 = \xi^2 M^2 - Q^2 + 2\xi P \cdot q \approx 0 \tag{2.42}$$

If we also consider the nucleon mass M^2 to be small compared to Q^2 we find:

$$\xi = \frac{Q^2}{2P \cdot q} \equiv x \tag{2.43}$$

So in this approximation, x is the fraction of nucleon momentum carried by the struck quark.

Similarly, the parton model provides insight into the physical meaning of the Lorentz invariant structure functions. If we define $q_f(x)dx$ $\{$ and $\overline{q}_f(x)dx$ $\}$ as the expectation value for the number of quarks $\{$ and antiquarks $\}$ of flavor f in the hadron whose momentum fraction lies in the interval $[x, x+dx]$, then in the parton model it can be shown that:

$$F_1(x) = \frac{1}{2} \sum_f z_f^2 \left(q_f(x) + \overline{q}_f(x) \right) \tag{2.44}$$

and

$$g_1(x) = \frac{1}{2} \sum_f z_f^2 \left(q_f(x) - \overline{q}_f(x) \right) \tag{2.45}$$

where the quark charge z_f enters due to the fact that the cross section is proportional to the squared charge of the target.

The Callan-Gross [9] relation mentioned previously gives F_2 in terms of F_1:

$$F_2(x) = 2xF_1(x) \tag{2.46}$$

but there is no simple physical interpretation of g_2 in the parton model.

2.5 Virtual Photon Cross Sections

The previous sections revealed that the inclusive scattering process can be described in terms of four structure functions. We now consider an alternative (but equivalent) formulation in which the inclusive process $\vec{e} + \vec{N} \rightarrow e + X$ is parameterized in terms of four virtual photoabsorption cross sections [13]:

$$\frac{d\sigma}{d\Omega dE'} = \Gamma\left(\sigma_T + \varepsilon\sigma_L + hP_x\sqrt{2\varepsilon(1-\varepsilon)}\sigma'_{LT} + hP_z\sqrt{1-\varepsilon^2}\sigma'_{TT}\right) \quad (2.47)$$

Here, ε is the ratio of longitudinal to transverse polarization of the virtual photon:

$$\varepsilon = \left[1 + 2\left(1 + \frac{\nu^2}{Q^2}\right)\tan^2\frac{\theta}{2}\right]^{-1} \quad (2.48)$$

which of course goes to zero when $Q^2 = 0$. Γ represents the flux factor:

$$\Gamma = \frac{\alpha}{2\pi^2}\frac{E'}{E}\frac{K}{Q^2}\frac{1}{1-\varepsilon} \quad (2.49)$$

which depends on the choice of the virtual photon flux K.**

The cross sections are all functions of the virtual photon energy ν and momentum transfer Q^2 in the lab frame, although we have suppressed the explicit dependence in equation 2.47. σ_T and σ_L represent the cross section for absorption of transverse and longitudinal virtual photons, while the remaining two cross sections represent longitudinal-transverse and transverse-transverse interference terms. Notice that both σ_L and σ'_{LT} decouple in the limit $Q^2 \to 0$. In the unpolarized case, σ_T reduces to the total photoabsorption cross section at $Q^2 = 0$. Finally, h represents the helicity†† of the incoming electron, and P_x (P_y) is the target polarization parallel (perpendicular) to the virtual photon momentum.

We now introduce $\sigma_{3/2}$ and $\sigma_{1/2}$, the helicity dependent photo-absorption cross sections for the polarized scattering of photons. The subscripts refer to the total photon plus target helicity projection. (See figure 2.2.) These two quantities are related to σ'_{TT} the "transverse-transverse" cross section through:

$$2\sigma'_{TT} = \sigma_{\frac{3}{2}} - \sigma_{\frac{1}{2}} \quad (2.50)$$

The relationship between the photoabsorption cross sections and the standard structure functions is straightforward [14]:

$$\sigma_T = \frac{4\pi^2\alpha}{mK}F_1 \quad (2.51)$$

**K is discussed in further detail below.

††See equation 3.4.

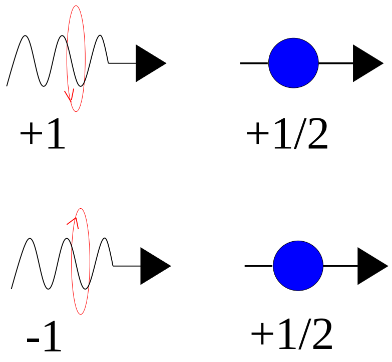

Figure 2.2: Helicity projection for the virtual photo-absorption cross sections $\sigma_{3/2}$ and $\sigma_{1/2}$.

$$\sigma_L = \frac{4\pi^2\alpha}{K}\left[\frac{F_2}{\nu}(1+\gamma^2) - \frac{F_1}{m}\right] \tag{2.52}$$

$$\sigma'_{LT} = -\frac{4\pi^2\alpha}{mK}\gamma(g_1+g_2) \tag{2.53}$$

$$\sigma'_{TT} = -\frac{4\pi^2\alpha}{mK}(g_1-\gamma^2 g_2) \tag{2.54}$$

where $\gamma^2 = Q^2/\nu^2$. The correspondence is reliant on the virtual photon flux K, which is not a well defined physical quantity. Several conventions have been proposed:

$$K_{\mathsf{A}} = \nu \tag{2.55}$$

$$K_{\mathsf{G}} = \sqrt{\nu^2+Q^2} \tag{2.56}$$

$$K_{\mathsf{H}} = \frac{W^2-M^2}{2M} = \nu - \frac{Q^2}{2M} \tag{2.57}$$

The first convention K_{A} simply associates the flux with the photon energy ν. The second, due to Gilman [15], chooses $|\vec{q}|$ the lab momentum of the virtual photon, and the final convention due to Hand [16], represents the equivalent energy necessary for the same reaction from a real photon. Notice that all three conventions reduce to ν for the real photon scattering at $Q^2 = 0$. In DIS all three conventions also give numerically similar results, but in the intermediate Q^2 region, K is strongly convention dependent.

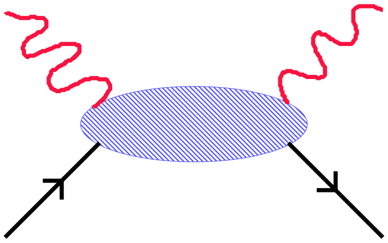

Figure 2.3: Compton scattering.

2.6 Compton Scattering

We now consider the elastic *real* photon scattering process

$$\gamma(k) + N(P) \to \gamma(k') + N(P') \tag{2.58}$$

The photon has four momentum k with $k'^2 = k^2 = 0$. In the lab frame $P^\mu = (M, 0)$ and $\omega = |\vec{k}|$ is the energy of the incoming photon, which is scattered at an angle θ. The incident and scattered energy are restricted by energy-momentum conservation to satisfy

$$\omega' = \frac{\omega}{1 + \frac{\omega}{M}(1 - \cos\theta)} \tag{2.59}$$

The linear polarization vectors of the photon $\varepsilon^\mu = (0, \vec{\varepsilon})$ satisfies $\vec{k} \cdot \vec{\varepsilon} = 0$ due to the transverse nature of real photons. If we set the coordinate z-axis to be along the photon momentum vector $\vec{k}$, linearly polarized photons are described as

$$\vec{\varepsilon}_x = (1, 0, 0) \tag{2.60}$$

$$\vec{\varepsilon}_y = (0, 1, 0) \tag{2.61}$$

and circularly polarized photons are given by

$$\vec{\varepsilon}_{\lambda=1} = \frac{1}{\sqrt{2}}(\vec{\varepsilon}_x + i\vec{\varepsilon}_y) \tag{2.62}$$

$$\vec{\varepsilon}_{\lambda=-1} = \frac{1}{\sqrt{2}}(\vec{\varepsilon}_x - i\vec{\varepsilon}_y) \tag{2.63}$$

with $\vec{\varepsilon}^{\,*}_{\lambda} \cdot \vec{\varepsilon}_{\lambda} = \delta_{\lambda'\lambda}$. The differential cross section [2] for Compton scattering is

$$\left(\frac{d\sigma}{d\Omega}\right) = \left(\frac{\omega'}{8\pi M\omega}\right)^2 |T_{fi}|^2 \tag{2.64}$$

with the T-matrix

$$T_{fi} = e^2 \varepsilon'^{*\mu} \varepsilon^{\nu} T_{\mu\nu} \tag{2.65}$$

and the Compton tensor $T_{\mu\nu}$ given by

$$T_{\mu\nu} = i \int d^4\xi \; e^{ik'\cdot\xi} \langle N_s(P') | \mathcal{T} J_\mu(\xi) J_\nu(0) | N_s(P) \rangle \tag{2.66}$$

For forward scattering $\vec{k'} = \vec{k}$ and the T-matrix reduces to

$$T_{fi}(\omega, 0) = (8\pi M) \; \chi_f^\dagger \left[f(\omega) \vec{\varepsilon'}^\dagger \cdot \vec{\varepsilon} + i g(\omega) \vec{\sigma} \cdot \left(\vec{\varepsilon'}^\dagger \times \vec{\varepsilon} \right) \right] \chi_i \tag{2.67}$$

where the χ are the Pauli spinors and f and g represent the non-spin flip and spin flip amplitudes respectively.

The total photo-absorption cross section is related to the imaginary part of the f amplitude by

$$\sigma_{\mathsf{Tot}} = \frac{4\pi}{\omega} Im f(\omega) \tag{2.68}$$

We can generalize the above discussion to treat virtual photon scattering by replacing k with q and keeping in mind that $q^2 \neq 0$. This is known as "virtual-virtual Compton Scattering" or V^{2}CS in the literature(e.g. [10]). It is interesting to note that $T_{\mu\nu}$ differs from the hadronic tensor only by the time ordering $\mathcal{T}$ of the electromagnetic currents. In fact, the hadronic tensor $W_{\mu\nu}$ is related to the forward virtual Compton tensor by:

$$W_{\mu\nu}(\nu, Q^2) = \frac{1}{2\pi M} Im \; T_{\mu\nu}(\nu, Q^2) \tag{2.69}$$

This relation indicates that we can expect the hadronic tensor components to be related to the Compton tensor components via standard Kronig and Kramers-type dispersion relations. We will exploit this feature extensively in section 4.6

CHAPTER 3

THEORETICAL TOOLBOX

In this chapter, we will examine some of the most common theoretical methods available to predict the Q^2 evolution of the structure functions from the real photon point to the DIS region. We also consider several extremely useful phenomenological models which provide some guidance to the Q^2 behaviour, although they are not, strictly speaking, a direct consequence of the underlying theory.

3.1 Chiral Perturbation Theory

QCD is the non-abelian gauge theory of colored quarks and gluons. The complete QCD lagrangian is [17]:

$$\mathcal{L}_{\mathtt{QCD}} = -\frac{1}{4g^2} G^{\alpha}_{\mu\nu} G^{\mu\nu}_{\alpha} + \overline{q} i \gamma^{\mu} D_{\mu} q - \overline{q} \mathcal{M} q \tag{3.1}$$

where G is the gluon field strength, q is the quark spinor, and $\mathcal{M}$ is the diagonal quark mass matrix.

For low energy interactions, it is impractical to deal directly with quarks and gluons in QCD. Instead, processes are best studied in terms of an effective theory that addresses composite hadrons as the *de facto* degrees of freedom. An effective lagrangian is formed that replaces 3.1 in the low energy limit, but which still reproduces the symmetries and symmetry breaking patterns of the fundamental theory [2].

Due to the small mass values of the u, d and s quark compared to typical hadronic mass scales*, we consider the limit where the quark masses vanish. Then equation 3.1 takes the form

$$\mathcal{L}_{\mathtt{QCD}} = \mathcal{L}^0_{\mathtt{QCD}} + \mathcal{L}'_{\mathtt{QCD}} \tag{3.2}$$

---

*e.g. the mass of the first non-Goldstone resonance M_{ρ}, or the nucleon mass M_p.

with

$$\mathcal{L}'_{\mathtt{QCD}} = -\overline{q}\mathcal{M}q \tag{3.3}$$

regarded as a perturbation to $\mathcal{L}^0_{\mathtt{QCD}}$. For this to be a reasonable approach, the eigenvalues of the quark mass matrix have to be small compared to the typical energy scale of any system under consideration.

Recall that the state of a free *massive* fermion is completely determined by its energy, momentum and helicity $\hat{h}$:

$$\hat{h} = \frac{\vec{\sigma} \cdot \vec{p}}{|\vec{p}|} \tag{3.4}$$

For a massless fermion, **chirality**[†] is identical to helicity, and is a constant of motion. The central idea of Chiral Perturbation Theory is that the massless left and right handed quarks defined by:

$$q_{\mathrm{L,R}} = \frac{1}{2}(1 \mp \gamma_5)q \tag{3.5}$$

do not interact with each other so that the theory admits a $U(3)_L \times U(3)_R$ symmetry. Explicit breaking of this symmetry is then treated as a perturbation. As with all effective field theories, at some high energy the theory will fail and must be superseded by a more fundamental approach.

3.2 Lattice Gauge Theory

Lattice Gauge Theory (LGT) is a rapidly developing field that provides a method for the non-perturbative calculation of hadron structure at low energies. In LGT the inherent difficulties of solving QCD analytically are avoided by discretizing space-time. Numerical methods requiring substantial investment of computer power are applied to solve the resulting discrete equations on the lattice.

Some calculations for the moments of the polarized structure functions have been performed (e.g. [18]), but the techniques are still relatively new and have not yet achieved high accuracy in describing dynamical processes.

3.3 The Operator Product Expansion

The operator product expansion (OPE) provides direct QCD predictions for the moments of the structure functions in the form of sum rules. No model

---

[†] from the Greek word for hand: χὲρι

is necessary, and the main results depend only on some very general results from Quantum Field Theory.

The expansion was introduced [19] as a way to evaluate the nonperturbative part of QCD calculations. The OPE gets its name because it allows the evaluation of products of operators (such as the electromagnetic currents $J_\mu(\xi)J_\nu(0)$) in the asymptotic limit. In the OPE, as the four dimensional spatial vector ξ becomes infinitesimal, the product can be expressed as a series [20]:

$$\lim_{\xi \to 0} \mathcal{O}_a(\xi)\mathcal{O}_b(0) = \sum_i C_{abk}(\xi)\mathcal{O}_i(0) \tag{3.6}$$

where we have chosen the coordinate origin to coincide with the point of application of the second operator.

The utility of this decomposition arises from the fact that the Wilson coefficients $C_{abk}(\xi)$ contain all the spatial dependence and can be calculated perturbatively in QCD. It is expected that only the first few terms in equation 3.6 will be significant. The expansion will be valid as long as ξ is small enough or equivalently, Q^2 large enough compared to the relevant mass scale $(\Lambda_{QCD})^2$.

The $\mathcal{O}_i$ are quark and gluon operators of dimension d and spin n, representing the fundamental fields in QCD. We introduce the concept of *twist* τ, which is defined as $\tau = d - n$. The contribution of any operator to $\ell_{\mu\nu}W^{\mu\nu}$, i.e. the differential cross section, is of order:

$$\omega^n \left(\frac{M}{Q}\right)^{\tau-2} \tag{3.7}$$

The lowest possible τ is twist-2, and higher twists are suppressed by increasing powers of $\frac{M}{Q}$. The reliable parts of the parton model (see section 2.4) map onto the leading twist part of OPE [21], while twist-3 and higher arise from quark-gluon interactions and non-zero quark mass effects.

Starting from the matrix element for virtual Compton scattering (see section 2.6) and then making a connection to the hadronic tensor $W_{\mu\nu}$ through the optical theorem (see section B.2), the twist expansion leads to an infinite set of sum rules for the structure functions, both spin-dependent and independent. Disregarding contributions beyond twist-3, the series for g_1 and g_2 are:

$$\int_0^1 x^{n-1} g_1(x, Q^2)dx = \frac{1}{2}a_{n-1} \qquad n = 1, 3, 5, \ldots \tag{3.8}$$

$$\int_0^1 x^{n-1} g_2(x, Q^2) dx = \frac{n-1}{2n}(d_{n-1} - a_{n-1}) \qquad n = 3, 5, \ldots \tag{3.9}$$

where a_{n-1} are the twist-2 and d_{n-1} the twist-3 matrix elements of the renormalized quark and gluon operators. Notice that 3.8 and 3.9 involve only odd moments due to the symmetry properties of the structure functions under charge conjugation.

These relations reveal that measurements at high Q^2 of the spin structure functions over the entire x range allow extraction of the higher twist matrix elements arising from parton interactions. The most striking consequence of this interaction is confinement, so the study of higher twists provides a tool to examine one of the fundamental properties of QCD. At low Q^2, we can expect the higher twist effects to become more and more significant and the twist expansion to break down.

3.3.1 Wandzura–Wilczek Relation

Combining equations 3.8 and 3.9, the leading twist terms cancel, and we get

$$\int_0^1 x^{n-1} \left(g_1(x, Q^2) + \frac{n}{n+1} g_2(x, Q^2) \right) dx = \frac{d_n}{2} \qquad n \geq 3 \tag{3.10}$$

If we set the twist-3 d_n terms to zero, and apply the convolution theorem for Mellin transforms to equation 3.10 we obtain the Wandzura–Wilczek [22] relation[‡]:

$$g_2^{\mathtt{WW}}(x, Q^2) = -g_1(x, Q^2) + \int_x^1 \frac{dy}{y} g_1(y, Q^2) \tag{3.11}$$

This relation shows that the leading twist part of the g_2 structure function is determined completely by g_1, and can therefore be interpreted in terms of the parton model.

The separation of $g_2(x, Q^2)$ into leading and higher-twist components can be expressed:

$$g_2(x, Q^2) = g_2^{\mathtt{WW}}(x, Q^2) + \overline{g}_2(x, Q^2) \tag{3.12}$$

$$\overline{g}_2(x, Q^2) = -\int_x^1 \frac{\partial}{\partial y} \left[\frac{m_q}{M} h_T(y, Q^2) + \zeta(y, Q^2) \right] \frac{dy}{y} \tag{3.13}$$

We see that, to twist-3, there are three contributions to g_2:

[‡] The OPE says nothing about the n=1 term of the g_2 series. [21]. Because of this, the derivation of the $g_2^{\mathtt{WW}}$ formulae shown here implicitly assumes that the Burkhardt–Cottingham sum rule (see equation 4.38) is true.

- $g_2^{\mathtt{WW}}$: The leading twist-2 term, which depends only on g_1
- h_T : Arises from the quark transverse polarization distribution. Also twist-2, this term is suppressed by the smallness of the quark mass.
- ζ : The twist-3 part which arises from quark-gluon interactions.

3.3.2 d$_2$ and Higher Twists

Equation 3.9 defined the twist-3 matrix elements d$_n$. Higher powers of n are suppressed by increasing factors of 1/Q^2, so in this section we restrict our consideration to the n = 2 element.

$$d_2(Q^2) = 3\int_0^1 x^2 \left[g_2(x,Q^2) - g_2^{\mathtt{WW}}(x,Q^2)\right] dx$$

We can re-express this as a higher moment of a simple linear combination of the g$_1$ and g$_2$ structure functions by making use of relation E.7.

$$d_2(Q^2) = \int_0^1 x^2 \left[2g_1(x,Q^2) + 3g_2(x,Q^2)\right] dx \tag{3.14}$$

d$_2(Q^2)$ measures the deviation of the g$_2$ structure function from leading twist behaviour. Experimentally, the x-weighting ensures that by far the most significant contribution to the integral comes from the large x region that is kinematically accessible at JLab.

3.3.3 Higher Twist Effects in g$_1$

The generalization of equation 3.8 to include all orders of higher twist is

$$\Gamma_1(Q^2) = \sum_{\tau=2,4,\ldots} \frac{\mu_\tau(Q^2)}{Q^{\tau-2}} \tag{3.15}$$

where $\Gamma_1(Q^2) = \int dx\ g_1(x,Q^2)$. Notice that the OPE sums over all possible states and requires inclusion of the elastic contribution in equation 3.15.

We can gain access to the higher twist contributions to Γ_1 by subtracting the leading ($\tau = 2$) twist $\mu_2(Q^2)$ term from the experimentally measured first moment [23, 24]. Up to $\mathcal{O}(\alpha_s^3)$ in the strong coupling constant for three quark flavors, the result for the leading twist terms of Γ_1 is given by [25, 26]:

$$
\begin{aligned}
\mu_2^{p(n)}(Q^2) &= \left[1-\left(\frac{\alpha_s}{\pi}\right)-3.58\left(\frac{\alpha_s}{\pi}\right)^2-20.22\left(\frac{\alpha_s}{\pi}\right)^3\right]\left(\pm\frac{1}{12}g_A+\frac{1}{36}a_8\right) \\
&+ \left[1-\frac{1}{3}\left(\frac{\alpha_s}{\pi}\right)-0.55\left(\frac{\alpha_s}{\pi}\right)^2-4.45\left(\frac{\alpha_s}{\pi}\right)^3\right]\frac{1}{9}\Delta\Sigma \qquad (3.16)
\end{aligned}
$$

The ± refers to proton and neutron respectively. The above expression depends on the following quantities[§]:

- α_s : The strong coupling constant.
- g_A : The non-singlet triplet axial charge measured in neutron β decay.
- a_8 : The octet axial charge, extracted from weak hyperon decays.
- $\Delta\Sigma$: The singlet axial current.

The first contribution beyond leading order to Eq. 3.15 is the $\frac{1}{Q^2}$ term:

$$\mu_4(Q^2) = \frac{1}{9}M^2\left[a_2(Q^2)+4d_2(Q^2)-4f_2(Q^2)\right] \qquad (3.17)$$

where a_2, the second moment of the g_1 arises from the target mass correction and is pure twist-2. We encountered d_2 in section 3.3.2, where it was revealed to be primarily twist-3. f_2 represents the only pure twist-4 contribution to $\mu_4(Q^2)$. Accurate determination of d_2 is necessary for the extraction of f_2.

The twist-3 and 4 operators contain all the interaction terms and collectively describe the response of the color electric and magnetic fields to the presence of the nucleon spin. This behaviour is contained in the color electric and magnetic polarizabilities χ_E and χ_B [27, 28] which are illustrated schematically in figure 3.1.

The relationship between the matrix elements and the polarizabilities is

$$\chi_E = \frac{2}{3}(2d_2+f_2) \qquad (3.18)$$

$$\chi_B = \frac{1}{3}(4d_2-f_2) \qquad (3.19)$$

3.3.4 Quark-Hadron Duality

In the 1970's Bloom and Gilman [31, 32] observed that the proton's unpolarized structure function $F_2(\nu, Q^2)$ in the resonance region roughly averaged

---

[§] For a more detailed discussion, see Ref [23].

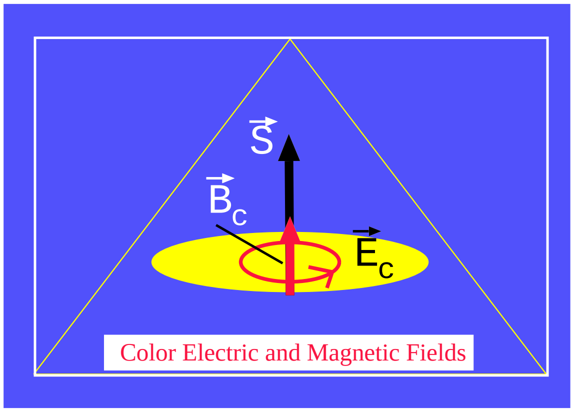

Figure 3.1: The response of the color electric and magnetic fields to the presence of the nucleon spin $\vec{S}$.

to the scaling limit value of $F_2(x)$. It appeared that the resonance contributions fell at roughly the same rate as the non-resonant background as Q^2 increases. The phenomenon is discussed in terms of "local" duality, in which the averaging is satisfied for each individual resonance and in terms of "global" duality, in which an average over all resonances is considered. Of course, demonstrations of duality will depend on the choice of scaling variable. The standard in recent years has become the Nachtman variable ξ which generalizes x to include non-zero quark mass effects:

$$\xi = \frac{2x}{1+\sqrt{1+\frac{4M^2x^2}{Q^2}}} \tag{3.20}$$

Figure 3.2 displays a recent confirmation [30] of duality in the proton and deuteron's unpolarized structure functions.

The initial work of Bloom and Gilman was expanded in refs. [33, 34, 35] to address duality in terms of the operator product expansion, by examining the twist expansion of the F_2 structure function. In this context, duality states that the moments of the structure functions in the resonance region are equal to the same moments evaluated in DIS, except for standard PQCD corrections. In this context, duality is expected to hold whenever higher twist corrections are small. More recently there has been several theoretical investigations into the manifestation of duality in the polarized structure functions. See for example [36, 37, 38]. An experiment [39] dedicated to investigating this phenomenon in the polarized structure functions

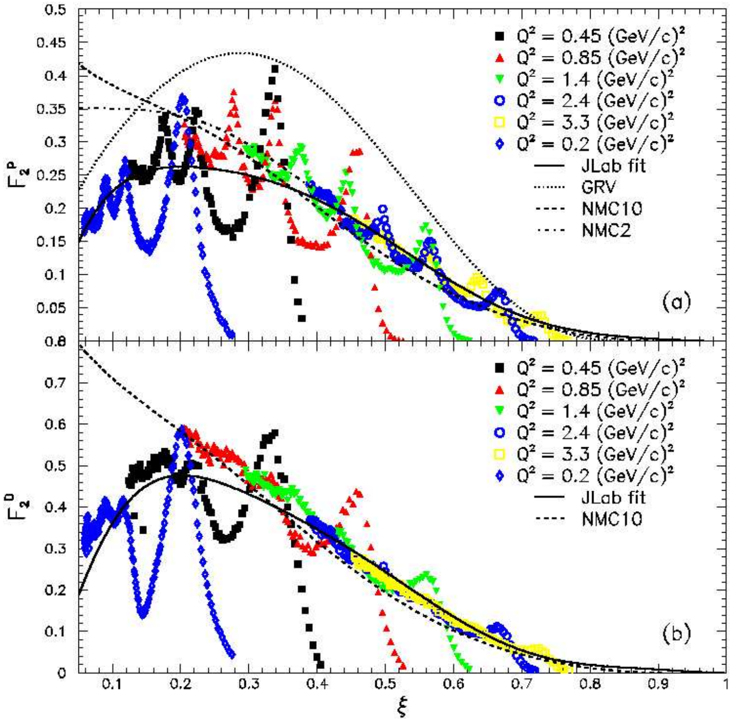

Figure 3.2: The F_2 structure function for hydrogen (a) and deuterium (b) plotted as a function of ξ. Also shown are several scaling curves: NMC parameterization at $Q^2 = 2\ GeV^2$ (NMC2) and $Q^2 = 10\ GeV^2$ (NMC10); JLab fit obtained using low Q^2 SLAC data a low ξ. In (a), the dotted curve is F_2 obtained from the input valence-like quark distributions of Gluck, Reya and Vogt [29]. *This figure reproduced from [30].*

was recently completed at JLab.

It is hoped that by understanding duality, we can understand the resonance region's connection to the parton picture of DIS. Duality also presents the possibility that measurement of the structure functions in the resonance region will allow determination of the structure functions in the high x scaling region which is otherwise inaccessible kinematically.

3.4 Phenomenological Model Predictions

Several models exist which parameterize existing world data in order to make phenomenological predictions in the kinematic regions of interest to E94-010. We will examine several in this section. In this discussion the following definitions will be needed:

$$I_1(Q^2) = \frac{2M^2}{Q^2}\int g_1(x,Q^2)dx \tag{3.21}$$

$$I_2(Q^2) = \frac{2M^2}{Q^2}\int g_2(x,Q^2)dx \tag{3.22}$$

$$I_T(Q^2) = \frac{2M^2}{Q^2}\int g_T(x,Q^2)dx \tag{3.23}$$

where $g_T = g_1 + g_2$.

3.4.1 MAID

The unitary isobar model MAID [40] relies on phenomenological fits to electro- and photo-production data for the nucleon from the single-pion production threshold to the conventional resonance region limit, $W = 2$ GeV. The major resonances[¶] are modeled using Breit-Wigner functions in order to construct the pion, eta and higher production channels. The contribution of the resonances to the transverse cross sections is given by:

$$\sigma_{\frac{1}{2}(\frac{3}{2})} = \frac{4M}{W_0\Gamma_0}A^2_{\frac{1}{2}(\frac{3}{2})}B(\nu,Q^2) \tag{3.24}$$

Here, $B(\nu,Q^2)$ represents the generalization to electroproduction of the Breit-Wigner form, M is the nucleon mass, W_0 is the mass of the resonance, Γ_0 is the resonance width and $A_{\frac{1}{2}(\frac{3}{2})}$ is the relevant photo-coupling helicity amplitude. A non-resonant background and vector meson exchanges are also included.

3.4.2 Burkert and Ioffe

Anselmino, Ioffe and Leader [41] proposed a vector meson dominance [42, 43] (VDM) inspired model for the I_1 integral that interpolates smoothly from the asymptotic value measured at high Q^2, down to the value required by

---

[¶] $P_{33}(1232)$, $P_{11}(1440)$, $D_{13}(1520)$, $S_{11}(1535)$, $F_{15}(1680)$, and $D_{33}(1700)$

the GDH sum rule[‖] at $Q^2 = 0$. A minimum of two parameters are needed for such a model. The functional form of the interpolating function chosen by the authors is:

$$I_1^{\mathtt{VDM}}(Q^2) = 2M^2 \left[\frac{1}{Q^2 + \mu^2} - c \frac{\mu^2}{(Q^2 + \mu^2)} \right] \Gamma_1(\infty) \tag{3.25}$$

where $\mu \approx M_\rho$ sets the scale of the Q^2 evolution and c is chosen such that $I_1^{\mathtt{VDM}}(0)$ satisfies the GDH sum rule. The authors argue that the two terms on the rhs of 3.25 plausibly represent the dominant two diagrams in a VDM description of the photon-nucleon interaction, although they have not been rigorously derived.

The original model ignored the large contribution of the resonant states at low Q^2, so it was updated in [44] and [45] to explicitly include contributions from the resonances up to $W = 1.8$ GeV, based on existing pion electroproduction data. The resonance model has become known as AO and does not consider any Born or other non-resonant terms.

The final model of Burkert and Ioffe for the I_1 integral of the nucleon is:

$$I_1(Q^2) = I_1^{\mathtt{VDM}}(Q^2) + I_1^{\mathtt{Res}}(Q^2) \tag{3.26}$$

where the parameter c in equation 3.25 is given by:

$$c = 1 + \frac{1}{2} \frac{\mu}{M} \frac{1}{\Gamma_1(\infty)} \left[\frac{\kappa^2}{4} + I_1^{\mathtt{Res}}(0) \right] \tag{3.27}$$

The mass M, anomalous magnetic moment κ and asymptotic values of the integral must be set according to which nucleon is being examined.

3.4.3 Soffer and Teryaev

The model of Soffer and Teryaev [46] starts from the assumption that the $I_T(Q^2)$ integral should exhibit smooth behaviour as it evolves from DIS to low Q^2.

The Burkhardt–Cottingham [47] sum rule[**] is assumed valid by the authors, which implies that the inelastic contribution to I_2 is given by [48, 49]:

$$I_2(Q^2) = \frac{\mu G_M(Q^2)}{4} \left[\frac{\mu G_M(Q^2) - G_E(Q^2)}{1 + \frac{Q^2}{4M^2}} \right] \tag{3.28}$$

[‖] See section 4.1.

[**] See equation 4.38.

At the real photon point, the GDH sum rule gives $I_1(0) = -\frac{\kappa^2}{M^2}$, while the Schwinger sum rule indicates $I_2(0) = \frac{\kappa(\kappa+e)}{4}$. Together, these results imply that $I_T(0) = \frac{\kappa e}{4}$ while as $\mathrm{Q}^2 \to \infty$, $I_T \to \frac{2M^2}{Q^2}\Gamma_1(x)$. The large Q^2 behaviour is set to match the existing world data.

For the proton, Soffer and Teryaev construct a smooth interpolation between the asymptotic limits of $I_T^p(Q^2)$. $I_1^p(Q^2)$ is then recovered after subtracting the $I_2^p(Q^2)$ contribution. A similar procedure is followed for the neutron, except the interpolating function is for the isovector difference $I_T^{p-n}(Q^2)$.

CHAPTER 4

SUM RULES AND MOMENTS

In the previous chapter it was revealed that several of the available theoretical tools are aimed at the structure function moments instead of the structure functions directly. In this chapter, we will look at some of the relevant moments measured by E94-010 and the sum rules that govern their behaviour. In particular, we will examine the first moments of g_1 and g_2, along with the higher moments that lead to the d_2 matrix element and the extended GDH sum.

4.1 The GDH Sum Rule

The Gerasimov-Drell-Hearn sum rule for *real* photon scattering at $Q^2 = 0$ is an important prediction of QCD that relies on only a few general assumptions:

1. Lorentz and gauge invariance in the form of the low energy theorem of Low [50], Goldman and Goldberger [51].
2. Unitarity in the form of the optical theorem.
3. Causality in the form of an unsubtracted dispersion relation [52] for forward Compton scattering.

Drell and Hearn [53] modestly described their role as "very simply . . . joining the dispersion relation and the low-energy theorem with the no-subtraction assumption" to form an experimentally testable sum rule. Gerasimov [54, 55], along with Hosoda and Yamamoto [56] independently derived this same result.

A sum rule for real photon scattering may seem like a peculiar topic with which to begin our discussion of the higher moments of electro-production structure functions, but we will see that the GDH sum rule provides a natural reference at the real photon point which can be extended to a much more general treatment involving virtual photon scattering at arbitrary Q^2. The details of the sum rule derivation are summarized in appendix B. Here we present the result for a spin-1/2 target:

$$\int_{\nu_{th}}^{\infty} \frac{\sigma_{3/2}(\nu) - \sigma_{1/2}(\nu)}{\nu} d\nu = -2\pi^2 \alpha \left(\frac{\kappa}{M}\right)^2 \tag{4.1}$$

The integration extends from the onset of the inelastic region, through the entire kinematic range and is weighted by the photon energy ν. M and κ represent the target mass and anomalous magnetic moment respectively. The helicity-dependent photo-absorption cross sections $\sigma_{1/2}$ and $\sigma_{3/2}$ were previously introduced in section 2.5.

Equation 4.1 reveals that a non-zero anomalous magnetic moment is intimately linked to the presence of an internal target structure with a complicated excitation spectrum. It is remarkable, in that it relates static properties of the target ground state to dynamic properties of *all* the excited states. Due to the $1/\nu$ weighting we expect that the low-lying mass resonances will have the most significant contribution to the sum rule. For the nucleons, ν_{thr} in equation 4.1 represents the pion production threshold, and we have the following predictions:

$$\begin{aligned} -2\pi^2 \alpha \left(\frac{\kappa}{m}\right)^2 &= -204\ \mu b \ \ (\text{ Proton;} \quad \kappa = +1.79\ ) \\ &= -234\ \mu b \ \ (\text{ Neutron;}\ \ \kappa = -1.91\ ) \end{aligned} \tag{4.2}$$

Measurements of the total photoabsorption cross section of the proton have been performed at MAMI [57] for photons of energy 200 – 800 MeV, and at ELSA in the range 680 – 3000 MeV. The preliminary combined result of these two experiments in the range 200 MeV $< \nu <$ 2800 MeV is [58]:

$$I_p^{\texttt{GDH}} = 255 \pm 5 \pm 12\ \mu\text{b} \tag{4.3}$$

Theoretical estimates [40] of the unmeasured regions reduce the value to approximately 210 μb, in pretty good agreement with the sum rule prediction.

Efforts to measure the threshold contribution below 200 MeV will soon be underway at HIγS [59], while the high energy region from 3 GeV to 5 GeV will be examined at JLab. Investigations [60] of the neutron using a deuterated butanol target* are also underway at MAMI and ELSA that will cover a photon energy range of 140 MeV to 3000 MeV.

---

*There are also plans for a ^{3}He target.

Arbitrary Target

Equation 4.1 can also be generalized to a target of arbitrary spin $\mathcal{S}$:

$$\int_{\nu_{th}}^{\infty} \frac{\sigma_P(\nu) - \sigma_A(\nu)}{\nu} d\nu = -4\pi^2 \alpha \cdot \mathcal{S} \left(\frac{\kappa}{m} \right)^2 \tag{4.4}$$

where, in this case, σ_P and σ_A represent the cross section for photoabsorption with the photon helicity parallel or anti-parallel to the target spin in its maximal state. For nuclear targets [61], ν_{th} represents the photodisintegration threshold†. We obtain the following sum rule prediction for the two lightest nuclei [62, 63]:

$$\begin{aligned} -4\pi^2 \alpha \cdot \mathcal{S} \left(\frac{\kappa}{m} \right)^2 &= -0.65\ \mu b \ (\text{ Deuteron; } \kappa = -0.143\ ) \\ &= -496\ \mu b \ (\ ^3\text{He; } \qquad \kappa = -8.366\ ) \end{aligned} \tag{4.5}$$

To get an idea of the relative size of the "nuclear" contribution to the sum rule, we divide the integral for ^{3}He into two regions, as shown in figure 4.1. Region I extends from the two-body breakup to the nucleonic pion production threshold, and region II extends from the pion production threshold to ∞. Since ^{3}He *roughly* approximates a free neutron due to the spin pairing of the protons, we can expect the contribution from the region II to be approximately -234 μb. Therefore the contribution in region I is necessarily quite large in order to satisfy the ^{3}He predicted value of -496μb.

The only photoabsorption channel available in region I is photodisintegration. Indeed, Arenhövel [63] points out that the disintegration channel must become significant at low Q^2 in order to satisfy the sum rule prediction for the deuteron. We can anticipate similar behaviour from the ^{3}He nucleus, although recent measurements [64] in the limited range $0 - 53$ keV reveal only a very small contribution thus far.

4.2 Experimental Generalization of the GDH Sum

The GDH sum can be generalized to include an arbitrary Q^2 dependence, i.e. to extend the integral away from the real photon point to treat virtual photons in electron scattering. Many different approaches have been proposed [65, 14], but the most straightforward seems to be to replace the

---

† $\nu_{th} = 2.2$ and 5.5 MeV for the deuteron and ^{3}He respectively

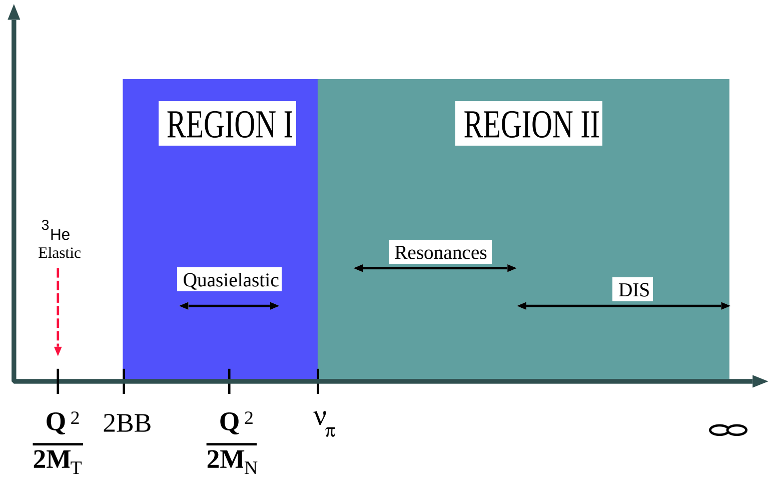

Figure 4.1: The relevant kinematic regions as a function of $\nu = E - E'$. The major distinction is between those reactions below the quasi-free pion production threshold (^{3}He elastic scattering, disintegration, and quasielastic scattering) and those above the pion threshold.

photoproduction cross sections in equation 4.1 with the corresponding quantities from electroproduction:

$$I(Q^2) \quad = \quad \int_{\nu_{th}}^{\infty} \frac{\sigma_{3/2}(\nu, Q^2) - \sigma_{1/2}(\nu, Q^2)}{\nu} d\nu \tag{4.6}$$

To gain insight into the physical meaning of the GDH integrand, we reconsider the formalism used to describe polarized photon scattering. The lhs of equation 4.1 involves the helicity dependent photo-absorption cross sections previously introduced in section 2.5. As such, equation 4.6 can be re-written in terms of the "transverse-transverse" cross section σ'_{TT}.

$$I(Q^2) = 2 \int_{\nu_{th}}^{\infty} \frac{K}{\nu} \frac{\sigma'_{TT}(\nu, Q^2)}{\nu} d\nu \tag{4.7}$$

or even in terms of the polarized structure functions:[‡]

$$\begin{aligned} I_A(Q^2) &= \frac{8\pi^2\alpha}{M}\int_{\nu_{th}}^{\infty}\left[g_1(\nu,Q^2)-\frac{Q^2}{\nu^2}\,g_2(\nu,Q^2)\right]\frac{d\nu}{\nu^2} \\ &= \frac{16\pi^2\alpha}{Q^2}\int_0^{x_{th}}\left[g_1(x,Q^2)-\frac{4M^2x^2}{Q^2}\,g_2(x,Q^2)\right]dx \qquad (4.8) \end{aligned}$$

where $x_{th} = Q^2/(2M\nu_{th})$.

As in the real photon case, it is expected that the integral for a nucleon target will be dominated by the lowest mass resonant states. Burkert and Li [7] in particular, point out the importance of the Δ isobar $P_{33}(1232)$ contribution at low Q^2. For a nuclear target, quasielastic scattering and electro-disintegration should dominate the integral, due to the ν-weighting. However, as Q^2 goes to zero, the quasielastic channel must necessarily vanish[§] as it does not survive in the real photon case. Figure 4.2 shows the MAID [40] model prediction for $I_A(Q^2)$ for the nucleons and for ^{3}He. Notice that the model is not constrained to the sum rule prediction at $Q^2 = 0$.

Although the proposed extension is quite natural experimentally, it has the drawback that there's "no rule for the sum" [66], so there is limited predictive power in equation 4.6. We will see an alternative formulation in section 4.3 that provides a theoretical prediction for the left hand side of equation 4.8 making it a true sum rule.

Asymptotic Limits of the Extended Sum

It is interesting to examine the asymptotic behaviour of the extended GDH sum as $Q^2 \to \infty$ and at $Q^2 = 0$. Starting with equation 4.8, and considering that g_2 decouples as $Q^2 \to 0$ we find:

$$\begin{aligned} \lim_{Q^2\to 0} I_A(Q^2) &= \frac{16\pi^2\alpha}{Q^2}\int_0^{x_{th}} g_1(x,Q^2)dx \\ &= \frac{16\pi^2\alpha}{Q^2}\,\overline{\Gamma}_1(Q^2) \qquad (4.9) \end{aligned}$$

[‡] The generalized GDH integral depends on the choice of virtual photon flux K. We have chosen the convention shown in equation 2.55 which allows comparison to existing chiral perturbation theory calculations at low Q^2. This also has the advantage that equation 4.7 takes an identical form as the real photon version.

[§] The physical mechanism is Pauli-blocking. When $|\vec{q}| < 2k_{fermi}$ the nucleon does not have enough energy to escape the nuclear potential well.

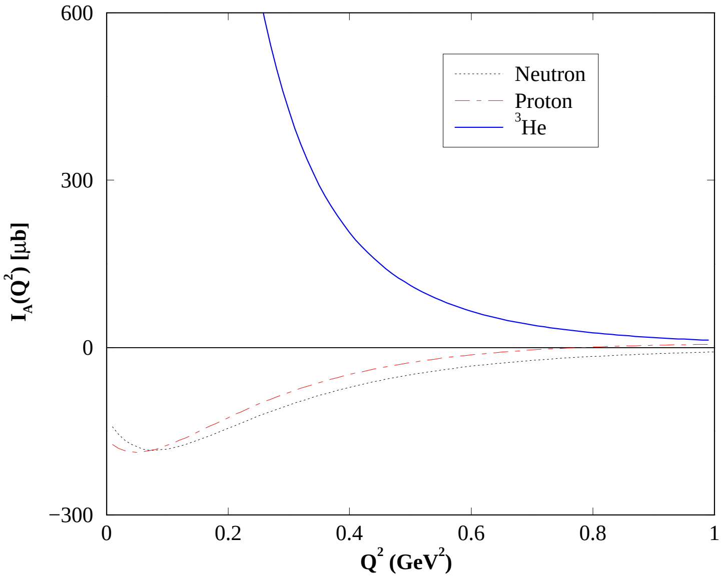

Figure 4.2: MAID2003 [40] prediction for the extended GDH sum $I_A(Q^2)$ in the resonance region. The ^{3}He prediction is an incoherent sum of the proton and neutron contributions combined with a PWIA estimate of the quasielastic channel as described in section E.2.1.

As $Q^2 \rightarrow \infty$, the second term on the right hand side of 4.8 falls off, and we obtain¶:

$$\begin{aligned} \lim_{Q^2\rightarrow\infty} I_A(Q^2) &= \frac{16\pi^2\alpha}{Q^2}\int_0^1 g_1(x)dx \\ &= \frac{16\pi^2\alpha}{Q^2}\Gamma_1 \end{aligned} \tag{4.10}$$

So we have the curious result that the two extreme limits of the extended sum have the same functional form, which depends only on the first moment of g_1.

¶As $Q^2 \rightarrow \infty$, the elastic and quasielastic contribution vanish and we can extend the integration to $x = 1$.

4.3 Dispersive Sum Rules at Arbitrary Q^2

Ji and Osborne [66] suggest a generalization of the GDH sum rule that takes advantage of the relationship between the forward virtual Compton amplitudes and the spin dependent structure functions. They point out that since the GDH sum rule is derived from the dispersion relation [67] for the invariant Compton amplitude $S_1(\nu, Q^2 = 0)$ at the real photon point, a generalized sum rule can also be constructed from the same dispersion relation at nonzero Q^2.

The derivation begins with the observation that the hadronic tensor for inclusive lepton scattering (equation 2.34):

$$W_{\mu\nu} = \frac{1}{4\pi} \int d^4\xi \; e^{iq\cdot\xi} \langle N_s(P)|J_\mu(\xi)J_\nu(0)|N_s(P)\rangle$$

is structurally quite similar to the tensor for forward virtual-photon Compton scattering (equation 2.66):

$$T_{\mu\nu} = i \int d^4\xi \; e^{iq\cdot\xi} \langle N_s(P)|\mathcal{T} J_\mu(\xi)J_\nu(0)|N_s(P)\rangle$$

In fact, the two tensors differ only by the time ordering of the product of electromagnetic currents.

As in the case of the hadronic tensor (see equation 2.36), the Compton tensor is constructed with the most general form that satisfies Lorentz symmetry, parity and time-reversal invariance. The anti-symmetric part of $T^{\mu\nu}$ is:

$$T^{[\mu\nu]} = -i\epsilon^{\mu\nu\alpha\beta} q_\alpha \Big[\; S_\beta S_1(\nu, Q^2) + (M\nu S_\beta - S\cdot q P_\beta) S_2(\nu, Q^2) \; \Big] \tag{4.11}$$

The two scalar functions S_1 and S_2 are known as the spin-dependent Compton amplitudes. The optical theorem relates them directly to the structure functions:

$$Im\ S_1(\nu, Q^2) = 2\pi G_1(\nu, Q^2) \tag{4.12}$$

$$Im\ S_2(\nu, Q^2) = 2\pi G_2(\nu, Q^2) \tag{4.13}$$

And Cauchy's integral theorem can therefore be used to formulate a set of Q^2-dependent dispersion relations [67]:

$$S_1(\nu, Q^2) = 4\int_{\frac{Q^2}{2M}}^{\infty} \frac{d\nu'\nu'}{\nu'^2 - \nu^2} G_1(\nu', Q^2) \tag{4.14}$$

$$S_2(\nu, Q^2) = 4\int_{\frac{Q^2}{2M}}^{\infty} \frac{d\nu'\nu}{\nu'^2 - \nu^2} G_2(\nu', Q^2) \tag{4.15}$$

Equations 4.14 and 4.15 take advantage of the properties under reflection:

$$\begin{aligned} S_1(\nu, Q^2) &= S_1(-\nu, Q^2) && (4.16) \\ S_2(\nu, Q^2) &= -S_2(-\nu, Q^2) && (4.17) \end{aligned}$$

which arise from crossing symmetry.

Using the dispersion relations, theoretical calculations (using χPT or LGT for example) of the Compton amplitudes can be directly compared to the experimentally measured structure functions.

4.3.1 The GDH Sum

We now consider $\nu = 0$ in equation 4.14 to obtain the Q^2 dependent relation:

$$\begin{aligned} S_1(0, Q^2) &= 4\int_{\nu_{el}}^{\infty} \frac{d\nu'}{\nu'} G_1(\nu', Q^2) && (4.18) \\ &= \frac{8}{Q^2}\int_0^1 g_1(x, Q^2) && (4.19) \end{aligned}$$

This serves as a natural extension of the GDH sum rule to virtual-photon scattering, and represents a Q^2-dependent sum rule provided theoretical predictions for the S_1 Compton amplitude can be extended beyond the low energy theorem results at $Q^2 = 0$.

To make explicit the relation of equation 4.18 to the GDH sum rule, we examine the limit as $Q^2 \to 0$. The sum rule excludes the elastic contribution so we consider the inelastic part of S_1:

$$\overline{S}_1(0, Q^2) = S_1(0, Q^2) - S_1^{el}(0, Q^2) \tag{4.20}$$

The low energy prediction of Low, Gell-mann and Goldberger [50, 51] states that:

$$\overline{S}_1(0, 0) = -\left(\frac{\kappa}{M}\right)^2 \tag{4.21}$$

The g_2 structure function decouples in the real photon limit, so equation 2.54 reveals that:

$$G_1(\nu, 0) = -\frac{1}{8\pi^2\alpha}\left[\sigma_{3/2}(\nu) - \sigma_{1/2}(\nu)\right] \tag{4.22}$$

If we insert these two results into equation 4.18, we recover the GDH sum rule of equation 4.1.

It is interesting to note that the standard I_A generalization of the GDH sum can also be related to the Compton amplitudes as follows [68]:

$$I_A(Q^2) = 2\pi^2\alpha \left[S_1(\nu, Q^2) - Q^2\ S_2(\nu, Q^2)\right] \tag{4.23}$$

4.3.2 The Bjorken Sum Rule

As $Q^2 \to \infty$, the following relation holds for the difference of the proton and neutron Compton amplitudes [66]:

$$S_1^p(0, Q^2) - S_1^n(0, Q^2) = \frac{4}{3Q^2} g_A \tag{4.24}$$

Equation 4.19 transforms this into the Bjorken sum rule, [69]

$$\Gamma_1^p - \Gamma_1^n = \frac{g_A}{6} \tag{4.25}$$

where g_A is the isovector axial charge of the nucleon, measured in nuclear β-decay, and $\Gamma_1 = \int_0^1 g_1 dx$.

This result was originally derived using Current Algebra and thus predates Quantum Chromodynamics. Nevertheless, it also follows from QCD. The relation depends only on isospin symmetry, i.e. the symmetry between down and up quarks. In a more modern treatment it is a consequence of the OPE expansion (equation 3.8) of Γ_1 for the proton and neutron. When evolved to finite Q^2 there are QCD radiative corrections and higher twist corrections so that equation 4.25 is generalized to:

$$\Gamma_1^p(Q^2) - \Gamma_1^n(Q^2) = \frac{g_A}{6} \cdot C_{\mathtt{NS}}(\alpha_s) + \frac{C_{HT}}{Q^2} \tag{4.26}$$

The higher twist correction coefficient is estimated [70, 71] to be small:

$$-25\text{MeV}^2 \leq C_{HT} \leq +30\text{MeV}^2$$

and the non-singlet QCD radiative corrections follow the form:

$$C_{\mathtt{NS}}(\alpha_s) = 1 - \sum c_i \left(\frac{\alpha_s(Q^2)}{\pi}\right)^i \tag{4.27}$$

with the first few coefficients [25, 26] given by: $c_1 = 1.0$, $c_2 = 3.5833$, $c_3 = 20.2153$, $c_4 = 130.0$, and $c_5 = 893.38$.

World data prior to E94-010 confirmed the sum rule to 10% [72, 73]. If the validity of the sum rule is accepted, equation 4.26 can also be used to extract the strong coupling constant $\alpha_s(Q^2)$ at low Q^2 [74].

Because of isospin symmetry, it is possible to write a "Bjorken" sum rule for any pair of mirror nuclei, ^{3}He and ^{3}H for example [75, 76]:

$$\Gamma_1^{(^3\mathrm{H})} - \Gamma_1^{(^3\mathrm{He})} = \frac{g_A^{tri}}{6} \cdot C_{\mathtt{NS}}(\alpha_s) \tag{4.28}$$

where g_A^{tri} is the axial vector coupling constant of the triton, measured in tritium decay.

If we take the ratio of the $A = 1$ to $A = 3$ Bjorken sum rules we get:

$$\frac{\Gamma_1^p - \Gamma_1^n}{\Gamma_1^{(^3\mathrm{H})} - \Gamma_1^{(^3\mathrm{He})}} = \frac{g_A}{g_A^{tri}} \tag{4.29}$$

and the QCD radiative corrections cancel exactly. Both g_A and g_A^{tri} have been precisely measured and their ratio is 0.956 ± 0.004. Comparison of the experimental value of equation 4.29 with the predictions using exact ^{3}He wavefunctions have been used to evaluate the size of off-shell corrections in ^{3}He and the effect of non-nucleonic degrees of freedom [75, 77].

4.3.3 The g_1 Sum Rule

The Q^2-dependent sum rule of equation 4.19 is the latest in a long progression of exciting results involving the lowest moment of the g_1 spin structure function. Early measurements of Γ_1^p at CERN [78] and SLAC [79] differed strongly from the prediction of the naive quark model and Ellis-Jaffe sum rule [80], sparking what became known as the "Spin Crisis". This spurred an intense theoretical and experimental endeavor which eventually concluded that the constituent quarks carry only about 30% of the nucleon spin [71, 81].

In addition, as $\mathrm{Q}^2 \to 0$ Γ_1, is closely related to the generalized GDH integral as discussed in section 4.2. The SLAC and CERN experiments reported results that were clearly positive, while the GDH sum rule prediction for Γ_1 at $\mathrm{Q}^2 = 0$ is large and negative. This indicated a very strong variation in the helicity structure of the photon-nucleon coupling between the region of asymptotic freedom and the real photon point. The expected variation was verified recently by the JLab CLAS collaboration [82] who observed a crossover of Γ_1^p near $\mathrm{Q}^2 = 0.3$ GeV^2. This strongly Q^2-dependent behaviour arises mostly from the electroexcitation of the nucleon resonances, which become dominant at low Q^2 [83], and signifies the transition from incoherent

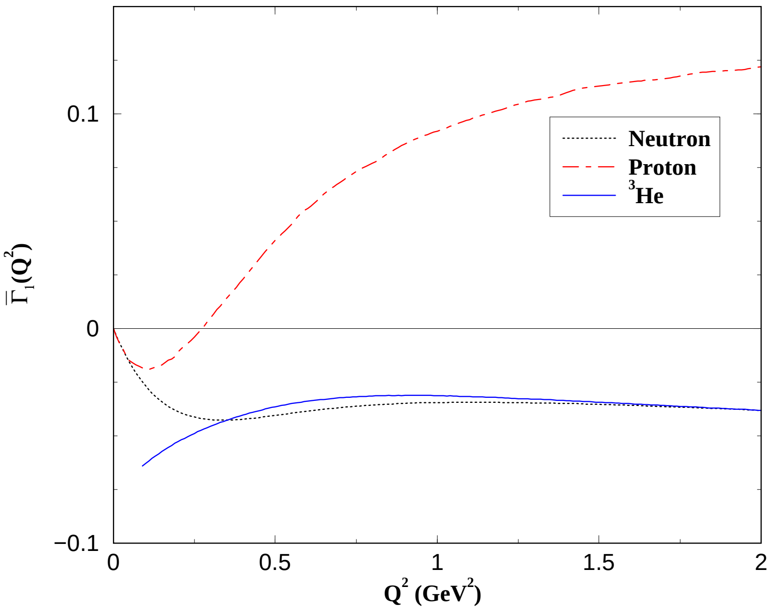

Figure 4.3: Model of Burkert and Ioffe [44, 45] for $\overline{\Gamma}_1(Q^2)$. The ^{3}He prediction is an incoherent sum of the proton and neutron contributions combined with a PWIA estimate of the quasielastic channel as described in section E.2.1.

parton scattering to resonance driven coherent scattering. Figure 4.2 shows the Burkert and Ioffe [44, 45] model prediction for $\overline{\Gamma}_1(Q^2)$ for the nucleons and for ^3He.

In chiral perturbation theory $\overline{S}_1$ can be expanded in a power series expansion with respect to the pion mass around $Q^2 = 0$:

$$\overline{S}_1(0, Q^2) = -\left(\frac{\kappa}{M}\right)^2 + \overline{S}_1'(0,0)\cdot Q^2 + \frac{1}{2}\overline{S}_1''(0,0)\cdot Q^4 + \ldots \qquad (4.30)$$

with

$$\overline{S}_1'(0,0) = \frac{a}{m^2\pi} + \frac{b}{m_\pi}\left[\,\log(m_\pi) + \beta\,\right] + \ldots \qquad (4.31)$$

The leading chiral term 'a' arises from Feynman diagrams in which the incoming or outgoing photon interacts with an intermediate pion. Heavy Baryon Chiral Perturbation Theory (HBCPT) calculations [66] reveal that this term vanishes and $\overline{S}_1(0, Q^2)$ is independent of Q^2 at leading order.

Unfortunately, the next to leading order contribution (NLO) is strongly Q^2 dependent and lead to the following predictions for the nucleons:

$$\begin{aligned}\overline{I}_1^p(Q^2) &= -\frac{\kappa_p^2}{4} + 6.85 \cdot Q^2 + \ldots &(4.32)\\ \overline{I}_1^n(Q^2) &= -\frac{\kappa_n^2}{4} + 5.54 \cdot Q^2 + \ldots &(4.33)\end{aligned}$$

Phenomenological models reveal the importance of the resonance contributions and in particular the $\Delta(1232)$ to the helicity dependent inclusive cross sections at low Q^2. This observation, along with the fact that the $\Delta(1232)$ is difficult to treat in HBCPT, lead Burkert [84] to propose the proton-neutron difference[‖], as a more suitable observable for extending the chiral expansion further away from the real photon point than possible for either nucleon alone:

$$\overline{I}_1^{p-n}(Q^2) = \frac{\kappa_n^2 - \kappa_p^2}{4} + 1.31 \cdot Q^2 + \ldots \quad (4.34)$$

4.3.4 The Burkhardt–Cottingham Sum Rule

We now reconsider equation 4.15 for the S_2 amplitude multiplied by an additional factor of ν:

$$\nu S_2(\nu, Q^2) = 4 \int_0^\infty \frac{d\nu' \nu^2}{\nu'^2 - \nu^2} G_2(\nu', Q^2) \quad (4.35)$$

It is also possible to directly form an unsubtracted dispersion relation for the function $S_2^* = \nu S_2$ which is even with respect to ν. Assuming that the S_2 amplitude vanishes faster than $1/\nu$, (or equivalently that g_2 obeys Regge theory at low x), we find:

$$S_2^*(\nu, Q^2) = 4 \int_0^\infty \frac{d\nu' \nu'^2}{\nu'^2 - \nu^2} \, G_2(\nu', Q^2) \quad (4.36)$$

Subtraction of equation 4.36 from equation 4.35 results in the following 'super-convergence' relation [67], valid for all Q^2:

$$0 = \int_0^\infty G_2(\nu, Q^2) d\nu \quad (4.37)$$

or making a simple transformation:

$$0 = \int_0^1 g_2(x, Q^2) dx \quad (4.38)$$

[‖] In which the Δ-resonance contribution cancels which is the Burkhardt–Cottingham [47] sum rule. The integration proceeds from 0 to $x = 1$ which necessitates inclusion of the elastic contribution in equation 4.38. At first glance, the sum rule appears to be a trivial consequence of the OPE expansion of Γ_2 (equation 3.9) for $n = 1$. But it has been pointed out [21] that the expansion is valid only for $n \geq 3$. The OPE actually gives no information about the BC sum rule.

Separating the elastic and inelastic contributions results in the following prediction from Schwinger [48, 49] for the inelastic part at all Q^2:

$$\overline{I}_2(Q^2) = \frac{1}{4} G_M(Q^2) \frac{G_M(Q^2) - G_E(Q^2)}{1+\tau} \tag{4.39}$$

which reveals that the I_2 integral has the following limiting cases:

$$\begin{aligned} I_2(Q^2) &\rightarrow \frac{1}{4}\mu_{\mathtt{A}}\kappa_{\mathtt{A}} && \text{for} \quad Q^2 \rightarrow 0 && (4.40) \\ I_2(Q^2) &\rightarrow \mathcal{O}(Q^{-10}) && \text{for} \quad Q^2 \rightarrow \infty && (4.41) \end{aligned}$$

Drechsel *et al.* [14] point out the rapid decrease with Q^2 follows from the asymptotic behaviour of the electromagnetic form factors predicted by perturbative QCD if logarithmic terms are neglected.

The B.C. sum rule was traditionally viewed as valid only in the scaling limit, although the derivation presented above is valid for all Q^2. There is however a healthy skepticism in the literature with a general consensus that the two most likely scenarios that would lead to a violation [85] are:

1. $\int_0^1 g_2(x, Q^2)dx$ does not exist, that is g_2 is singular or exhibits non-Regge behaviour at low x.

2. g_2 exhibits a delta function singularity at $x = 0$.

It is these criteria for a possible violation that have lead some authors to conclude [46] that "the B.C. integral is either zero or infinite". Of course, a singularity at $x = 0$ would be impossible to observe and the existing low x data has exhibited reasonable agreement with Regge behaviour.

The Burkhardt–Cottingham sum rule is satisfied to first order in α_s for a quark target in PQCD [86], and to lowest order in α_{em} in QED [49]. The sum rule was also tested with a complete one loop calculation for a nucleon target in [10]. Finally, it should be recalled that the validity of the Wandzura–Wilczek relation implies the Burkhardt–Cottingham result since equation 4.38 can be obtained directly from 3.11 by integration.

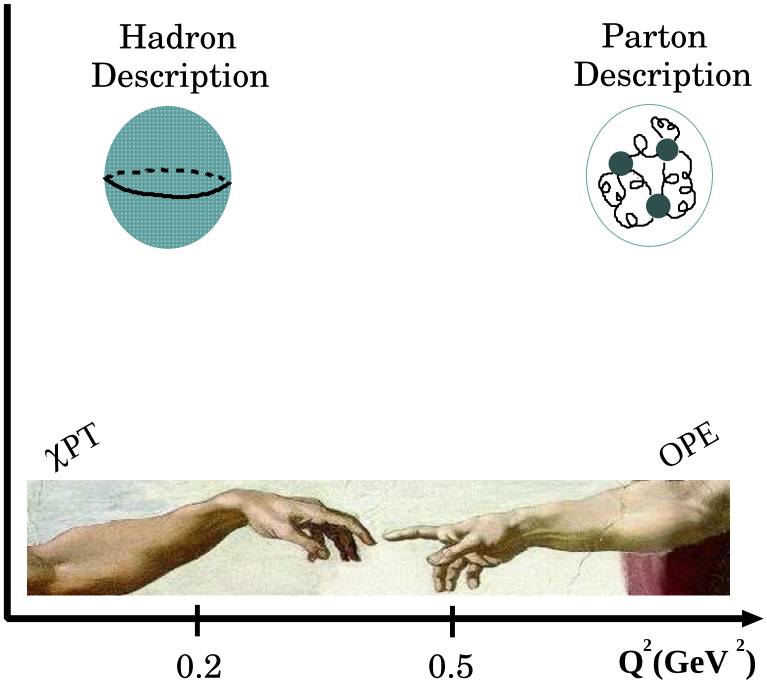

Figure 4.4: Connecting the partonic and hadronic descriptions.

4.4 Summary

At large Q^2, the spatial resolution of the incident electron probe is high and the interaction can be viewed as an incoherent sum of scattering from individual partons. In this kinematic region, the structure function moments can be expressed in a perturbative expansion in α_s, and higher twist expansion in $1/Q^2$. As Q^2 decreases, the higher twist effects of the OPE should grow in significance until the expansion breaks down. Ji and Osborne [66] argue that the relevant scale parameter is the average parton transverse momentum $k_\perp$. They use this fact to conclude that the $1/Q^2$ expansion should be valid down to about 0.5 GeV^2. In any event, the OPE should break down completely as we approach Λ^2_{QCD} from above.

On the other hand, chiral perturbation theory extends the low energy theorem predictions away from the real photon point at $Q^2 = 0$. This approach views electron scattering as a coherent interaction in which the underlying partonic degrees of freedom are ignored. It is argued that this effective theory can be used to describe the Q^2 evolution of the Compton amplitudes up to about 0.2 GeV^2. In the intermediate 'window' region, the interaction can not be simply understood in either the partonic or hadronic view, but is necessarily some complicated mixture of the two effective theories. This makes experimental data in this range extremely useful in testing extensions to the existing tools and to provide a benchmark for any future calculations such as those expected from lattice gauge theory. It is in this region that the E94-010 collaboration performed a precision measurement of the neutron and ^{3}He spin structure functions which will be described in the remainder of this thesis.

CHAPTER 5

THE EXPERIMENT

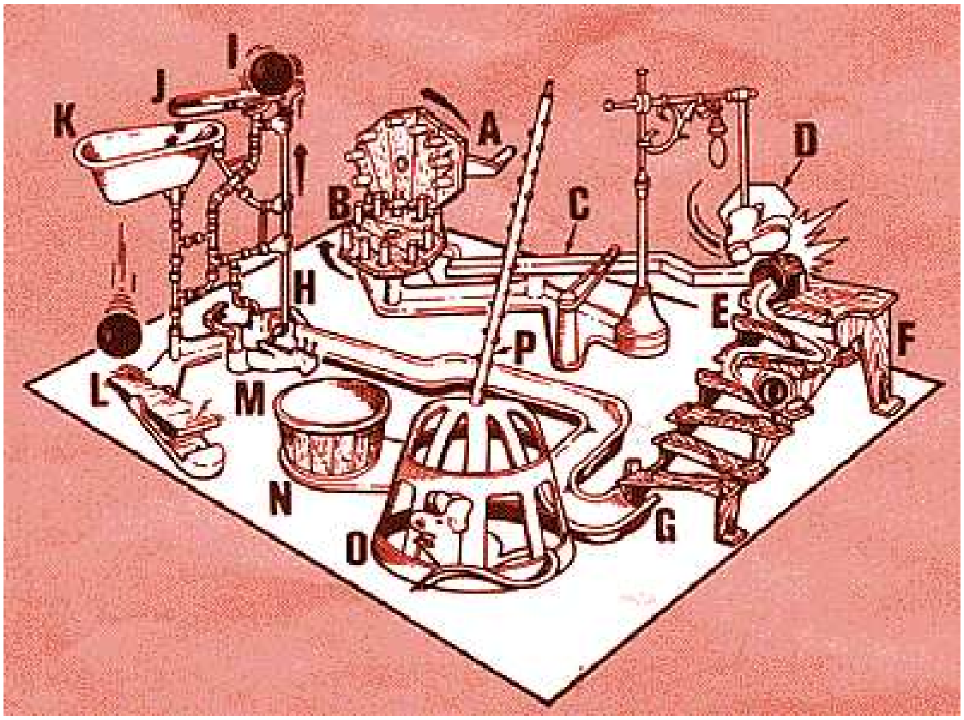

Experiment 94-010 ran in Jefferson Lab Hall A from Sept. 25th to December 24th 1998. It represents a precise inclusive polarized cross section measurement at low momentum transfer ($0.1<Q^2<0.9$ GeV^2) in the threshold, quasielastic, and resonance regions. The kinematic coverage is shown in figure 5.1. The goal of the experiment was to extract the ^{3}He and neutron spin-dependent structure functions $g_1(x,Q^2)$ and $g_2(x,Q^2)$ and ultimately the relevant higher moments of these quantities. Longitudinally polarized electrons of incident energy from 0.9 GeV to 5.1 GeV were scattered from a

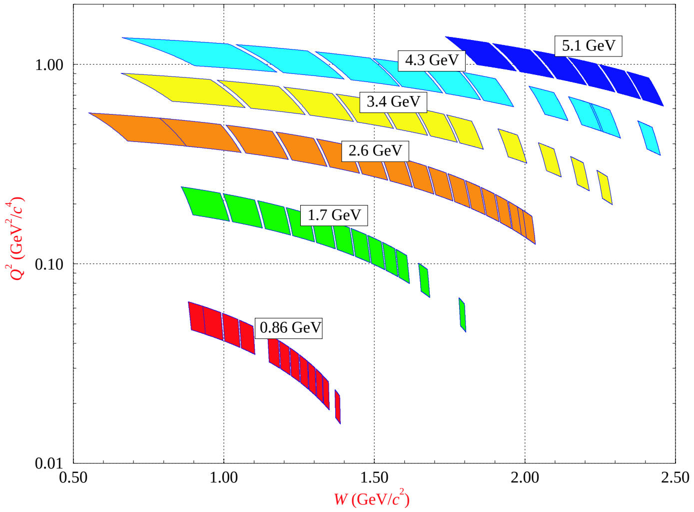

Figure 5.1: Kinematic Coverage of E94-010

high pressure polarized ^{3}He target. The beam helicity was pseudo-randomly flipped at 1 or 30Hz as 1-15 μA was rastered on the glass ^{3}He target cell. In order to extract both polarized structure functions, longitudinal and transverse target polarization was maintained.

The experiment utilized two nearly identical high resolution magnetic spectrometers positioned at 15.5° with respect to the beamline. Beam polarization was monitored about once every four days with a Møller polarimeter. Average beam polarizations was 71%. A Mott polarimeter also monitored the initial beam polarization at the injector before acceleration. At the time of E94-010 this polarimeter experienced various hardware difficulties and the Mott polarimetry results were not used in the final analysis.

Particle ID was provided by a gas Čerenkov and total absorption shower counter. The resulting pion rejection was about 10^4, which was more than sufficient to control the pion contamination in our data.

In this chapter, we will discuss the Continuous Electron Beam Accelerator Facility (CEBAF), and the experimental setup in Hall A.

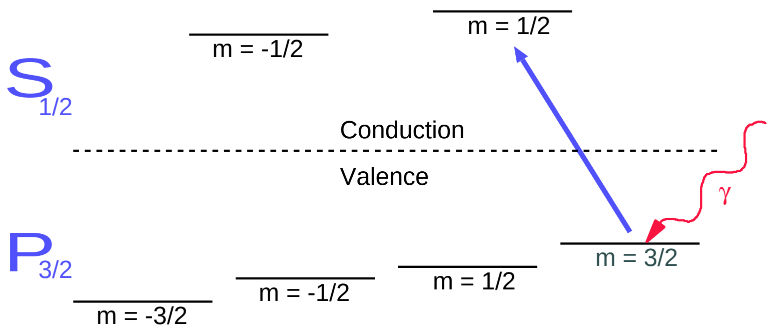

Figure 5.2: Energy level diagram for doped GaAs.

5.1 The Accelerator

The JLab polarized electron source [87] utilizes a phosphorus doped strained GaAs cathode illuminated with a polarized diode laser. The 1497 MHz diode laser operates at 780 nm and can provide up to 100 μA of polarized beam. The diode laser can be swapped out and replaced with a Titanium Sapphire (Ti:Sap) laser, allowing production of polarized beam of up to 200 μA.

The cathode [88] consists of several layers of GaAs doped to varying degrees with phosphorus. The doping creates a strain on the GaAs in the active layer, thereby breaking the degeneracy of the $P_{3/2}$ level of the valence band as shown in figure 5.2. Left-handed circularly polarized light incident on the cathode is then able to promote electrons in the m=3/2 sublevel of the valence band to the m=1/2 sublevel of the conduction band, where the electron is able to escape. The electrons are emitted in a direction opposite to the incident laser and therefore have right-handed helicity.

The electron beam helicity is alternated to enable the measurement of asymmetry and cross section differences. It is desirable to perform this helicity flipping quickly in order to limit the impact of any time dependent systematic effects. The source laser passes through a pockel cell which rapidly varies the helicity of the beam in a pseudo-random fashion at 1 or 30Hz. A removable half-wave plate can also be inserted into the laser beam to reverse the helicity. This was done several times during E94-010 in order to evaluate helicity dependent systematic effects.

The polarized electrons are then accelerated to 45 MeV before being injected into the first linac. See figure 5.3. The linacs consist of 20 superconducting cryomodules, each composed of 8 superconducting niobium rf cavities cooled to 2K. The cavities are able to produce a field gradient of

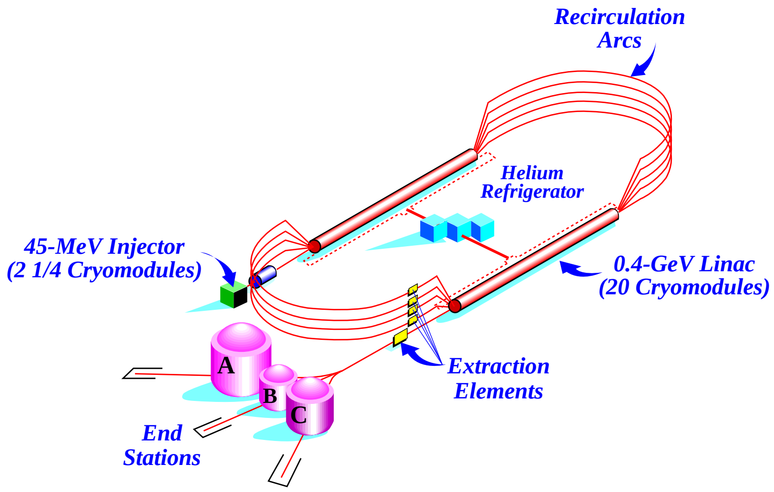

Figure 5.3: CEBAF machine configuration.

7 MeV/m and organize the beam into as many as three 499 MHz bunches. After the first linac, the electrons enter a re-circulation arc and are directed into the second linac where they can be accelerated again. At this point, an electron bunch will either enter the second recirculation arc, eventually making up to 5 passes through the machine, or it can be separated and sent to the halls using rf separators and septum magnets. Each linac was nominally designed to accelerate electrons by 400 MeV, but this value can be adjusted. The maximum beam energy after 5 passes is presently just below 6 GeV.

5.2 Hall A Beamline

5.2.1 Beam Current Monitors

The first piece of equipment along the beamline within Hall A is the Beam Current Monitors (BCMs) [89, 90]. The monitors are contained within a temperature controlled, magnetically shielded enclosure about 25 meters upstream of the target [91]. The box contains two resonant cavities, which perform relative measurements of the beam current. One BCM is upstream and another downstream of the Unser [92], a parametric current transformer, which performs an absolute measurement and is used to calibrate the BCMs. See figure 5.5.

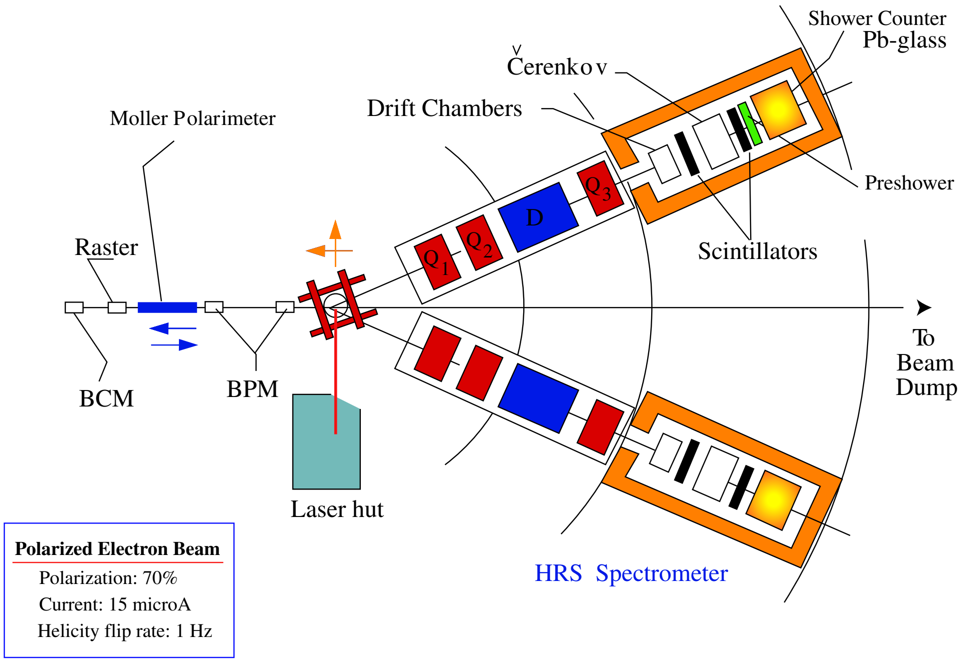

Figure 5.4: JLab experimental Hall A.

The cavities are made of stainless steel cylinders, 15.48 cm in diameter and 15.24 cm in length, and are resonantly tuned to the beam frequency of 1497 MHz. The Q[*] is highly sensitive to the ambient temperature necessitating thermal shielding and temperature control. Inside, there is a coaxial antennae running along the outer shell which couples to the cavity and transmits any induced signal to the external electronics. Another reference antennae within the cavity can be excited at 1497 MHz with a known current for calibration.

The electron beam excites the resonant transverse mode TM_{010} of the cavity at 1497 MHz. This is picked up by the antennae creating an RF output signal whose voltage is proportional to the beam current. Immediately outside the cavity, the 1497 MHz signal is stepped down to 1 MHz to avoid attenuation. At this point, the signal is split into two paths [93]. One signal will be integrated and recorded by the scalars. The other signal will be sampled and leads to the EPICS data stream.

The "sampled" signal is fed to a high precision digital AC voltmeter. The

---

[*] Quality Factor

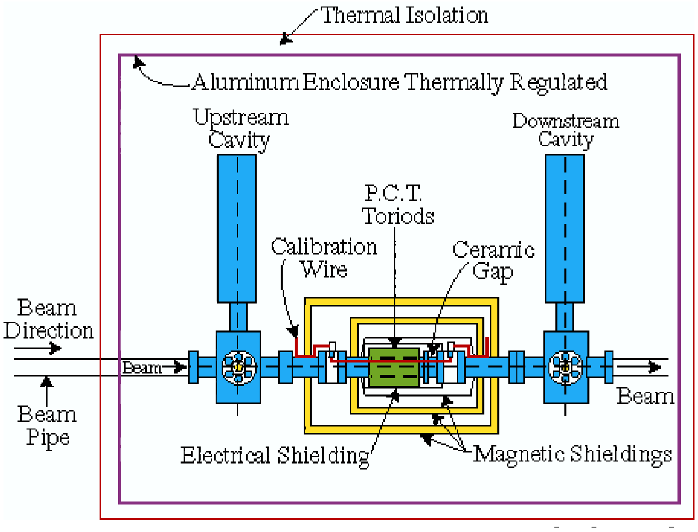

Figure 5.5: Schematic of Beam Current Monitor apparatus. *Reproduced from* [91].

meter provides the rms average over one second of the input signal. This signal is proportional to the average charge accumulated over the sampling period. At semi-regular intervals (4 to 50s) the sampled value is processed by EPICS and entered into the data stream. Beam trips and fluctuations can be missed entirely by this sampling procedure and this makes it undesirable for use in absolute charge determination.

The "integrated" signal is fed to an RMS-to-DC converter which outputs a DC voltage proportional to the beam current. The constant voltage is input to a VTOF[†] converter which outputs a signal whose frequency is proportional to the input voltage. This sinusoidal wave is fed to the 200 MHz VME scalers which simply count each incident pulse. The accumulated number of scaler counts will be proportional to the total charge. In practice, the RMS-to-DC converter is non-linear below 5 μA, so the signal is amplified by a factor of 1, 3 and 10 before the converter. Therefore, the two cavities each output 3 signals, referred to as X1, X3, and X10 respectively, which are in turn fed to the VME crates in both spectrometers. This leads in principle to 12 redundant scaler records of the charge. During the experimental run,

---

[†] Voltage to frequency convertor.

one of the cavities was more stable than the other and the signals with lower amplification departed from linearity at low current. For these reasons E94-010 utilized the HRS-R downstream X10 signal for all charge determination.

As mentioned above, the cavities provide a relative value and must be calibrated with an absolute measurement. The Unser, which is a toroidal parametric transformer serves this purpose. The toroid responds to the DC magnetic field created by the presence of the beam. It can provide an absolute measurement at large currents, but at lower currents the absolute uncertainty, 250 nA, becomes prohibitive and the offset drifts significantly over the course of a few minutes.

The Unser is calibrated with a internal reference wire carrying a current of 2 mA from a precision current source. Then it, in turn, is used to calibrate the cavities by making a measurement of the beam current at the highest available current, typically about 50 μA. The beam is cycled on and off at one minute intervals to compensate for the drifting offset. The measurement typically takes about one half hour and interrupts beam delivery to all the Halls.

The cavities and their associated electronics are highly linear, so once they have been calibrated with the Unser at high current the calibration can be extrapolated reliably to the lower currents typically used for the ^{3}He target. The overall system is estimated to be accurate to better than 1% down to 1 μA.

5.2.2 Raster

The electron beam enters the hall focused to a diameter of approximately 100 μm. A fast raster is used to spread the heat load of the beam across the face of the target and to limit dramatic variations in target density. The raster [94] is located 23 m upstream from the target. It consists of a horizontal and vertical air core coils each oscillating according to a sinusoidal pattern at approximately 20 kHz. See figure 5.6. The phase shift between the two patterns is $\pi/2$ and the amplitude is modulated with a 49 Hz square root function of time [94]. The resulting two-dimensional profile is ellipsoidal with a flat density and an approximate diameter of 4 mm.

5.2.3 Beam Position Monitors

There are two beam position monitors (BPMs) located 7.534 and 1.286 meters upstream of the target. The BPMs consist of four wire antennas coaxial with the beam. See figure 5.7. When the beam passes within the

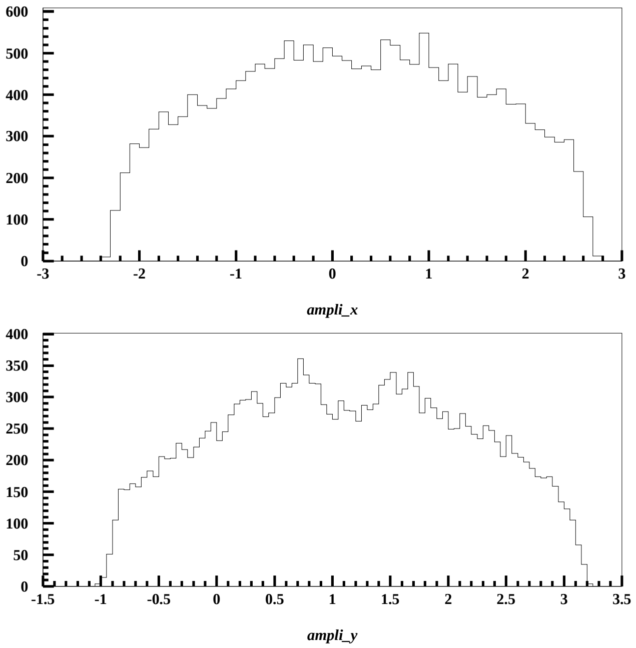

Figure 5.6: Projection of the raster pattern on horizontal and vertical axis. *Reproduced from* [94].

antennae array, a signal is induced that is inversely proportional to the beam-antennae distance. The BPMs are calibrated by two superharps adjacent to the BPMs. The superharps perform an invasive measurement of the beam position by scanning three thin wires, oriented vertically and at ± 45°, across the electron beam. This causes a shower of radiation which can be detected in a photomultiplier. The BPMs are accurate to ± 20 μm at 10μA.

5.2.4 Beam Polarization

The cross section for polarized Møller scattering is sensitive to both the incident and target electron polarizations. The Møller polarimeter [89, 96] utilizes this relation to extract the beam polarization in Hall A. The cross section for Møller scattering [97] can be expressed as:

$$\frac{d\sigma}{d\Omega} = \left(\frac{d\sigma}{d\Omega}\right)_0 \left[1+\sum_{i,j} P_B^i \cdot A_{ij} \cdot P_T^j \cdot\right] \qquad (5.1)$$

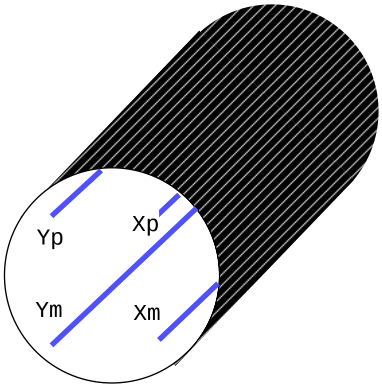

Figure 5.7: Antennae within the beam position monitors. The electron beam runs along central axis.

$$\tag{5.2}$$

Here $\left(\frac{d\sigma}{d\Omega}\right)_0$ is the unpolarized cross section:

$$\left(\frac{d\sigma}{d\Omega}\right)_0 = \left[\frac{\alpha(1+\cos\theta_{cm})(3+\cos^2\theta_{cm})}{2m_e\sin^2\theta_{cm}}\right]^2 \tag{5.3}$$

A_{ij} is known as the *analyzing power*, which depends only on the scattering angle θ_{cm} in the center of mass frame. P^i_B and P^i_T are the beam and target polarizations projected on the three spatial axes, respectively. Once the analyzing power and target polarization are determined, it is straightforward to extract the beam polarization. We orient our coordinate system so that the z-axis is along the electron beam and the y-axis is normal to the scattering plane. Then in the case of a longitudinally polarized target and beam the analyzing power reduces to:

$$A_{zz} = -\frac{(7+\cos^2\theta_{cm})\sin^2\theta_{cm}}{(3+\cos^2\theta_{cm})^2} \tag{5.4}$$

In practice, the Møller asymmetry is measured instead of the cross section. As a ratio of cross sections, the asymmetry is insensitive to many of the cross section systematics but retains its dependence on the beam and

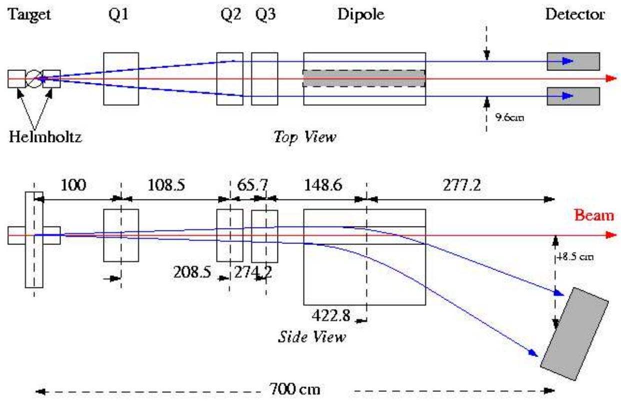

Figure 5.8: Møller polarimeter schematic. *Reproduced from* [95].

target polarizations. A schematic of the polarimeter is shown in figure 5.8. The target is a 13.9 μm Cobalt-Iron ('Supermendur') alloy cooled to 115K and placed in a magnetic field of 28 mT provided by a Helmholtz coil. Typical target polarizations of 7.6% are detected with a pickup coil pair during NMR measurements. The relative error of approximately 3% on the target polarization dominates the total Møller systematic error.

Downstream of the target, a series of three quadrupoles act to focus the scattered electrons into two beams that emerge parallel to the beam axis after the final quadrupole. A dipole magnet is then used to divert the scattered electrons to the detector and to separate Møller from Mott scattered electrons. The incident electron beam passes through a 4 cm diameter hole in a magnetically shielded partition within the dipole and proceeds undeflected to the beam dump. The two beams of scattered electrons pass on either side of the partition and enter the detectors. The detectors, which are used in coincidence, consist of a scintillator and 4 lead glass shower blocks.

The Møller polarimeter has an operational range of 0.8 to 6.0 GeV and operates with 0.2 to 5.0 μA of beam. The polarimetry measurement is necessarily invasive and typically requires one hour of beam time. There were 26 such Møller measurements performed during E94-010 with an average

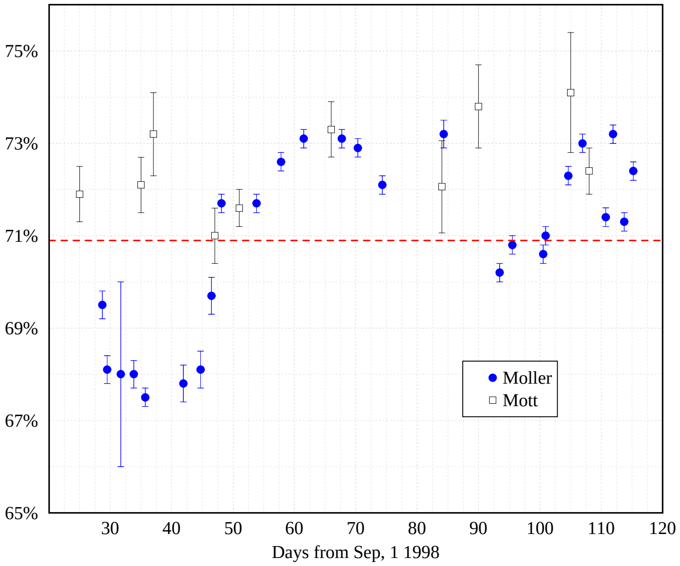

Figure 5.9: Beam Polarimetry measurements. Dashed line is the average of the Møller polarimeter measurements. The Mott values were not used in this analysis and are shown only for reference.

polarization of about 71%. A total uncertainty of 4% relative was assigned to the beam polarization measurements. The results are shown in figure 5.9.

5.2.5 Incident Beam Energy

Arc Energy Determination

A charged particle beam will be deflected by a known angle when it passes through a magnetic field. The force on the particle is:

$$\frac{d\vec{p}}{dt} = e\vec{v} \times \vec{B} \tag{5.5}$$

and the deflection of a particle of momentum $\vec{p}$ in a magnetic field is:

$$d\theta \approx \tan\theta = \frac{d\vec{p}}{\vec{p}} \tag{5.6}$$

These two equations lead to a simple relation between the energy and deflection angle:

$$E = \frac{e}{\theta}\int \vec{B} \cdot d\vec{l} \tag{5.7}$$

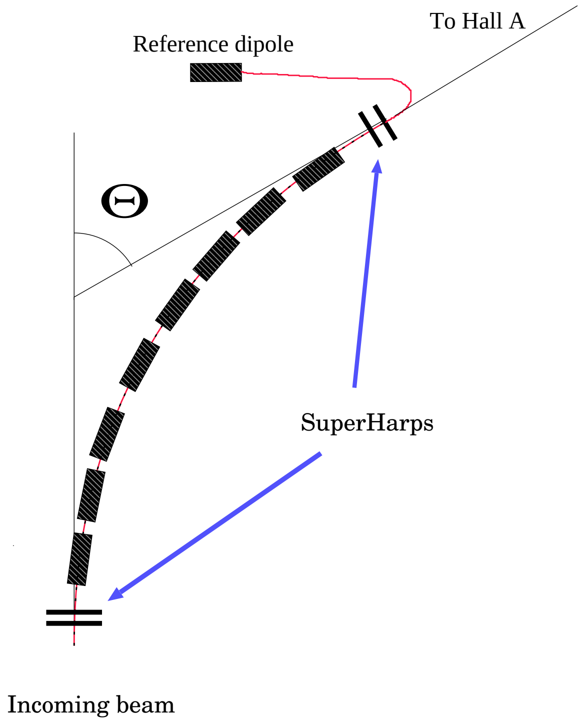

Figure 5.10: Configuration of the Arc used in the incident beam energy measurement.

The JLab electron beam is deflected by 34.3 degrees in the beam switchyard before passing into Hall A [98]. See figure 5.10. This is accomplished in the 42 meter long "Arc" by eight dipole magnets, coupled with nine quadrupoles. The dipole magnets are under vacuum in the beamline which makes access difficult. The magnetic field is instead measured in a ninth identical dipole magnet that is connected in series with the others but outside the beam enclosure.

The deflection angle θ is determined with two pairs of 'SuperHarps', one prior to and one after the Arc. Knowledge of the magnetic field and deflection angle leads to the beam energy through use of equation 5.7. The arc method [99] provides an absolute accuracy on the order of $2 \cdot 10^{-4}$.

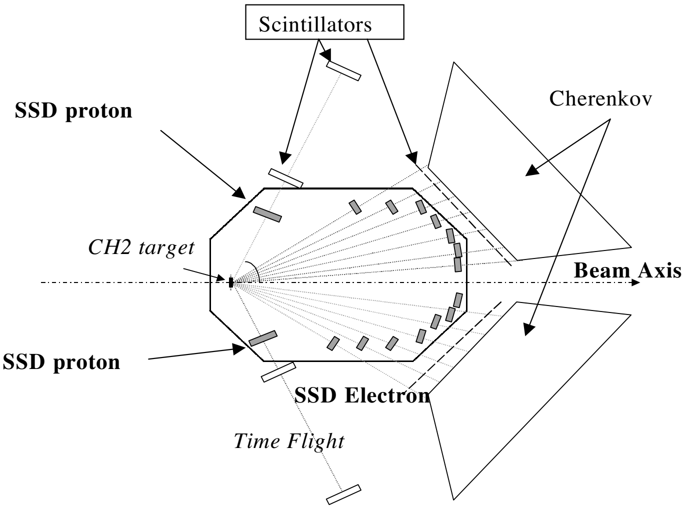

Figure 5.11: Schematic of *ep* energy measurement setup.

eP Energy Determination

The Hall A *eP* energy measurement makes use of the fact that for the elastic $e + p$ reaction the scattering angles of the electron and proton (θ_e and θ_p respectively) are related to the energy E of the incoming electron in a straight-forward way:

$$E = M_p \frac{\cos\theta_e + \sin\theta_e/\tan\theta_p - 1}{1 - \cos\theta_e} + O\left(\frac{m_e^2}{E^2}\right) \tag{5.8}$$

The experimental device is shown schematically in figure 5.11 The target proton is provided by a rotating thin film (10-30μm) of CH2 located 17m upstream of the Hall A target pivot [99]. The electron and proton are measured in coincidence by two sets of detectors symmetrically placed about the beamline. When the two measurements are added, any error due to misalignment of the detectors is canceled in first order. The proton detectors are fixed at 60 degrees while the electron detectors can be moved from 9 to 41 degrees, corresponding to an energy range of 0.5 to 6.0 GeV. The proton detector consists of two scintillator planes, combined with a silicon strip detector (SSD), while the electron detector consists of a scintillator plane and a cerenkov counter in addition to a silicon strip.

Three beam energy measurements were performed using the *ep* device during E94-010. The results are shown in table 5.1.

Elastic Scattering from ^{3}He

E94-010 recorded elastic scattering data for the ^{3}He target for our two lowest incident energies. The elastic form factor drops dramatically as Q^2 increases and we were unable to discriminate the elastic peak from the overlapping quasielastic spectrum at the remaining energies of E94-010. However, for our two lowest energy data sets the elastic data can be used as an independent check of the incident energy. The initial energy, scattering angle, and scattered electron energy are kinematically constrained by:

$$E' = \frac{E}{1 + E/M(1 - \cos\theta)} \tag{5.9}$$

The elastic energy results are listed in table 5.1. Further details of the analysis can be found in [100].

Incident Beam Energy Values

The results for the three different energy measurement techniques are summarized in table 5.1. A careful study of the systematic uncertainties of all the measurements was performed by A. Deur [101], which lead to the final values used in the E94-010 analysis.

Table 5.1: Incident energies in MeV .

Arc	eP	Elastic	Used in Analysis
......	......	862.0 ± 0.86	862.0
......	......	1717.9 ± 1.72	1717.9
......	1717.9 ± 0.44	1716.9 ± 1.72	1716.9
2581.1 ± 1.3	......	......	2580.5
3385.0 ± 1.7	3381.8 ± 0.60	......	3381.8
4238.2 ± 2.1	4236.2 ± 0.79	......	4238.6
5058.2 ± 2.5	......	......	5058.2

5.3 The Spectrometers

The standard Hall A detector configuration includes two high resolution spectrometers (HRS) [89]. See figure 5.4. The spectrometers were initially equipped for the (e,e′p) reaction. Hence they were known as the 'Hadron' and 'Electron' arms. For E94-010, both arms were set to negative polarity and configured for electron detection. As such we will refer to them from hereon as HRS-L and HRS-R.

5.3.1 Magnets

Focusing is provided by three superconducting quadrupoles. Q_1 is convergent in the vertical plane while Q_2 and Q_3 are responsible for the transverse focusing. A 6.6 m long superconducting dipole with a vertical bend of 45° provides the angular separation and in conjunction with the vertical drift chambers (see section 5.4.1), provides a momentum resolution of $2{\cdot}10^{-4}$. The magnets configuration is QQDQ. The resulting horizontal angular resolution is better than 2 mrad. Further spectrometer characteristics are summarized in table 5.2.

The superconducting magnets are cooled by the 1800 W helium End Station Refrigerator (ESR) which is dedicated to providing liquid helium to the three End Station magnets and cryo-target. Coolant flow control and device monitoring is performed using the EPICs control system (See section 7.1).

The magnetic field in the dipoles is monitored with an array of NMR probes that cover the range 0.17-2.10 T. They are accurate to 10^{-5}. A Hall probe is also present within the dipole and can be used to extend the field measurements to lower magnetic fields. The quadrupole fields are all monitored with Hall probes.

The spectrometer central momentum is related to the magnetic dipole field to first order by[‡]:

$$P_0 = \Gamma \cdot B_0 \tag{5.10}$$

Elastic scattering from a thin carbon target accompanied by a beam energy measurement was used to determine the spectrometer constant Γ for each arm [102].

5.3.2 Collimator

At the entrance to the HRS there are two remotely movable collimators. The first, largest collimator is made of 80 mm thick tungsten with an vertical by horizontal aperture of 121.8mm by 62.9mm. The aperture increases

---

[‡] There are small higher order corrections to this expression.

to 129.7mm by 66.8mm at the rear of the first collimator. The second collimator, also made of tungsten, is 50.0mm by 21.3mm at the entrance and expands to 53.2mm by 22.6mm at the exit. Just beyond the collimators is the removable sieve slit, a 5mm thick tungsten plate perforated with 49 evenly spaced holes (see figure 7.16. The sieve is used in optical studies of the magnetic transport properties of the spectrometer.

The first larger collimator was inserted for all of E94-010. During typical data taking the smaller collimator was also inserted, but was removed on several occasions to study the acceptance.

Table 5.2: Characteristics [89] of the HRS.

Bending angle	45°
Optical length	23.4 m
Mom. range (HRS-L)	0.3 - 4.0 GeV/c
Mom. range (HRS-R)	0.4 - 3.2 GeV/c
Mom. acceptance	$-4.5\% < \delta p/p < +4.5\%$
Mom. resolution	1×10^{-4}
Dispersion at the focus	12.4 m
D/M	5.0
Angular range (HRS-L)	12.5° - 150°
Angular range (HRS-R)	12.5° - 130°
Ang. acceptance (hori.)	±30 mrad
Ang. acceptance (vert.)	±60 mrad
Ang. resolution (hori.)	0.5 mrad
Ang. resolution (vert.)	1.0 mrad
$\Delta\Omega$ at $\delta p/p = 0$, $y_0=0$	6 msr
Trans. length acceptance	±5 cm
Trans. position resolution	1 mm

5.3.3 Spectrometer Survey

The nominal scattering angle for both spectrometers in E94-010 was 15.5°. The actual value was determined using a combination of the spectrometer encoder values and dedicated surveys. Table 5.3 summarizes the results for the data analyzed in this thesis. Further details can be found in [103].

Late in the experiment the spectrometer arms were moved briefly, then returned to approximately 15.5°, hence the two slightly different sets of central angles in table 5.3. Five incident beam energies from 0.8 to 4.2

Table 5.3: Survey Results for E94-010. Beamline upstream is positive for the horizontal pointing. Up is positive for the vertical pointing. All lengths are in mm. All angles are in degrees. Error on survey values are of the order of 0.5mm [104]

	10/6-12/12	12/13-12/24
HRS-L Spectrometer Angle	15.503°	15.495°
HRS-L Horizontal Pointing	-0.36	0.48
HRS-L Vertical Pointing	0.62	0.58
HRS-R Spectrometer Angle	15.528°	15.508°
HRS-R Horizontal Pointing	-3.8	-1.11
HRS-R Vertical Pointing	...	0.82

Spectrometer	Before 12/12/98	After 12/13/98
HRS-L Horizontal Pointing	-0.05±0.64	0.18±0.43
HRS-R Horizontal Pointing	-5.18±0.74	-3.48±0.75

Table 5.4: HRS Mispointing as determined from carbon foil optics study.

GeV were run during the first time period, while 5.1 GeV was run after the spectrometer was moved. E94-010 devoted beamtime to scattering from seven thin carbon foils for both of these situations. From this data we can check the results in table 5.3 for the horizontal pointing.

The foils were evenly spaced over a length of 40 cm. Foil # 4 was positioned at the origin of the target coordinate Z_{beam}, which coincides with the geometric center of Hall A [105]. Fig. 5.12 is a schematic showing the placement of the carbon foils and the pointing of the arms. Note that the mispointing is greatly exaggerated in the figure. We plot the Z_{beam} distribution of the carbon foils in figs. 5.13 to 5.16. Notice that the left arm does not see foil #7, while the right arm misses foil #1.

From the position of the central foil ΔZ, we can determine the spectrometer horizontal mispointing $M = \Delta Z \sin\theta$. To reduce the error, we take the weighted average of the mispointing determination for six[§] foils. The results are shown in table 5.4.

The HRS-L results for the mispointing are consistent with zero and agree

---

[§] Only the central five foils can be fit reliably for the Hadron Arm.

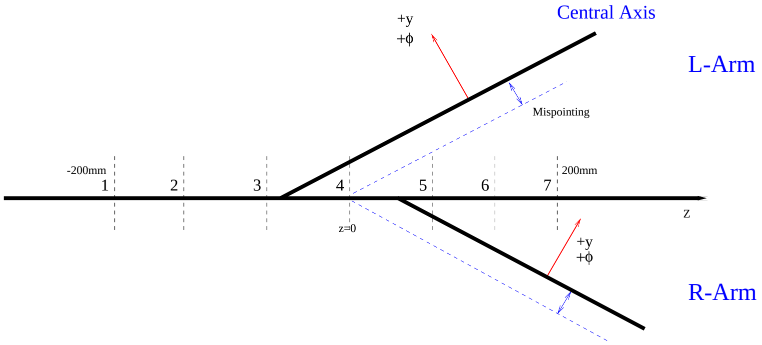

Figure 5.12: The placement of carbon foils used to determine the central angle and mispointing for the HRS.

with the survey within error. The HRS-R results, on the other hand, differs significantly from the survey/encoder values. The HRS-R pointing is found to be large with a substantial uncertainty. This was one of the principle reasons that the HRS-R data was not utilized in the cross section analysis.

5.4 Detector Package

E94-010 utilized elements of the standard Hall A detector package. The configuration is outlined in figure 5.17. A double-planed Vertical Drift Chamber was used to determine particle trajectory and, in conjunction with the dipole, provided the momentum analysis. A pair of plastic scintillator planes formed the trigger, while the first plane alone provided the timing reference for the VDC drift analysis. Particle ID was provided by a gas Čerenkov and lead-glass shower counter. The main difference in the two detector packages is that HRS-L was equipped with a total absorption calorimeter, while HRS-R possessed only a thin lead-glass layer.

We now describe the various detector elements in detail.

5.4.1 Vertical Drift Chamber

An ionizing particle passing through a gas will create electron-ion pairs. If the gas is placed under high voltage, the electrons will then accelerate towards the positive anode. Collisions with the gas molecules limit the maximum velocity which can be reached, so the behaviour is characterized by an average or ‘drift’ velocity. If the electric field is strong enough, the

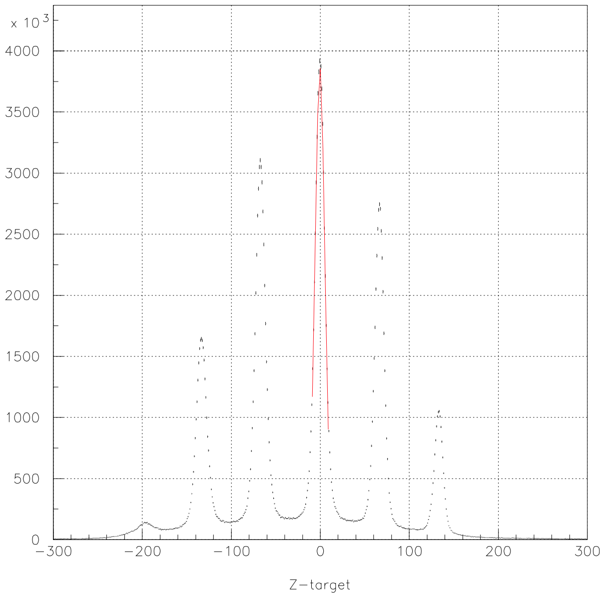

Figure 5.13: HRS-L carbon foil data,15.503°.

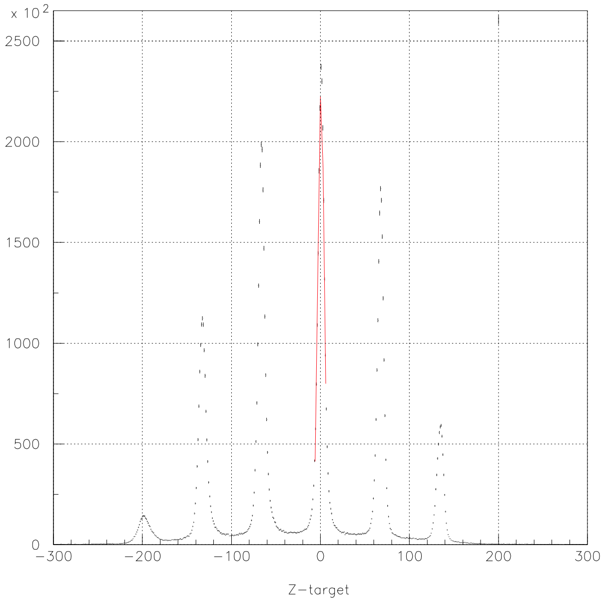

Figure 5.14: HRS-L carbon foil data,15.495°.

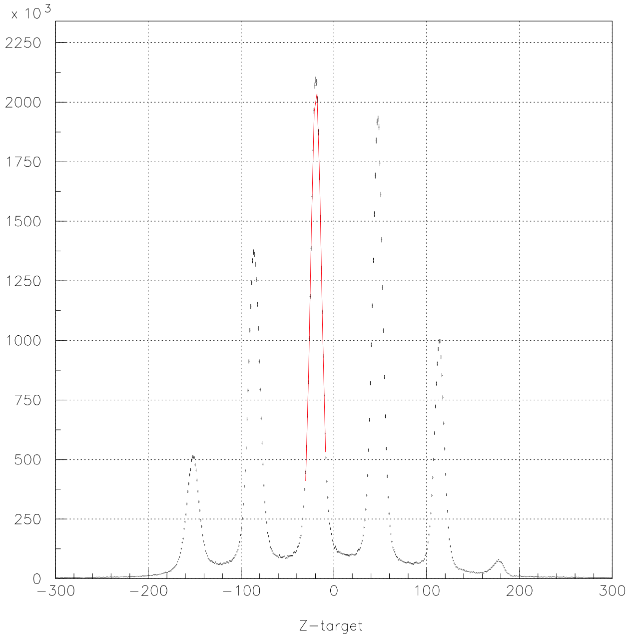

Figure 5.15: HRS-R carbon foil data, 15.528°.

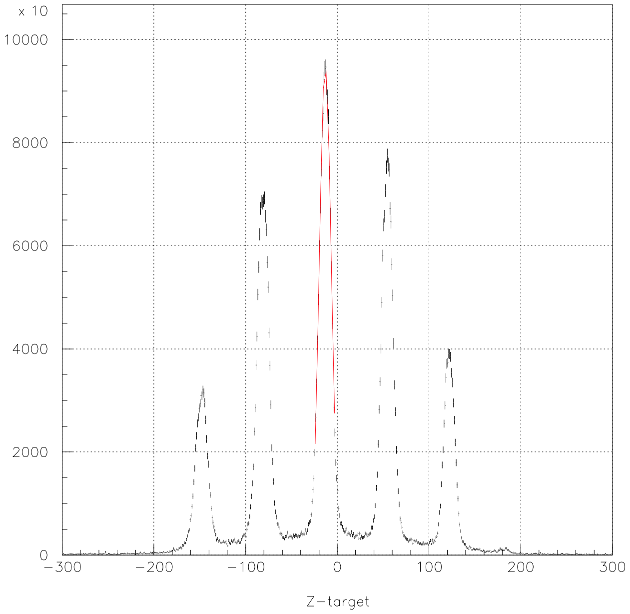

Figure 5.16: HRS-R carbon foil data, 15.508°.

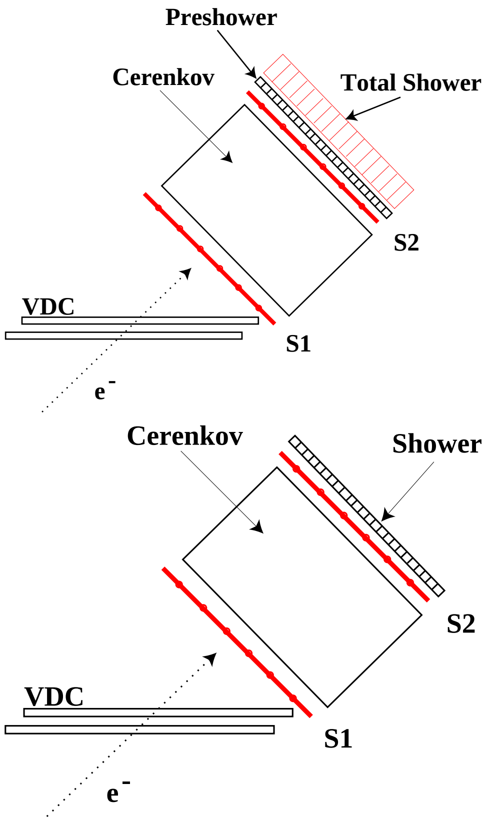

Figure 5.17: Detector package for HRS-L (top) and HRS-R (bottom).

initial ionized electron can be accelerated to the point that it creates secondary ionization, which in turn initiates further ionization, etc. The net result is an avalanche of electrons at the anode which boosts the detectable signal [106].

These properties are utilized in the Hall A Vertical Drift Chambers [107] or VDC. There are two VDC's in each spectrometer, with the lower plane approximately coincident with the spectrometer focal plane. The two chambers are separated by a vertical distance of 0.335 m. See figure 5.17 and 5.18. Each VDC consists of two orthogonal planes of 400 4% gold-plated 20μm tungsten wires. They are set with a uniform tension of 0.7N to compensate for the electrostatic repulsion of the wires. The first and last 16 wires on each frame are used for field shaping, leaving 368 active sensing wires, 60 cm

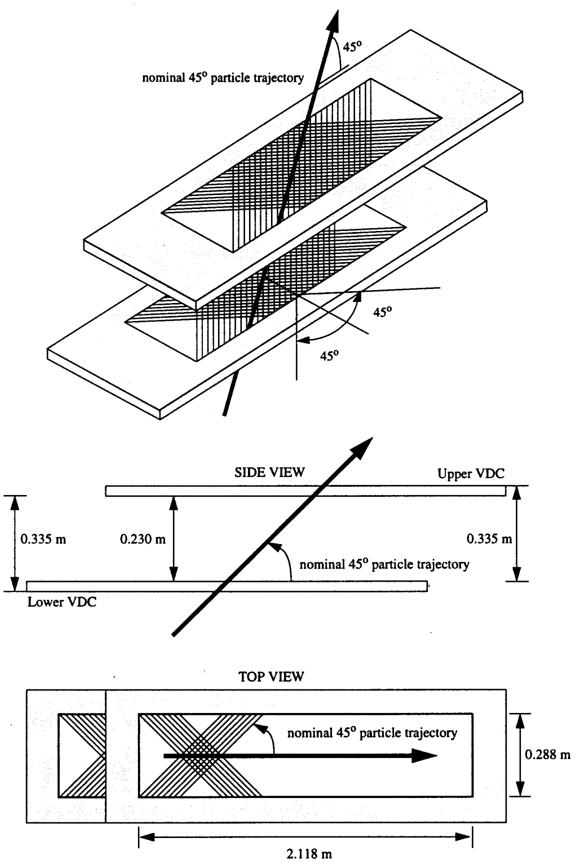

Figure 5.18: Vertical Drift Chambers. For relative location in the detector stack, see figure 5.17. *Reproduced from* [107]

in length. The high voltage cathode planes are held at -4kV, while the sensing anode wires are grounded. The entire apparatus is bathed in a 65/35 (by volume) gas mixture of 99.999% pure argon and 99.0% pure ethane, which is bubbled through a 0°C bath of ethanol. The argon provides the ionizing medium, while the ethane acts to absorb photons created in the avalanche. The gas is continuously flowed at a rate of 10 l/hr in order to provide the homogenous steady state dry gas needed for constant drift velocity.

The wire spacing was chosen so that an electron with the nominal trajectory of 45° will cross the drift cells of 5 sensing wires. See figure 5.19. An electron with the most extreme possible angle of 52° will still encounter

3 drift cells. An ionized electron will travel from the ionization point to the sense wires along the constant field lines established by the high voltage planes until they encounter the radial high-field region immediately surrounding the wire. They then accelerate dramatically, creating many secondary ionizations. TDC values of the signal hits and knowledge of the drift velocity($\approx 50\mu$m/ns) enables perpendicular projection back to the initial electron trajectory for the 5 wires. These five points are then linearly fit to determine the cross over point. The orthogonal wire planes determine the particle's two-dimensional cartesian coordinates. The use of two identical VDC then allows determination of the trajectory.

The single wire efficiency is better than 99%. Since a typical reconstructed track involves 4 to 6 wires the overall efficiency is essentially 100%, although it degrades dramatically if contaminants infiltrate the chambers. The spatial resolution has been determined to be 225 μm per plane [107].

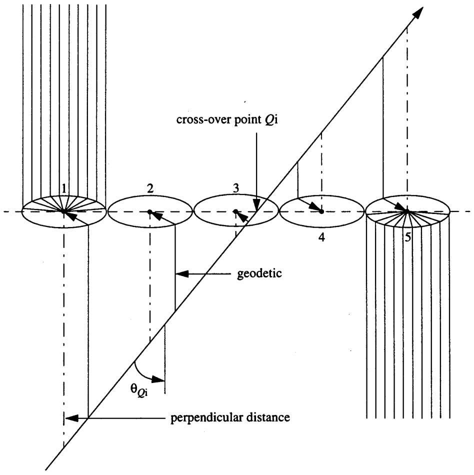

Figure 5.19: VDC Drift cell geometry. *Reproduced from* [107].

5.4.2 Hodoscopes

Two plastic scintillator planes, separated by about 2 meters, provided the main trigger for E94-010. That is, they determined when the DAQ should begin and stop recording data. Each plane consists of six overlapping 5 mm thick paddles, and each paddle is viewed by two photomultipliers. The timing resolution of the paddles is 0.30 ns.

Each event was evaluated to see if it satisfied the three requirements to be classified as an S_{ray}:

1. The left and right phototubes on a paddle in S_1 both fire.
2. The left and right phototubes on a paddle in S_2 both fire.
3. The S_1 and S_2 paddles are aligned along a plausible track, i.e., the track is reasonably[¶] close to 45°.

The S_{ray} criteria was evaluated with a Memory Lookup Unit (MLU) which, for a specific combination of logical input signals, provides a programmed series of logical output signals. Then the event was classified as one of the following four Event Types:

HRS-L	HRS-R	Logic
T_1	T_3	S_{ray} criteria satisfied
T_2	T_4	(S_1 signal OR S_2 signal) AND Čerenkov signal

Note that T_2 is exclusive to T_1, and T_3 is exclusive to T_4. T_2 and T_4 events present a measure of the scintillator inefficiency since they represent otherwise good events that one of the scintillators failed to detect. This inefficiency gradually increased over the course of the experiment reaching a maximum of 13%. The cause of this phenomenon is discussed in section 7.4.1.

Each trigger is counted by the scalers before being sent to the Trigger Supervisor (TS). The TS applies the prescale factor and determines whether the DAQ should record the event. Each of the event types 1 to 4 can be individually pre-scaled so that only a fraction of the actual events are considered by the DAQ. When the DAQ is busy, the event will be missed. This happens, for example, during the short time (300-400μs) it takes for the DAQ to build an event or when the DAQ is fulfilling an input/output request. This is known as the software deadtime.[‖] The scaler trigger counts are used offline to correct for the deadtime.

[¶] Specifically, if the event triggers paddle i in the first scintillator plane, then it must trigger paddle i or $i \pm 1$ in the second plane.

[‖] There is also a hardware deadtime due to the response time of the detectors. This is negligible when compared to the software deadtime.

The T_2 and T_4 events exhibited a large helicity-dependence in the deadtime. As such they were excluded from the asymmetry analysis, with the reasoning that the scintillator inefficiency will effect both helicity states equally and the efficiency correction cancels out in the ratio. For the unpolarized cross section analysis, these events were corrected by the relevant prescale factor and added back into the main trigger events.

5.4.3 Čerenkov Radiation

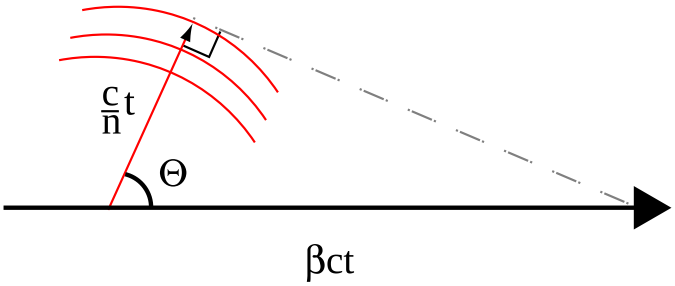

Figure 5.20: Čerenkov radiation

The velocity of light is reduced when travelling through a transparent medium such as a gas, so that a high energy particle with velocity βc may exceed the velocity of light $\frac{c}{n}$ within the medium.** When this happens, an "electromagnetic shockwave" [106] occurs, analogous to the sonic boom created by a supersonic aircraft. The wave is emitted in a conical pattern as shown in Fig. 5.20, with half angle θ given by:

$$\cos\theta = \frac{1}{\beta n} \tag{5.11}$$

The threshold for production of Čerenkov radiation is:

$$\beta c \geq \frac{c}{n} \tag{5.12}$$

The existence of a threshold which depends critically on the particle velocity makes the detection of Čerenkov light a very effective method to discriminate between species of differing mass.

[**] The particle's velocity is of course still limited to the speed of light in vacuum, c.

The Hall A Čerenkov Detectors

HRS-L and HRS-R both possess threshold gas Čerenkov detectors for use in particle identification. The Čerenkov tanks utilize atmospheric pressure CO_2 with an index of refraction of 1.00041 [108]. This results in a half-cone angle θ of roughly 1.6 degrees, so the light is emitted mostly in the forward direction. Using equation (5.12) and the fact that $\gamma = (1-\beta^2)^{-\frac{1}{2}}$ and

$$E = \gamma mc^2 = \sqrt{m^2c^4 + p^2c^2} \tag{5.13}$$

we can easily determine the threshold energy for production of Čerenkov radiation for electrons and for pions. We find that the minimum momentum necessary for an electron to trigger the Čerenkov is only about 18 MeV/c while any pion with a momentum below 4.87 GeV/c will not trigger the detector. The range of spectrometer momenta covered in experiment E94-010 is roughly 300 MeV/c to 3.6 GeV/c. For all these settings, incident electrons will radiate Čerenkov light, while pions will not. This provides the primary method of removing pion contamination from the data.

Čerenkov detector details

The two detectors have identical cross-sections but differing lengths. The HRS-L detector is 1.5 m long while the HRS-R is only 1.0 m in length. The detectors house 10 rectangular profile, spherical mirrors. Each mirror is positioned to reflect collected light to a dedicated photo-multiplier tube (Burle 8854) [108]. The mirrors sit in two columns of 5 at the rear of the tanks, and are made of light-weight ($\sim 5.5 \times 10^{-3}$ radiation lengths) materials to minimize attenuation of the incident electrons.

5.4.4 Lead Glass Shower Detector

An electromagnetic cascade of energetically degraded secondaries (γ, e^+, e^-) results when an energetic particle enters a dense material. As the cascade propagates, most of the original particle's energy is converted to heat and light. A calorimeter or 'shower detector', relies upon collection of this light to determine a particle's energy. The calorimeter is typically segmented into many individual cells or blocks with each block being monitored by a photomultiplier tube.

The HRS-L calorimeter consists of two segmented layers. The first 'preshower' layer is made of $48(24 \times 2)$ blocks of TF-1 lead glass. Each of the preshower blocks are $10cm \times 10cm \times 35cm$. The second shower layer

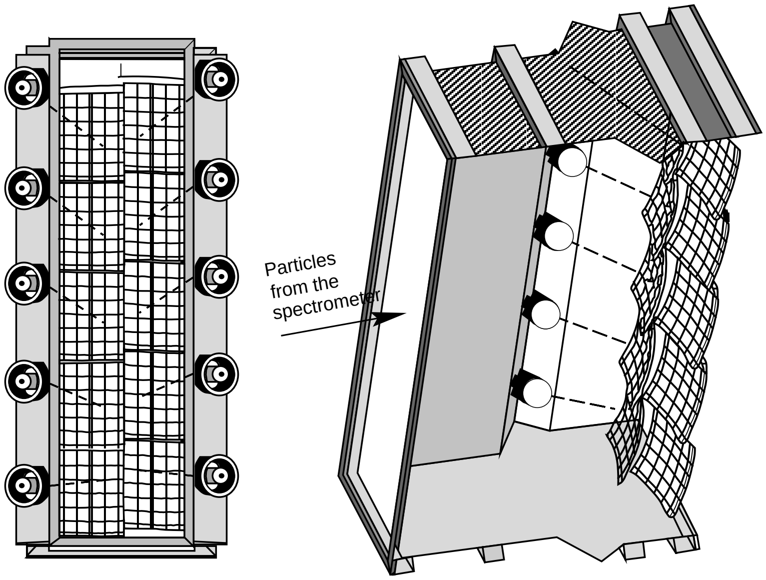

Figure 5.21: HRS-L Čerenkov detector schematic. *Reproduced from [108].*

is made of $96(48 \times 2)$ blocks of SF-5 lead glass. Each of the shower blocks are $15cm \times 15cm \times 35cm$ [109]. A schematic of the HRS lead-glass is shown in figure 5.23 and it's relative location in the detector stack can be seen in figure 5.17. The HRS-R shower detector consists of a single layer of $32(16 \times 2)$ lead glass blocks arranged as shown in Fig. 5.17

We will discuss the shower detectors performance in further detail in section 7.4.4.

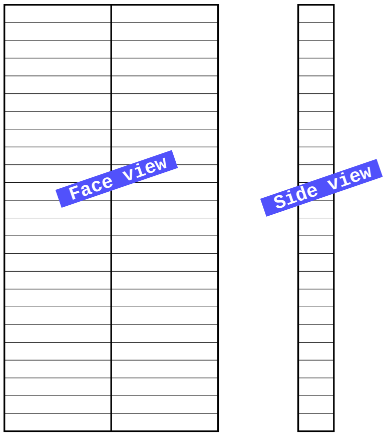

Figure 5.22: HRS-L preshower lead glass detector.

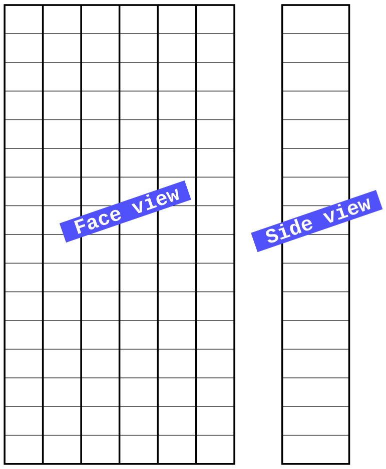

Figure 5.23: HRS-L shower lead glass detector.

CHAPTER 6

THE POLARIZED ^{3}HE TARGET

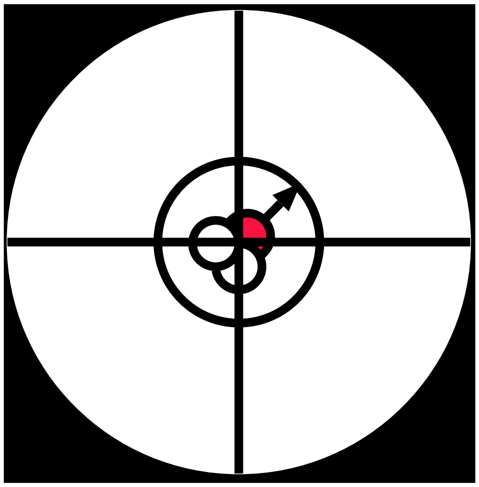

The JLab polarized ^{3}He target can lay claim to a distinguished lineage, having evolved from earlier apparatus [110, 111] used in the seminal SLAC spin structure program. Significant modifications and improvements were implemented for E94-010 which represents the first use of polarized ^{3}He at JLab. This necessitated an intense commissioning period that extended right up to the final day before the experiment began. In this chapter, we will examine the polarization process and experimental setup in detail.

Polarized ^{3}He provides a practical polarized neutron target since the ground state configuration is dominated by an S-wave contribution in which the protons are spin-paired. To polarize the JLab ^{3}He target, an alkali metal vapor (rubidium) is optically pumped. Rubidium is chosen because the D_1 line* lies in the near infrared and can be easily pumped with commercially available laser sources. The rubidium polarization is then transferred

---

*The D_1 line represents the energy splitting between the ground state $S_{1/2}$ and $P_{1/2}$ levels as shown in figure 6.1.

from the valence electron to the ^{3}He nucleus by spin exchange collisions. Maximum polarizations obtained with this method approach 50%, although there has been an intense effort in recent years to push this value significantly higher with novel techniques such as using Xenon as a substitute for the alkali metal.

6.1 Thermal Distribution of ^{3}He Polarization

As a spin-1/2 nucleus, the ^{3}He magnetic moment has only two possible orientations with respect to the magnetic holding field. This leads to two discrete energy levels. The populations of such a two-level system follow a Boltzman distribution. That is:

$$\begin{aligned} N_+ &= N \cdot e^{-\frac{E_+}{kT}} \\ N_- &= N \cdot e^{-\frac{E_-}{kT}} \end{aligned} \tag{6.1}$$

where $N = N_+ + N_-$ and $E_\pm$ is the potential energy of the dipole when it is anti-aligned or aligned with $\vec{B}$, and k is the Boltzman constant.

The potential energy of a dipole (in this case the ^{3}He nucleus) in a magnetic field is:

$$W = -\vec{\mu_3} \cdot \vec{B} \tag{6.2}$$

where $\vec{\mu_3} = -2.1276 \cdot \mu_N$ is the magnetic moment of ^{3}He and $\mu_N = \frac{e\hbar}{2M_p}$ is the nuclear magneton.

The polarization P is determined by:

$$\begin{aligned} P &= \frac{N_+ - N_-}{N_+ + N_-} \\ &= \frac{e^{-\frac{E_+}{kT}} - e^{-\frac{E_-}{kT}}}{e^{-\frac{E_+}{kT}} + e^{-\frac{E_-}{kT}}} \\ &= \frac{1 - e^{-\frac{(E_- - E_+)}{kT}}}{1 + e^{-\frac{(E_- - E_+)}{kT}}} \\ &= \frac{1 - e^{-\frac{2\mu B}{kT}}}{1 + e^{-\frac{2\mu B}{kT}}} \end{aligned}$$

so

$$P \sim \frac{\mu B}{kT} \tag{6.3}$$

6.2 Optical Pumping of Rubidium

Equation 6.3 reveals that thermal polarization techniques are inadequate to achieve the high polarization values necessary in typical $^3\vec{He}(\vec{e}, e')X$ scattering experiments. For example, the thermal polarization of a ^{3}He sample cooled to 200mK in a 10T field would still only be about 3.9%.

The techniques of optical pumping are not directly applicable to this problem since the ^{3}He S-P energy splitting lies in the far ultraviolet region where practical light sources are unavailable. Instead, a two-step process is used, wherein rubidium is optically pumped and then the rubidium polarization is transferred to the ^{3}He nucleus. In this process, target cells containing about 10 atmospheres of ^{3}He, along with a small admixture of rubidium and nitrogen are placed in a magnetic field of about 30 gauss to provide the necessary energy level splitting. (See Fig. 6.1.)

The energy levels[†] of rubidium placed in a magnetic field depends on the quantum numbers of the system and the magnitude of the magnetic field. The quantum numbers of the rubidium system are:

- $S = \frac{1}{2}$: The intrinsic spin of the electron.
- L: The orbital angular momentum of the electron. Spectroscopic notation is used in which the value of L is given by a letter with the following correspondence: $S = 0, P = 1, D = 2, F = 3, \ldots$
- J: The total angular momentum of the electron, where $\vec{J} = \vec{L} + \vec{S}$, and J is constrained to the range: $(L + S, L + S - 1 \ldots \leq J \leq \ldots L - S)$
- I: The angular momentum of the nucleus.
- F: The resultant angular momentum of the atom, where $\vec{F} = \vec{I} + \vec{J}$, and F is constrained to the range: $(I + J, I + J - 1, \ldots \leq F \leq \ldots I - J)$
- m_F: The z-component of $\vec{F}$ where $m_\mathrm{F} = F, F - 1, \ldots, -F$

Transitions between levels of different F are known as hyperfine transitions and follow the selection rule $\Delta F = 0, \pm 1$. Zeeman transitions occur between different m$_F$ levels and follow similar restrictions: $\Delta m_F = 0, \pm 1$.

Naturally occurring rubidium consists of approximately 72% ^{85}Rb and 28% ^{87}Rb. The JLab target utilizes right circularly polarized light from a

---

[†] The energy levels are specified with the notation N^{2S+1}L$_J$, where N denotes the electron shell, S is the intrinsic spin of the electron, L is the orbital angular momentum of the electron, and J is the vector sum of $\vec{L}$ and $\vec{S}$.

diode laser array centered at 794.7 nm to stimulate the transition of the ^{85}Rb valence electrons from the 5^2S$_{1/2}$ sublevels to the 5^2P$_{1/2}$ sublevels subject to the selection rule $\Delta m = +1$. This rule follows from conservation of angular momentum since the incident circularly polarized photons carry exactly one unit of angular momentum.

The excited electrons can then decay by a $\Delta m = 0, \pm 1$ transition, since the photon can be emitted in any direction, not only along the quantization axis defined by the magnetic field. If they are reabsorbed, D$_1$ photons making $\Delta m = -1$ transitions would act to depopulate the $F = 3$ levels, including the sublevel we are trying to saturate, so photon emission is suppressed by the introduction of a small amount of N$_2$ buffer gas. Rb-N$_2$ collisions radiationlessly de-excite the Rb, although a few percent of the excited atoms still decay by emitting a D$_1$ or D$_2$ photon. D$_2$ photons [‡] are present because electrons in the 5^2P$_{1/2}$ state can make the small jump to the 5^2P$_{3/2}$ state due to their thermal energy[§].

After relaxation, the ground state electrons are able to absorb another photon. That is, all electrons except for those in the $F = 3, m = +3$ state, because there is no $m = 4$ state available from the D$_1$ transition. Eventually, the majority of atoms collect in the $m = 3$ sublevel and the Rb ensemble becomes magnetically oriented. Of course, this entire process can be performed with left circularly polarized light, with the final result being a majority of valence electrons in the ground state $m = -3$ sublevel instead.

6.3 Spin Exchange

The cross section for spin exchange between the Rb valence electron and the ^{3}He nucleus is about 10^{-24} cm^2 (a *huge* cross section by nuclear physics standards) and the rate of transfer [112] of polarization from the rubidium valence electron to the ^{3}He nucleus is given by:

$$\gamma_{se} = \langle \sigma_{se} v \rangle [Rb] \tag{6.4}$$

where $\langle \sigma_{se} v \rangle = 1.2 \cdot 10^{-19}$ cm^3 s^{-1} is the velocity averaged ^{3}He-Rb spin exchange rate constant [113], and [Rb] is the rubidium number density.

[‡] The D_2 line represents the energy splitting between the ground state $S_{1/2}$ and $P_{3/2}$ levels as shown in figure 6.1.

[§] The energy gap between the $^2P_{1/2}$ state and the $^2P_{3/2}$ state is about 0.03 eV. The kinetic energy, $\frac{3}{2}kT$ is about 0.065 eV at the operating temperature of 230°C in the target pumping chamber. So the two states become thermally mixed.

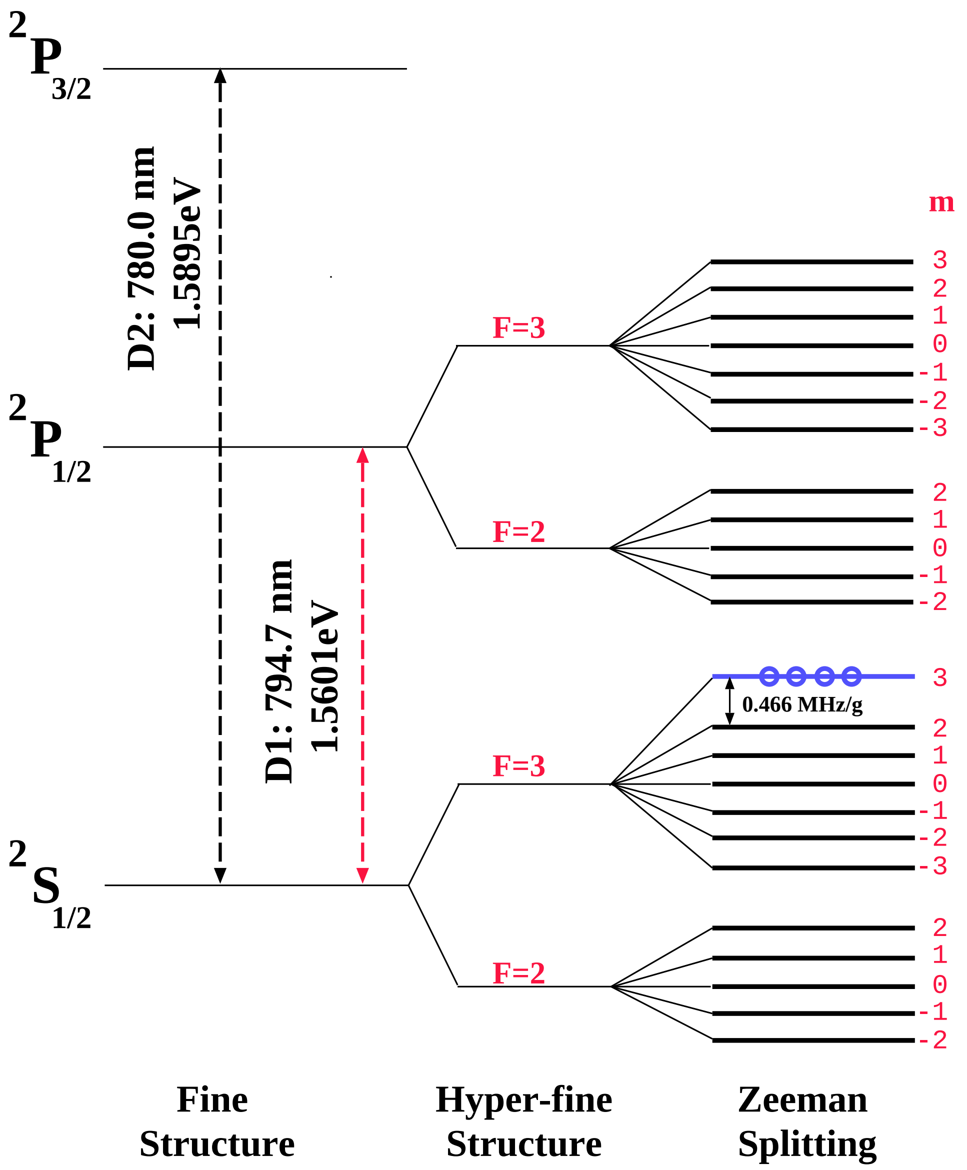

Figure 6.1: Energy level diagram for ^{85}Rb, I=5/2. Polarized photons tuned to the rubidium D_1 line are used to excite electrons from the ground state to the $P_{1/2}$ sublevels. The selection rules ensure that the ground state $m = 3$ sublevel becomes saturated.

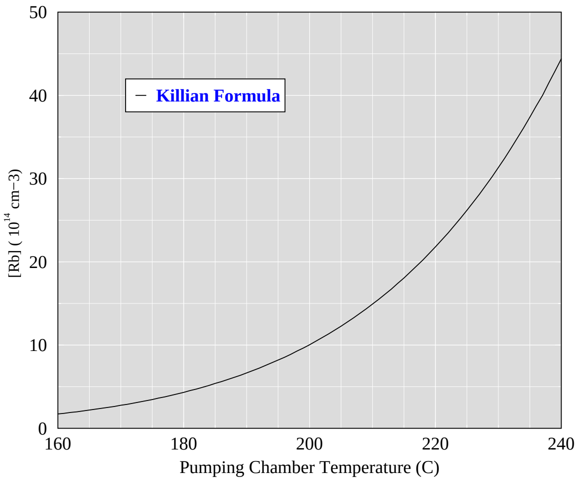

Figure 6.2: Temperature dependence of rubidium density as predicted by Killian [114]

The temperature dependence of the Rb density can be described by the Killian formula: [114]

$$[Rb] = \frac{10^{10.55 - \frac{4132}{T}}}{1.38 \cdot 10^{-16} T} \tag{6.5}$$

which is illustrated in figure 6.2. Wagshul [115] showed that this formula is accurate up to at least 180°C. Above 200°C the formula tends to overestimate the density. At typical JLab target operating temperatures (170°C), equation 6.5 predicts a rubidium number density of about $2.7 \cdot 10^{14}$ cm^{-3}, so the spin exchange rate is expected to be about $(8.5\text{h})^{-1}$.

6.4 Rate of Polarization

The population of ^{3}He atoms in the $+1/2$ state is described by the differential equation [115]:

$$\frac{dn_+}{dt} = \left(\frac{\Gamma}{2} + \gamma_{se}\ n_{Rb+}\right) n_- - \left(\frac{\Gamma}{2} + \gamma_{se}\ n_{Rb-}\right) n_+ \tag{6.6}$$

where $n_\pm$ ($n_{Rb\pm}$) are the fractional ^{3}He (Rb) populations. That is, $n_+ + n_- = 1$. γ_{se} is the Rb-^{3}He spin exchange rate and Γ is the total relaxation rate which we describe further in section 6.5.

Solving the differential equation we can evaluate the ^{3}He polarization $P = n_+ - n_-$ as a function of time:

$$P(t) \quad = \quad \frac{\gamma_{se} P_{Rb}}{\gamma_{se} + \Gamma} \left[1 - e^{-(\gamma_{se}+\Gamma)t}\right] \tag{6.7}$$

where Γ is the total relaxation rate, P_{Rb} is the Rb polarization and we have assumed $P(t = 0) = 0$.

At equilibrium:

$$P \longrightarrow \left(\frac{\gamma_{se}}{\gamma_{se} + \Gamma}\right) P_{Rb} \tag{6.8}$$

The time it takes to reach equilibrium is characterized by the time constant $(\gamma_{se} + \Gamma)$. So we need $\gamma_{se} \gg \Gamma$ and large values of P_{Rb} in order to achieve highly polarized ^{3}He.

6.5 Relaxation Mechanisms

There are several relaxation mechanisms that compete with the spin exchange and act to destroy the polarization. The total relaxation rate without beam is given by:

$$\Gamma \quad = \quad \Gamma_D + \Gamma_w + \Gamma_\nabla \tag{6.9}$$

Here, Γ_D signifies the relaxation rate due to the ^{3}He-^{3}He magnetic dipolar interaction [116]. This causes a relaxation rate of

$$\Gamma_D = \frac{[^3He]}{744}\ h^{-1} \tag{6.10}$$

which at typical target densities translates to about $(70h)^{-1}$.

Γ_w is the relaxation due to magnetic impurities in the glass wall that disorient the noble gas spins [117]. This mechanism is amplified in glass that is permeable to ^{3}He such as pyrex, which has a wall relaxation rate of about $(3h)^{-1}$. When glass that is impermeable to ^{3}He, such as Corning 1720, is used the depolarization rate is reduced to $(30h)^{-1}$ or less [118]. Typical cells used in E94-010 had excellent wall relaxation rates of about $(90\mathrm{h})^{-1}$.

Finally, Γ_∇ represents the relaxation rate due to the ^{3}He spins interacting with gradients in the magnetic holding field:

$$\Gamma_\nabla = D\frac{|\nabla B_x|^2 + |\nabla B_y|^2}{B_z^2} \tag{6.11}$$

where D is the ^{3}He self-diffusion constant, B_z is the holding field and

$$|\nabla B_i|^2 = \left(\frac{\partial B_i}{\partial x}\right)^2 + \left(\frac{\partial B_i}{\partial y}\right)^2 + \left(\frac{\partial B_i}{\partial z}\right)^2 \tag{6.12}$$

To ensure that the field gradients do not pose a significant source of depolarization we require the lifetime due to magnetic field inhomogeneity to be greater that 100 hours. This implies that the gradients must be less than about 35 mG/cm for typical running conditions at a holding field of 26 gauss. Field mapping [119] of the JLab Helmholtz coils was used to optimize the coil orientation, allowing us to achieve a relaxation rate on the order of $(1000h)^{-1}$, well within the above stated requirements.

Taking into consideration the various contributions listed above, the total relaxation rate in the absence of beam for typical cells used at JLab is about $(50\mathrm{h})^{-1}$. Finally, the high energy electron beam ionizes ^{3}He atoms as it passes through the cell and thus introduces another relaxation mechanism [120, 121].

6.6 Experimental Setup

Figures 6.3 shows a schematic of the target and related polarimetry equipment. The longitudinal or transverse holding field of up to 30 gauss is provided by two pairs of Helmholtz coils. Only one pair shown in figure 6.3. The target is a double chambered glass cell containing approximately 10 atm of ^{3}He, with a small admixture of N_2 and Rb. The lower target chamber is approximately 40 cm long with a diameter of approximately 1.8 cm, while the spherical pumping chamber has a typical diameter of 2.5 inches.

The pumping chamber is placed within an air blown oven that is used to vaporize the rubidium within. In order to monitor the target density, five RTDs[¶] were evenly spaced along the length of the target cell. Two additional RTDs were located within the oven, directly on the face of the pumping chamber. After the rubidium is sufficiently heated, it is optically pumped using about 100 watts of circularly polarized diode laser light. An RF (Radio Frequency) coil operating at 92kHz is used to flip the ^{3}He spins during NMR polarization measurements. The resonance is detected by the pickup coils located along the length of the target cell. The small coil just above the pumping chamber is used during EPR measurements to induce the Zeeman transition which is then detected with a photodiode.

[¶] Resistive temperature device

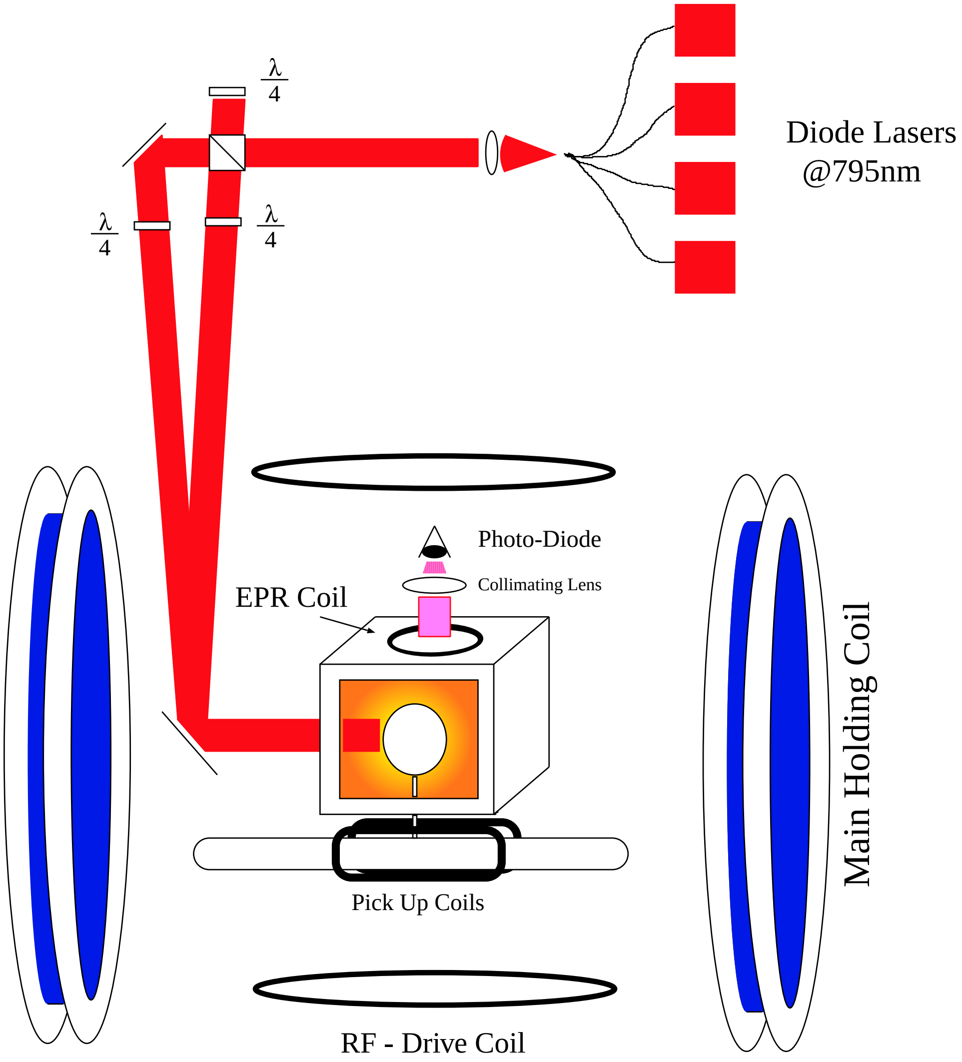

Figure 6.3: The polarized ^{3}He target.

The two polarimetry techniques are discussed in further detail in sections 6.7 & 6.8.

6.7 Electron Paramagnetic Resonance

In the absence of polarized ^{3}He, the Zeeman splitting of the $F = 3$ sublevels of the Rb ground state is proportional to the holding field:

$$\nu = \kappa_z \cdot B \tag{6.13}$$

where $\kappa_z = 0.466$ MHz/G. The presence of magnetically oriented ^{3}He causes a small but measurable increase in this splitting which is proportional to the ^{3}He polarization. The polarized target holding field is typically 25.5 gauss, which causes a level splitting of about 11.8 MHz.

To measure the deviation $\Delta\nu$ from this value, a small coil is used to probe the rubidium energy levels. An oscillating magnetic field at the proper frequency will be able to excite the $m = 3$ to $m = 2$ transition of the $F = 3$ ground state sublevel. This increases the number of $m = 2$ ground state atoms that can be excited by the incident laser light, and there is a corresponding increase in the number of photons emitted as these excited states decay. At resonance, the EPR coil frequency equals the Zeeman frequency and the fluorescence is maximized [‖].

The change of the Zeeman frequency due to the polarized ^{3}He magnetic field can be determined by flipping the ^{3}He spins while monitoring the resonance frequency as shown in figure 6.4. Initially the spins will add to the main holding field and after they will subtract. By taking the difference of the measured frequencies in these two states we can extract $\Delta\nu$ and hence the polarization.

The frequency variation is related to the ^{3}He polarization by [122]:

$$\Delta\nu = \left[\frac{8\pi}{3}\frac{\mu_0}{4\pi}\left(\frac{d\nu}{dB}\right)\kappa_0\mu_3[^3He]\right]\mathbf{P}_3 \tag{6.14}$$

for the $F = I + 1/2, m = \pm F$ state. Here, $\left(\frac{d\nu}{dB}\right)$ is a factor that depends only on the magnetic field and κ_0 is a temperature dependent factor

$$\kappa_0 = 4.52 + 0.00934 \cdot T[^\circ C] \tag{6.15}$$

[‖] Since the cell is bathed in D_1 pumping light from the lasers, it is difficult to detect the small variation in D_1 light due to the increased intensity. Instead, a D_2 filter is used and we detect the resonance from the D_2 light.

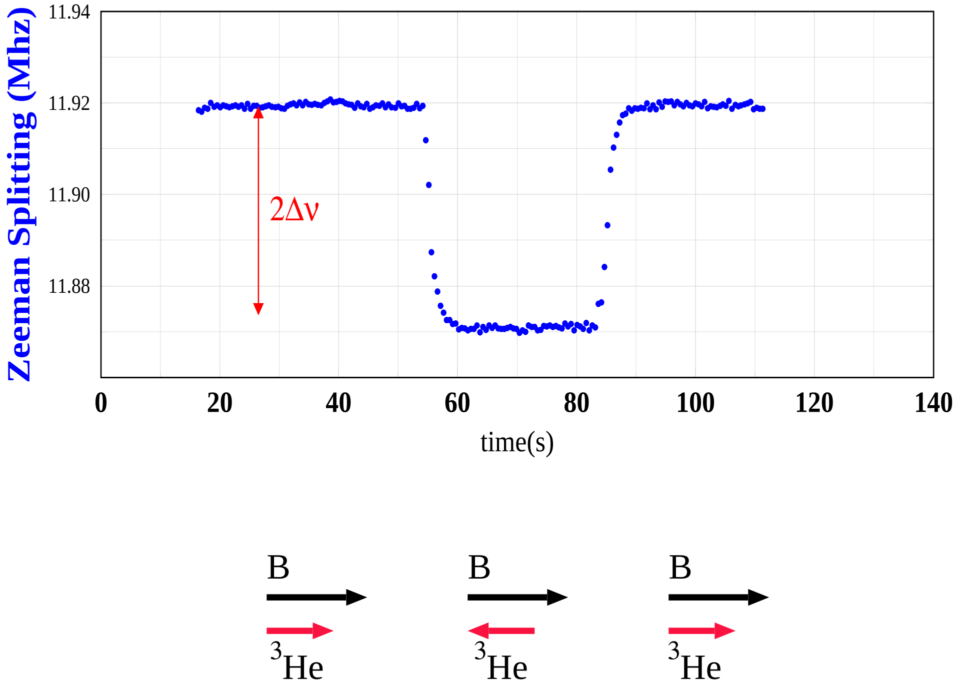

Figure 6.4: EPR spectrum. Top panel shows the measured Zeeman splitting while the bottom shows the relative configuration of the magnetic holding field and ^{3}He spins.

6.8 Nuclear Magnetic Resonance

6.8.1 Classical Description

The classical equation of motion for a spin $\vec{J}$ in a magnetic field $\vec{H}$ is:

$$\frac{d\vec{J}}{dt} = \vec{M} \times \vec{H} \tag{6.16}$$

where $\vec{M} = \gamma\vec{J}$ is the associated magnetic moment and γ is the gyromagnetic ratio. The motion of $\vec{J}$ is described by precession of $\vec{M}$ around the field $\vec{H}$ at the Larmor frequency γH.

If we introduce a field $\vec{H}_1$=H$_1[\hat{i}\cos(wt) + \hat{j}\sin(wt)]$ that rotates around the z axis at frequency ω, then the equation of motion becomes:

$$\frac{d\vec{M}}{dt} = \vec{M} \times \gamma(\vec{H}_0 + \vec{H}_1)$$

In the rotating frame the equation of motion is:

$$\begin{aligned}\left(\frac{d\vec{M}}{dt}\right)_{rel} &= \frac{d\vec{M}}{dt} + \vec{\omega} \times \vec{M} \\ &= \vec{M} \times \gamma(\vec{H}_0 + \vec{H}_1) + \vec{\omega} \times \vec{M} \\ &= \vec{M} \times [\hat{k}(\omega_0 - \omega) + \hat{\imath}'\omega_1]\end{aligned} \tag{6.17}$$

This has the standard form of a magnetic moment in a magnetic field. So the motion in the rotating frame is a precession around the effective field:

$$H_{eff} = \frac{\hat{k}(\omega_0 - \omega) + \hat{\imath}'\omega_1}{\gamma}$$

The effective field will point in a direction θ with respect to the z-axis such that:

$$\tan\theta = \frac{\omega_1}{\omega_0 - \omega} \tag{6.18}$$

The motion in the absolute frame is obtained by superposing the rotation at frequency ω about the z-axis to the motion in the rotating frame. It is apparent that if the holding field H_0 is ramped through the resonance $\mathrm{H}_0 = \omega/\gamma$ the angle θ will go from 0 to 180°, that is the spin will flip. At resonance $\omega_0 = \omega$ and the magnetic moment will be precessing around the z-axis at 90°. This resonance can be detected in a pair of inductance coils. The detected signal will be proportional to the transverse magnetization:

$$S \propto \sin\theta = \frac{\omega_1}{\sqrt{(\omega_0 - \omega)^2 + \omega_1^2}} \tag{6.19}$$

6.8.2 Quantum Mechanical Description

As a spin 1/2 system in a magnetic field, the ^{3}He nucleus has two discrete energy levels: $\pm(\mu_3 B_0)$ depending on the orientation of the magnetic moment with respect to the field. A magnetically oriented ensemble can be induced to make transitions from one level to the other by resonant frequency photons. The frequency of resonance is $\omega = 2\frac{\mu_3 B_0}{\hbar}$.

6.8.3 Experimental Method

To detect the resonance, an RF magnetic field is applied to the target orthogonally to the holding field as shown in figure 6.5. The polarization is

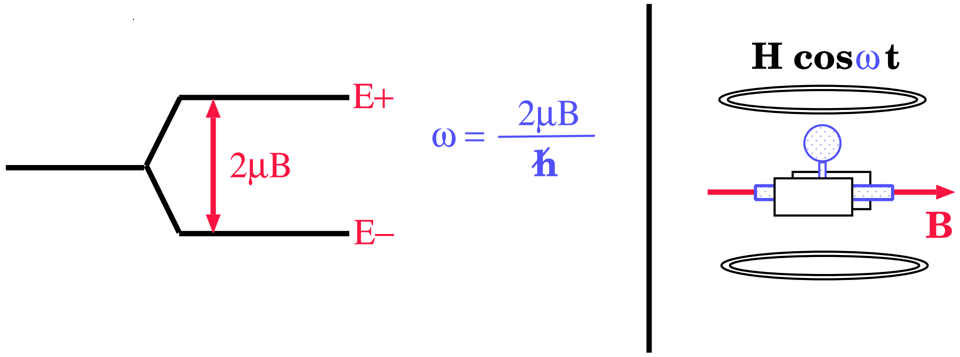

Figure 6.5: Left: Energy level splitting. Right: RF and pickup coil placement for NMR Polarimetry.

measured by holding the RF frequency fixed and sweeping the main magnetic field through the RF resonance. At resonance, the spins flip and this is detected by a pair of pickup coils placed around the cell. The precessing ^{3}He nuclei induce an AC voltage in the pickup coils which is detected with a lock-in amplifier referenced to the RF frequency. The detected signal is proportional to the ^{3}He polarization. An absolute polarization can be determined by calibrating the NMR apparatus with an identical water sample. The polarization of the water sample is known in advance as it follows a Boltzman distribution.

The sweep must be slow enough that the spins can follow the direction of the changing field. This "adiabatic" condition is satisfied if the Larmor frequency of the precessing spins is large compared to the rate of change of direction of the field $\frac{d\theta}{dt}$. On the other hand the spins can not be kept in resonance so long that the transverse decay time T_2 becomes relevant. These two limits lead to the adiabatic fast passage (AFP) conditions:

$$\frac{1}{T_2} \ll \frac{1}{H_1}\frac{dH_0}{dt} \ll \gamma H_1 \tag{6.20}$$

6.9 E94-010 Target Characteristics

Details of the E94-010 ^{3}He target analysis can be found in [123] and [124]. In this section, we only summarize the results.

There were six target cells used during the experimental run. (See table 6.1). Each had roughly the same dimensions, but exact values the cells

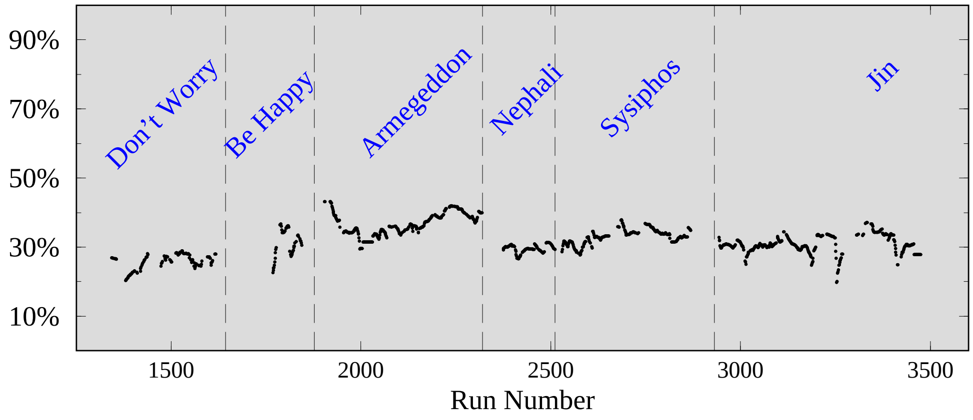

Figure 6.6: Target polarization vs. run number

Target	Run period	$\langle P \rangle$
Don't Worry	Sep. 26 - Oct. 07	29%
Be Happy	Oct. 09 - Oct. 18	37%
Armegeddon	Oct. 18 - Nov. 03	43%
Nepheli	Nov. 03 - Nov. 12	31%
Sysiphos	Nov. 12 - Nov. 25	38%
Jin	Nov. 25 - Dec. 24	37%

Table 6.1: Average target polarization.

Table 6.2: Target density in amagats.

Target	Density at room temp.	Operating density
Don't Worry	9.939	12.249
Armageddon	10.176	12.324
Be Happy	9.342	11.533
Nepheli	11.336	13.778
Sysiphos	8.182	9.942
Jin	8.419	10.236

can be found at [125]. The density of the target [126] in amagats** is shown in table 6.2.

For E94-010 the EPR polarimetry technique was used only for calibration of the final NMR results. Figure 6.6 displays the polarimetry values for each of the experiment target cells. The systematic uncertainty of the final polarimetry values is 4% [124, 123]. The moderate polarization together with the high density combine to create what is presently the highest luminosity polarized target in the world with $\mathcal{L} \approx 10^{36}(\mathrm{cm} \cdot \mathrm{s})^{-1}$.

[**] 1 amagat $= 2.6868 \cdot 10^{19}$ atoms cm^{-3} at standard temperature and pressure.

CHAPTER 7

ANALYSIS

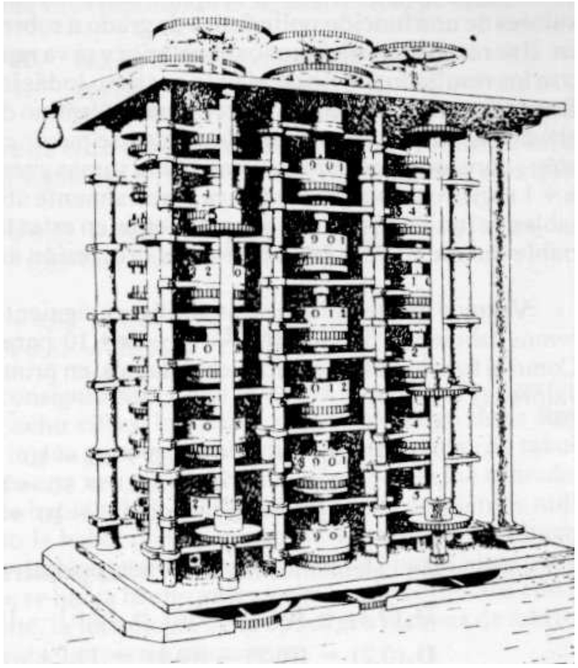

7.1 Data Acquisition

E94-010 logged 2694 individual runs of approximately one hour each at 186 unique momentum settings. Upwards of 6 billion events, requiring almost 4 terabytes of storage were recorded to tape. There are three main types of instrument data that are relevant to the experiment:

1. ADC and TDC values from the spectrometer detector package.

2. Scaler values from the spectrometer and beamline, including the beam helicity information from the accelerator.

3. EPICS (Experimental Physics and Industrial Control System) slow control readouts of the magnet currents, target parameters, BPMs, BCMs, etc. EPICS is used to monitor and control the background processes of Hall A that are not directly relevant to the measured physics quantities, but nevertheless are crucial to reliable data taking.

All the above information is organized and combined by CODA, the 'CEBAF Online Data Acquisition' [127].

The ADC, TDC and scaler crates all follow the fastbus or VME standard [128]. These crates are read by the Readout Controllers (ROCs), which are CODA routines. The ROCs organize the crate information according to the CODA data format and pass it over the network to the next routine, which is the Event Builder (EB). The EB takes the output of the various ROCs and builds the event according to the CODA data structure. The Event Recorder (ER) finally writes the event to disk in a CODA datafile. The datafiles reside on the Counting House hard drives for a short time, then are copied to the robotic tape silo and deleted to make room for new files.

A typical event contains readouts from the ROC1(2) readout of the HRS-L(R) ADCs, and TDCs and the ROC14 readout of beamline information. The scalers are inserted in the data stream every few seconds and at the end of run. The EPICS values are inserted at the start and end of run, as well as periodically throughout the run, though not as frequently as the scalers.

We ran for most of the experiment with a single trigger supervisor which handled the triggers from both spectrometers under one data acquisition. For more information on the trigger see section 5.4.2. For a short period we switched to two independent DAQs, one for each spectrometer, each with its own trigger supervisor. This increased the typical data acquisition rate from 2kHz to 5kHz.

7.2 From Tape to Histogram

The standard Hall A software analysis tool is ESPACE [129], the **E**xperiment **S**canning **P**rogram for Hall **A** **C**ollaboration **E**xperiments. The Espace package performs the following tasks:

- Decoding of the CODA data file.

- Particle tracking and reconstruction of various target variables.

- Histogramming of detector and reconstructed quantities.
- ADC software gain and timing calibration.

Espace was used for the majority of the online analysis in order to quickly verify the quality of the incoming data. Each run was replayed soon after it was recorded to check proper detector behaviour and reconstruction. All the hardware calibration and efficiency studies were performed using the standard Espace routines.

For the offline analysis, the CODA data files were passed through a software event filter to exclude events that created no track in the VDC and other junk events. The standard Espace event filter was modified in order to exclude the unwanted events and to output the results as an columwise ntuple. Large runs which had been split across several datafiles were combined at this stage to produce a single ntuple file. The overall reduction in file size was substantial (about a factor of twenty) since the ntuple was compressed according to the RZ [130] file format. This procedure had the ancillary benefit of requiring an order of magnitude less CPU time than standard Espace.

Software cuts, histogram creation and filling was accomplished in the analysis package NTANAL. NTANAL is a fortran based routine that utilizes the Cernlib HBOOK package. Detector and cut efficiency corrections were applied to the data at this stage as well. The modified Espace filter and NTANAL package were both authored by S. Choi.

From this point, cross sections and asymmetries were extracted from the histogram files using HBOOK routines called from dedicated fortran codes written specifically for this purpose.

7.3 Physics Analysis Overview

From the raw number of scattered events counted, we form the unpolarized cross sections and the asymmetries. The cross section analysis is detailed in chapter 8.

Asymmetries were measured while the target polarization was held parallel ($A_{||}$) and perpendicular ($A_{\perp}$) to the longitudinally polarized incident electrons. The asymmetries are related to the raw counts of electrons in each helicity state by:

$$A = \frac{1}{f \cdot P_t \cdot P_b} \left(\frac{N_+ - N_-}{N_+ + N_-} \right) \tag{7.1}$$

with P_b and P_t the beam and target polarization respectively, and f the dilution factor arising from scattering from any unpolarized material (primarily nitrogen gas within the target cell).

In the asymmetry analysis, careful checks were performed to ensure reasonable agreement between left and right arm spectrometer results before the data from the two arms were combined.

From the cross sections and asymmetries we form the polarized cross section differences $\Delta\sigma_{||,\perp}$ in the parallel and perpendicular configurations, respectively via:.

$$\Delta\sigma_{||,\perp} = 2\ A_{||,\perp} \cdot \sigma_{raw} \tag{7.2}$$

with σ_{raw} given by equation 8.1. Notice that the dilution factor f enters linearly into the raw cross section, so that the product $(A \cdot \sigma_{raw})$ is free from the dilution effects.

Radiative corrections (see appendix C) must now be applied to the data. The spin-independent external corrections are applied using the classical treatment of Mo and Tsai [131, 132] as implemented in ref. [133]. The spin-dependent internal radiative corrections were applied using the approach described in [134] and developed in [135]. The program POLRAD [136] is based on this approach but is designed for use in DIS. The code was modified for use in the resonance region by S. Choi [137] using the E94-010 data directly as input. It was later generalized to include the quasielastic region by this author.

The first step in the radiative corrections is the removal of the background caused by the elastic radiated tail. This tail is created by events that either: a) radiate a photon prior to interacting with the target particle and then scatter elastically, or b) scatter elastically and then radiate a photon prior to detection. The elastic cross section grows quickly at low Q^2, so this background can be quite significant. We used a modified version of ROSETAIL [138] to calculate the external polarized elastic tail, and POLRAD [136] for the internally radiated polarized tail.

At this point the structure functions are extracted from the corrected cross section differences according to:

$$\begin{aligned} g_1 &= \frac{MQ^2}{4\alpha^2}\frac{y}{(1-y)(2-y)}\left[\Delta\sigma_{||} + \tan\frac{\theta}{2}\Delta\sigma_{\perp}\right] && (7.3) \\ g_2 &= \frac{MQ^2}{4\alpha^2}\frac{y^2}{2(1-y)(2-y)}\left[-\Delta\sigma_{||} + \frac{1+(1-y)\cos\theta}{(1-y)\sin\theta}\Delta\sigma_{\perp}\right] && (7.4) \end{aligned}$$

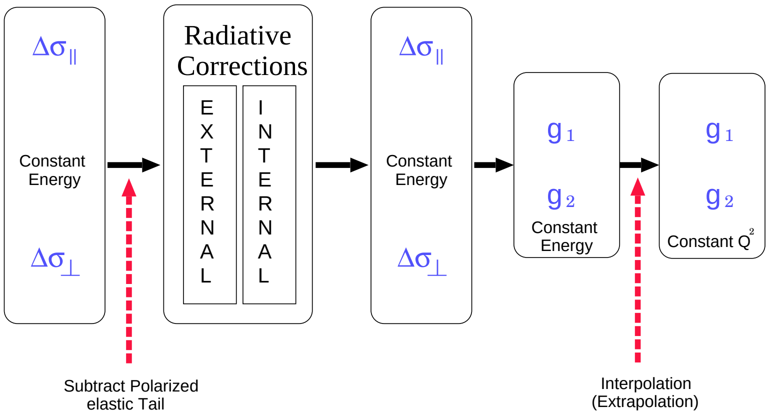

Figure 7.1: Analysis flow diagram.

And finally the structure functions are interpolated (or in some rare instances extrapolated) to constant Q^2 from the measured values at constant energy. Fig. 7.1 shows the flow of the analysis from the polarized cross section differences to the final structure functions.

7.4 Detector Calibrations and Efficiencies

7.4.1 Scintillators

T_2 and T_4 events provide a measure of the scintillator inefficiency since they represent otherwise good events that one of the scintillators failed to detect. This inefficiency gradually increased over the course of the experiment reaching a maximum of 13% (See figure 7.2). A constant flow of ^{4}He was directed at the glass target cell windows in order to reduce electron beam induced heating. Thus, a large volume of helium was released directly into the experimental hall. It is believed that the gradual degradation of the scintillator performance was caused by this helium gas penetrating the scintillator phototubes and compromising the tube vacuum. However, as shown in the figure, the inefficiency contributes less than 1% error (statistical) to the cross sections.

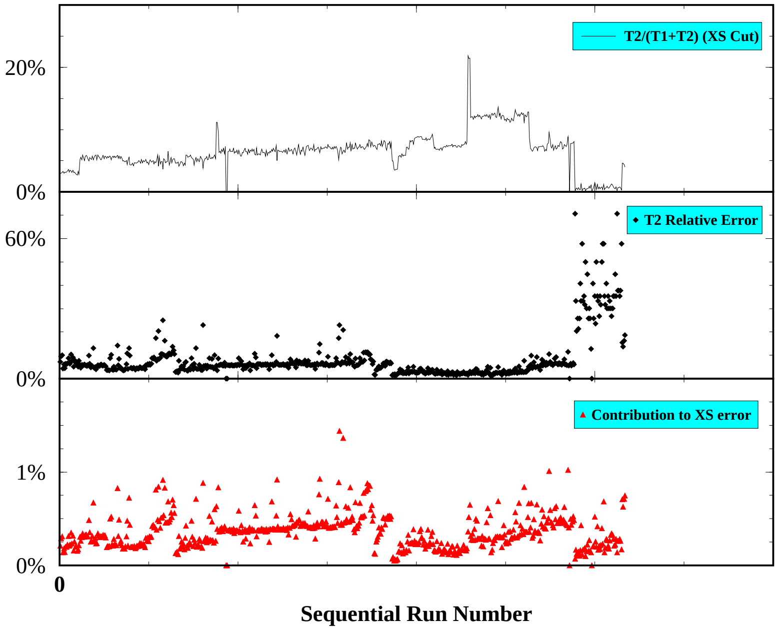

Figure 7.2: HRS-L scintillator performance vs. Run Number. **Top panel:** Scintillator inefficiency. **Middle panel:** Relative error on inefficiency correction. **Bottom panel:** Contribution of scintillator inefficiency correction to cross section systematic error.

7.4.2 VDC

The Vertical Drift Chamber detection efficiency was found to be 99.92% and 99.7% respectively for HRS-L and HRS-R. The inefficiency of the tracking algorithm was also evaluated. This is necessary since good events with a bad track (or no track) will be removed in error. Espace can discriminate up to four tracks for one event. Of course, if all goes well, an event should have a single track. Any other situation may signify a problem.

The VDC performance was analyzed by A. Deur who found that approximately 99% of the events are single track events after reasonable cuts have been applied to the čerenkov and shower detectors. Roughly another one percent are classified as two track events with a negligible number of events possessing zero, three or four tracks. Details can be found in [139]. For the final analysis, only single track events were retained, with the two track events treated as an inefficiency.

7.4.3 Čerenkov

Full details of the Čerenkov analysis can be found in [140]. Here we outline the procedure and present the main results.

Calibration

As stated in section 5.4.3, the Čerenkov detector contains ten individual mirrors that collect the Čerenkov light and focus it onto dedicated photomultipliers. Ultimately, the ten photo-multiplier tube outputs are summed, and a cut on the final ADC distribution is used to discriminate pions from electrons. Before this can be done, the offsets and gains of the tubes must be adjusted by editing the relevant lines in the Espace detector database*.

Figs. 7.3 and 7.4 show the ADC outputs for the ten HRS-L mirrors before and after the gain and pedestal adjustment have been made. The central location of the broad peak with maximum around channel 2000 is proportional to the average number of photo-electrons produced from the cathode by an incident photon, while the narrow peak just above channel 200 represents the threshold for production of a single photo-electron.

The Čerenkov software cut is made just below the single photo-electron peak to exclude any event that didn't trigger the device. As such, we chose to calibrate the ten photo-tubes such that each of the single photo-electron peaks are located at the same ADC channel.

Stability

A check of the Čerenkov photo-tube stability is displayed in figure 7.5, which shows the ADC channel location of the single photo-electron peak (averaged over ten mirrors) as a function of spectrometer central momentum for all six incident energies. It can be seen that the output is quite stable except for a few settings in the 2.5 GeV and 5.1 GeV data. This data was taken late in the experiment (Dec. 11-21, 1998) when the scintillator trigger thresholds were lowered (See discussion in Reference [142]).

---

*The database contains two scalar values for each of the ten Čerenkov mirrors. The first value represents the channel location of the phototube pedestal, while the second represents the software gain to be applied to each ADC output. For more information regarding the layout of the database see [129] and [141].

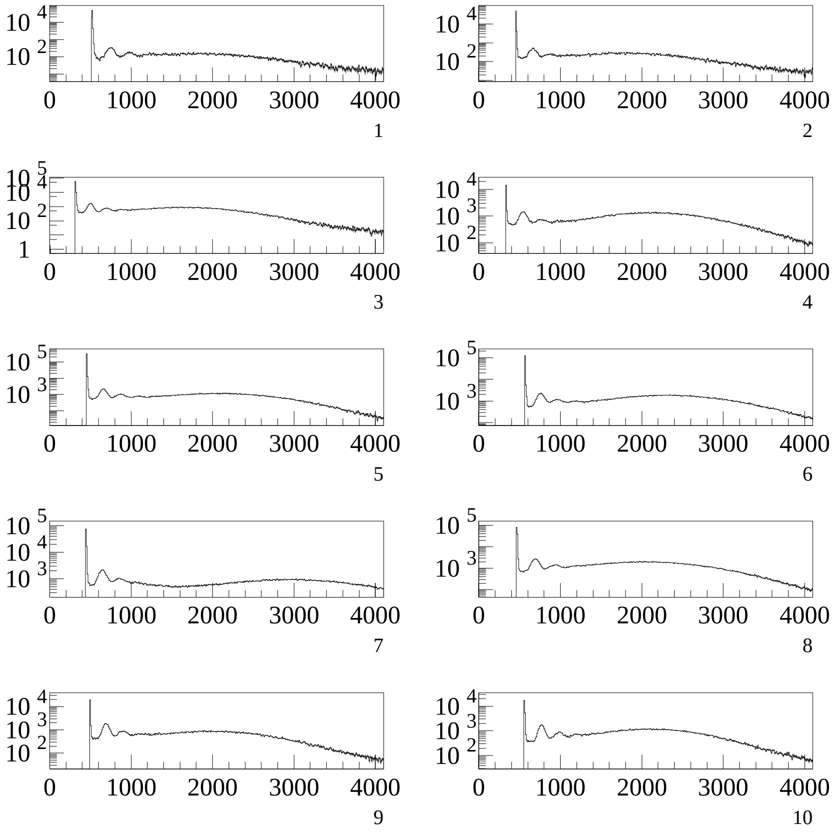

Figure 7.3: HRS-L raw Čerenkov ADC for each individual mirror.

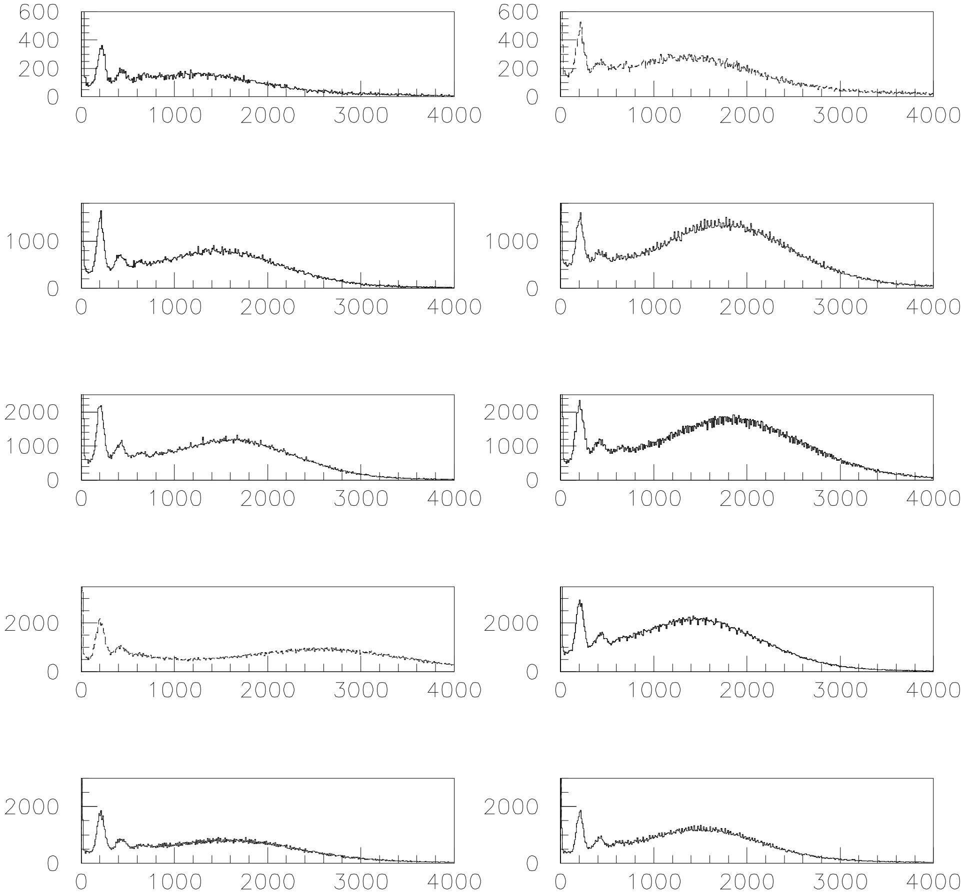

Figure 7.4: HRS-L calibrated Čerenkov ADC for each individual mirror.

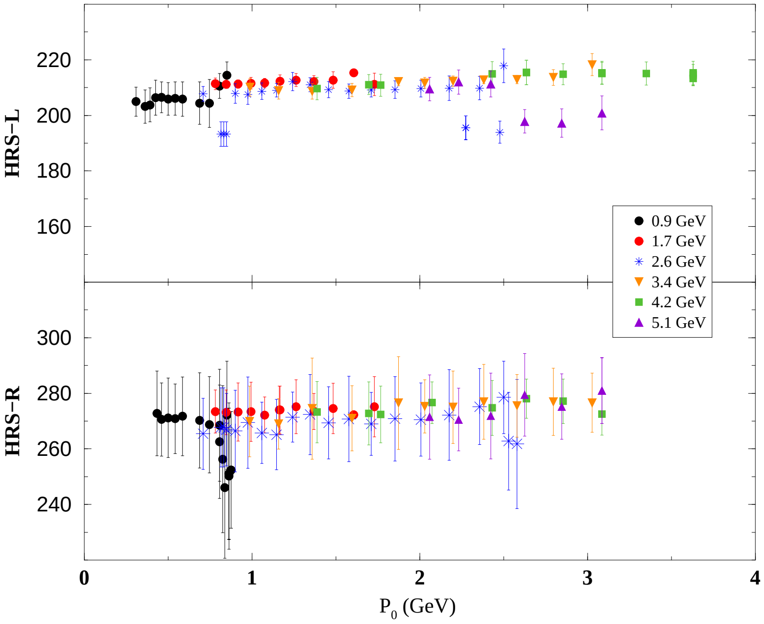

Figure 7.5: Čerenkov single photo-electron peak vs momentum. Each symbol represents a different incident beam energy. **Top panel**: HRS-L. **Bottom panel**: HRS-R. The central value represent the ADC channel of the single photo-electron peak averaged over ten mirrors. The error bars measure the standard deviation of the ten values.

Detection Efficiency

The Čerenkov ADC spectrum can be approximated with a Poisson distribution, with a mean value μ, where μ represents the average number of photo-electrons produced. As such, $e^{-\mu}$ represents the probability of emitting zero photoelectrons and the detection efficiency can be expressed as $\epsilon = 1 - e^{-\mu}$.

Comparing the location of the broad peak maximum in figure 7.4 with the single photo-electron peak, we can see that the photo-tubes produce from 6 to 14 photo-electrons, on average. This means we should expect a detection efficiency of better than 99%.

We measured the Čerenkov detector efficiency by using the shower detector to select a good electron sample and then counting how many of those events also triggered the Čerenkov. Results were chosen from kinematics below the pion production threshold to ensure selection of good electron events. We found the detection efficiency to be better than 99.9% and 99.5% for HRS-L and HRS-R respectively. The slightly better performance of HRS-L is expected due to the extended length of the left arm Čerenkov tank.

Cut Efficiency

The application of the software cut invariably removes some good electrons along with the unwanted events. Events that fail to trigger the Čerenkov will are tagged with an ADC value of zero or 10^9, depending on the initial calibration. We chose an optimized cut from ADC channel 150 to 16000 in order to exclude the unwanted events while keeping the number of excluded good electrons less than 1%. The data was later corrected for this small inefficiency.

7.4.4 HRS-L Lead Glass Calorimeter

Full details of the calorimeter analysis can be found in [142]. Here we outline the procedure and present the main results.

As noted in section 5.4.4, the shower detectors are segmented into many individual lead glass blocks, with each block monitored by a single photomultiplier tube. Since the cascade is in general spread laterally over several adjacent blocks, the output must be integrated over the entire detector volume to obtain the total detectable signal. When the calorimeter has been calibrated properly, the total deposited energy E, will agree with the particle's incident energy, or momentum p in the relativistic case.[†] A plot of E/p after calibration will look like Fig. 7.6. Since the final peak is actually the sum of all the individual outputs of the phototubes, the width of this peak provides a measure of how well the device has been calibrated.

Calibration

The calibration procedure is discussed in detail in Ref. [109]. The standard method entails generation of a new calibration for every kinematic setting investigated. This can be a lengthy process and becomes unreliable when there are hardware problems with any of the blocks or phototubes, as there were during certain runs of E94-010. As an alternative, we used a single set of calibration constants, optimized for one well behaved mid-momentum

---

[†] Note that this assumes that the detector is thick enough for all of the incident particle's energy to be absorbed. This is the case for HRS-L but not for HRS-R.

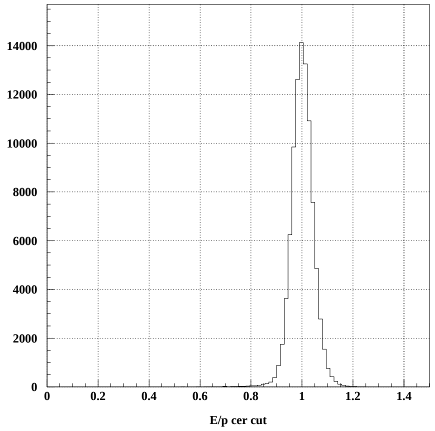

Figure 7.6: E/p for properly calibrated shower

range run (20411, E_0 = 2.591 GeV, P_0 = 1.579 GeV/c), and then applied to all the data.

Fig. 7.7 shows the peak position, E/p, and normalized width, σ/E, for each HRS-L spectrometer setting once the calibration has been applied. A variation of less than 3% in peak position is seen for most of the runs. The low outliers represent data taken late in the experiment (Dec. 11-21, 1998) when the scintillator detector threshold was lowered. Since the scintillator provides the trigger, lowering the threshold allowed more low energy particles into the data, which skews the distribution to lower values of E/p. The data with larger than normal E/p were recorded near the limits of the spectrometer magnetic field settings. In this region, the dipole NMR probe becomes unreliable, so the gaussmeter was used instead. (See section 5.3.1). The greater than expected values of E/p reflect an offset in the momentum calculated from the gaussmeter and the more reliable NMR probes. For these few runs, the calorimeter output was used to calibrate the hall probe to the NMR probe results.

The energy resolution of a calorimeter, expressed in terms of the normalized width σ/E, improves with increasing energy. Previous experiments that utilized lead glass calorimeters [143] obtained resolutions of $5\%/\sqrt{E}$. We found that our calorimeter resolution behaves as $5.3\%/\sqrt{E}$ as shown in fig 7.7.

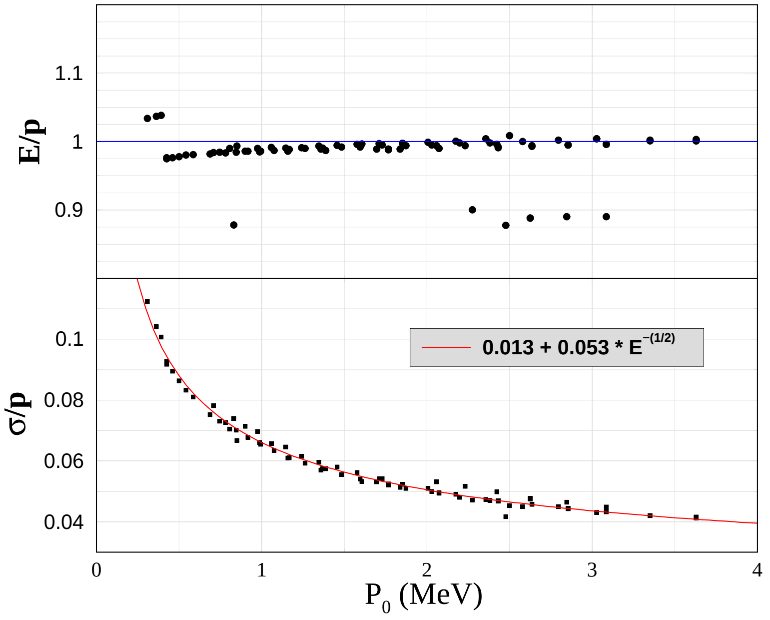

Figure 7.7: Calibrated output for HRS-L calorimeter. **Top panel**: E/p central value vs. momentum. **Bottom panel**: Calorimeter energy resolution vs. momentum.

Detection Efficiency

Good electrons are selected from T1 events, along with an acceptance cut and the requirement that the Čerenkov detector was triggered. We then determine how many of these events also trigger both the preshower and shower. The detection efficiency was greater than 99% for almost all runs. The exception is the previously mentioned "hall probe runs" where the spectrometer dipole NMR probe was unavailable.

Cut Efficiency

A two dimensional cut on the preshower and shower detector was applied to exclude low energy 'junk' events and pions. (See fig. 7.8). The choice of cuts was optimized so that the pion suppression is large while the total number of good events excluded by the cuts was always less than 1%.

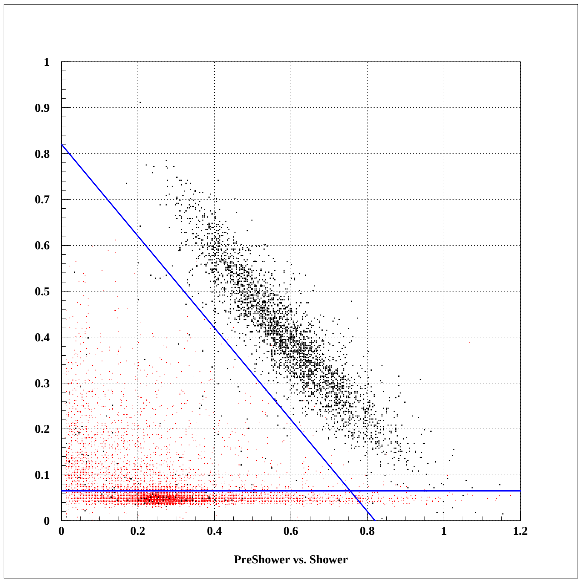

Figure 7.8: Energy deposition in HRS-L calorimeter. Pions and other low energy events that fail to trigger the Čerenkov are highlighted in red.

7.4.5 HRS-R Lead Glass Shower Detector

The right HRS contains only a thin layer of lead glass, similar in dimension to the preshower layer of the left arm. As such, it can not be classified as a calorimeter, but is still very effective for pion discrimination.

Calibration

The right arm shower detector was assembled for and commissioned during E94-010. As such, the existing Espace calibration software was not able to be used. Instead, for each block, good electron events were selected in which only this particular block was fired. This is to avoid showers where the total signal is spread over two or more blocks. The software gain of each block is then manually adjusted to set the shower output normalized by particle momentum to unity. As in the case of HRS-L, a single calibration was performed and the result applied to all kinematics. Fig. 7.9 tracks the resulting shower output throughout the experiment. Here the ratio of shower/p decreases with increasing momentum, since only a small portion of the scattered particle's energy is sampled by the detector. Again we see that

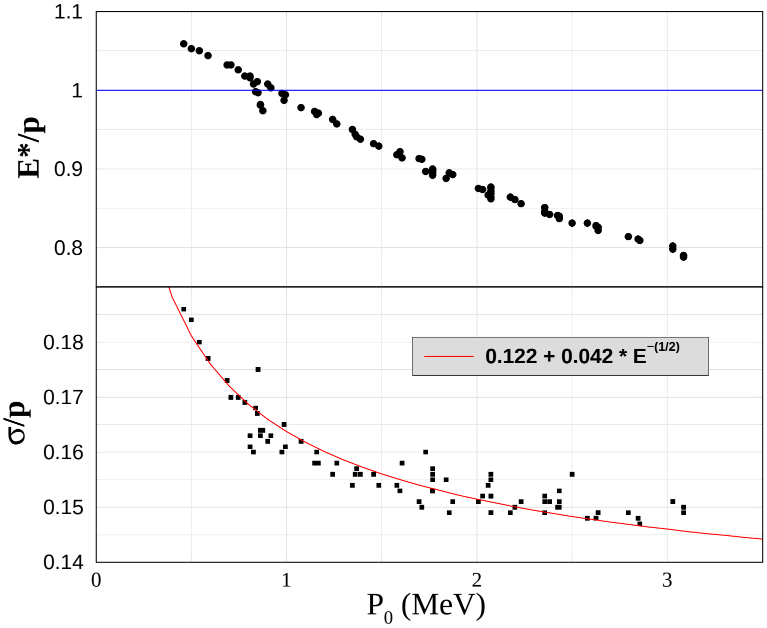

Figure 7.9: Calibrated shower output for HRS-R. **Top panel**: Normalized shower output vs. momentum. (The output is labeled E* to emphasize that the HRS-R shower is not thick enough to be considered a calorimeter.) **Bottom panel**: Resolution vs. momentum.

the width decreases with increasing energy, although the resolution σ/E is much poorer than in the HRS-L shower detector.

Detection Efficiency

There is an inconvenient vertical gap in the HRS-R shower blocks that reduced the efficiency compared to the left arm. Nevertheless, the detection efficiency was found to be greater than 99% for all of E94-010.

Cut Efficiency

The HRS-R shower cut is chosen so that the number of good electrons excluded by the cut is less than 0.5%. We saw in the last section that about 1% of good events pass through the vertical gap between the two columns of blocks. These events have not triggered the shower and will also be removed

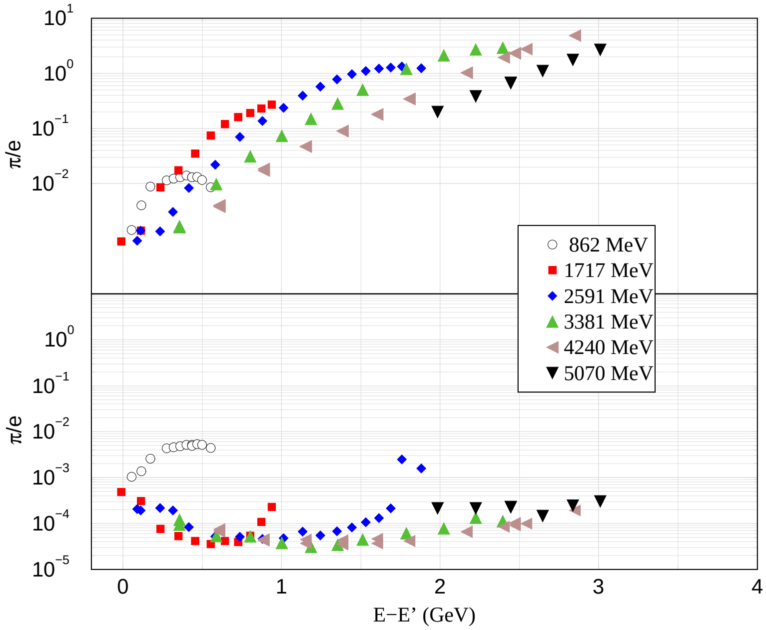

Figure 7.10: Effect of particle ID Cut on π/e ratio (HRS-L).

by the cut. A maximum of 1.5% of good events will therefore be excluded by the cut.

7.5 Particle ID Cuts

In the kinematic range of experiment E94-010, the principal unwanted particle produced is the pion. The negatively charged pion can masquerade as an electron in the detectors and must be removed from the data. The Čerenkov detector provides the primary method of separating pions from electrons, but their characteristic signal in the calorimeter (see fig. 7.8) can also be used to tag pions in the data.

The ratio of pions to electrons in our data, i.e. the pion contamination, reached a maximum of about 5 to 1. After the combined PID software cuts are applied to the Čerenkov and shower detectors, the pion contamination is reduced by over four orders of magnitude. The Čerenkov and shower each contribute roughly equally to this suppression. Final results are shown in figs. 7.10 and 7.11, while tables of the results can be found in [142]. The

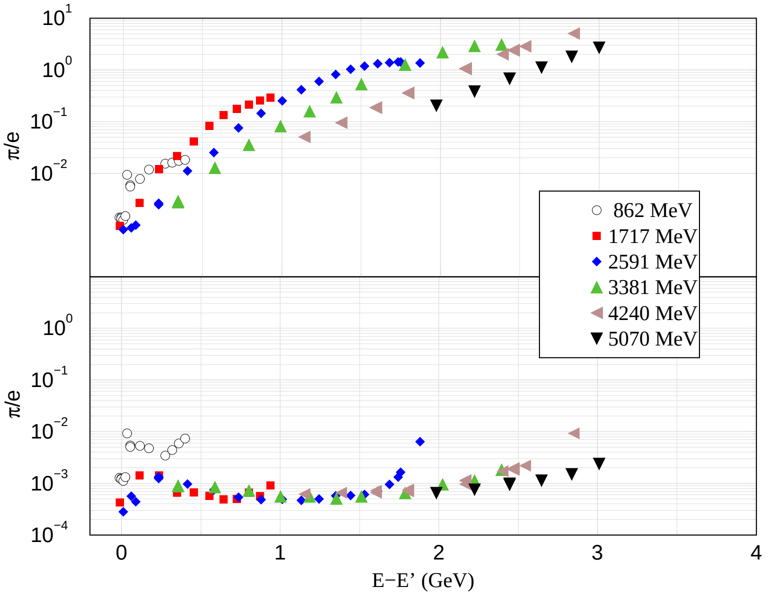

Figure 7.11: Effect of particle ID Cut on π/e ratio (HRS-R).

method we use to evaluate pion contamination overestimates the number of pions present after the PID cuts substantially in kinematics where the pion contamination is small to begin with as explained in [142]. The apparent reduced suppression for our lowest incident energy is an artefact of this conservative pion estimate.

7.6 Spectrometer Optics

The optical properties of the spectrometers are parameterized in the Transport Tensor which relates quantities measured in the spectrometer detector coordinate system with the reconstructed quantities in the target coordinate system. We begin by defining the respective cartesian systems.

7.6.1 Target Coordinate System

The origin of the target system is the hall center, defined by the intersection of the electron beam and the vertical symmetry axis of the hall which passes through the target center. $\hat{z}_{tg}$ is directed from the origin to the spectrometer

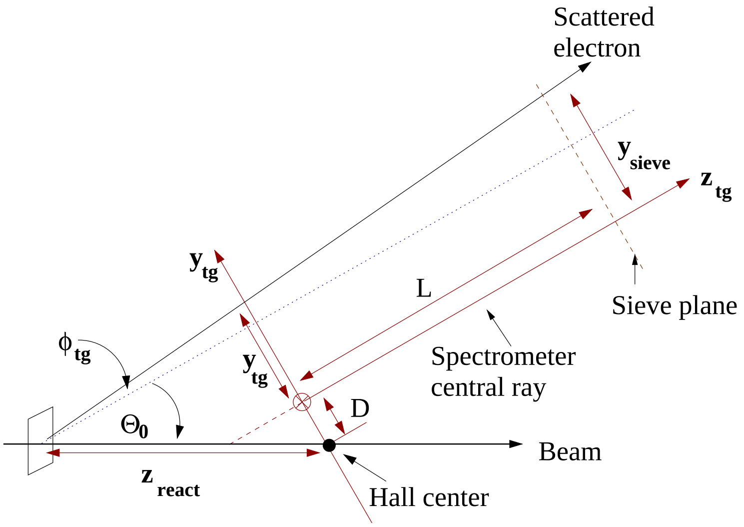

Figure 7.12: Coordinates for electrons scattering from a thin foil target. L is the distance from Hall center to the sieve plane, while D is the horizontal displacement of the spectrometer axis from its ideal position. The spectrometer central angle is denoted by θ_0. Not that x_{tg} and x_{sieve} are vertically down (into the page). *Reproduced from [89].*

central sieve slit hole[‡], with $\hat{x}_{tg}$ directed vertically down into the earth. The scattering plane trajectory ϕ_{tg} is defined by $\tan\phi_{tg} = y_{tg}/L$ and the out of plane variable θ_{tg} is defined by $\tan\theta_{tg} = x_{tg}/L$, where L is the distance from the origin to the sieve slit. All these quantities are displayed in figure 7.12

7.6.2 Detector Coordinate System

The origin of the detector coordinate system coincides with the overlap of wire number 184 in the U_1 and V_1 VDC plane as shown in figure 7.13. $\hat{x}_{det}$ and $\hat{y}_{det}$ lay in the plane of the VDC with $\hat{x}_{det}$ pointing away from the center of curvature of the dipole magnetic field. $\hat{z}_{det}$ is perpendicular to the VDC plane pointing vertically away from the earth as shown in figure 7.14.

[‡] This of course implies that each spectrometer has its own target coordinate system.

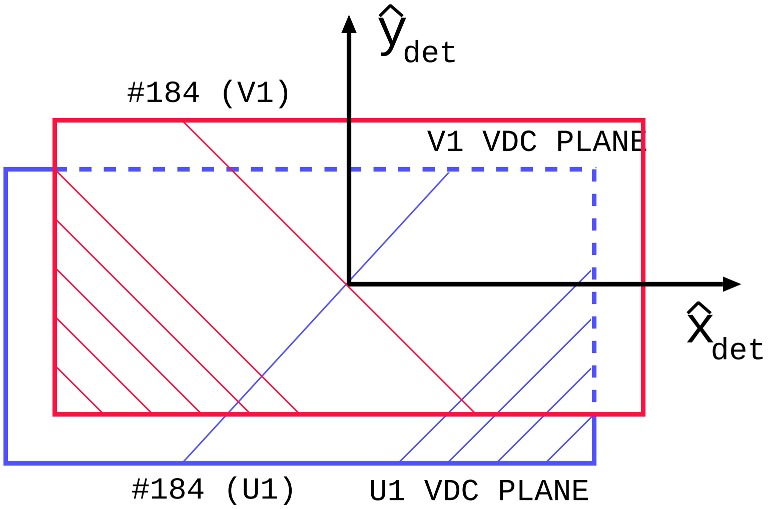

Figure 7.13: Detector coordinate system, Top view. The origin of the detector coordinate system is defined by the overlap of the 184th wire in the U_1 and V_1 VDC plane.

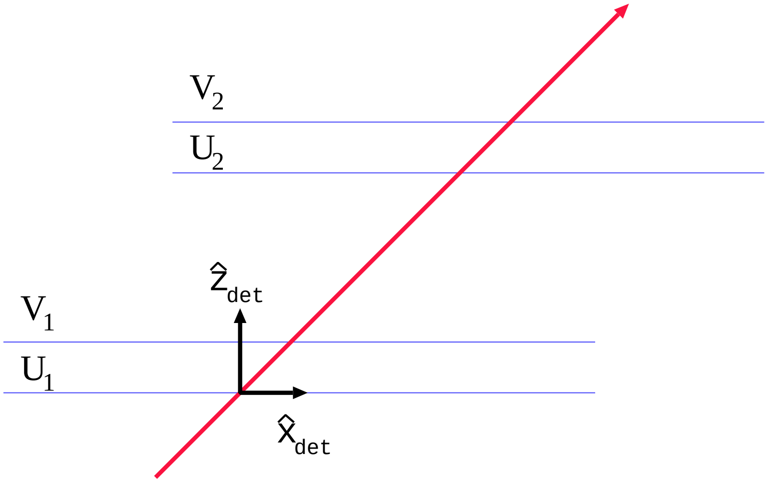

Figure 7.14: Detector coordinate system, Side view.

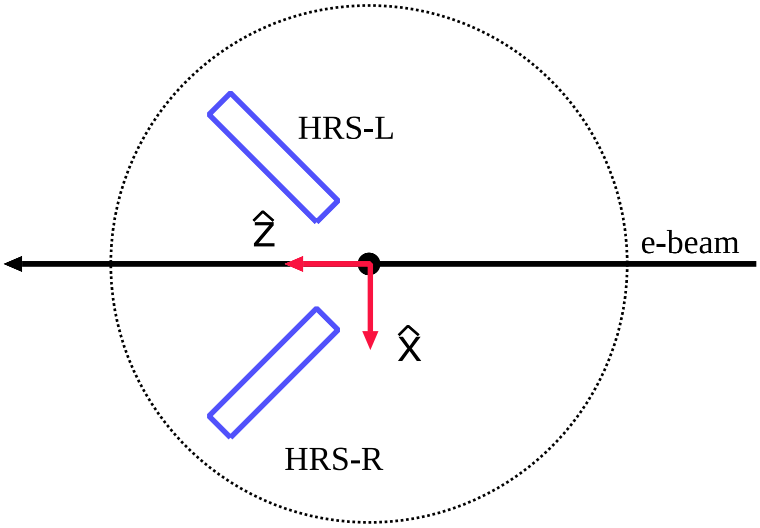

Figure 7.15: Hall A coordinate system.

7.6.3 Transport Tensor

From the observed detector plane quantities, the events location in the focal plane is determined. To first order, the reconstructed target quantities are related to the focal plane quantities by [144]:

$$\begin{pmatrix} \delta_{tg} \\ \theta_{tg} \\ y_{tg} \\ \phi_{tg} \end{pmatrix} = \begin{bmatrix} \langle\delta|x\rangle & \langle\delta|\theta\rangle & 0 & 0 \\ \langle\theta|x\rangle & \langle\theta|\theta\rangle & 0 & 0 \\ 0 & 0 & \langle y|y\rangle & \langle y|\phi\rangle \\ 0 & 0 & \langle\phi|y\rangle & \langle\phi|\phi\rangle \end{bmatrix} \cdot \begin{pmatrix} x_f \\ \theta_f \\ y_f \\ \phi_f \end{pmatrix} \qquad (7.5)$$

Here, the off-axis events vanish due to the mid-plane symmetry of the spectrometer. The actual transformation is carried to 5th order, so equation 7.5 must be generalized to a tensor relation between focal plane and reconstructed quantities. The BPM and raster information must be incorporated into the reconstruction as well. This results in three further coordinates (x_{beam}, y_{beam}, z_{beam}), representing the event coordinates in Hall A. The origin of the Hall A coordinate system coincides with the target system origin defined above. Positive z_{beam} corresponds to the downstream beam direction, and positive y_{beam} is directed away from the Earth's center.

The transport tensor is initially based on the design parameters, physical

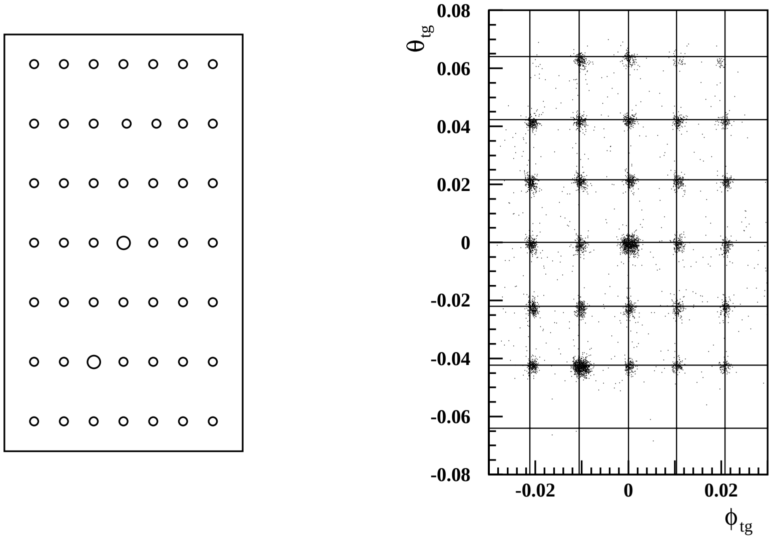

Figure 7.16: Spectrometer sieve slit collimator (left) and resulting hit pattern (right). *Reproduced from [89].*

surveys, and magnetic field mappings of the magnets. The tensor is optimized using carbon foil scattering data taken with the sieve slit collimator (see figure 7.16) inserted at the spectrometer entrance. The thin carbon foils are surveyed to ensure the interaction vertex is precisely known, and the sieve slit ensures that the trajectory of detected events is well defined. During these 'optics' runs, the beam is not rastered and the beam offset is held to within a few hundred μm of zero, to eliminate x_{beam} & y_{beam} from consideration.

7.7 Spectrometer Acceptance

The angular acceptance of the spectrometers does not necessarily coincide with the geometrically defined aperture. Instead, the acceptance depends critically on the particle momentum, interaction vertex and trajectory. As such, the acceptance is modeled using monte carlo techniques.

A large number of rays are generated with random trajectories covering an illumination region larger than the actual acceptance (see section 8.1 for further details). The ranges of the momentum spread and point of origin are chosen to be greater than that of the physically possible events.

The transport properties of the spectrometer magnets, combined with the known physical placement of all apertures within the spectrometer allows us to determine whether a specific randomly generated ray will pass through to the detector focal plane. We can then extract the acceptance from the ratio of total generated events to those that make it through the spectrometer transport functions and all analysis cuts. The transport function used in this analysis was generated by Xiaodong Jiang [145].

7.8 Acceptance Cuts

A comprehensive study was performed to evaluate the ability of the simulation to reproduce the reconstructed target quantities [146]. It was found that the simulation performed well, but only over a limited range. The study allowed us to chose an optimized set of cuts on ϕ_t, θ_t, y_t and δ to be used in the cross section analysis:

- $|\phi_t| \leq 15$ mrad
- $|\theta_t| \leq 30$ mrad
- $|Z_{beam}| \leq 6$cm
- $|\phi_t - 0.375 y_t| \leq 0.025$
- $|\phi_t + y_t| \leq 0.020$

Figs. 7.17, 7.18 show the comparison of ^{3}He data and simulation after application of the above cuts. The data was taken with an incident energy of 3.4 GeV and a central spectrometer momentum of 0.9 MeV. This kinematic was chosen because the missing mass (2.3 GeV) lies beyond the resonance region, and the physics variation across the acceptance is expected to be well described by a simple Mott behaviour. In the comparison, the simulation results are weighted by the Mott cross section. The agreement is good, except for δ at the edges. This region is removed later by a cut on the variable ν.

The asymmetry is a ratio of cross sections and as such the acceptance cancels out. Because of this fact, we were able to use a much larger cut for the asymmetries:

- $|\phi_t| \leq 40$ mrad
- $|\theta_t| \leq 60$ mrad

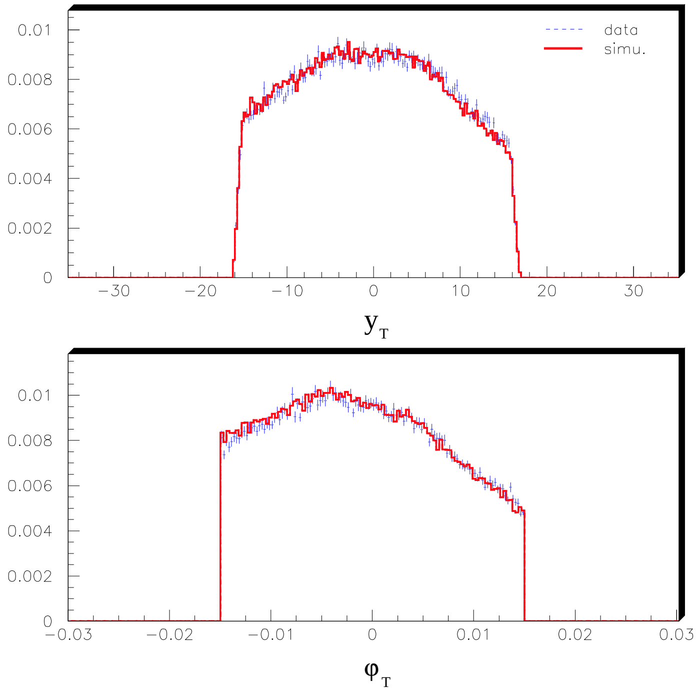

Figure 7.17: ^{3}He data target variables y_t (top) & ϕ_t (bottom) with final cut. Positive y_t corresponds to downstream events in this plot.

- $|y_t| \leq 35$ cm

7.9 Good Run Selection

Several conditions are used to reject problematic runs from the analysis. Below we list the conditions required for a run to be used in the asymmetry analysis:

- Beam helicity asymmetry less than 1%.
- Dead time less than 40%.
- Helicity correlated dead time correction less than 5%.

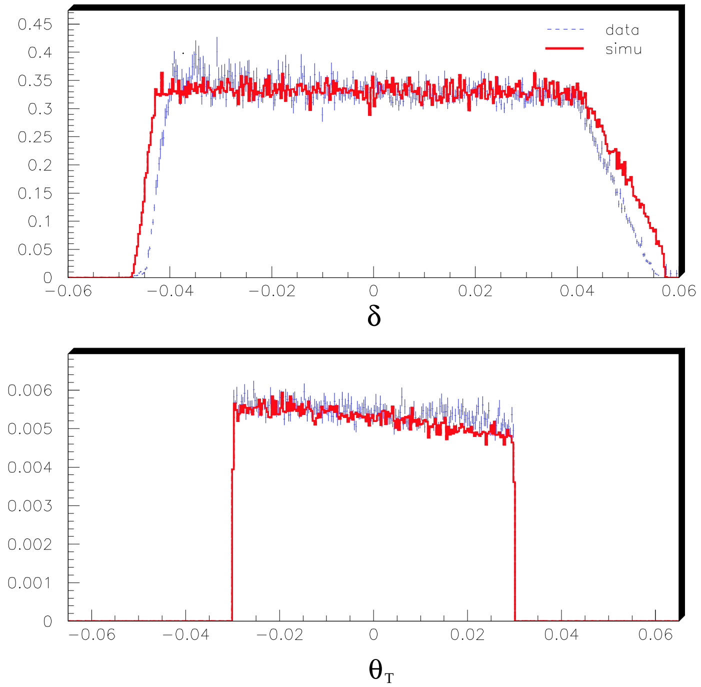

Figure 7.18: ^{3}He data target variables δ_P (top) & θ_t (bottom) with final cut.

- Statistical error less than 5%.
- No runs with prescaler greater than 10.
- No runs shorter than 9 mins.

For the cross section analysis, only runs from the HRS-L longer than 9 mins where included in the analysis.

CHAPTER 8

^{3}HE UNPOLARIZED CROSS SECTIONS

There are four major steps in the production of the unpolarized ^{3}He cross sections:

1. Formation of the raw cross sections from the counting rates and scalers.
2. Subtraction of the nitrogen dilution and elastic tail contributions.
3. Radiative corrections.
4. Finite acceptance effect corrections.

We will discuss each of these steps in detail in the following sections. We note here that several of the raw cross section spectra required extra individual treatment to address difficulties encountered during the experimental run. These details are described in appendix F.

8.1 Raw Cross Sections

The unpolarized experimental cross section is given by:

$$\sigma_{raw} = \left(\frac{d\sigma}{dE'd\Omega}\right)_{raw} = \frac{N_f^*}{N_i\rho} \times \frac{1}{\Delta Z \Delta\Omega \Delta E'} \tag{8.1}$$

Where:

- N_f^* is the number of scattered electrons detected, corrected for detector and software efficiencies, prescalers and for deadtime.
- N_i is the number of incident electrons. We determine this from the total charge measured with the DX10 BCM.
- ρ is the density of the target.
- ΔZ is the length of the target seen by the spectrometer.

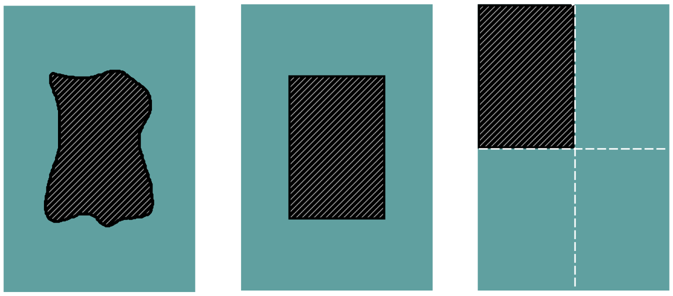

Figure 8.1: HRS acceptance. Left: the actual acceptance. Middle: Idealized acceptance. Right: Idealized acceptance translated for clarity.

- $\Delta E'$ is the energy spread of the scattered electrons for each spectrometer setting.
- $\Delta\Omega$ is the angular acceptance.

As mentioned in section 7.7, the acceptance was simulated via a monte carlo technique. Twenty million events (N_{in}) with random rays were generated over an illuminated area covering a solid angle ($\Delta\Omega_{mc}$) of 50 mSr. The rays originated from along a simulated target length (ΔZ_{mc}) of 60 cm, and covered a random momentum spread ($\Delta E'_{mc}$) of ±7%. The number of events (N_{out}) that made it through the transport functions as well as the same cuts that were applied to the data were then recorded.

In order to understand how the simulation is used to determine the acceptance, we consider figure 8.1. In the first panel, the light colored region represents the illumination space over which the simulation generates random events. The central dark area represents the region through which an incident particle that enters will emerge at the focal plane. In the middle panel, we imagine a simpler rectangular region which covers the same solid angle as our actual acceptance. In the final panel, we translate this region and it becomes clear that in this particular case only one fourth of the events that are randomly distributed over the illumination region will pass. Generalizing, we conclude that:

$$\frac{N_{out}}{N_{in}} = \left(\frac{\Delta\Omega}{\Delta\Omega_{mc}}\right) \tag{8.2}$$

This of course assumes a point like target and scattered electrons with a well defined momentum. In practice, we must account for the finite target length and scattered electron momentum spread, so equation 8.2 is generalized to*:

$$\frac{N_{out}}{N_{in}} = \left(\frac{\Delta\Omega}{\Delta\Omega_{mc}}\right)\left(\frac{\Delta E'}{\Delta E'_{mc}}\right)\left(\frac{\Delta Z}{\Delta Z_{mc}}\right) \tag{8.3}$$

From this relation we can deduce the solid angle $\Delta\Omega$.

8.1.1 Raw Cross Section Systematic

The detection efficiency of the Čerenkov [140] is practically 100% so the error on this correction is negligible. The calorimeter [142] was over 99% efficient so we take a conservative estimate of 1% error on this correction. The scintillator† and VDC [139] efficiencies also contribute at the 1% level.

The particle ID cuts on the Čerenkov and calorimeter were optimized to be more than 99% efficient so the error introduced by correcting for the cut inefficiency is limited to 1% for each device [142, 140].

The y_t relative uncertainty of ±0.3 mm contributes about 1.9% to the systematic, and the ϕ_t and θ_t relative uncertainty of ±0.2 and ±0.5 mrad contribute 1.7% and 1.3% respectively to the cross section [148]. We assume that the deadtime error is negligible since the scalers are highly accurate. The charge [149] is known to about 1%. The scattered electron energy is known to about 0.5%.

The target fill density (ρ_0) at room temperature is known to 2.3% [150]. The target pumping chamber is heated to accommodate the optical pumping process which leads to a variation of the running density (ρ) in the target chamber. The lower target chamber temperature is quite stable($T_t \approx 327$K) with an uncertainty of approximately 1 K. The upper pumping chamber temperature (T_p) has a greater uncertainty (± 20°) due to the presence of the high power incident laser light.

The expected variation of the density with pumping chamber temperature T_p is:

$$\frac{\rho}{\rho_0} = \left(1 + \frac{V_{pump}}{V_{total}}\left(\frac{T_t}{T_p} - 1\right)\right)^{-1} \tag{8.4}$$

where V_{pump} (V_{total}) is the pumping chamber (total) volume, and we've used the ideal gas law. The predicted density variation with respect to T_p is illustrated in figure 8.2. The plot is normalized to the density at T_p =

---

*Notice that ΔZ, $\Delta E'$, and $\Delta\Omega$ are constrained by the cuts discussed in section 7.8.

†See section 7.4.1 and ref. [147].

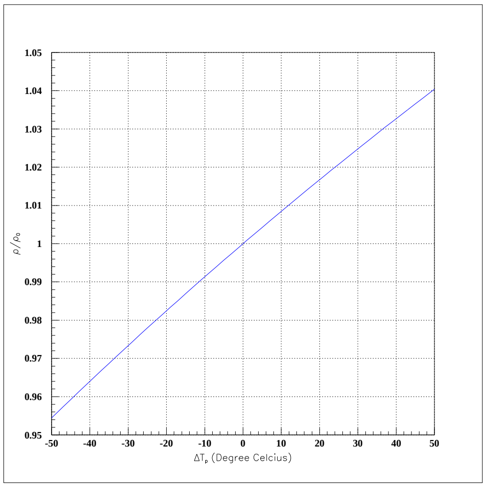

Figure 8.2: Variation of the density with pumping chamber temperature. See equation 8.4.

486K, and assumes that the target cell temperature stays constant at 327K. We can see that the uncertainty of the pumping chamber temperature leads to an additional 1.8% uncertainty [151] in the density.

The raw cross section systematic errors are summarized in table 8.1. Two other analyses([152] and [148]) came to similar conclusions about the size of the error.

Cut Variation

In section 7.8 we chose an optimized cut on the acceptance and target variables. To evaluate the performance of the acceptance simulation, we have examined how sensitive the cross section is to variations in this cut. Further details[‡] can be found in reference [153]. Table 8.2 lists the six cuts utilized in the study. The first three cuts vary θ and ϕ, while the final three vary the cut on target length. Cut number three is similar to the actual cut used to produce final cross sections as described in section 7.8. Therefore, we take the cross section produced with this cut as our baseline and compare the resulting cross section from all other cuts to this.

[‡] Here, we generalize the analysis of reference [153] to include the quasielastic region.

Detection Efficiency: Čerenkov	0%
Detection Efficiency: Calorimeter	1%
Detection Efficiency: Scintillator	1%
Detection Efficiency: VDC	1%
PID Cut Efficiency: Čerenkov	1%
PID Cut Efficiency: Calorimeter	1%
Reconstructed variable : y_t	1.9%
Reconstructed variable : $\Delta\Omega$	2.1%
Charge	1.0%
Energy	0.5%
Target density	2.9%
Total	4.8%

Table 8.1: Raw cross section systematics.

CUT	ϕ (mrad)	θ (mrad)	z (mm.)
1	± 5	±30	±60
2	±15	±10	±60
3	±15	±30	±60
4	±15	±30	±15
5	±15	±30	±30
6	±15	±30	±90

Table 8.2: Cuts used to evaluate the cross section cut systematic uncertainty.

E_0(GeV)	δ_{cut}	δ_{spect}
0.9	2.8 %	9.3 %
1.7	1.8 %	6.9 %
2.5	3.0 %	3.2 %
3.4	3.0 %	6.7 %
4.3	3.3 %	3.8 %
5.1	2.4 %	5.6 %

Table 8.3: $\delta_{\mathbf{cut}}$: Systematic variation of the cross section with acceptance cuts (See equation 8.6). $\delta_{\mathbf{spect}}$: Difference between HRS-L and HRS-R raw cross sections.

Specifically, we evaluate:

$$\Delta X_i \quad = \quad \frac{\sigma_i^A - \sigma_i^B}{\sigma_i^A} \tag{8.5}$$

Here, σ_i^A is the optimized cross section of cut three, σ_i^B is the alternative cross section obtained using a different cut, and i refers to a particular bin in ν. An error due to the cut variation is estimated by summing over all bins in ν:

$$\delta_{cut} \quad = \quad \sqrt{\frac{\sum^{N} \Delta X_i^2}{N}} \tag{8.6}$$

with the summation beginning at the two-body breakup threshold. The largest cross section variation among all the cuts evaluated is taken as an estimate of the cut systematic and is listed in the second column of table 8.3.

The value of δ_{cut} is in some sense an independent evaluation of the error on the product $\Delta Z \cdot \Delta\Omega$ and it compares reasonably well to the estimate of the uncertainty on this product listed in table 8.1

Spectrometer Comparison

There were a number of problems that arose with the HRS-R cross section analysis that lead us to believe that these spectra were less reliable than the HRS-L counterparts. Some of the factors that pointed to this conclusion were:

- There was a blockage of the HRS-R acceptance for most of the 862 MeV data set. This is believed to be caused by a bundle of target RTD lead wires that became dislodged. See appendix F.
- There is a large uncertainty in the radiation length of materials transversed before HRS-R [154].
- The acceptance was not studied in detail as it was on HRS-L [146, 155].
- There was a significant horizontal mis-pointing of HRS-R. This mis-pointing was not accurately determined (see section 5.3.3), which led to a large uncertainty in the central scattering angle.

For these reasons, it was decided to use only the HRS-L data for the absolute cross section measurement. However, even with the known problems with the HRS-R spectra they can serve as a rough check of the HRS-L cross sections. In this section, we compare the results of the two arms. We form a quantity δ_{spect}, similar to that defined in equation 8.6, but here, σ_i^A is the cross section for HRS-L and σ_i^B is the cross section for HRS-R. The resulting δ_{spect} for each energy is shown in table 8.3. We note that this comparison is performed before the radiative corrections have been applied. There are significant differences in the thickness of materials seen by each spectrometer which lead to a reduction of δ_{spect} after the radiative corrections.

8.1.2 Tail Subtraction and Nitrogen Dilution

The experimentally measured raw cross sections contain contributions from a small admixture of nitrogen introduced to facilitate polarization of the cells. In addition, there can be large contributions from elastic radiative tails. The elastic radiative tail is created when electrons emit a photon before interacting with the target nucleus and then scatter elastically. The scattering takes place at a lower incident energy with a correspondingly larger cross section. It is usually most noticeable as the electron energy approaches zero and can lead to a very large rising tail at large ν.

These contributions must be removed before the radiative corrections can be applied. The inelastic ^{3}He cross section is extracted from the raw cross section as follows:

$$\sigma_{exp} = \sigma_{raw} - \sigma_{3el} - 2.0 * R(\sigma_N + \sigma_{Nel}) \tag{8.7}$$

where:

- $\sigma_{exp} = \left(\frac{d\sigma}{dE'd\Omega}\right)_{exp}$ is the unpolarized ^{3}He cross section before R.C.
- $\sigma_{raw} = \left(\frac{d\sigma}{dE'd\Omega}\right)_{raw}$ is the raw cross section of Eq. 8.1.
- $\sigma_N = \left(\frac{d\sigma}{dE'd\Omega}\right)_N$ is the Nitrogen inelastic cross section.
- σ_{3el} is the ^{3}He elastic radiative tail.
- σ_{Nel} is the Nitrogen elastic radiative tail.
- R $= \left(\frac{\rho_{N_2}}{\rho_{^3He}}\right)$ is ratio of Nitrogen to ^{3}He gas densities [156] in the target cell.

The elastic ^{3}He and N_2 radiative tails were calculated following the formalism from [131]. The exact[§] solution was implemented using the code **ROSETAIL.F** [138], which was updated to utilize the elastic form factors of reference [157] and [158, 159] for Nitrogen and ^{3}He respectively. The radiated tail from the Nitrogen elastic peak was found to be negligible for all incident energies. The ^{3}He radiated tail was small for all energies except 862 MeV, where it contributed a substantial amount in the quasi-elastic region. See figure 8.13. The **ROSETAIL.F** code assumes a point like target with no acceptance corrections. These corrections are negligible unless the tail is a sizable fraction of the cross section, which is the case for 862 MeV. A monte carlo [160] was used to simulate acceptance and extended target effects for the tail subtraction at this energy.

The Nitrogen inelastic cross section was calculated using the Quasi-Free Scattering (QFS) code [161] (see section 8.5.3). We have modified [162] the initial code to include external radiative corrections, and to improve the agreement with existing data in the quasielastic region.

The raw cross sections are rebinned if necessary to smooth out statistical fluctuations. The raw cross sections are not all continuous as a function of $\nu = E - E'$, since not all E94-010 spectrometer settings overlap. The cross sections are fit and interpolated to fill in the missing kinematics and to locate each bin at convenient values of ν. Spline fitting or linear interpolation are used. Beyond the resonance region, it was sometimes necessary to use a 2^{nd} or 3^{rd} order polynomial to give satisfactory agreement with the data.

Finally, all data below the two-body breakup threshold (elastic peak + 5.5 MeV) is excluded. We now have pure ^{3}He inelastic cross sections, although the radiative corrections still need to be unfolded from these spectra. These "clean" cross sections σ_{exp} can be seen in figs. 8.3 to 8.8.

8.1.3 Cross Section Errors before Radiative Corrections

The statistical error on the extracted ^{3}He cross section must be adjusted to account for the removal of non-^{3}He events from the sample.

$$\delta\sigma_{exp} = \sqrt{(\frac{\sigma_{exp}}{\sigma_{raw}})}\delta\sigma_{raw} \qquad (statistical) \tag{8.8}$$

The systematic error on the extracted ^{3}He cross section is estimated as follows:

$$(\delta\sigma_{exp})^2 = (\delta\sigma_{raw})^2 + (\delta\sigma_{3el})^2 + 4R^2\left[(\delta\sigma_N)^2 + (\delta\sigma_{Nrad})^2 + (\delta\sigma_{Nel})^2\right] \tag{8.9}$$

[§] i.e. the "peaking approximation" was not used.

E_s - E_p (MeV)	Exact	Peaking	Δ_{Exact}
20	3.7330	3.3557	10.1 %
100	0.6244	0.6057	3.0 %
300	0.2275	0.2317	1.8 %
500	0.1934	0.1851	4.3 %
700	0.3048	0.2435	20.0 %
800	0.5435	0.4080	24.9 %

Table 8.4: Comparison of the radiated elastic tail from our peaking approximation code to the exact results calculated in ref. [131] for E_s=1 GeV. Cross section are in μb/MeV-sr.

E_s - E_p (MeV)	Exact	Peaking	Δ_{Exact}
200	17.26	16.14	6.5%
500	4.533	4.283	5.5%
1000	2.250	2.228	0.9%
2500	1.665	1.591	4.4%
4000	5.690	4.202	26.1%

Table 8.5: Same as table 8.4. E_s=5 GeV

E_0 (MeV)	$\delta\sigma_{raw}$	$\delta\sigma_N$	$\delta\sigma_{Nrad}$	$\delta\sigma_{Nel}$	$\delta\sigma_{3el}$	$\delta_{R.C.}$
862	4.8	52.0	10.0	20.0	5.0	15.0
1717	4.8	7.0	10.0	20.0	5.0	5.0
2581	4.8	21.0	10.0	20.0	5.0	5.0
3381	4.8	25.0	10.0	20.0	5.0	5.0
4238	4.8	27.0	10.0	20.0	5.0	5.0
5058	4.8	27.0	10.0	20.0	5.0	5.0

Table 8.6: Contributions to the cross section systematic uncertainty for σ_{exp}. See text for explanation of the listed quantities. Values are in percent.

where:

- $\delta\sigma_{raw}$ is the systematic error associated with the raw cross sections. See table 8.1.

- $\delta\sigma_{3el}$ is the error on calculation of ^{3}He elastic tail. We estimate this to be less than 5% from comparison of Amroun *et al.* [158, 159] and McCarthy *et al.* [163] form factors.

- $\delta\sigma_N$ is the uncertainty on the QFS Nitrogen inelastic calculation. It ranges from 7%-52% and was evaluated by comparing the QFS quasielastic results for carbon to the world data [162]. The error on the Delta peak calculation was always found to be less than 10%, and in any case much smaller than the quasielastic error. It was ignored along with any error of the higher resonances.

- $\delta\sigma_{Nrad}$ is the error on the radiative corrections to the inelastic nitrogen model. The modified radiative correction routines were tested for elastic electron–proton scattering and compared to the exact prediction of Mo and Tsai [131]. The results are shown in Table 8.4 and Table 8.5. We see that our peaking approximation code does quite well as long as the energy loss is not too great. 10% is taken as the error on the nitrogen radiative correction.

- $\delta\sigma_{Nel}$ is the error on the nitrogen elastic tail and represents the maximum quoted error (20%) on the Dally *et al.* [157] form factors. This error contributes very little to the final results as the nitrogen elastic tail is mostly negligible for our data.

The various contributions to the systematic error are summarized in table 8.6.

8.2 Radiative Corrections

Radiative corrections are performed using the program RADCOR.F [164] The original code was based on the formalism of Mo and Tsai [131] as implemented by Miller [165], but makes several approximations based on the assumption that target thickness before and after scattering are equal. To rectify this, and to update the code to a more recent approach, we have rewritten the radiative correction subroutines [162] to use the peaking approximation formalism of Stein *et al.* [133]. The final unfolded cross sections

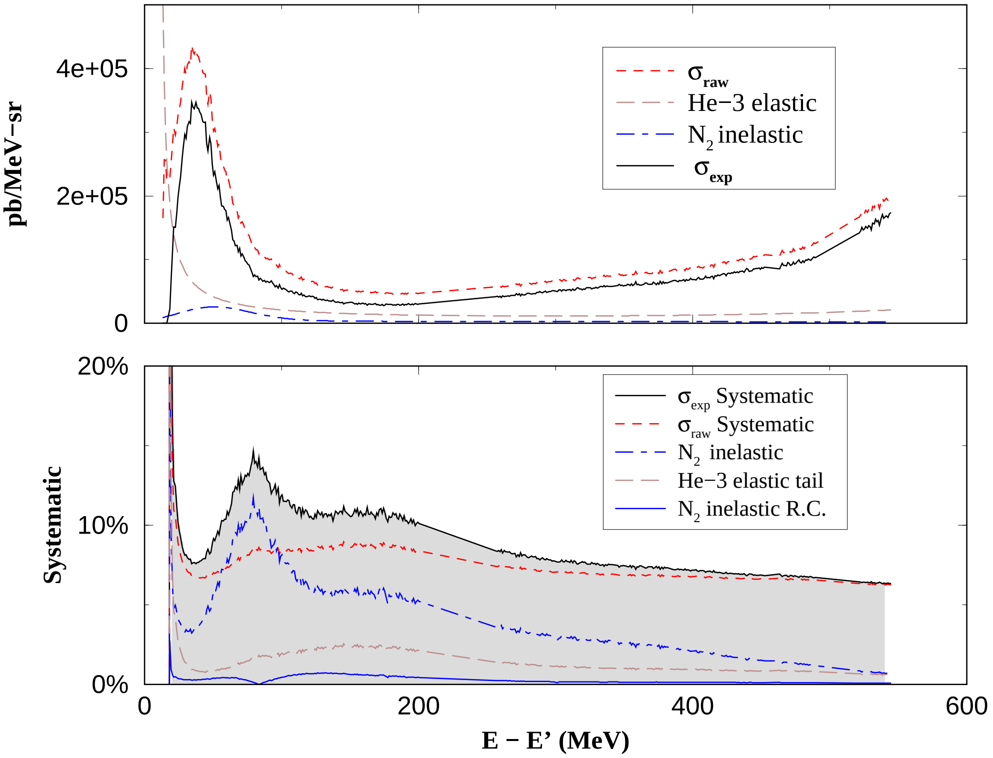

Figure 8.3: $E_0 = 862$ MeV cross section. **Top**: Subtraction of elastic tails and nitrogen dilution from the raw cross sections. **Bottom**: Total systematic uncertainty before radiative corrections and the various contributions.

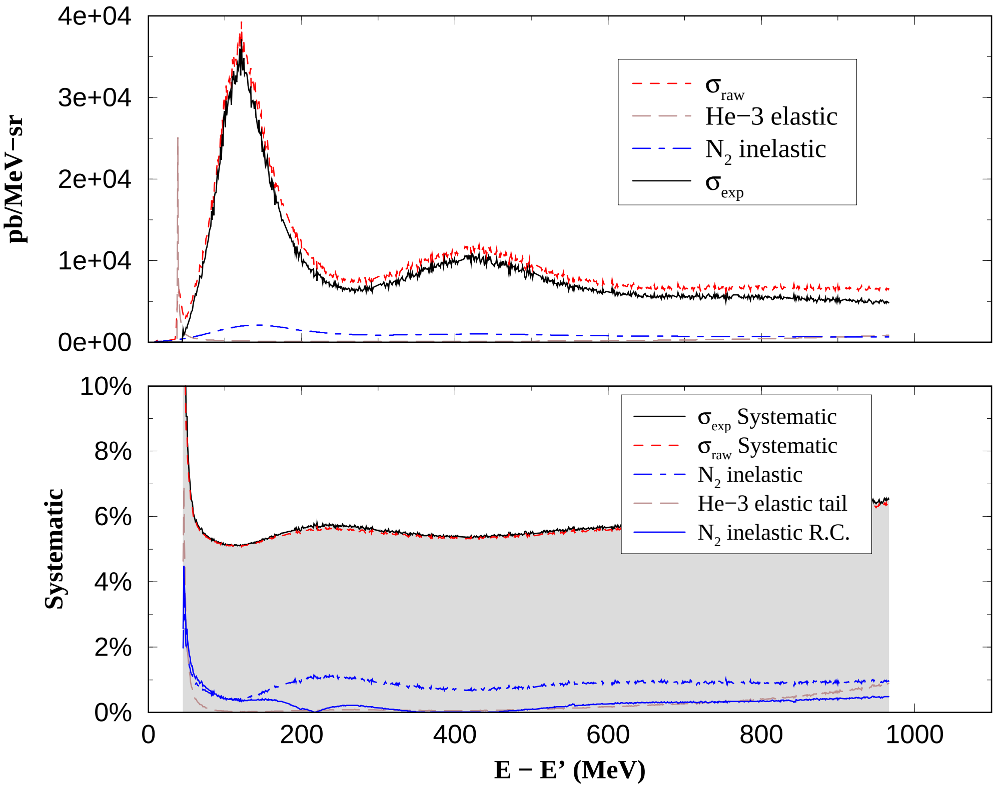

Figure 8.4: $E_0 = 1717$ MeV cross section. **Top**: Subtraction of elastic tails and nitrogen dilution from the raw cross sections. **Bottom**: Total systematic uncertainty before radiative corrections and the various contributions.

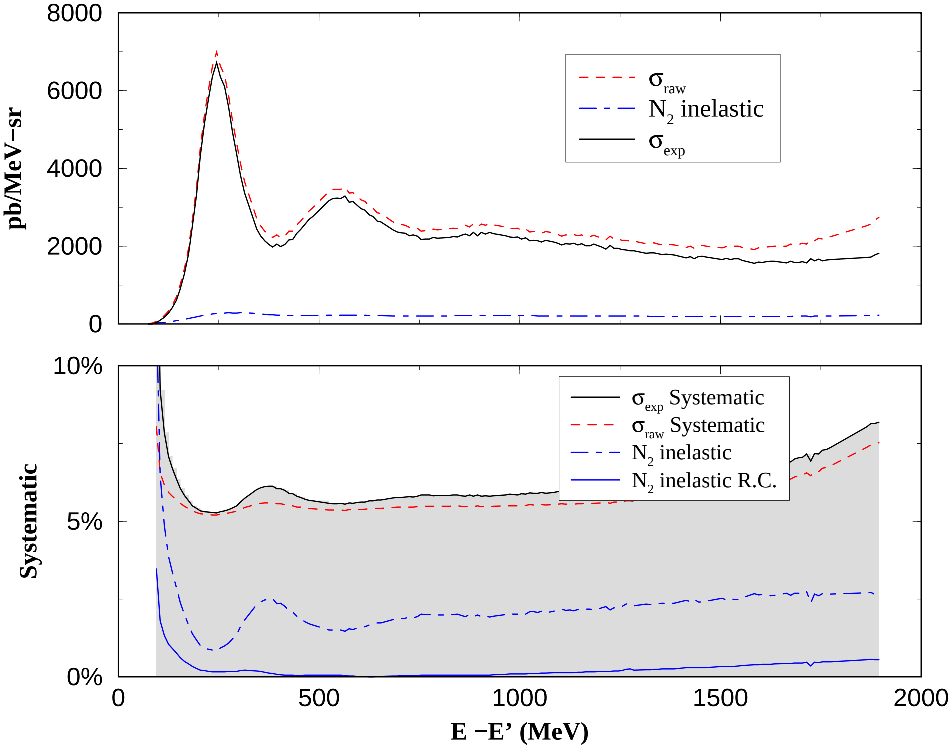

Figure 8.5: $E_0 = 2581$ MeV cross section. **Top**: Subtraction of elastic tails and nitrogen dilution from the raw cross sections. **Bottom**: Total systematic uncertainty before radiative corrections and the various contribution.

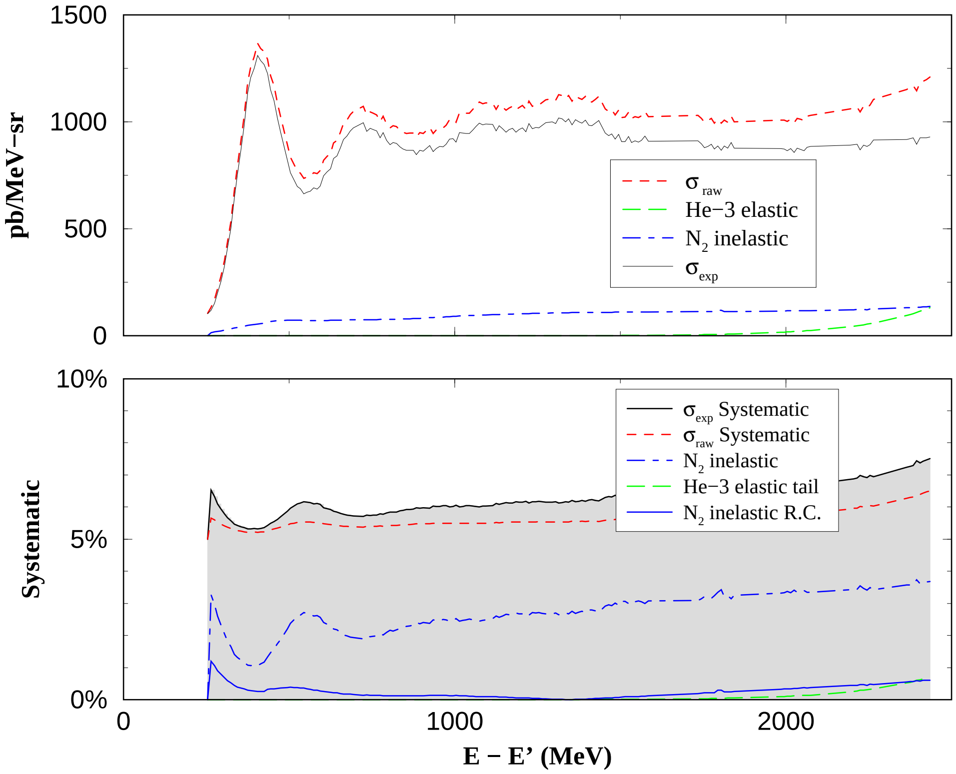

Figure 8.6: $E_0 = 3382$ MeV cross section.**Top**: Subtraction of elastic tails and nitrogen dilution from the raw cross sections. **Bottom**: Total systematic uncertainty before radiative corrections and the various contributions.

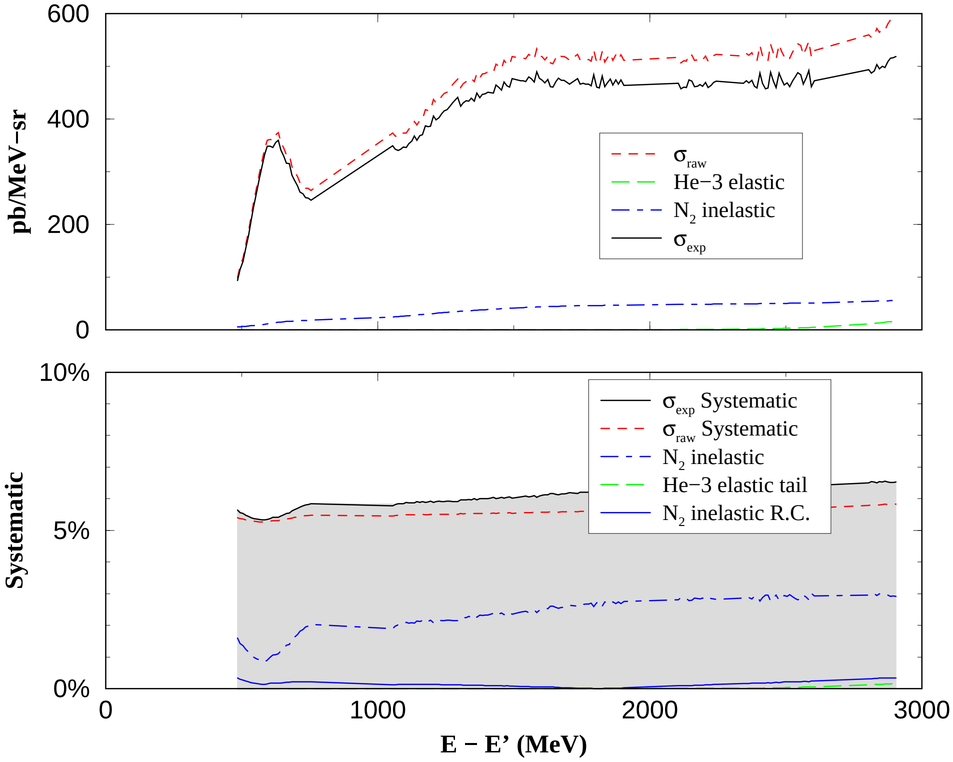

Figure 8.7: $E_0 = 4239$ MeV cross section. **Top**: Subtraction of elastic tails and nitrogen dilution from the raw cross sections. **Bottom**: Total systematic uncertainty before radiative corrections and the various contributions.

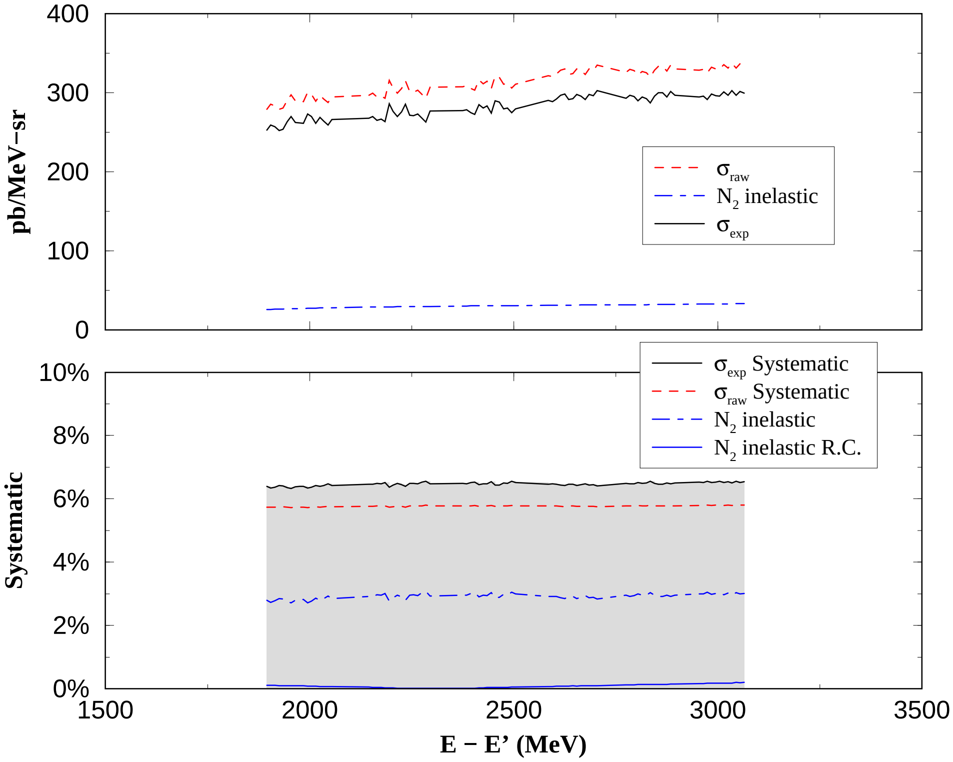

Figure 8.8: $E_0 = 5058$ MeV cross section.**Top**: Subtraction of elastic tails and nitrogen dilution from the raw cross sections. **Bottom**: Total systematic uncertainty before radiative corrections and the various contributions.

are shown in fig. 8.12 as a function of invariant mass W, and in more detail in figs. 8.13 to 8.23 as a function of energy loss $E - E'$.

A more detailed examination of the radiative corrections is given in Appendix C.

8.3 Finite Acceptance Correction

The measured cross section represents an average over the solid angle defined by the spectrometer and the analysis cuts. To evaluate the effect that this averaging has on the cross sections, we divided the acceptance into 500 separate regions. The QFS model [161] (see section 8.5.3) is used to calculate the cross section at each of the corresponding scattering angles. The average over these 500 results is compared to the result at a nominal scattering angle of 15.5° in order to determine a normalization factor. This factor is less than 2% for most of the spectra, but can jump to as high as 5% at the peak of the Quasielastic region. For full details see reference [155].

8.4 Final Systematic Error

The final error is obtained by combining the error of eq. 8.9 with the error due to the radiative corrections. The error on the radiative corrections, δ_{RC}, is taken to be 5% of the correction. For our lowest energy this estimate is inflated to 15% to account for the lack of lower energy data. This leads to a final systematic error given by:

$$(\delta\sigma_{born})^2 = \left(\delta\sigma_{exp} \times \frac{\sigma_{born}}{\sigma_{exp}}\right)^2 + \left(\delta_{RC} \times \frac{\sigma_{born} - \sigma_{exp}}{\sigma_{born}}\right)^2 \tag{8.10}$$

In appendix D and ref. [154], it is revealed that we know the target radiation lengths to an accuracy of 5 to 9%. Variations in the thickness before scattering of up to 35% were found to have negligible effect on the radiative correction procedures. The sensitivity to the material after scattering was tested by varying the nominal glass wall thickness of target *Armegeddon*¶ by $\pm 1\sigma$ in the radiative corrections procedure. It was found that the cross section varies by less than 3% over the majority of the spectra including the quasielastic region. In the dip region, the sensitivity jumps to 5%. These variations were found to be small compared to the final systematic.

¶A cell made of GE180 glass that has a considerably larger radiation length than all other cells, which were composed of Corning 1720.

In general, we find that the final statistical error is about 1% while the systematic error varies from 5.5 to 9%. For our lowest incident energy the systematic estimate is inflated to account for the lack of lower energy data needed in the radiative corrections.

8.5 Cross Section Evaluation

In this section, we perform some basic checks to ensure that the radiative corrections are performed properly and compare our data to previous experimental results. We also examine the predictions of several calculations and phenomenological models.

8.5.1 Radiative Corrections Check

E94-010 recorded data with two different target cells for the incident energies of 1.7 GeV and 4.2 GeV. Both data sets cover the quasielastic region. Targets *Be Happy* and *Armegeddon* were used for the 1.7 GeV data. These two glass cells were made from Corning 1720 and GE180 respectively and, as such, have considerably different radiation thicknesses (see appendix D). Comparison of the cross sections obtained with these cells before and after radiative corrections are shown in figure. 8.9. Figure 8.10 shows a similar study performed with the 4.2 GeV data. For this data set, we are comparing spectra from the target cells *Nepheli* and *Sysiphos* both constructed from Corning 1720. These two cells had very similar wall thicknesses, so the spectra before the radiative corrections do not differ as much as the previous set of cells.

Figs. 8.9 and 8.10 imply that we know the radiation lengths of our targets and that we are applying the unfolding technique properly. The fact that the radiatively corrected spectrum obtained from independent measurements agree within a few percent also gives us increased confidence in the estimated systematic uncertainty.

8.5.2 Comparison to Existing ^{3}He Data

Marchand *et al.* [166] performed a measurement of the ^{3}He longitudinal and transverse response functions R_L and R_T in the quasielastic and Δ excitation regions for $250 < |\vec{q}| < 700$ MeV at the Saclay linear accelerator. Ueng [167] and Dow [168] performed a similar measurement in the range $150 < |\vec{q}| < 700$ MeV at the M.I.T. Bates linear accelerator facility. The

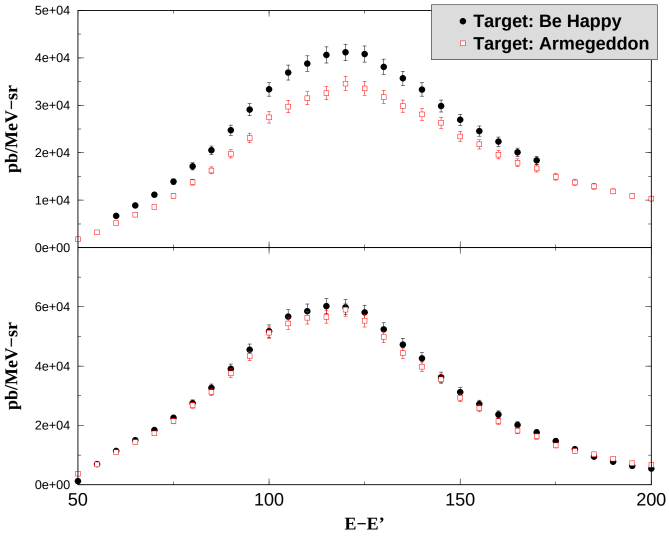

Figure 8.9: Cross section in the quasielastic region before (top panel) and after (bottom panel) radiative corrections. Incident energy is 1.7 GeV.

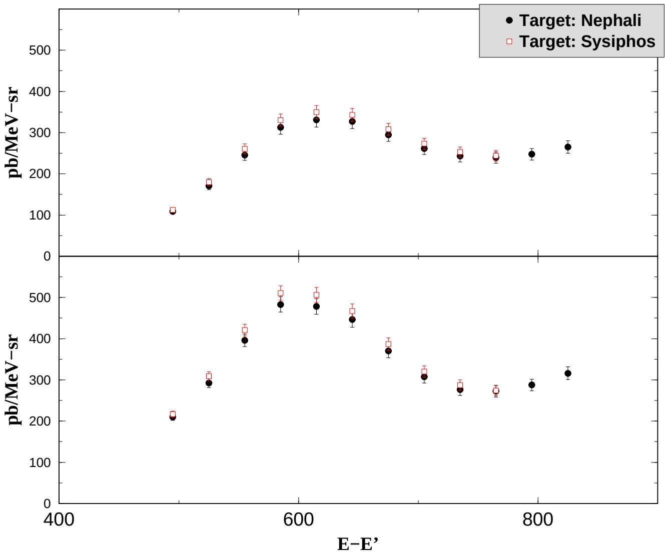

Figure 8.10: Cross section in the quasielastic region before (top panel) and after (bottom panel) radiative corrections. Incident energy is 4.2 GeV.

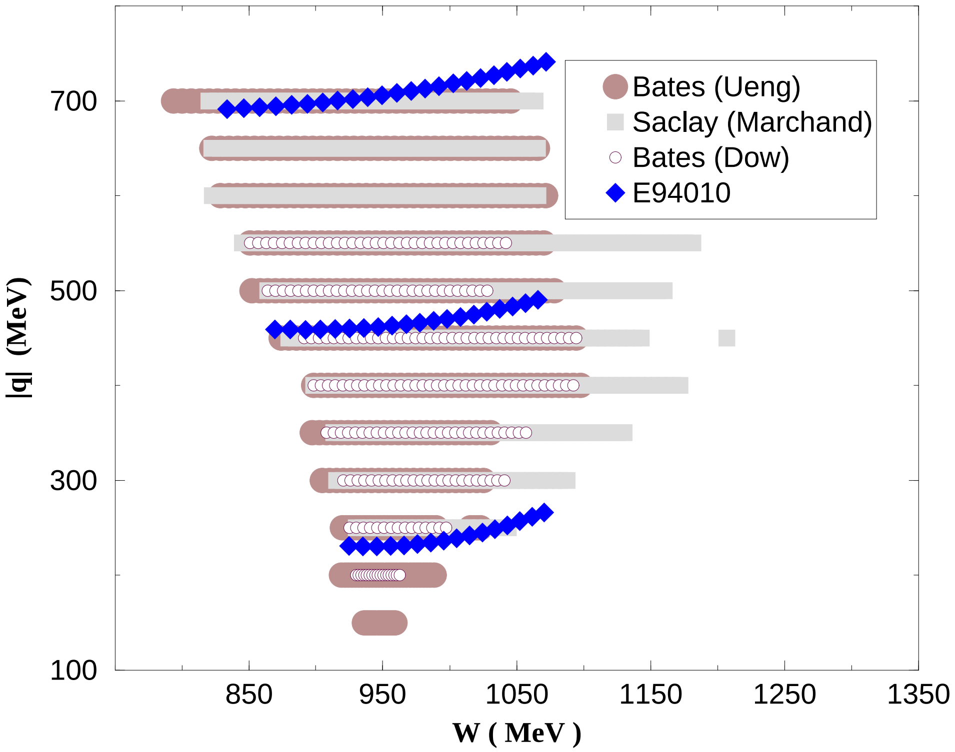

Figure 8.11: Kinematic coverage of Bates and Saclay L-T separation: $|\vec{q}|$ vs. W. Filled square: Marchand *et al.* [166]. Filled circle: Ueng [167]. Open circle: Dow [168]. Filled diamonds represent the three lowest incident energies of E94-010 in the quasielastic region.

results represent two independent analyses of the same Bates data and agree for the most part within error, although there are small discrepancies.

The kinematic coverage of the Bates and Saclay experiments are shown in figure 8.11. On this same plot, we display the region covered by the lowest three incident energies of E94-010 in the quasielastic region. We have interpolated the measured response functions with respect to $|\vec{q}|$ and W to perform a cross section comparison with our data via equation 2.2.4. The cross sections obtained in this fashion are shown in figs. 8.13 to 8.15.

8.5.3 Theoretical Calculations and Models

In the quasielastic region a calculation [169] of the ${}^3\vec{H}e(\vec{e},e')X$ cross sections was provided by S. Scopetta [170] for all six incident energies[‖] of E94-010. A spin dependent spectral function [171] is utilized, updated to include the treatment of doubly polarized electron scattering from nuclei described in ref. [172]. The spectral function was obtained from a realistic three body wave function. Various two and three-nucleon forces[**] have been considered and the Coulomb interaction has been taken into account.

The calculation is performed in the context of the plane wave impulse approximation (PWIA) in which the electron interacts with a single nucleon and the nucleon is ejected from the nucleus with no further interaction with the remaining spectator pair or any hadrons produced in the interaction. The spectral function approach that is utilized addresses both Fermi motion and binding effects. Major effects not addressed are the final state interactions (FSI) mentioned above, meson exchange currents (MEC), and the presence of the Δ in the bound state [169]. The FSI in particular are expected to be large at low Q^2 (< 0.1 GeV^2), while for $Q^2 > 0.25$ GeV^2 PWIA calculations have previously been shown to be in good agreement with experimental data [173, 174]. The inclusion of FSI to the calculation is underway [170, 169]. The MAID2000 model[††] predictions (see section 3.4.1) for the nucleon response in the resonance region was used to complete the Scopetta spectra to $W = 2$ GeV.

The phenomenological QFS [161] model of J. Lightbody and J. O'Connell parameterizes world data for inelastic electron scattering from nuclei in the impulse approximation using five reaction channels:

1. Quasielastic scattering on a bound nucleon.
2. Two nucleon emission in the dip region.
3. $\Delta(1232)$ resonance electroproduction.
4. $W = 1500$ and 1700 MeV resonance electroproduction.

[‖] The incident energies used in the calculation are: 862.0, 1720.0, 2591.0, 3384.0, 4255.0 and 5070.0 MeV, which differ slightly from the actual incident energies (see section 5.2.5).

[**] The Argonne v14 potential, RSCv8 and Brazil and Tucson-Melbourne three-nucleon interaction. The model dependence was found to be at the few percent level.

[††] The MAID neutron results have simply been multiplied by $M_{{}^3He}/M_n$ and in this sense the inelastic prediction above the pion threshold is not exact and is only included for a crude comparison.

5. A non-resonant Q^2 dependent background term.

QFS has been used widely to estimate counting rates for inclusive electron scattering experiments, although it is not expected to give precise results. We have modified the initial code to include external radiative corrections, and to improve the agreement with existing data in the quasielastic region. Complete details can be found in reference [162]. There are three free parameters (the Fermi momentum of the target nucleus k_f, the nucleon separation energy ϵ_s, and the Δ separation energy ϵ_Δ) that the user may adjust to better match the experimental data[‡‡]. The quasielastic peak is described as a gaussian centered at an energy loss of $Q^2/2M_N + \epsilon_s$. The width of the peak is proportional to the fermi momentum and momentum transfer $|\vec{q}|$. The area under the peak is constrained to equal the incoherent sum of elastic scattering from the individual nucleons, which are described with a standard dipole form factor. The $\Delta(1232)$ is assumed to be totally transverse in nature, and is represented by a Lorentzian shape with a width determined from 1) the natural width of the Δ, 2) the Fermi motion which is proportional to $|\vec{q}|k_{fermi}/M$, and 3) a term reflecting the dependence on nuclear medium. The higher resonances are also assumed to be completely transverse in nature and are fit with a similar functional form.

The measured quasielastic cross sections are also compared to a non-relativistic full Faddeev calculation provided by J. Golak [175], which includes both final state interactions and meson exchange current effects. The 3N force is included in the inclusive calculation of the scattering process as described in [176], and the nucleon form factors used are from ref. [177]. The NN potential used is AV18 [178] while the Urbana IX 3N force [179, 180] is used in both the initial 3N bound state [181], and the final scattering state. The charge dependence of the NN forces are accounted for using an approximation method as described in [182]. All electromagnetic contributions (including Coulomb) to the NN interaction are included in the initial bound state. The Coulomb contribution is however missing from the final state. MEC contributions consistent with AV18 [183, 184] are contained in the charge density and in its spatial components.

The Faddeev calculation is compared to our two lowest energy spectra where relativistic effects are expected to be small. Comparison with both the Faddeev and PWIA calculations in the quasielastic region are shown in figs. 8.13 to 8.17. For completeness, plots of the unpolarized ^{3}He cross sections over the entire measured range are shown in figs. 8.18 to 8.23.

[‡‡] Reasonable agreement with the E94-010 ^{3}He data is found with a choice of 130.0 MeV, 10.0 MeV, and 15.0 MeV respectively.

8.5.4 Conclusion

In figure 8.12, we begin by noting the prominent quasielastic peak which dominates the spectra compared to the contribution of the resonances. As Q^2 increases, the quasielastic reaction falls off rapidly. The first resonance $\Delta(1232)$ also displays a dramatic Q^2 dependence as we would expect from equation 2.20. There is significant Fermi broadening of the resonance peak at larger incident energy and the dominant higher resonances at $W = 1500$ and 1700 MeV are barely distinguishable from the non-resonant background. This background grows in importance as we approach the kinematic region of deep inelastic scattering.

At the lowest incident energy, we observe a rapidly rising background which overwhelms the resonances. This phenomenon was studied in detail by A. Deur [160] who concluded that it was due to multiple scattering initiated prior to the target cell. Since these events must originate from unpolarized material they are expected to have no effect on the polarized cross sections.

For an incident energy of 862 MeV, the E94-010 data is consistent with the Bates analyses over the entire quasielastic region. This region requires a slight extrapolation for the Saclay data as we approach the quasielastic peak from above and is the likely cause of the small disagreement of the Saclay point at $\nu = 40$ MeV. For the $E_0 = 1717$ MeV data set, the E94-010 data agrees well with the previous measurements on the low energy side of the peak. However, there is a small but non-negligible discrepancy on the high energy side. The most likely explanation for this difference is revealed in fig. 8.11, where it is clear that this region requires a much larger interpolation in $|\vec{q}|$ than the low energy side. Finally, the 2581 MeV data set agrees well with the Saclay data on the low energy side of the quasielastic peak but, similar to the 1717 MeV data set, there is a small disagreement on the high energy side of the peak where extrapolation is required.

As expected, the PWIA calculation is not very accurate at the low Q^2 of our first incident energy (fig. 8.13), where the neglected final state interactions are expected to be significant [171]. However, as Q^2 increases, the agreement with data improves dramatically as shown in figs. 8.15 and 8.16.

The full Faddeev calculation reproduces the E94-010 data extremely well at an incident energy of 862 MeV. For this spectra, the final state interactions are expected to be large and the necessity of their inclusion is evident from the comparison to the PWIA result. The calculation is also in good agreement with the 1717 MeV unpolarized cross section on the low energy side of the quasielastic peak. On the high energy side, the curve diverges slightly from the data, most likely due to the increasing importance of relativistic effects.

For reference, we also show the QFS model and Scopetta's implementation of the MAID model in the resonance region in figs. 8.18 to 8.23. The MAID model results clearly show the need for inclusion of a non-resonant DIS background. The QFS model provides reasonable results over most spectra. In particular, the resonances are reproduced extremely well for incident energies of 1.7 GeV, and 2.5 GeV. At higher energy the model agrees at the 20 to 30% level. The model's quasielastic prediction has been adjusted by a Q^2-dependent term to improve agreement with the data as described in ref. [162].

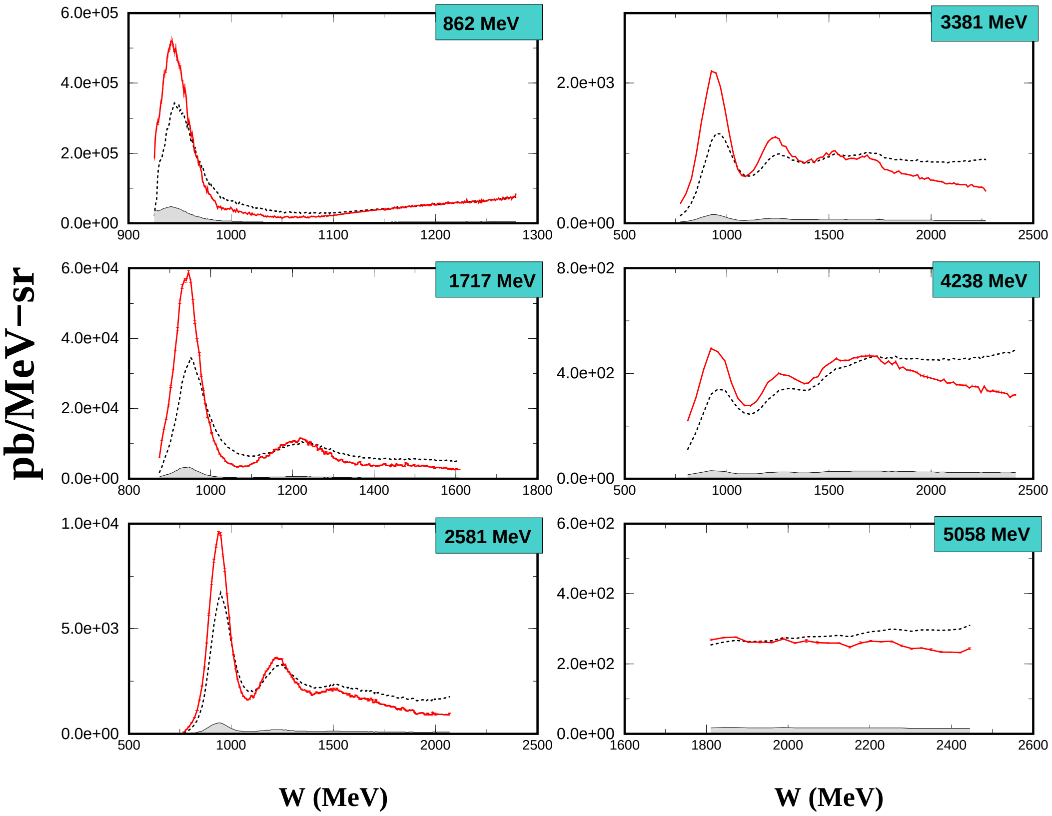

Figure 8.12: E94-010 unfolded cross sections. Dotted line: experimental cross section σ_{exp} as defined in eq. 8.7. Solid line: unfolded Born cross section σ_{born}, with statistical error. Systematic uncertainty is given by solid band on x-axis.

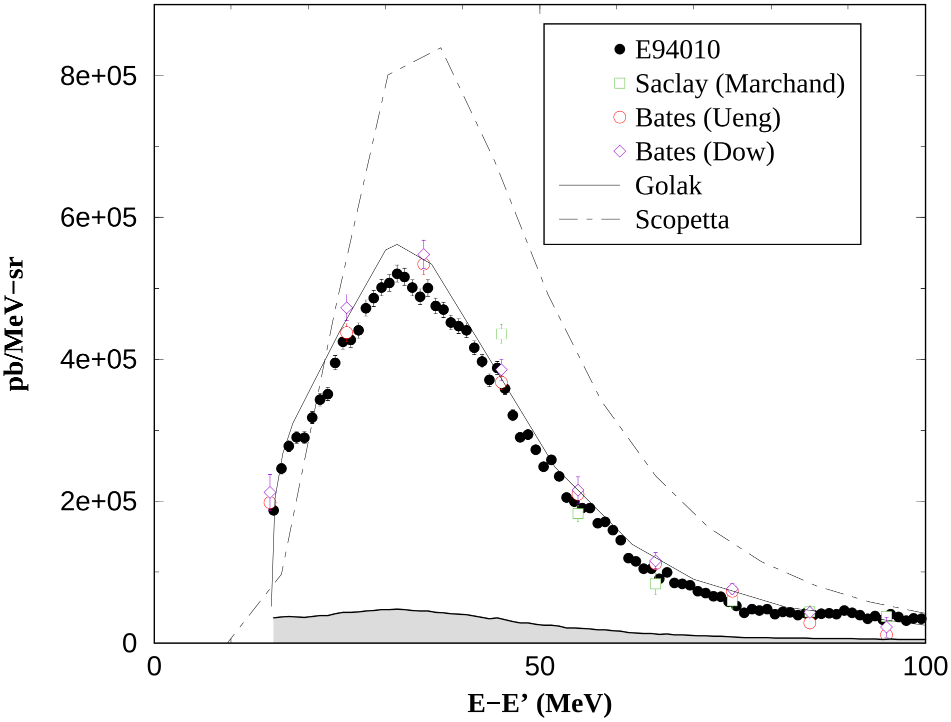

Figure 8.13: ^{3}He unpolarized Born cross section in the quasielastic region. Incident energy: 862 MeV. $Q^2 \approx 0.04$ GeV^2 at Q.E. peak. Solid circle: E94-010. Statistical errors are on the data points, systematic uncertainty is represented by the grey band. Open square: Marchand *et al.* [166]. Open circle: Ueng [167]. Open diamond: Dow [168]. See text for explanation of curves.

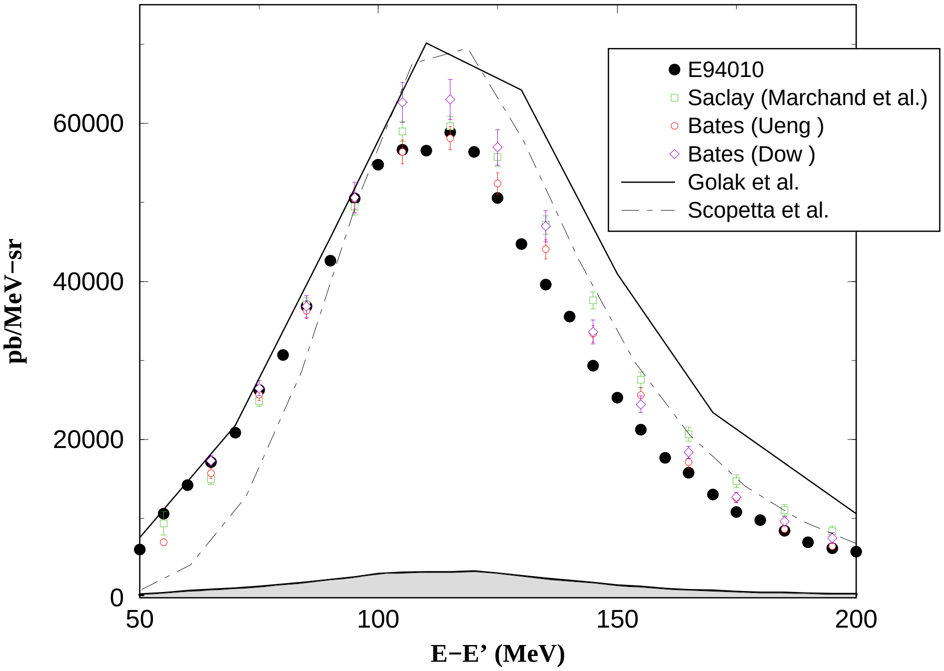

Figure 8.14: ^{3}He unpolarized Born cross section in the quasielastic region. Incident energy: 1717 MeV. $Q^2 \approx 0.19$ GeV^2 at Q.E. peak. Solid circle: E94-010. Statistical errors are on the data points, systematic uncertainty is represented by the grey band. Open square: Marchand *et al.* [166]. Open circle: Ueng [167]. Open diamond: Dow [168]. See text for explanation of curves.

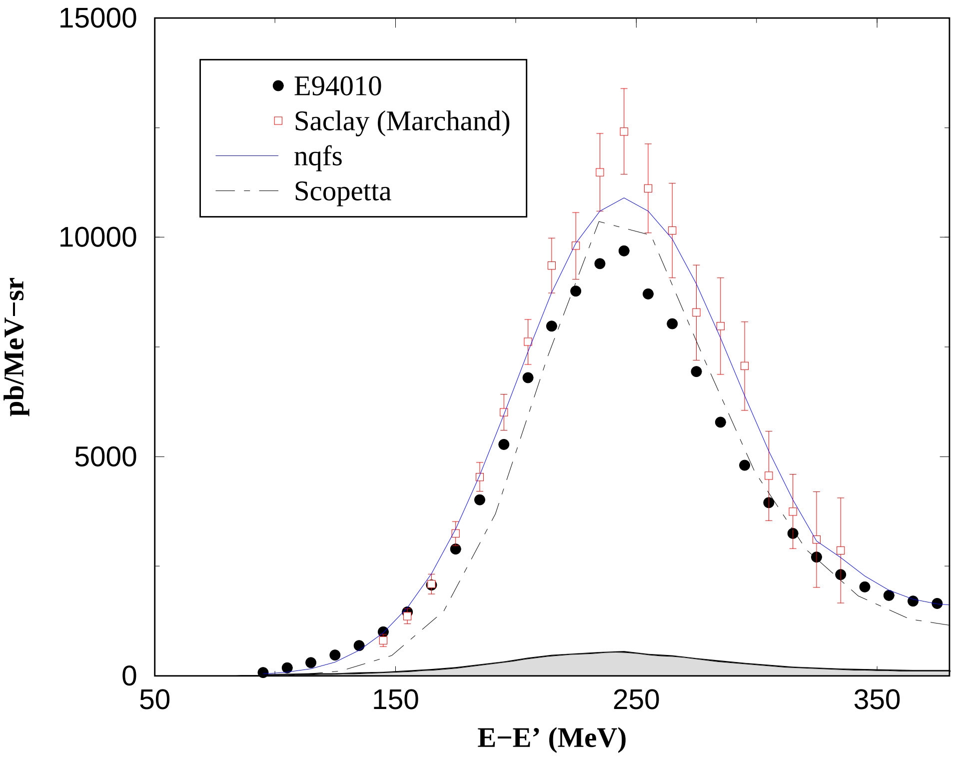

Figure 8.15: ^{3}He unpolarized Born cross section in the quasielastic region. Incident energy: 2581 MeV. $Q^2 \approx 0.43$ GeV^2 at Q.E. peak. Solid circle: E94-010. Statistical errors are on the data points, systematic uncertainty is represented by the grey band. Open square: Marchand *et al.* [166]. See text for explanation of curves.

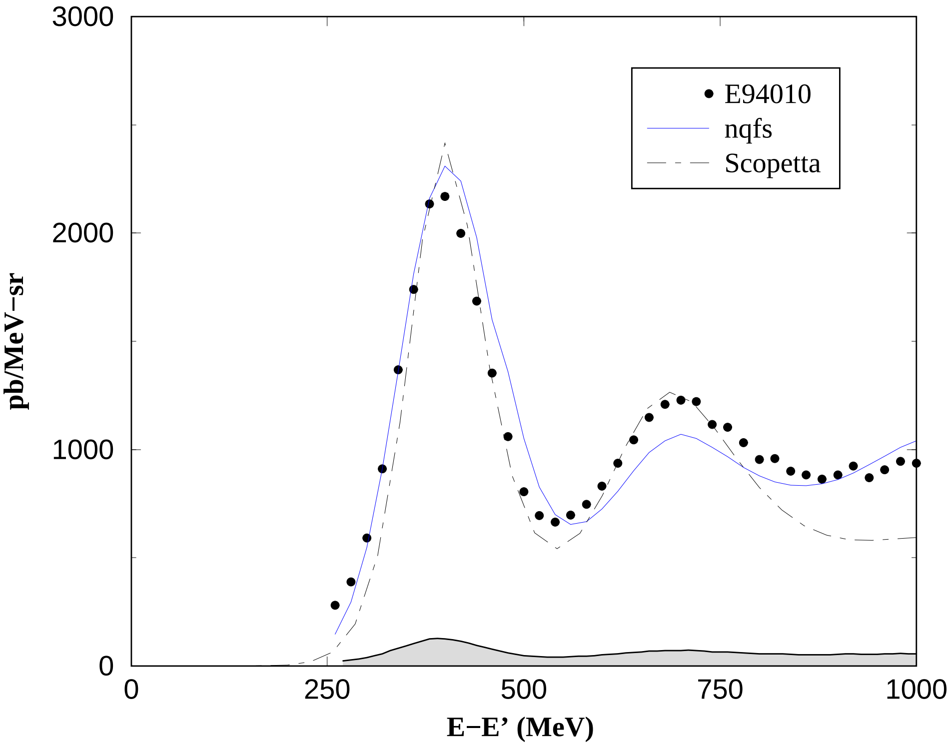

Figure 8.16: ^{3}He unpolarized Born cross section in the quasielastic region. Incident energy: 3382 MeV. $Q^2 \approx 0.77$ GeV^2 at Q.E. peak. Solid circle: E94-010. Statistical errors are on the data points, systematic uncertainty is represented by the grey band. See text for explanation of curves.

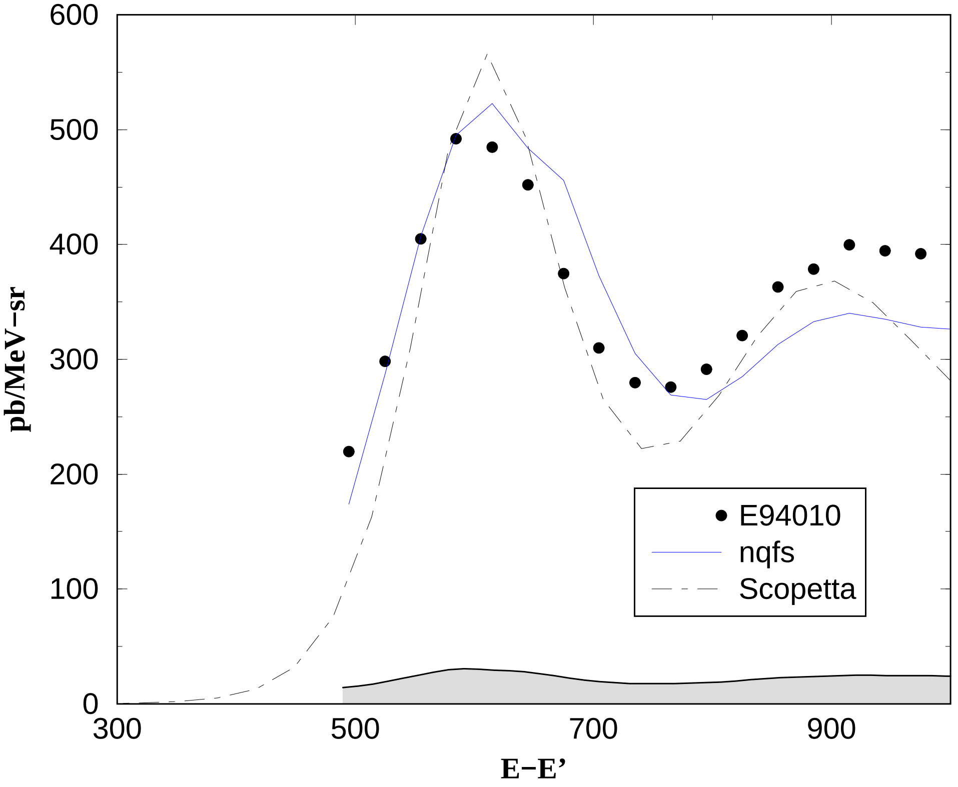

Figure 8.17: ^{3}He unpolarized Born cross section in the quasielastic region. Incident energy: 4239 MeV. $Q^2 \approx 1.1$ GeV^2 at Q.E. peak. Solid circle: E94-010. Statistical errors are on the data points, systematic uncertainty is represented by the grey band. See text for explanation of curves.

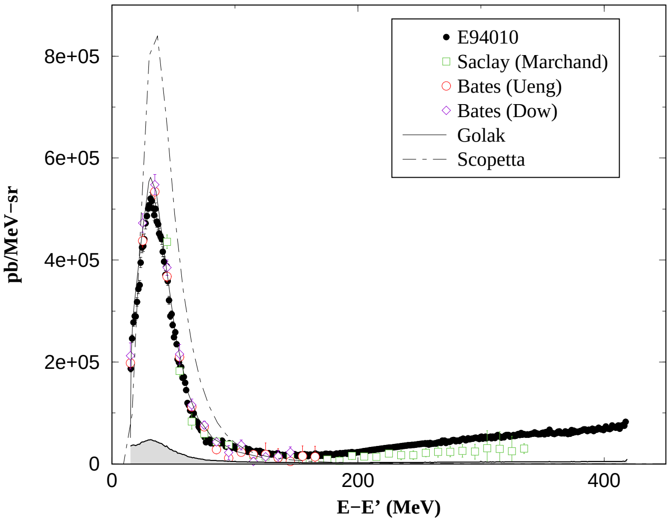

Figure 8.18: Born cross section. Incident energy: 862 MeV.

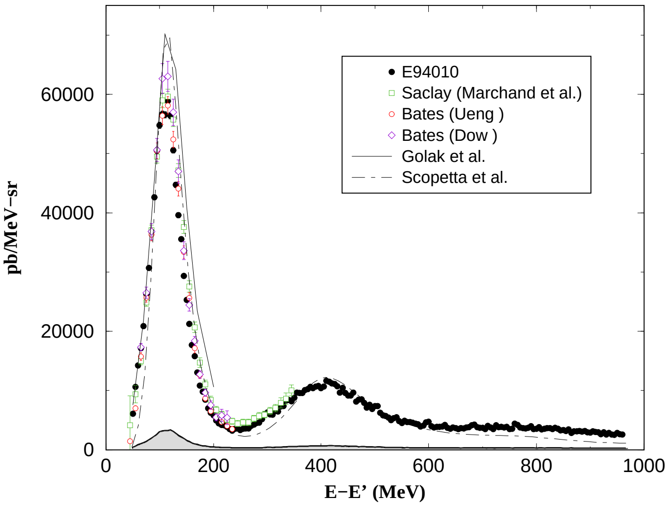

Figure 8.19: Born cross section. Incident energy: 1717 MeV.

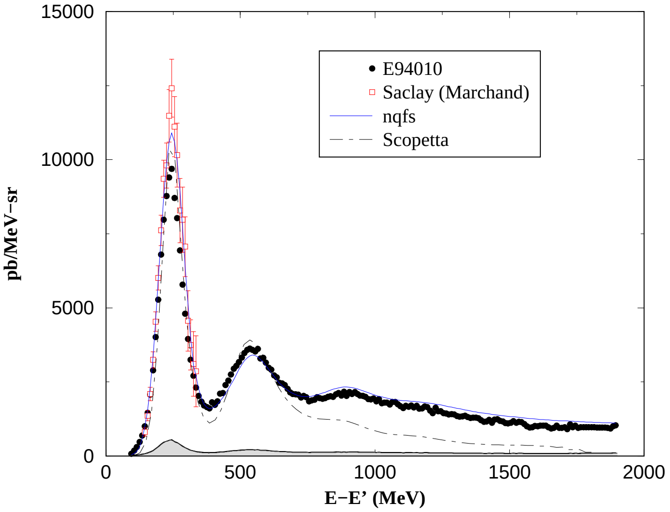

Figure 8.20: Born cross section. Incident energy: 2581 MeV

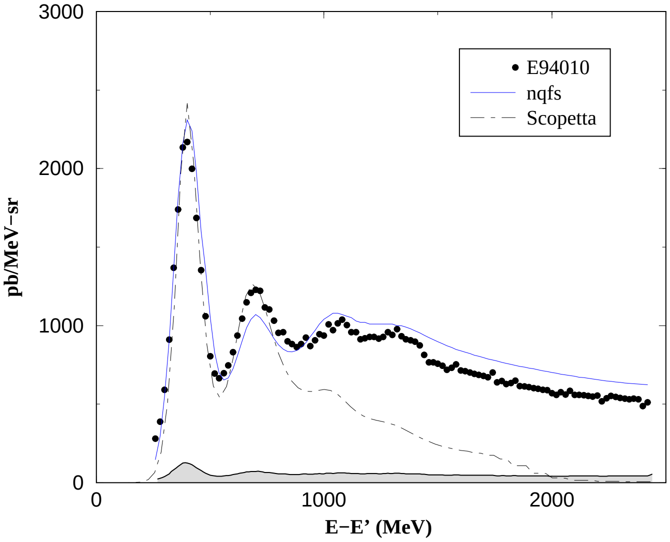

Figure 8.21: Born cross section. Incident energy: 3381 MeV

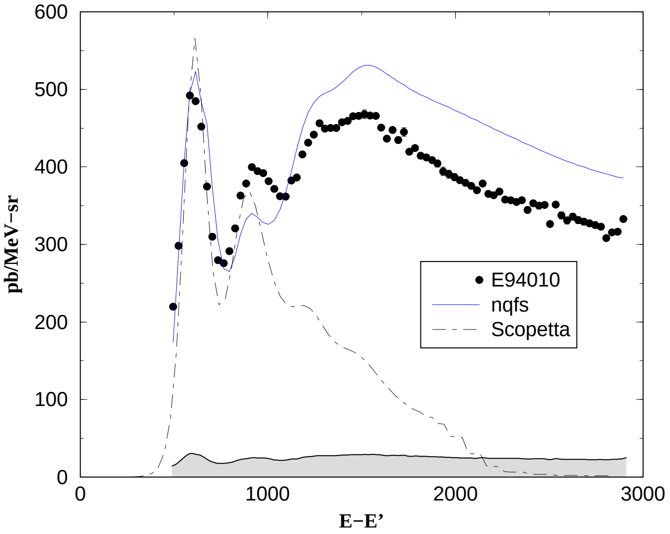

Figure 8.22: Born cross section. Incident energy: 4238 MeV

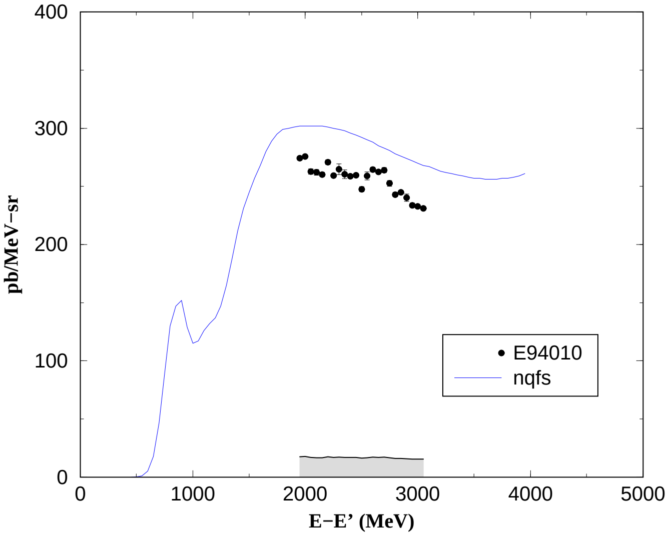

Figure 8.23: Born cross section. Incident energy: 5058 MeV

CHAPTER 9

^{3}HE POLARIZED QUANTITIES

In this chapter we present the final results for the polarized ^{3}He asymmetries, cross sections and structure functions along with the virtual photoabsorbtion cross sections σ'_{TT} and σ'_{LT}.

9.1 Asymmetries

The physics asymmetries in either parallel or perpendicular configuration are defined as:

$$A = \frac{1}{P_t P_b} \frac{N'_- - N'_+}{N'_- + N'_+} \tag{9.1}$$

where P_t and P_b are the target and beam polarizations respectively. $N'_\pm$ represent the number of counts in either helicity state. The prime indicates that they have been corrected for software deadtime, prescalers and normalized by the corresponding incident charge for each helicity state: $Q_\pm$. Notice that we do not correct the asymmetry for dilution. This is because the asymmetries are not analyzed directly but are always combined with the raw cross sections to form polarized cross section differences, and in this product the dilution factor cancels. For reference, we note that the dilution factor arising from the presence of the small amount of nitrogen quencher gas in the cell was estimated using the QFS model [161] as detailed in chapter 8. We found that typically $0.85 < f < 0.95$.

To measure the systematic effect of any false asymmetries, we measured the asymmetry arising from unpolarized ^{12}C and N$_2$, along with empty target runs. A. Deur [101] analyzed these runs and concluded that the false asymmetry was compatible with zero. For reference, we list a summary of the results in table 9.1.

The systematic uncertainty on the asymmetries is dominated by the polarimetries. The polarimetry uncertainty is 4% (relative) for both target and beam respectively, which are added in quadrature. The physics

Target	False asymmetry
Nitrogen	$6.8 \cdot 10^{-5} \pm 1.1 \cdot 10^{-4}$
Carbon	$2.1 \cdot 10^{-5} \pm 1.3 \cdot 10^{-4}$

Table 9.1: False asymmetry measured with nitrogen reference cell and with carbon foil target.

asymmetries before radiative corrections are shown in fig. 9.1, with parallel configuration represented by filled circles and perpendicular configuration represented with filled squares. Large negative elastic radiative tails are observed at low ν for the first and second incident energies. This background must of course be subtracted from the spectra before we can extract the polarized structure functions. The perpendicular asymmetry in the quasielastic region (centered at approximately $\nu = Q^2/(2M_n)$) is typically larger than its parallel counterpart. Also we see a cross-over in both configurations as ν passes through the single pion production threshold. We note that in stark contrast to the unpolarized cross sections displayed in chapter 8, the asymmetries are only weakly Q^2-dependent. This is particularly true in the region of the Δ resonance, where the parallel asymmetry is about -2.0% for all incident energies*, corresponding to a Q^2 range of approximately 0.05 to 1.0 GeV^2. The perpendicular asymmetry is largely a mirror image of the parallel asymmetry in the Δ region and we will comment further on this intriguing result in section 9.4. After the Δ resonance, the asymmetries are small, but as the energy loss ν increases and we approach the onset of deep inelastic scattering, the parallel asymmetry grows larger while the perpendicular asymmetry is small and consistent with zero. The interpretation of this behaviour will become clear when we examine the polarized structure functions in section 9.4.

9.2 Polarized Cross Sections

The raw cross section differences are defined by:

$$\Delta\sigma_{raw} = 2A\sigma_{raw} \tag{9.2}$$

where A represents the asymmetry in equation 9.1 and σ_{raw} is defined in equation 8.1. The systematic uncertainties are added in quadrature.

---

*Note that the 5058 MeV incident energy data is well above the resonance region.

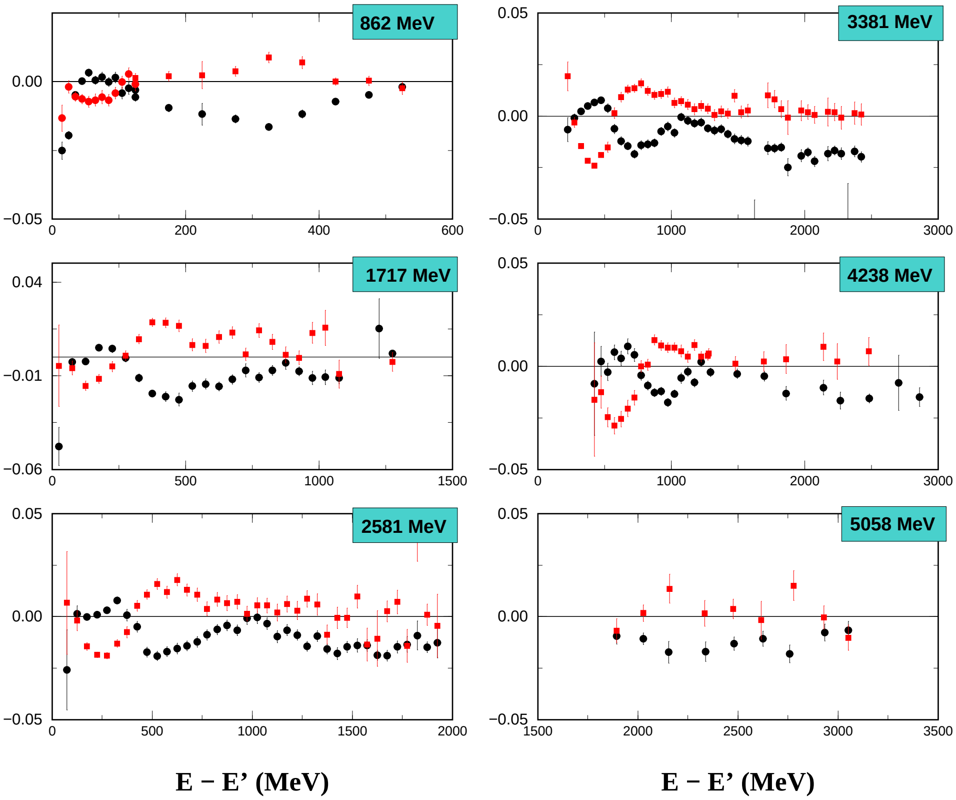

Figure 9.1: E94-010 asymmetries for six incident energies at 15.5°. Circles: $A_{||}$, squares: $A_{\perp}$. Error bars represent statistical uncertainty only. Note: these spectra represent results prior to radiative corrections and are not corrected for the dilution factor.

The polarized elastic radiative tail must be subtracted and radiative corrections applied (see appendix C) to obtain $\Delta\sigma$:

$$\Delta\sigma = \Delta\sigma_{raw} - \Delta\sigma_{tail} + \Delta\sigma_{RC} \tag{9.3}$$

We assume 20% uncertainty on the elastic tail subtraction[†]. The radiative corrections uncertainty was estimated by considering a wide variety of initial starting points for the POLRAD iterative procedure. Less than 20% variation [137] in the correction was found, which is taken as the uncertainty. For $E_0 = 862$ MeV, we had no data at lower incident energy and were forced to use several models as the starting point of the unfolding. Less than 40% variation was found, which was used as the uncertainty [137] for this spectra. The final systematic is obtained by summing the above contributions in quadrature.

In figures 9.2 to 9.6, we display the polarized cross section differences of equation 9.3. Solid symbols represent the parallel configuration, while the perpendicular settings are represented with open symbols. Both statistical and full uncertainties are displayed on the points. The data is compared to the PWIA calculation of ref. [170] and the full Faddeev calculation of ref. [175], which were described in detail in section 8.5.3. As in the unpolarized case, the full calculation reproduces our data extremely well for our lowest incident energy, where in the quasielastic region the momentum transfer is approximately 0.04 GeV^2. The cross-over at around $W = 930$ MeV is tracked perfectly in the parallel configuration, while the agreement is slightly worse for the perpendicular data. At higher ν, both configurations are replicated well by the full curve. The PWIA calculation reproduces the general features of the data (the cross-over for example) but differs in absolute magnitude by several sigma. In fact, the peak structure we see in the data seems to be damped out too strongly in the PWIA calculation. In the $\Delta(1232)$ region the model reproduces the resonance structure, but shows a clear difference in Δ separation of about 20 MeV from the data. In fig. 9.3, $Q^2 \approx 0.19$ at the quasielastic peak, and we are reaching the limits of applicability of the full calculation, while approaching a momentum transfer where the PWIA approach is expected to do well. The most important contribution missing from the PWIA curve is expected to be the FSI, and we can clearly see their importance at low ν compared to the full calculation. On the low energy side of the quasielastic peak the PWIA curve performs worse

---

[†] Reference [101] estimates an uncertainty of 10% due mostly to the elastic form factors. To this we add the variation observed when shifting the elastic tail spectra by ±1 MeV with respect to its nominal position to obtain 20%.

than on the high energy side, which is at higher Q^2. There is a considerable broadening of the peak structure in the perpendicular setting compared to the data. Nevertheless, the general features are reproduced and the zero crossing tracked exactly. The PWIA calculation overestimates the parallel data considerably at low ν, but otherwise is in rough agreement with the full calculation. In the resonance region, the MAID model again does a fair job with a noticeable offset of about 20 MeV from the data. At higher incident energies, relativistic effects increase in significance and the full calculation is not valid. We show only the PWIA calculation, which reproduces the general features but displays a surprising lack of agreement with the polarized data, considering the results displayed for the unpolarized cross sections in figs 8.14 to 8.16.

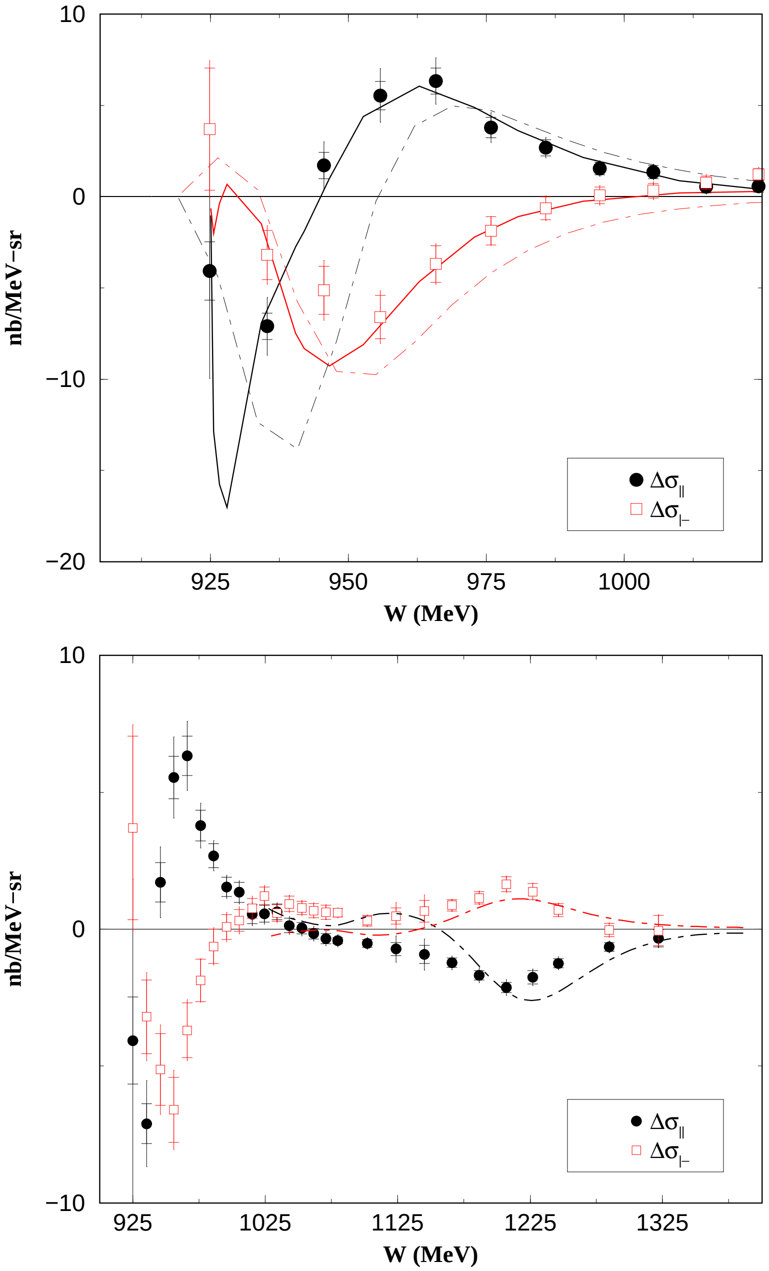

Figure 9.2: $E_0 = 862$ MeV. **Top**: Polarized cross section difference for parallel and perpendicular configuration in the Q.E. region. Inner (outer) error bars represent statistical (total) uncertainty. Dot-dashed curve: PWIA [170]. Solid curve: Full calculation [175]. **Bottom**: Same as top panel, but including resonance region.

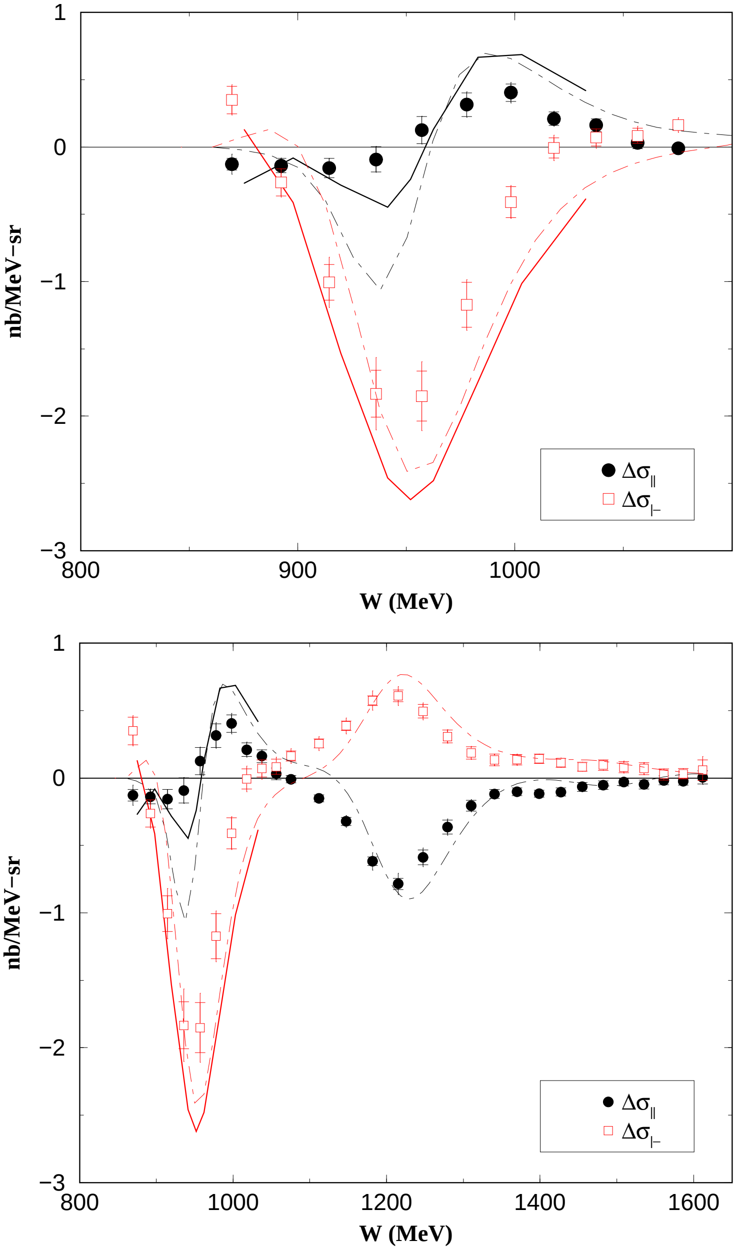

Figure 9.3: $E_0 = 1717$ MeV. **Top**: Polarized cross section difference for parallel and perpendicular configuration in the Q.E. region. Inner (outer) error bars represent statistical (total) uncertainty. Dot-dashed curve: PWIA [170]. Solid curve: Full calculation [175]. **Bottom**: Same as top panel, but including resonance region.

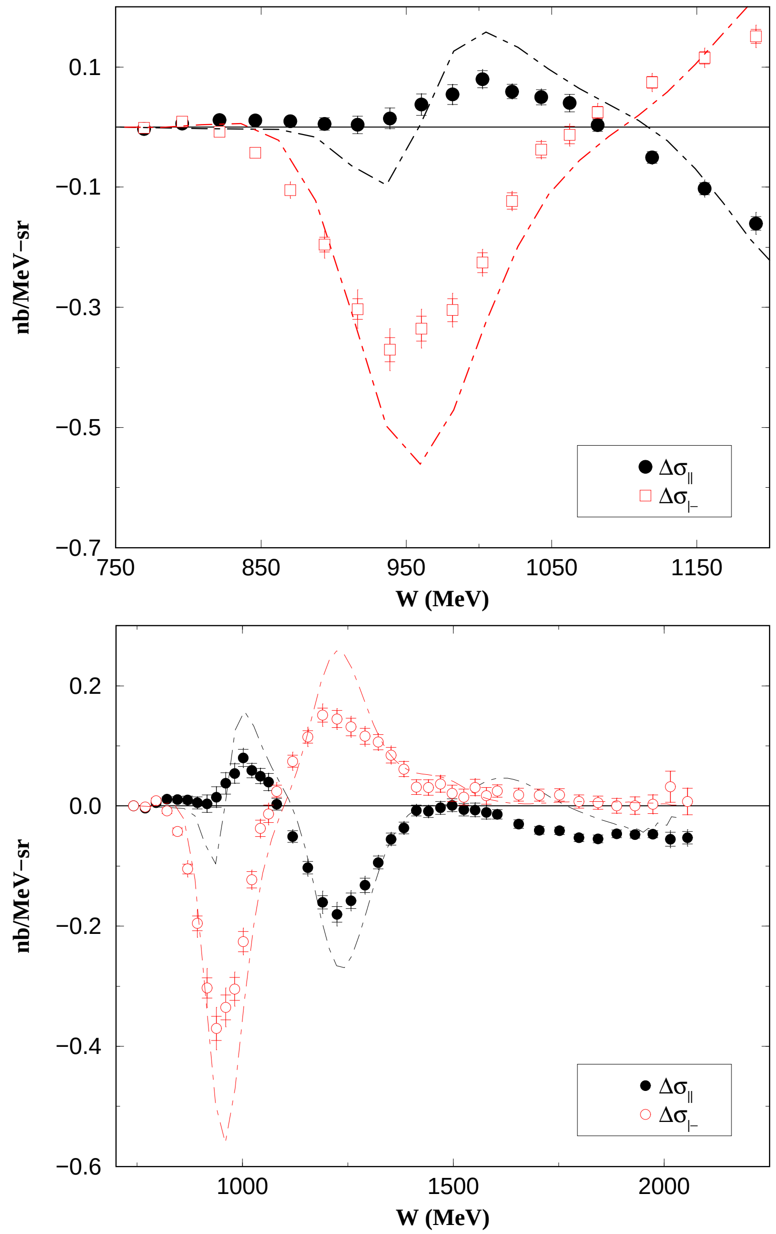

Figure 9.4: $E_0 = 2581$ MeV. **Top**: Polarized cross section difference for parallel and perpendicular configuration in the Q.E. region. Inner (outer) error bars represent statistical (total) uncertainty. Dot-dashed curve: PWIA [170]. **Bottom**: Same as top panel, but including resonance region.

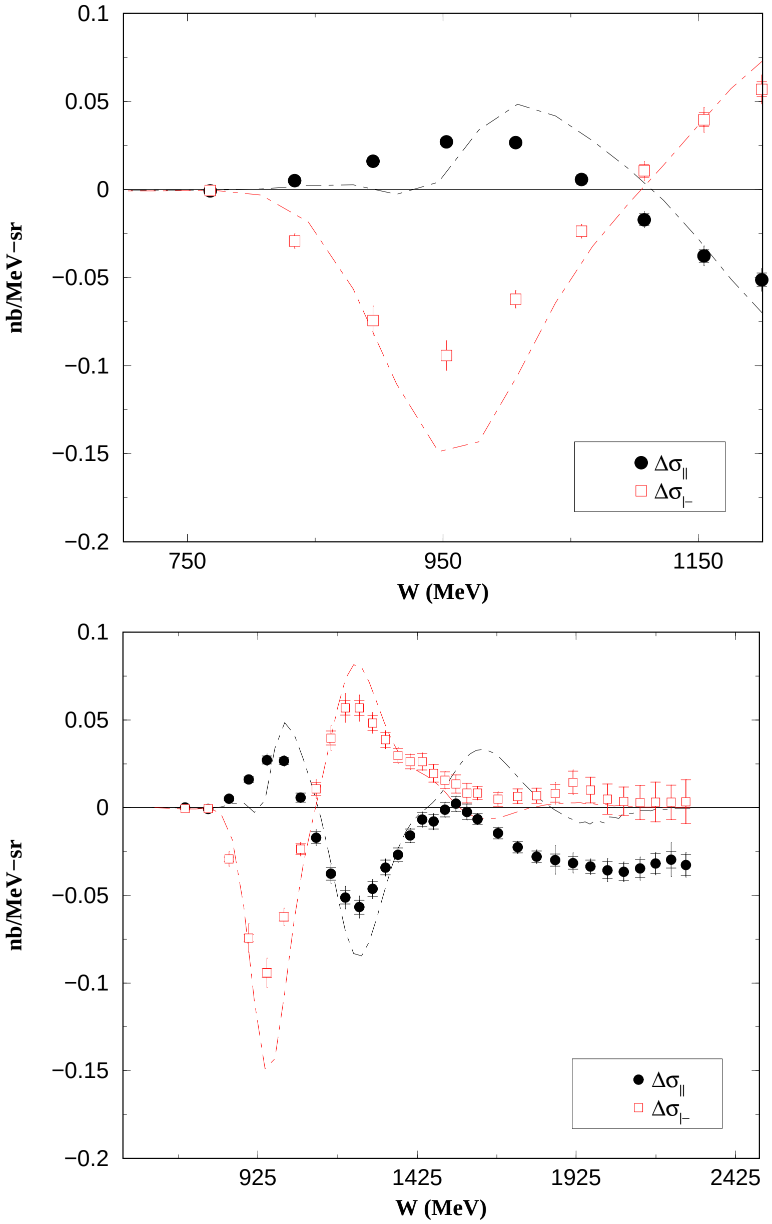

Figure 9.5: $E_0 = 3382$ MeV. **Top**: Polarized cross section difference for parallel and perpendicular configuration in the Q.E. region. Inner (outer) error bars represent statistical (total) uncertainty. Dot-dashed curve: PWIA [170]. **Bottom**: Same as top panel, but including resonance region.

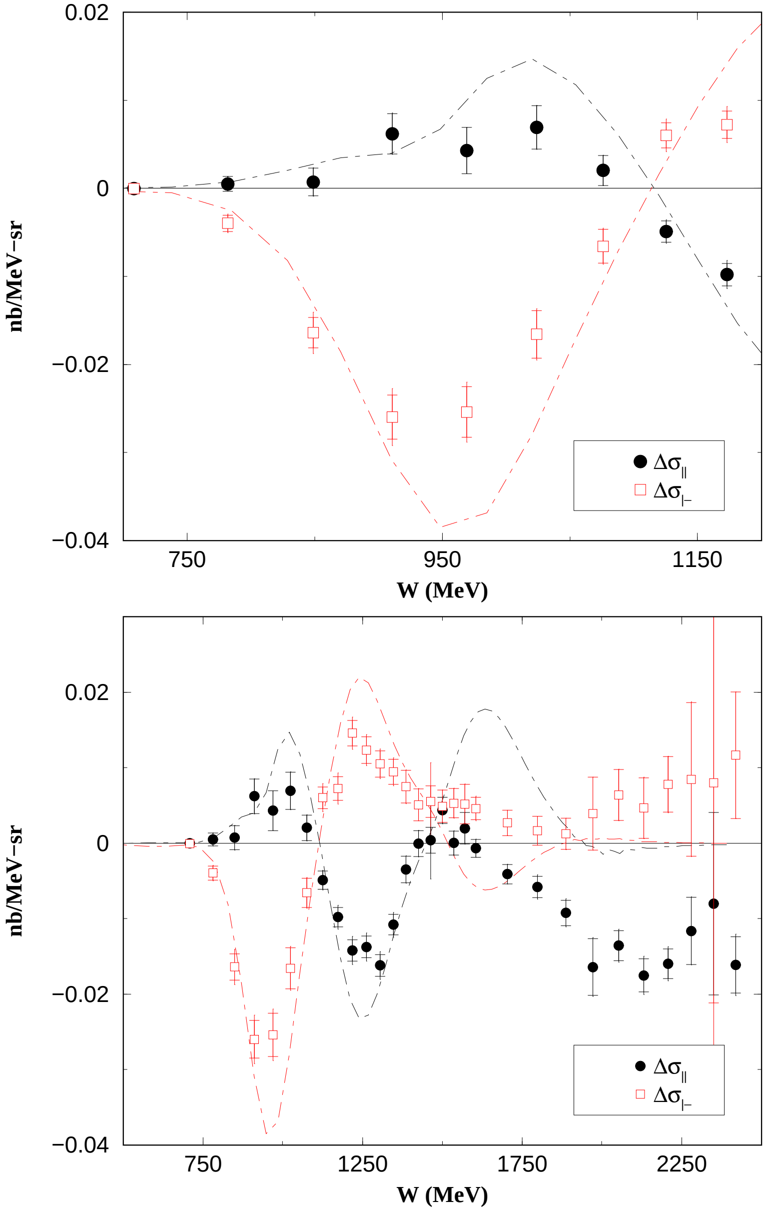

Figure 9.6: $E_0 = 4239$ MeV. **Top**: Polarized cross section difference for parallel and perpendicular configuration in the Q.E. region. Inner (outer) error bars represent statistical (total) uncertainty. Dot-dashed curve: PWIA [170]. **Bottom**: Same as top panel, but including resonance region.

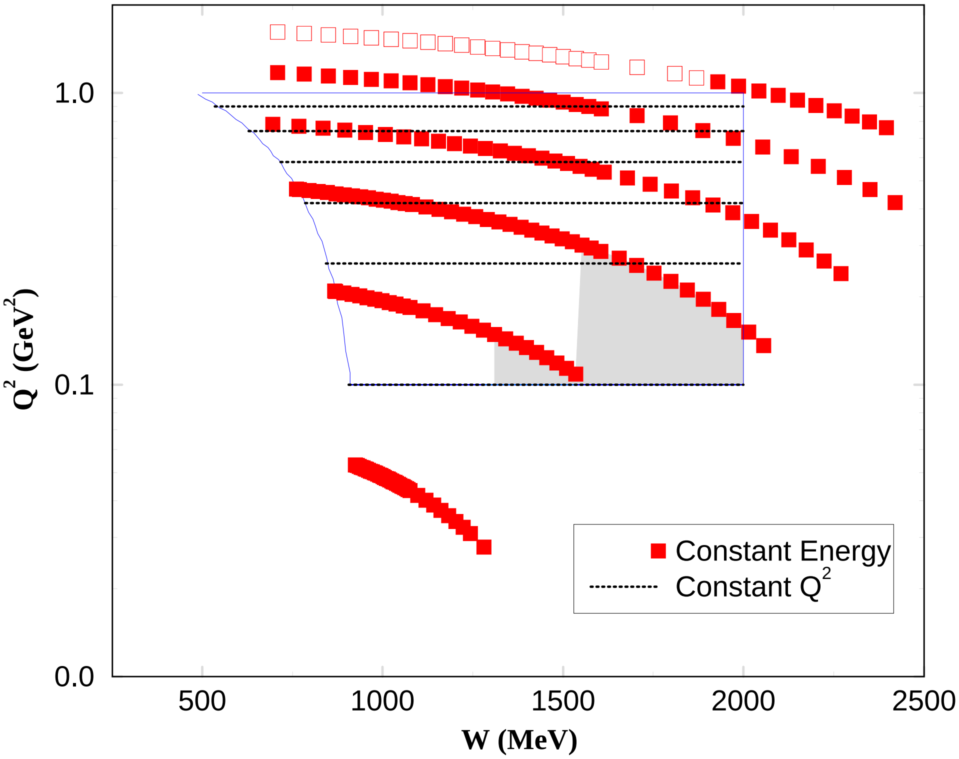

Figure 9.7: E94-010 kinematic region. The filled squares represent the central positions of the measured data, while the open squares indicate regions where we were required to use a model in order to perform the radiative corrections. The black dashed lines are the desired contours of constant Q^2. The region of interest is bounded by the ^{3}He two-body breakup threshold on the left and the nominal start of DIS scattering ($W = 2$ GeV) on the right. The gray areas represent regions where extrapolation is necessary.

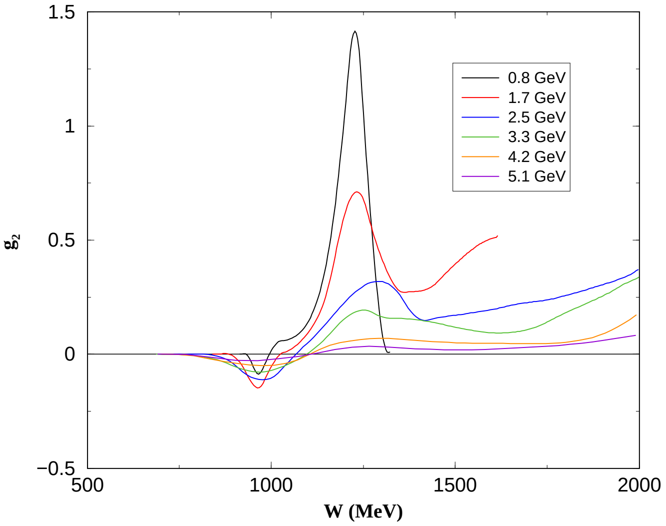

Figure 9.8: Fit of $g_2^{\mathtt{^3He}}$ as a function of W for six incident energies.

9.3 Interpolation and Extrapolation

Our data has been measured at constant energy and must be evolved to constant momentum transfer before we can perform the integrations called for in the various sum rules. Figure 9.7 illustrates that a two step interpolation is required with respect to W and Q^2. We initially consider $g_2^{\mathtt{^3He}}$, which scales well with respect to W. As a first step, the six data sets are interpolated to obtain equal binning in W as shown in fig. 9.8. This results in up to six data points at various Q^2, but constant W. This data set is then interpolated to the desired intermediate Q^2.

W also appears as a good interpolation variable for g_1 above the pion threshold (see fig. 9.9), but in the quasielastic region the spectrum does not scale well with invariant mass. Instead we create an artificial scaling variable Z_{g_1} in which the g_1 maxima, minima and zero crossings are aligned (see fig. 9.10). Again, this results in up to six data points at various Q^2. This data set is then interpolated to the desired Q^2. In this fashion, we obtain 6 sets of data interpolated to evenly spaced Q^2 values from 0.1 to 0.90 GeV. If the number of interpolated points at a particular Q^2 is greater than the initial number of measured points, the statistical error is adjusted to account for this artificial increase in data points.

The systematic error associated with the interpolation is estimated by

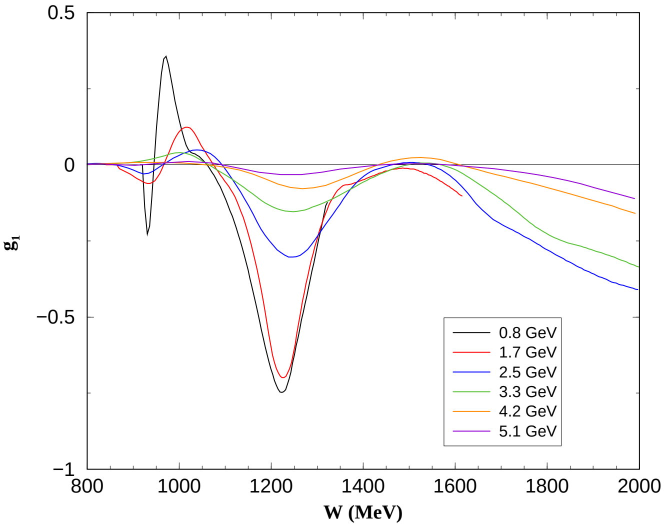

Figure 9.9: Fit of $g_1^{^3\mathrm{He}}$ as a function of W for six incident energies.

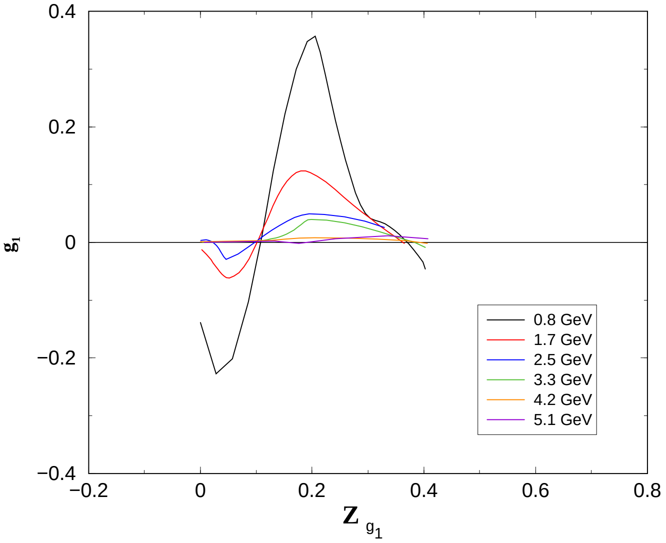

Figure 9.10: Fit of $g_1^{^3\mathrm{He}}$ as a function of Z_{g_1} in the quasielastic region ($W < 1080$ MeV).

varying the interpolation degree used. The W interpolation is performed using either a linear or quadratic interpolation and the Q^2 interpolation is performed using either a first, second or third degree interpolation. The standard deviation of these six possible methods is taken as the uncertainty. The variation arising from the different orders of Q^2 interpolation can be substantial, so in order to reduce this systematic we use the following technique, which is illustrated in fig. 9.11:

1. An exponential fit is subtracted from the data as a function of Q^2.
2. The interpolation is performed on the residual which has a much smaller Q^2 variation.
3. The exponential background is added back to the interpolated point in order to avoid any bias that may occur due to the choice of an exponential to describe the Q^2 behaviour.

In the regions where extrapolation is required, we compare our results to the MAID [40] model and take the full difference as an additional uncertainty.

9.4 Polarized Structure Functions

We now present the spin structure functions briefly mentioned in the previous section. g_1 and g_2 are formed from the polarized cross section differences according to the following relations:

$$g_1 = \frac{MQ^2}{4\alpha^2}\frac{y}{(1-y)(2-y)}\left[\Delta\sigma_{\|} + \tan\frac{\theta}{2}\Delta\sigma_{\perp}\right] \tag{9.4}$$

$$g_2 = \frac{MQ^2}{4\alpha^2}\frac{y^2}{2(1-y)(2-y)}\left[-\Delta\sigma_{\|} + \frac{1+(1-y)\cos\theta}{(1-y)\sin\theta}\Delta\sigma_{\perp}\right] \tag{9.5}$$

In figure 9.12, the ^{3}He structure functions are plotted as measured at constant energy. The error bars represent total uncertainties, and the curves represent a spline fit to the data. Notice that the ^{3}He mass is used in Bjorken variable, so $x = 1$ corresponds to ^{3}He elastic scattering. Interpolating to constant momentum transfer results in the spectra displayed in figure 9.13, which we now discuss. Proceeding from right to left along the x axis the first noticeable feature corresponds to the quasielastic reaction. After the quasielastic there is a dramatic cross-over for both structure functions at an x corresponding to the quasifree pion production threshold. At lower x still is the $\Delta(1232)$ resonance where we find that g_1 is approximately equal and

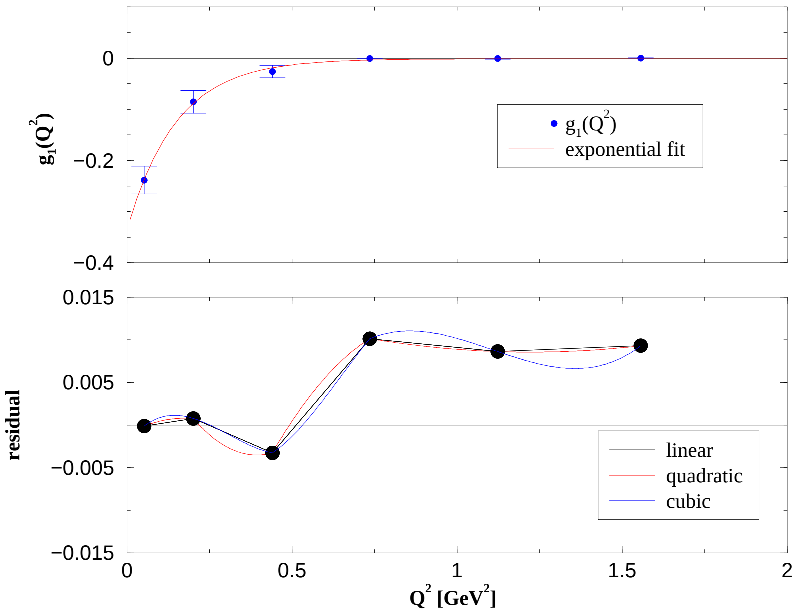

Figure 9.11: Top Panel: $g_1^{\mathtt{^3He}}$ as a function of Q^2. Solid curve is an exponential fit to the data. Bottom Panel: Various fits to the residual.

opposite to g_2 for most of the spectra. Our first clue in interpreting this behaviour, comes from the Wandzura–Wilczek relation:

$$g_2^{\mathtt{WW}}(x, Q^2) = -g_1(x, Q^2) + \int_x^1 \frac{dy}{y} g_1(y, Q^2)$$

which reveals that at leading twist, we can expect $g_2 \approx -g_1$ as long as the integral contribution is small. This is certainly the case as x approaches 1 in the Δ region. The Wandzura–Wilczek relation appears to describe the behaviour of the structure functions well in the $\Delta(1232)$ resonance, implying that higher twist corrections are relatively small. However, this simple interpretation is not quite complete[‡]. For a fuller understanding, we recall that the $\Delta(1232)$ is predominantly an M_{1+} transition [14] and that our unpolarized cross sections are described well in the $\Delta(1232)$ region with only a transverse contribution. This suggests that the transverse-longitudinal cross section σ'_{LT} should be highly suppressed. Equation 2.53 reveals that

---

[‡] We also note that as expected the leading twist description is clearly insufficient in the Q.E. region, where the nucleon form factors behave as $\mathcal{O}(\mathrm{Q}^{-10})$.

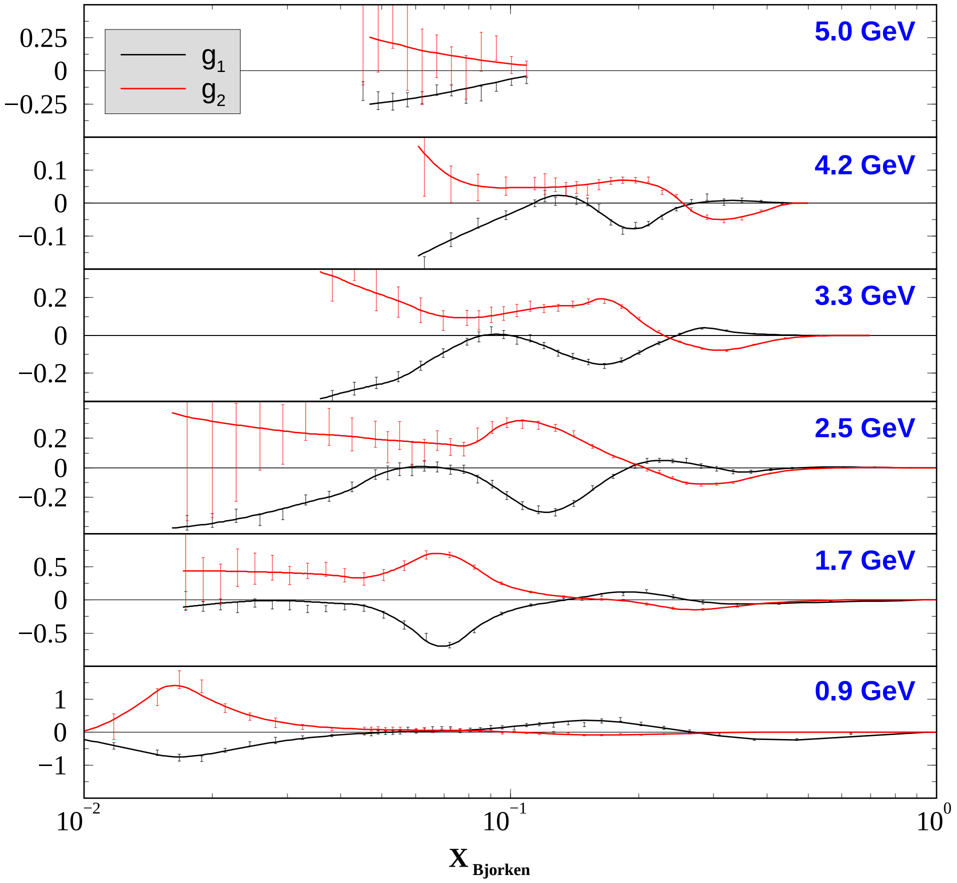

Figure 9.12: ^{3}He structure functions as measured at constant energy.

$\sigma'_{LT} \propto (g_1 + g_2)$, so the vanishing of σ'_{LT} would be signaled by an equal and opposite g_1 and g_2, which is approximately observed in the data.

At low x, beyond the resonances, the structure functions behave mostly as expected from the parton model and previous DIS experiments: g_1 tends to grow larger, while g_2 is consistent with zero (although with quite large uncertainty) in this region where transverse momenta are typically neglected. Relations 9.4 and 9.5 reveal that for our kinematic settings, g_1 is primarily sensitive to the parallel configuration data with only about 14% contribution from the perpendicular data. On the other hand, g_2 is clearly dominated by the perpendicular data with only a small (3 – 14%) contribution from the parallel data. This explains the behaviour of the asymmetries at large

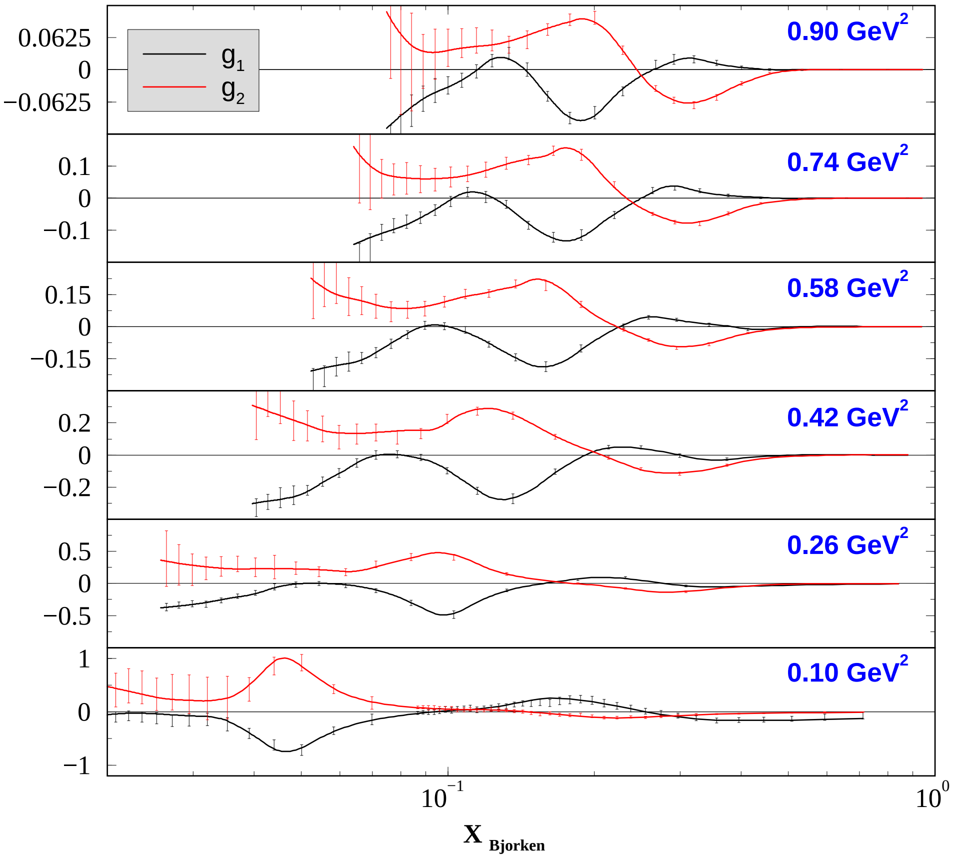

Figure 9.13: Polarized structure functions interpolated to constant Q^2.

energy loss noted in section 9.1.

Finally, figure 9.14 provides a different perspective of the same data by comparing it to the DIS results of earlier SLAC measurements [185, 186, 187, 111, 72]. We note that the resonance curves clearly average to the DIS scaling curve. This is similar to behaviour observed previously in the unpolarized structure functions [31, 32, 30], but represents the first experimental indication of Bloom-Gilman Duality in polarized ^{3}He structure functions.

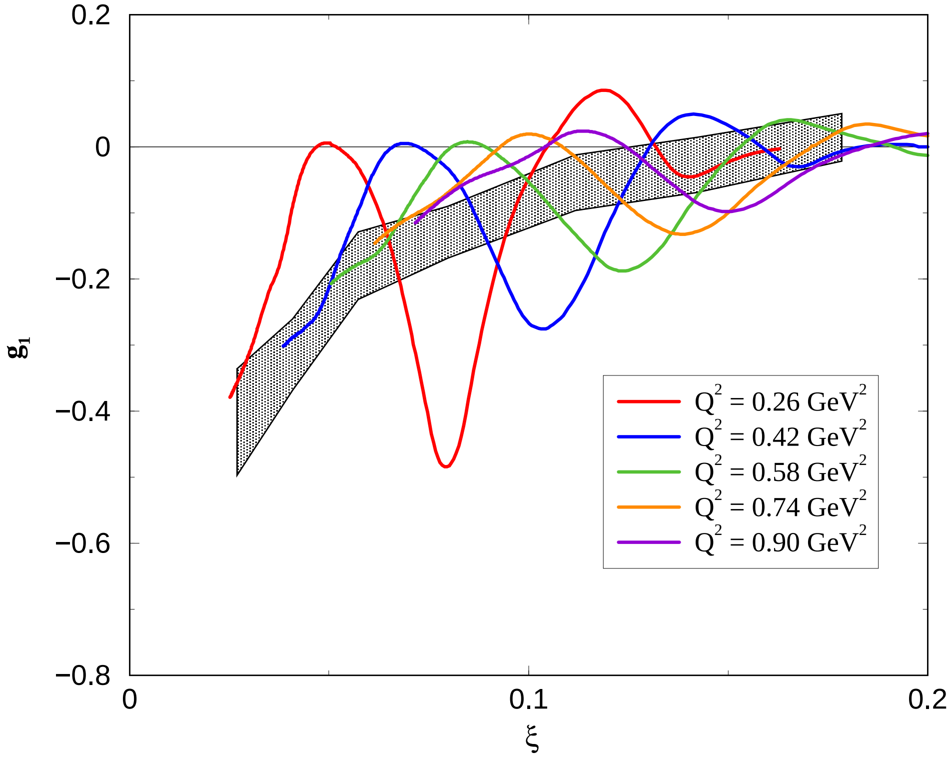

Figure 9.14: $g_1^{^3\mathrm{He}}$ as a function of Nachtman variable ξ. The solid lines are fits to the E94-010 data at various Q^2, while the gray band represents a DIS measurement of $g_1^{^3\mathrm{He}}$ performed at SLAC [185, 186, 187, 111, 72].

9.5 The Transverse-Transverse Cross Section σ'_{TT}

The spin structure can also be described in terms of the virtual photoabsorbtion cross sections of equations 2.54 and 2.54. Figure 9.15 displays the integrand of the GDH sum rule σ'_{TT}/ν as measured for six incident energies. The interpolation to constant Q^2 follows a similar technique to that described in section 9.3 for the g_1 structure function. The results are plotted in figure 9.16. The dominant feature is the large positive contribution of the quasielastic reaction. The $\Delta(1232)$ resonance provides a significant negative contribution at the highest momentum transfers, but is dwarfed in importance by the quasielastic as Q^2 is reduced. The other interesting feature of these plots is the spectra in the threshold region. Our data hints

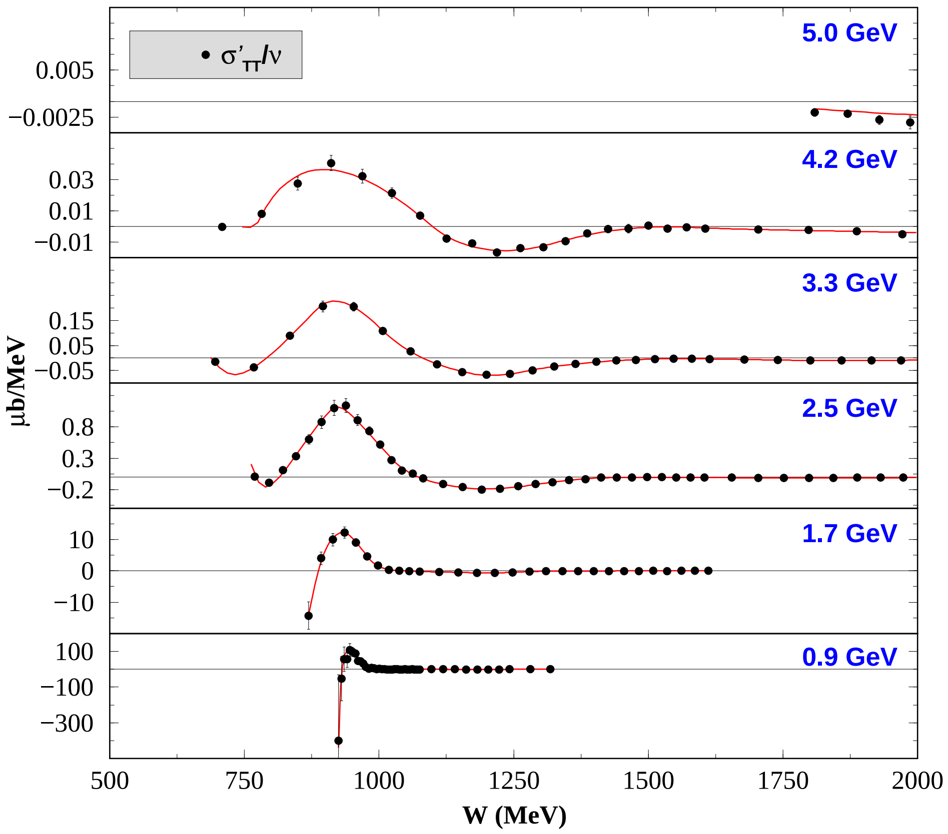

Figure 9.15: ^{3}He GDH integrand as measured at constant energy. Error bars represent total uncertainty. The curves are spline fits to the data.

at a significant negative contribution from the electrodisintegration channel which tends to grow larger as Q^2 is reduced. This phenomenon has been discussed by Arenhövel [63] as the expected mechanism for the satisfaction of the deuteron GDH sum rule prediction. It would be quite interesting to examine this region with higher statistical certainty to precisely determine its contribution to the ^{3}He GDH sum.

9.6 The Longitudinal–Transverse Cross Section σ'_{LT}

Although it was not a main focus of E94-010, our data provides a rare look at the longitudinal–transverse cross section σ'_{LT} (see figure 9.17). Drechsel

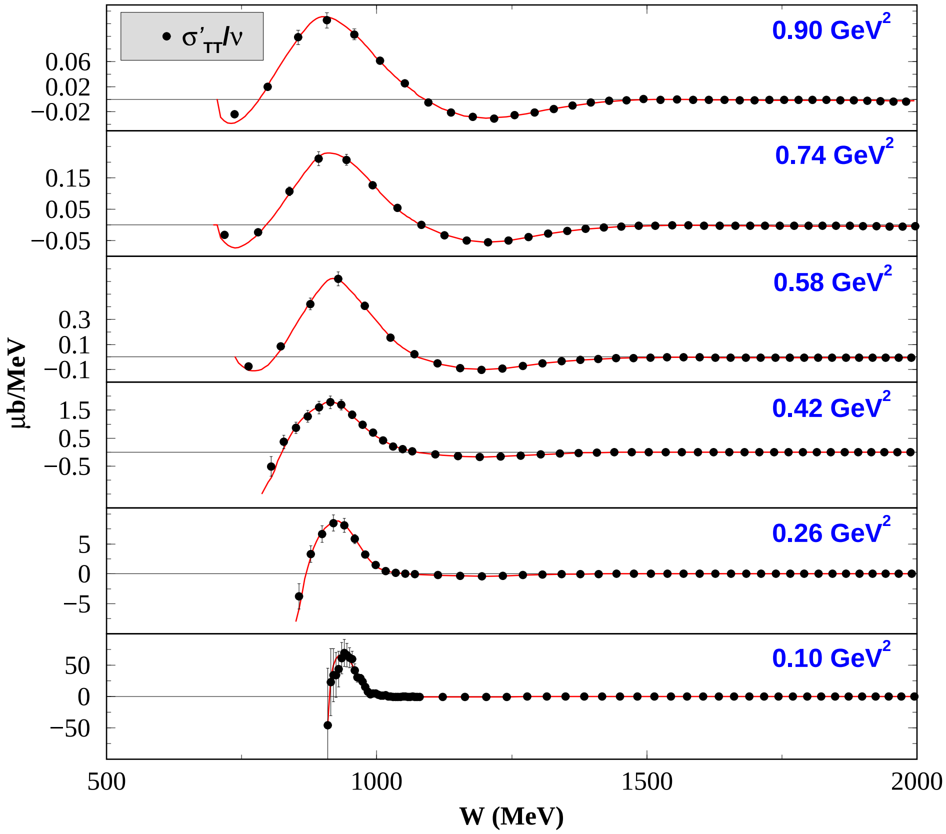

Figure 9.16: ^{3}He GDH integrand interpolated to constant Q^2. Error bars represent total uncertainty. The curves are spline fits to the data.

et al. [14] point out that σ'_{LT} enters the I_1 integral as $(\gamma\sigma'_{LT})$[§] and the I_2 integral as σ'_{LT}/γ. This is in clear contrast to the standard definitions of the GDH integral which are deliberately constructed to eliminate this interference term. Recalling the discussion of section 9.4, we note that σ'_{LT} is vanishingly small in the region of the $\Delta(1232)$, as expected due to the transverse nature of the resonance. The longitudinal-transverse interference term must of course vanish for real photon scattering, so it is with interest that we note that σ'_{LT} only grows in magnitude as the incident energy is decreased.

[§] $\gamma = Q/\nu$.

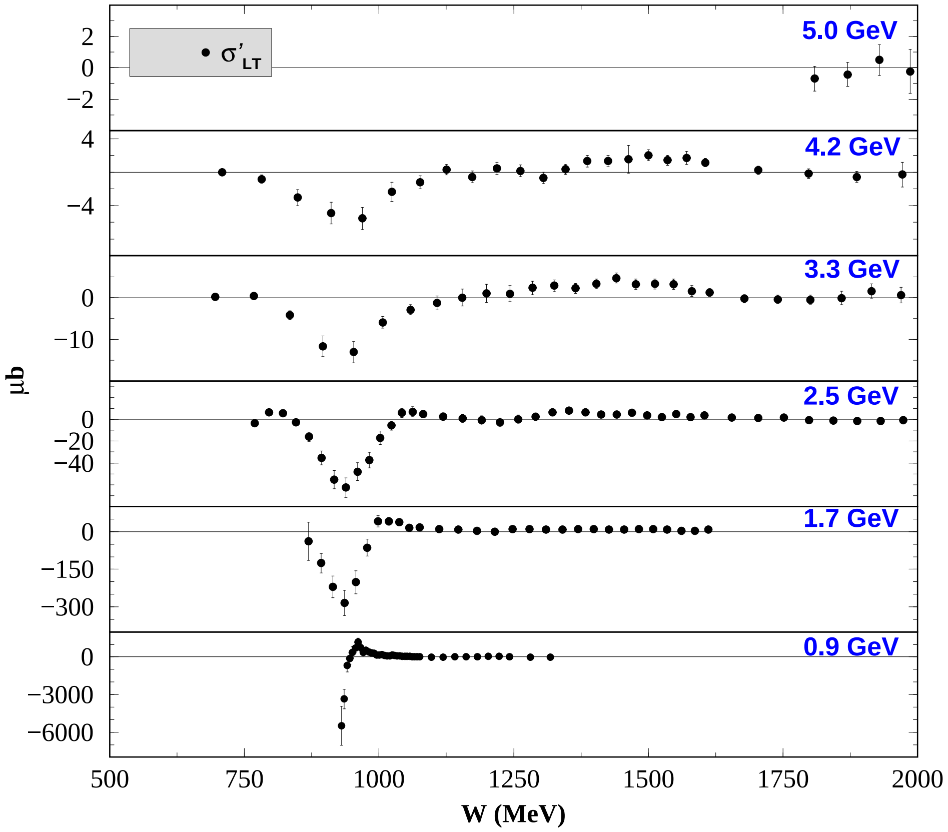

Figure 9.17: ^{3}He σ'_{LT} as measured at constant energy. Error bars represent total uncertainty.

CHAPTER 10

STRUCTURE FUNCTION MOMENTS

The polarized quantities at constant Q^2 are integrated* from the two-body breakup threshold to a maximum W of 2 GeV. From the data, we are able to evaluate the first moments of $g_1^{^3\mathrm{He}}$ and $g_2^{^3\mathrm{He}}$ along with the extended GDH sum. We begin our discussion by describing the characteristics that are common to all the following plots.

10.1 Plot Quantities

In figures 10.1 to 10.3 we plot quantities with the following labels:

- **E94010** : The E94-010 measured data integrated from two-body breakup through the quasielastic and resonance regions to a maximum W of 2 GeV.
- **E94010 + DIS** : These points include an estimate of the unmeasured region above the resonances. For the extended GDH sum we utilize a parameterization of σ'_{TT} [188] for $2 < W < \sqrt{1000}$ GeV. We also use this parametrization for Γ_1 by assuming that the factor $\gamma^2 g_2$ in equation 2.54 can be neglected in DIS. The DIS contributions to Γ_2 and d_2 are estimated using the Wandzura-Wilczek relation (specifically equation E.2).
- **MAID** : The phenomenological model MAID2003 [40]. We have combined the model predictions for proton and neutron using relation A.9, ignoring other nuclear effects. The model covers the kinematic range extending from the pion production threshold to $W = 2$ GeV. We have included an estimate of the contribution below the pion production threshold using the technique discussed in section E.2.1. Because

---

*The integration subroutine is based on the Simpson technique and has been cross checked against a simple trapezoidal method approach.

of the range covered, the MAID results should be compared to the points labeled **E94010**.

- **He-3 Elastic** : The ^{3}He elastic contribution to the integral at $x = 1$, evaluated from the ^{3}He elastic form factors of ref. [159], as described in appendix E.2.

The systematic uncertainty on the points labeled **E94010** is represented with a light grey band on the axis in figures 10.1 to 10.3. It is defined as

$$\Delta I^2 = I^2 \left[\delta_{xs}^2 + \delta_{P_b}^2 + \delta_{P_t}^2\right] + \Delta_{rc}^2 + \Delta_{int}^2 + \Delta_{ext}^2 + \Delta_{tail}^2 \tag{10.1}$$

where I represents one of the integrated quantities (Γ_1 for example) and:

- $\delta_{xs} = 5\%$: the raw unpolarized cross section systematic.
- $\delta_{P_b} = 4\%$: the beam polarimetry systematic.
- $\delta_{P_t} = 4\%$: the target polarimetry systematic.
- Δ_{rc} : the radiative corrections uncertainty discussed in section 9.2.
- Δ_{int} : the interpolation systematic discussed in section 9.3.
- Δ_{ext} : the extrapolation systematic discussed in section 9.3.
- Δ_{tail} : the uncertainty arising from the elastic tail subtraction.

Adding an estimate of the unmeasured DIS contribution to the integrals results in a further systematic uncertainty. For Γ_1 and the GDH integral we use the quoted errors of the DIS parametrization of ref. [188]. For Γ_2 and d_2 we assume a 20% uncertainty arising from the g_2^{WW} estimate of g_2.

The elastic contribution to the Γ_2 integral results in an additional 5% uncertainty from the elastic form factors. These uncertainties are shown as the dark grey band in figures 10.1 to 10.3. The total error would be these two bands added in quadrature.

10.2 The First Moment of g_1

At small Q^2, the inelastic part of Γ_1:

$$\overline{\Gamma}_1(Q^2) = \Gamma_1(Q^2) - \Gamma_1(Q^2)^{elastic} \tag{10.2}$$

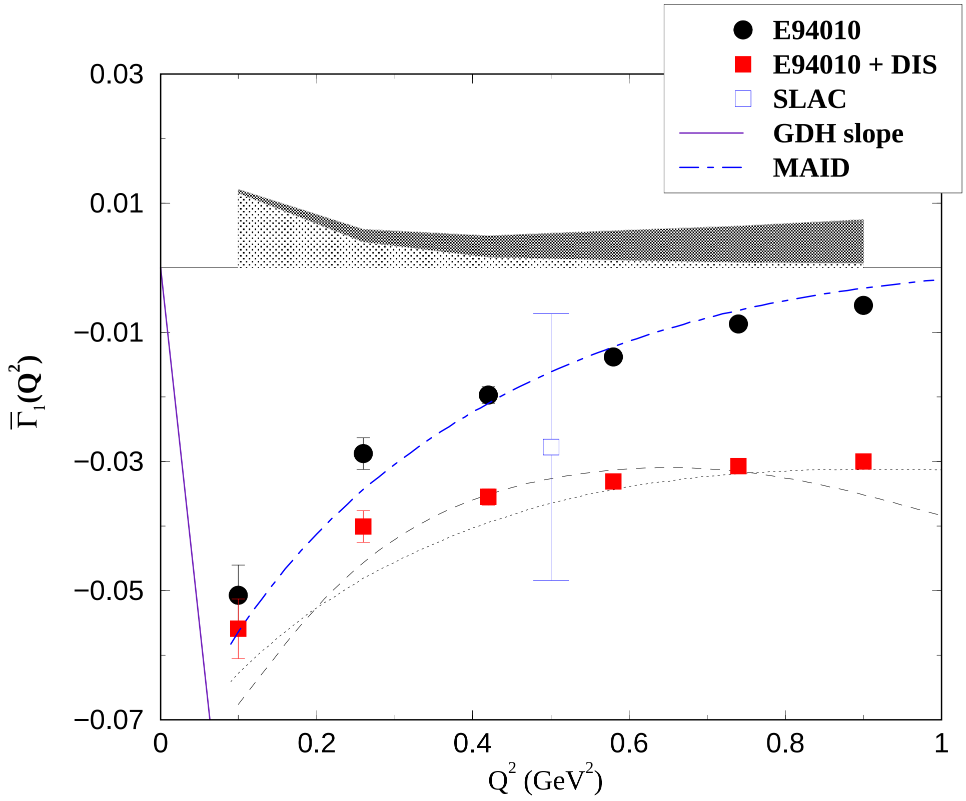

Figure 10.1: $\overline{\Gamma}_1$, the first moment of $g_1^{^3He}$. Solid circles: E94-010 ^{3}He data for $W_{2bb} < W < 2$ GeV. Solid squares: E94-010 ^{3}He data plus DIS parameterization from ref. [188] integrated to $W = \sqrt{1000}$ GeV. Open squares : SLAC [185, 186, 187, 111, 72]. Dot-Dashed line : MAID2003 model [40] of resonance region. Dotted line : Burkert and Ioffe [44, 45] model for full integral. Dashed line : Soffer and Teryaev [46] model for full integral. Solid line : GDH sum rule prediction for the slope at $Q^2 = 0$.

Q^2	E94010	Stat.	Syst.	E94010 + DIS	Total Syst.
0.10	-0.0507	0.00462	0.0115	-0.0559	0.0122
0.26	-0.0288	0.00245	0.0040	-0.0401	0.0060
0.42	-0.0197	0.00128	0.0016	-0.0355	0.0050
0.58	-0.0138	0.00101	0.0018	-0.0331	0.0057
0.74	-0.0087	0.000688	0.0008	-0.0307	0.0065
0.90	-0.0058	0.000682	0.0006	-0.0300	0.0075

Table 10.1: $\overline{\Gamma}_1(Q^2)$. See text for explanation of listed quantities.

is related to the anomolous magnetic moment of ^{3}He via

$$\overline{\Gamma}_1(Q^2) = \int_0^{x_0} g_1(x, Q^2)\, dx = -\frac{Q^2}{8M^2}\kappa^2 + \mathcal{O}\left(\frac{Q^4}{M^4}\right) \tag{10.3}$$

where x_0 represents the two-body breakup threshold. The leading term follows from relation 4.9 and reveals that $\overline{\Gamma}_1(Q^2)$ must vanish at $Q^2 = 0$. It also provides a prediction for the slope of $\overline{\Gamma}_1(Q^2)$ in the immediate vicinity of $Q^2 = 0$. The higher order terms have been evaluated for a nucleon target by Ji *et al.* [66, 189] and Bernard *et al.* [190, 10]. Chiral calculations for the three-body system are considerably more difficult and will most likely not be available for several more years [191]. At large Q^2, $\Gamma_1(Q^2)$ is governed by the twist expansion of equation 3.15.

In figure 10.1 we present the measured values of $\overline{\Gamma}_1(Q^2)$ (solid circles) at six values of Q^2 from 0.10 GeV^2 to 0.90 GeV^2. Statistical uncertainties are shown on the data points, while the systematic error is represented by the grey band on the x-axis. Previous data from SLAC [185, 186, 187, 111, 72] (open squares) are compatible with our data but with considerably larger errors. The total integral (solid squares) includes an estimate of the contribution from the unmeasured DIS region [188] up to $W = \sqrt{1000}$ GeV. We note that the ^{3}He elastic contribution falls essentially to zero by Q$^2 \approx$ 0.4 GeV^2, so that $\overline{\Gamma}_1(Q^2)$ is approximately equal to $\Gamma_1(Q^2)$ above this point.

At $Q^2 = 0$ we have plotted the slope predicted by the GDH sum rule for ^{3}He. Our data is trending away from zero at low Q^2 and indicate that there must be a dramatic transition occurring below 0.10 GeV^2. We eagerly await the results of recently completed JLab experiment E97-110 [192], an extension of E94-010 to the range $0.01 < Q^2 < 0.5$ GeV^2. The phenomenological model MAID integrated to a maximum W of 2 GeV is shown with the dot-dashed line. The strength below the pion threshold has been added to the

Q^2	E94010	Stat.	Syst.	+ DIS	+ Elastic	Total Syst.
0.10	0.01233	0.002422	0.002846	0.006944	0.001453	0.00420
0.26	0.01142	0.001622	0.001255	0.002427	0.001928	0.00308
0.42	0.00923	0.001218	0.000842	0.000596	0.000561	0.00257
0.58	0.00765	0.000985	0.000740	0.000613	0.000613	0.00215
0.74	0.00433	0.000985	0.000521	-0.000690	-0.000690	0.00153
0.90	0.00189	0.000925	0.000863	-0.001710	-0.001720	0.00158

Table 10.2: $\Gamma_2(Q^2)$. See text for explanation of listed quantities.

MAID model using the method described in E.2.1. MAID agrees very well with our data at all Q^2 investigated. The model of Burkert and Ioffe [44, 45] is shown with the dotted line and reproduces the full integral within errors. The dashed line representing the model of Soffer and Teryaev [46] tracks the data but exhibits oscillations at large Q^2 not observed in the measured integral.

Finally, we note that at large momentum transfer, $\Gamma_1(Q^2)$ appears to be nearly independent of Q^2. This is consistent with an OPE interpretation in which the higher twist effects become negligible at large Q^2 and the Q^2 evolution is driven by logarithmic pQCD effects alone. It is however somewhat surprising to observe this behaviour below 1.0 GeV^2 in a region where the higher twist effects are conventionally expected to be quite significant. This indication of small higher twist effects is consistent with the appearance of duality in the structure function g_1 as shown in figure 9.14 and discussed in section 3.3.4.

Our results combined with polarized tritium data would also provide a high precision test of the fundamental Bjorken sum rule which is free from the nuclear corrections presently needed to evaluate the nucleon contributions. In addition, it has been suggested that the upper limit of applicability for χPT calculations would be pushed to higher Q^2 by taking isospin differences as discussed in [84]. It would clearly be advantageous to investigate the triton structure functions in this kinematic range in the future.

We also point out that our $\Gamma_1(Q^2)$ data is a direct test of the sum rule of equation 4.19, and should provide a valuable constraint on future calculations of the S_1 Compton amplitude.

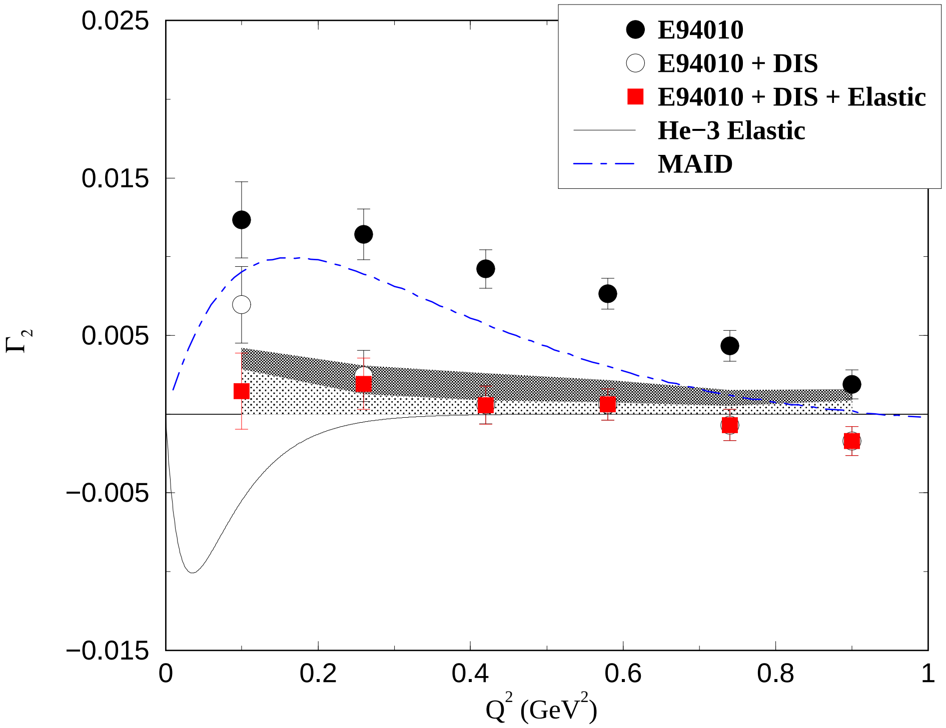

Figure 10.2: Γ_2, the first moment of g_2^{3He}. Solid circles: E94-010 ^{3}He data for $W < 2$ GeV. Open circles: E94-010 ^{3}He data plus DIS estimate from Wandzura-Wilczeck relation. Solid squares: E94-010 ^{3}He data plus DIS estimate from Wandzura-Wilczeck relation plus elastic contribution at $x = 1$. Dot dashed line: MAID2003 model [40]. Solid black line : ^{3}He elastic contribution [159].

10.3 The First Moment of g_2

Experimental measurements of g_2 are scarce and only recently has the B.C. sum rule been evaluated for the first time [193]. The SLAC E155x collaboration measured $\Gamma_2(Q^2)$ at $Q^2 = 5$ GeV^2 for the proton and deuteron for an x range of $0.02 \leq x \leq 0.8$. Combining the E155x, E155 and E143 data and including an estimation of the unmeasured low x region using the g_2^{WW} relation results in:

$$\Gamma_2^p(5\mathrm{GeV}^2) = -0.022 \pm 0.008 \text{ (SLAC)} \tag{10.4}$$

$$\Gamma_2^D(5\mathrm{GeV}^2) = -0.002 \pm 0.011 \text{ (SLAC)} \tag{10.5}$$

This is a surprising result as one target is consistent with the B.C. sum rule while the other violates it by almost three standard deviations. It is also difficult to interpret a finite non-zero result, in light of the most likely scenarios considered for violation discussed in section 4.3.4. Confirmation of these results would clearly call for a re-evaluation of some of the very basic principles that go into the B.C. sum rule derivation.

Combining the above results incoherently, we obtain the following value for ^{3}He.

$$\Gamma_2^{^3\mathrm{He}}(5 \text{ GeV}^2) = 0.0142 \pm 0.0215 \text{ (SLAC)} \tag{10.6}$$

In figure 10.2 we plot the E94-010 measured values of $\Gamma_2(Q^2)$ as the solid circles at six values of Q^2 below 1 GeV^2. Statistical uncertainties are shown on the data points, while the systematic error is represented by the grey band on the x-axis. The open circles include an estimate of the unmeasured DIS region based on the leading twist Wandzura-Wilczeck relation. The total integral (solid squares) also includes the elastic contribution at $x = 1$ which is evaluated from the Amroun *al.* [159] ^{3}He elastic form factors. This must be considered when comparing to the Burkhart–Cottingham sum rule and is represented by the solid negative curve. As with $\Gamma_1(Q^2)$ the elastic contribution is negligible above our second data point. The phenomenological model MAID integrated to a maximum W of 2 GeV is shown with the dot-dashed line. We have included an estimate of the contribution below the pion production threshold using the technique discussed in section E.2.1. MAID follows the trend of our measured points but differs in absolute value especially at larger Q^2.

All of our data points are consistent with the Burkhart–Cottingham sum rule. Data from this same experiment has also been used to test the Burkhart–Cottingham sum rule for the neutron (See appendix A.2 and

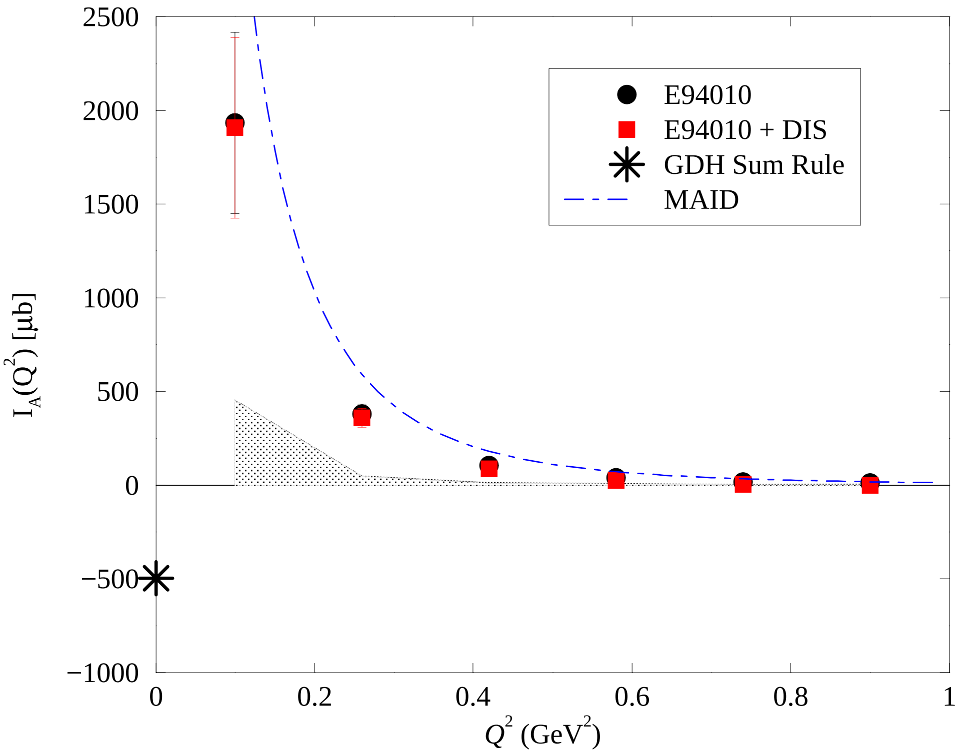

Figure 10.3: The extended GDH sum for ^{3}He. Solid circles: E94-010 ^{3}He data for $W < 2$ GeV. Solid squares: E94-010 ^{3}He data plus DIS parametrization from ref. [188]. Dot-dashed blue line: MAID2003 model [40]. Star : The GDH sum rule prediction for ^{3}He at $Q^2 = 0$.

reference [194]) It is interesting to notice that in the case of the neutron the sum rule is satisfied primarily due to the cancellation of the resonance and elastic contributions, while for ^{3}He the elastic contribution is mostly unimportant. Instead, we see a balance struck between the large positive contribution from the integral above the pion threshold and a large negative contribution from the quasielastic region.

10.4 Extended GDH sum

Figure 10.3 displays our measured values (solid circles) of the extended GDH sum $I_A(Q^2)$ as defined in equation 4.8. Including the DIS contribution

Q^2	E94010	Stat.	Syst.	E94010 + DIS	Total Syst.
0.10	1933.70	482.66	452.60	1908.20	456.02
0.26	380.32	51.41	47.32	359.35	50.84
0.42	106.11	9.87	10.61	88.18	14.16
0.58	40.56	2.23	6.50	24.89	10.03
0.74	17.81	0.78	2.11	3.91	5.58
0.90	11.57	0.54	2.97	-0.91	6.38

Table 10.3: $I_A(Q^2)$. See text for explanation of listed quantities.

of reference [188] (solid squares) has only a minor effect on the integral due to the $1/\nu$-weighting of the integral and the prominence of the quasielastic contribution. The negative sum rule prediction at $Q^2 = 0$ stands in stark contrast to the large positive value of our data at $Q^2 = 0.10$. On the other hand, the phenomenological model MAID tracks the behaviour of the data well.

CHAPTER 11

CONCLUSION AND DISCUSSION

> We are at the very beginning of time for the human race. It is not unreasonable that we grapple with problems. But there are tens of thousands of years in the future. Our responsibility is to do what we can, learn what we can, improve the solutions, and pass them on.
>
> **Richard Feynman**

E94–010 performed the first measurement of the ^{3}He (neutron) spin structure functions in the intermediate Q^2 range 0.1 to 0.9 GeV^2, which bridges the gap from the confinement regime at low momentum transfer, to the large Q^2 region where the constituents behave with asymptotic freedom. Our data is uniquely positioned to test the limits of applicability of both χPT and the twist expansion, while providing a high precision benchmark in the region where neither of these two approaches are expected to work. As lattice gauge theory techniques become more sophisticated, our data will provide strict constraints with which to test the new calculations.

This experiment analyzed a remarkable amount of data which has been used to investigate many of the neutron's spin–dependent properties, including: 1) the extended GDH sum [195], 2) the spin structure function moments [194], 3) color polarizabilities and higher twist effects [24], 4) the generalized spin polarizabilities [196], 5) and the Bjorken sum rule for the proton–neutron difference [74], which is a cooperative effort with the JLab Hall B CLAS collaboration [197, 82]. The work covered in this thesis investigates the spin structure function moments of ^{3}He, and in principle could be extended to extract all of the above quantities in the nuclear context.

We now review the major results presented in the previous chapters. $\Gamma_2^{^3\mathrm{He}}(Q^2)$ satisfies the Burkhardt–Cottingham sum rule due to a subtle cancellation of inelastic and quasielastic contributions. The ^{3}He elastic portion of the integral is found to be mostly insignificant, in contrast to ref. [194]

where the interplay of neutron elastic and inelastic contributions directly leads to the vanishing of the integral. Our result would benefit by a more sophisticated treatment of the DIS contribution to the integral, either by model prediction or direct measurement of $g_2(x)$. In addition, the E94-010 tests of the ^{3}He and neutron B.C. sum rule improve significantly on the precision of previous world data.

We observe that the g_1 structure function exhibits indications of Bloom–Gilman duality. This behaviour, along with the Q^2–evolution of the first moment, qualitatively points to relatively small higher twist effects in the kinematic region of E94-010 contrary to expectation. An analysis following the approach of ref. [24] but in the nuclear context, would be beneficial to quantitatively determine the size of the higher twist contributions to $\Gamma_1^{^3\mathrm{He}}(Q^2)$, and to examine how the color polarizabilities are modified in a nuclear medium. Measurement of the g_1 structure function of tritium in the same kinematic range as E94-010 would allow a high precision test of the $A = 3$ Bjorken sum rule, free from nuclear effects.

The ^{3}He GDH integral is dominated by a positive quasielastic contribution which largely outweighs the negative contribution of the resonances. It is interesting to note that the quasielastic spectra consistently grows in significance as Q^2 decreases. We expect this trend to reverse at some finite value of Q^2 due to the vanishing of this reaction channel for real photon scattering. The ^{3}He GDH sum points to some interesting behaviour below 0.1 GeV^2. The sum trends to large positive values as Q^2 is decreased, while the sum rule prediction at the real photon point calls for a negative result. If we assume the continuity of σ'_{TT} as $Q^2 \to 0$, as in the nucleonic case [198], our results indicate the necessity of a dramatic turnover in $I_A(Q^2)$. The range $0.01 < Q^2 < 0.5$ GeV^2 has been investigated in an extension [192] of E94-010. Analysis is underway and we eagerly await the first results. Our σ'_{TT} data shows some indication of a large negative contribution from the threshold region as Q^2 approaches zero. This region would be well served by a high precision investigation to reduce the related uncertainty and precisely determine the electrodisintegration contribution to the sum.

We have tested the limits of a full three-body Faddeev calculation against both polarized and unpolarized cross section data. A corresponding PWIA calculation performs well at large momentum transfer for the unpolarized data but meets with varying degrees of success when compared to the E94-010 spin-dependent cross sections. The phenomenological model MAID provides quite good characterization of the structure function moments, despite the fact that we have virtually ignored nuclear corrections.

In conclusion, the E1xx collaborations [185, 186, 187, 111, 72] at SLAC, the EMC [199] and SMC [200] collaborations at CERN and the HERMES collaboration [201] at DESY have measured the spin structure of the nucleons in deep inelastic scattering, mostly above 1 GeV^2, while E94-010 and other JLab experiments have covered (or will soon cover) the momentum transfer range of $0.01 < Q^2 < 2$ GeV^2. This wealth of experimental data will approach a nearly complete determination of the spin structure functions in the near future. We expect that this will contribute to a better understanding of the dynamics of non–perturbative QCD and help to stimulate a full understanding of the confinement region.

APPENDIX A

NEUTRON RESULTS

E94-010 published results on both the extended GDH sum [195], and the spin-dependent structure function moments [194] of the neutron. We have performed an independent analysis of this data in order to check the previous results and to increase confidence in our own ^{3}He results presented in chapters 9 and 10. We first consider the technique used to extract the neutron from our experimental ^{3}He data, then we present the parallel analysis.

A.1 Neutron Extraction from ^{3}He

When ^{3}He is described in terms of a pure symmetric S state wave function the proton contribution to the spin-dependent properties vanishes due to the Pauli pairing of the two proton spins. In this sense, ^{3}He represents an ideal free neutron target. This simplistic picture is complicated by three main obstacles:

1. Any realistic ^{3}He wavefunction must contain admixtures of other contributing states, namely the S$'$ and D states.
2. The neutron is not free but subject to the binding within the nucleus.
3. The neutron is undergoing Fermi motion within the nucleus which significantly dampens the resonance peaks. This is also sometimes referred to as Doppler broadening.

We will now look at three possible methods [202, 83], in order of increasing complexity, to address the nuclear corrections to the measured ^{3}He structure functions with the goal of accessing the corresponding neutron quantities.

A.1.1 Nuclear Effects: Naive Approach

We define $\mathrm{P}^{\pm}_{p(n)}$ as the probability to have a proton or neutron with spin aligned with the ^{3}He spin. In the absence of any nuclear effects, i.e. if

^{3}He was a perfect polarized neutron target, we would make the following observations:

$$\begin{aligned} P_n^+ &= 1 \\ P_n^- &= 0 \\ P_p^+ &= 1/2 \\ P_p^- &= 1/2 \end{aligned} \tag{A.1}$$

For the structure functions and measured asymmetry we would find:

$$g_{1(2)}^3(x) = g_{1(2)}^n(x) \tag{A.2}$$

$$A^3(x) = f_n \cdot A^n \tag{A.3}$$

where $f_{p(n)}$ represents the proton(neutron) dilution:

$$f_{p(n)} = \frac{F_2^{p(n)}(x)}{2F_2^p(x) + F_2^n(x)}$$

A.1.2 Nuclear Effects: Effective Polarization Approach

The next step of sophistication involves using a realistic ^{3}He wavefunction with S$'$ and D components due to the proton polarization. However, at this stage, we still ignore the Fermi motion and binding effects. If we define $P_{S'}$ and P_D as the percentage of S' and D waves in the complete wavefunction, then we obtain:

$$\begin{aligned} P_n^+ &= 1 - \Delta \\ P_n^- &= \Delta \\ P_p^+ &= 1/2 - \Delta' \\ P_p^- &= 1/2 + \Delta' \end{aligned} \tag{A.4}$$

with $\Delta = \frac{1}{3}[P_{S'} + 2P_D]$ and $\Delta' = \frac{1}{6}[P_D - 2P_{S'}]$. We can then define the effective nucleon polarizations* as:

$$p_p = P_p^+ - P_p^- = -0.028 \pm 0.004 \tag{A.5}$$

$$p_n = P_p^+ - P_p^- = 0.86 \pm 0.02 \tag{A.6}$$

---

*The numerical values of Friar *et al.* [203] were used for Δ, Δ' in evaluating the effective polarizations.

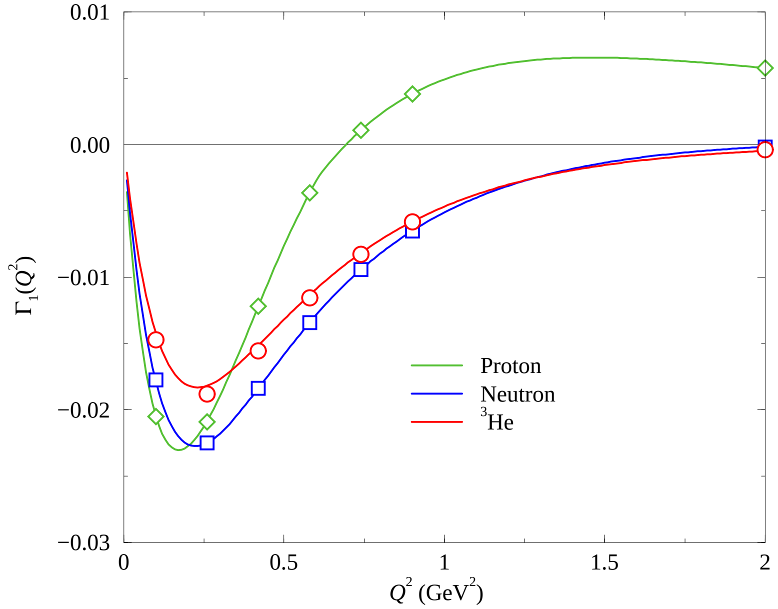

Figure A.1: $\overline{\Gamma}_1$: Comparison of effective polarization approach (solid line) to full convolution calculation (open symbols).

In this approach we obtain the following approximation:

$$g^3_{1(2)}(x) = 2p_p g^p_{1(2)}(x) + p_n g^n_{1(2)}(x) \tag{A.7}$$

$$A^3(x) = 2f_p p_p A^p(x) + f_n p_n A^n(x) \tag{A.8}$$

We will examine in the next section how good of an approximation this is.

A.1.3 Nuclear Effects: Convolution Approach

In the most sophisticated approach that we will consider, the Fermi motion and binding effects are included by convoluting the relevant proton and neutron structure functions $g^{p(n)}_{1(2)}$ to obtain a realistic nuclear structure function $g^A_{1(2)}$. The general convolution integral for scattering from a spin-1/2 target in the impulse approximation is quite involved and we will not reprint it here. We state only the surprising conclusion of ref. [202] that the g^A_1 structure function depends only on $g^{p(n)}_1$ while the g^A_2 structure function has contributions from both $g^{p(n)}_1$ and $g^{p(n)}_2$.

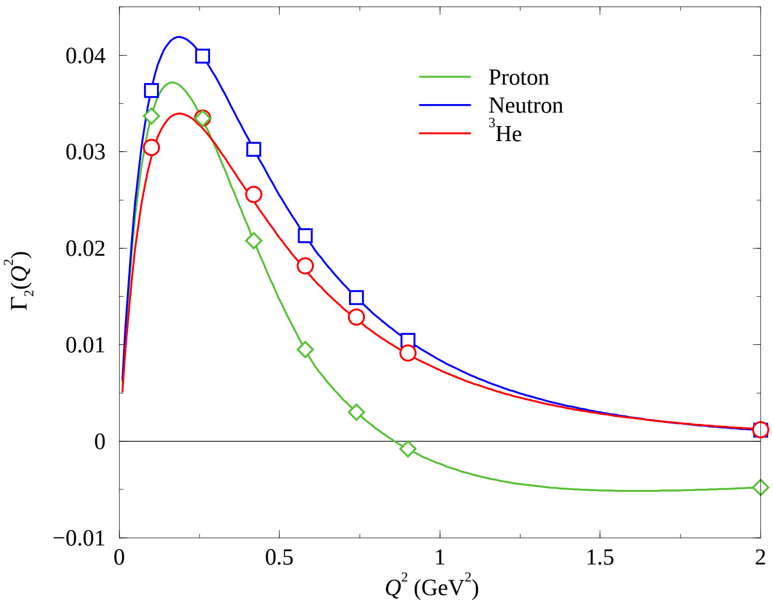

Figure A.2: $\overline{\Gamma}_2$: Comparison of effective polarization approach (solid line) to full convolution calculation (open symbols).

Using a model for the nucleon spin structure functions, the convolution can be evaluated to obtain the nuclear spin structure functions g_1^A and g_2^A in the quasielastic, inelastic and DIS regions. With regard to the use of equation A.7 to extract the neutron from ^{3}He, Ciofi Degli Atti and Scopetta [83] conclude the following:

1. In DIS, equation A.7 provides excellent agreement with the full convolution approach.

2. In the resonance region, using equation A.7 would lead to very unreliable results. This is due to the significant broadening of the resonance peaks due to Fermi motion and binding effects.

3. In both the resonance and DIS regions, integrating equation A.7 leads to:

$$I^3(Q^2) \quad = \quad 2p_p I^p(Q^2) + p_n I^n(Q^2) \tag{A.9}$$

where $I^3(Q^2)$ can represent the GDH sum or any of the structure function moments. The authors conclude that equation A.9 is accurate

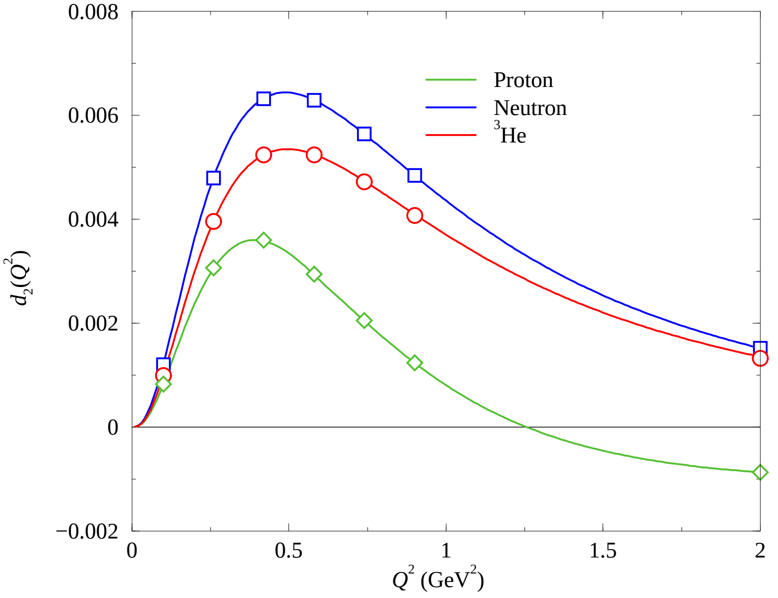

Figure A.3: $\overline{d}_2$: Comparison of effective polarization approach (solid line) to full convolution calculation (open symbols).

to better than 5% down to $Q^2 = 0.5$ GeV^2. Below 0.5 GeV^2, the error raises to about of 10% at 0.1 GeV^2.

The results of a similar study performed by W. Melnitchouk [204, 205] which support these conclusions are shown in figures A.1 to A.3 for $\overline{\Gamma}_1, \overline{\Gamma}_2$, and $\overline{d}_2$. The structure functions used in this study are from the MAID [40] model. It is clear that equation A.9 is in excellent agreement with the full calculation for the integrated neutron quantities at all Q^2 considered.

A.2 Parallel results

In the following plots, we compare our results (labeled 'Slifer') to the published results (labeled 'Choi') of refs [195, 194]. Quantities labeled ^{3}He refer to the measured data starting from the pion production threshold to an upper limit of $W = 2$ GeV†. Notice that these data points *do not* include any contribution from the quasielastic or ^{3}He disintegration region,

---

†Region II in figure 4.1

and should not be confused with the full ^{3}He results presented in chapter 9.

To extract the neutron from our polarized ^{3}He data, we followed the prescription of Ciofi degli Atti and Scopetta [202, 83], which assumes that equation A.9 is a good approximation for quantities involving integrals of the structure functions. These extracted neutron results are labeled 'resonanance'. An estimate of the DIS contribution to Γ_1 and $I_A(Q^2)$ was added to our measured neutron results using the Regge parametrization of world data provided in ref. [188]. For Γ_2 and d_2 we used the leading twist part of g_2 as given by the Wandzura-Wilchek relation[‡]. The systematic error of the measured data is shown on the horizontal axis with the light grey band. An estimate of the uncertainty of the DIS contributions is shown with a dark grey band.

The primary goal of this exercise is to cross check the two independent analyses, so we present no interpretation of the results. The curious reader is directed to refs. [195] and [194] for a full discussion. We note that the DIS estimate of ref. [188] seems to be implemented differently in the two analyses. This discrepency should be resolved but has no impact on the actual measured neutron data of E94–010. A clear difference is found between the two analyses in the $Q^2 = 0.26$ GeV d_2 data point. This discrepency has not been resolved as yet. For all data points the results of the two analyses agree well within the quoted error.

[‡] See equation E.2.

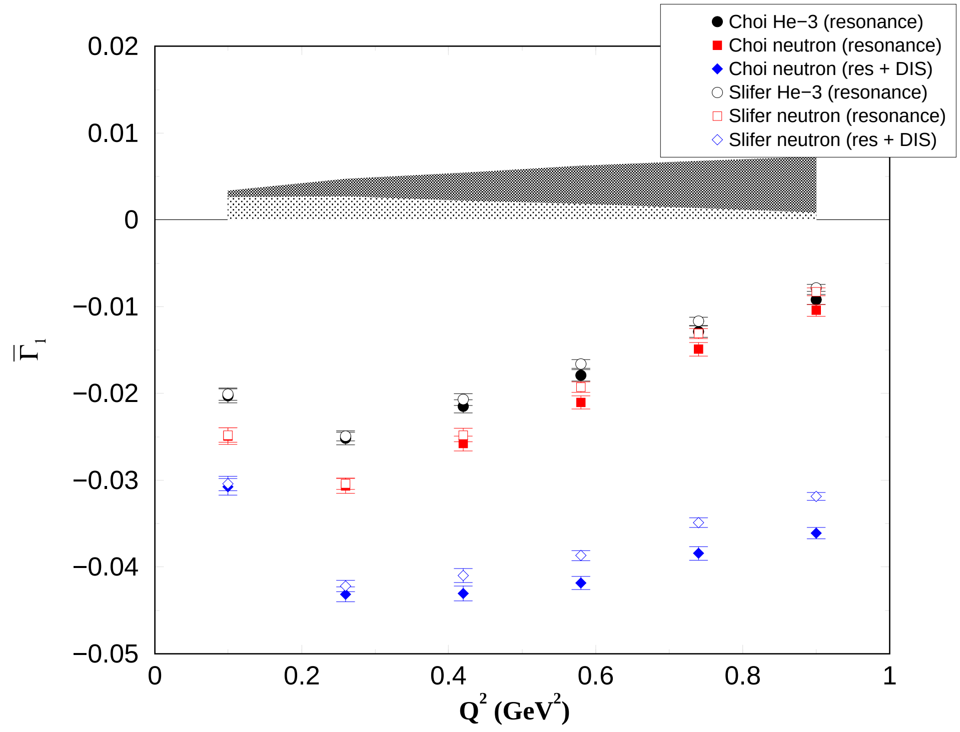

Figure A.4: $\overline{\Gamma}_1$: Comparison of published results to parallel analysis.

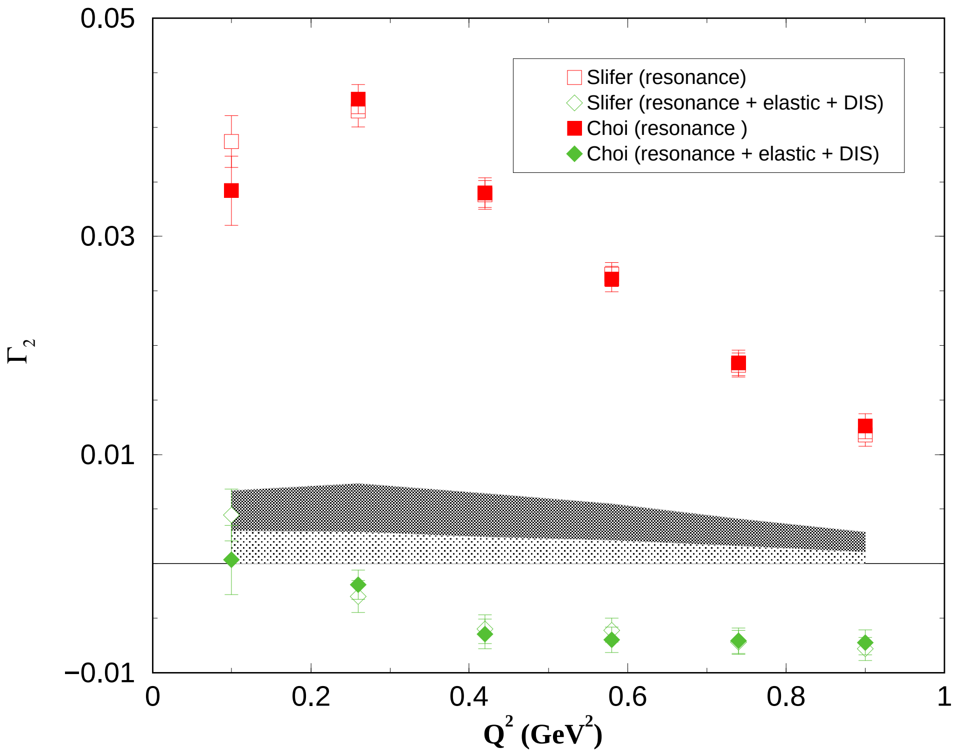

Figure A.5: $\overline{\Gamma}_2$: Comparison of published results to parallel analysis.

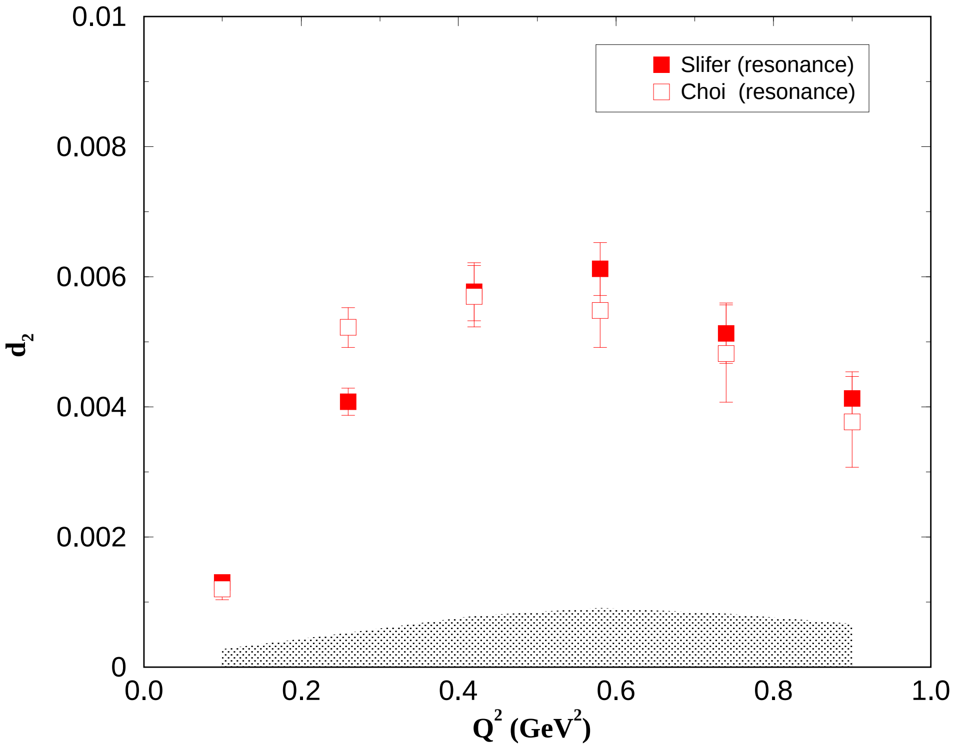

Figure A.6: $\overline{d}_2$: Comparison of published results to parallel analysis.

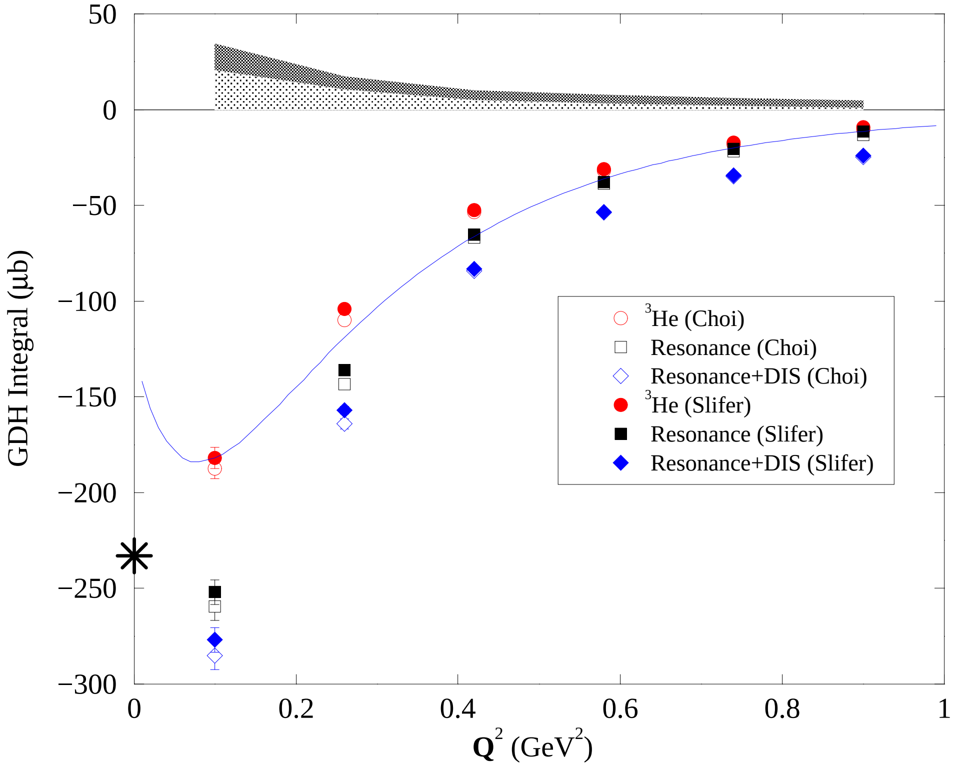

Figure A.7: $I_A(Q^2)$: Comparison of published results to parallel analysis.

APPENDIX B

GDH SUM RULE DERIVATION

The GDH Sum rule relies on a few very general assumptions.

1. Lorentz & Gauge Invariance in the form of the low energy theorem of Low [50], Gell-mann & Goldberger [51].
2. Unitarity in the form of the Optical Theorem.
3. Causality in the form of an unsubtracted Dispersion relation. The exact form of the dispersion relation used assumes crossing symmetry.

We will now briefly examine each of these inputs before synthesizing them to form the desired sum rule.

B.1 Low Energy Theorem

The nucleon forward Compton amplitude T(ν) for *real* photon scattering from a spin 1/2 target can be written as [206]:

$$T(\nu) = \vec{\epsilon_f^*} \cdot \vec{\epsilon_i}\; u(\nu) + i(\vec{\epsilon_f^*} \times \vec{\epsilon_i}) \cdot \vec{\sigma}\; v(\nu) \tag{B.1}$$

where u(ν) is the spin-independent and v(ν) is the spin-dependent part of the amplitude. $\vec{\epsilon_i}$ and $\vec{\epsilon_f}$ refer to the incident and scattered transverse polarization of the photon respectively, and $\vec{\sigma}$ is the nucleon polarization. As $\nu \to 0$ the Low Energy Theorem [50, 51] expresses the real and imaginary parts as an expansion in powers of ν:

$$\begin{aligned} u(\nu) &= -\frac{e^2}{4\pi m} + (\alpha + \beta)\nu^2 + O(\nu^4) \\ v(\nu) &= -\frac{e^2\kappa^2}{8\pi m^2}\nu + \gamma\nu^3 + O(\nu^5) \end{aligned} \tag{B.2}$$

Here $\alpha(\beta)$ is the electric (magnetic) polarizability of the nucleon, κ is the anomalous magnetic moment, and γ is the forward polarizability. Notice that the leading term $\frac{e^2}{m}$ is simply the classical Thomson scattering result.

The Low Energy Theorem predictions are independent of the detailed dynamics of the bound state under consideration [66].

B.2 Optical Theorem

The Optical theorem follows directly from Unitarity. It makes the connection between the imaginary part of the amplitudes and the photon-nucleon absorption cross sections.

$$\begin{aligned}\text{Im } u(\nu) &= \frac{\nu}{8\pi}(\sigma_{1/2} + \sigma_{3/2}) \\ \text{Im } v(\nu) &= \frac{\nu}{8\pi}(\sigma_{1/2} - \sigma_{3/2}) \qquad \text{(B.3)}\end{aligned}$$

Here the subscripts 1/2 & 3/2 refer to the total spin projection of the composite system.

B.3 Dispersion Relations

Kronig and Kramers introduced the use of dispersion relations [207] into physics in their treatment of optics. Broadly speaking, any set of equations that give the real part of a complex function in terms of an integral of the imaginary part (and vice versa) is classified as a dispersion relation.

Given a function f, such that:

$$f(x_0) = u(x_0) + iv(x_0)$$

where f(z) is analytic in the upper half plane and on the real axis and

$$\lim_{|z|\to\infty} f(z) = 0$$

Then, starting from the Cauchy integral formula, it can be shown that:

$$\begin{aligned}u(x_0) &= \frac{1}{\pi}\int_{-\infty}^{+\infty} \frac{v(x)}{x - x_0}dx \\ -v(x_0) &= \frac{1}{\pi}\int_{-\infty}^{+\infty} \frac{u(x)}{x - x_0}dx \qquad \text{(B.4)}\end{aligned}$$

where the principal value of all complex arguments is implied. Using Crossing Symmetry, (i.e. $f(-x) = f^*(x)$) we can rewrite the above integrals as:

$$\begin{aligned}u(x_0) &= \frac{2}{\pi}\int_{0}^{\infty} \frac{xv(x)}{x^2 - x_0^2}dx \\ -v(x_0) &= \frac{2}{\pi}\int_{0}^{\infty} \frac{x_0u(x)}{x^2 - x_0^2}dx \qquad \text{(B.5)}\end{aligned}$$

B.3.1 Causality and the Dispersion Relations

Causality in simplest form states that effect can not precede cause in any physical process. The connection between causality and the dispersion relations is provided by the Titchmarsh theorem [208]. This theorem states that for any square integrable real function f(w) (and its fourier transform f(t)), that if any one of the following three statements is true, then the other two are also necessarily true:

1. f(t) is zero for t < 0.
2. f(z) is analytic and square integrable in the complex plane
3. The real and imaginary parts of f(z) are Hilbert transforms of each other. That is they satisfy relations of the form shown in Eqs. B.4

B.4 Synthesis

Having all the pieces we need, we now follow through on the derivation. The starting point is equation B.5

$$-v(\nu) \;=\; \frac{2}{\pi}\nu\int_{th}^{\infty}\frac{u(\nu')}{\nu'^2\left(1-\frac{\nu}{\nu'}^2\right)}d\nu'$$

where we start the integral from the lowest lying inelastic channel since the cross section vanishes at lower incident photon energies.

Taking the limit as $\nu \to 0$ and inserting Eq. B.3 we get:

$$\begin{aligned} v(\nu) &= \frac{1}{4\pi^2}\nu\int_{th}^{\infty}\frac{\nu'(\sigma_{3/2}-\sigma_{1/2})}{\nu'^2}d\nu' \\ v(\nu) &= \frac{1}{4\pi^2}\nu\int_{th}^{\infty}\frac{(\sigma_{3/2}-\sigma_{1/2})}{\nu'}d\nu' \qquad \text{(B.6)} \end{aligned}$$

Comparing Eq. B.6 to Eq. B.2 we can finally form the sum rule:

$$\begin{aligned} -\frac{e^2\kappa^2}{8\pi^2m^2} &= \frac{1}{4\pi}\int_{th}^{\infty}\frac{(\sigma_{3/2}-\sigma_{1/2})}{\nu'}d\nu' \\ -\frac{e^2\pi\kappa^2}{2m^2} &= \int_{th}^{\infty}\frac{(\sigma_{3/2}-\sigma_{1/2})}{\nu'}d\nu' \end{aligned}$$

or

$$\int_{th}^{\infty}\frac{(\sigma_{3/2}-\sigma_{1/2})}{\nu}d\nu \;=\; -2\pi^2\alpha\left(\frac{\kappa}{m}\right)^2 \qquad \text{(B.7)}$$

This result is for a spin-1/2 half target. If we wish to consider a target of arbitrary spin $\mathcal{S}$, equation B.7 is modified slightly [62] to

$$\int_{th}^{\infty} \frac{(\sigma_{3/2} - \sigma_{1/2})}{\nu} d\nu \quad = \quad -4\pi^2 \alpha \cdot \mathcal{S} \left(\frac{\kappa}{m} \right)^2 \tag{B.8}$$

APPENDIX C

RADIATIVE CORRECTIONS

The theoretical analysis of cross sections typically assumes that the interaction can be described in terms of the leading-order process shown in figure 2.1. The inconvenient reality is that scattering as depicted in figure 2.1 does not occur in nature. There are are higher order (in α) loop corrections to figure 2.1, as well as bremsstrahlung and ionization effects that must be considered. The goal of the “radiative corrections” is to account for all these effects. The corrections fall into four categories:

- Ionization, otherwise known as Landau straggling.
- Virtual photon one loop diagrams.
- Internal and External Bremsstrahlung.

We will now treat each of these contributions in turn.

C.1 Ionization

During passage through the target and surrounding materials the electron loses energy due to ionization through Møller scattering. This effect contributes a few MeV loss per g/cm^2 of material and is almost independent of the incident energy. It is roughly proportional to the thickness of the material t (in radiation lengths). For an electron of energy ϵ, Landau [209] showed that the most probable energy loss due to ionization is:

$$\Delta = t \cdot x_0 \left[ln \frac{atx_0}{\epsilon} + 1 - 0.5772 \right] \tag{C.1}$$

where:

$$a = \frac{2\pi N \alpha^2}{m} \frac{Z}{A} \approx 0.154 MeV \frac{Z}{A} \tag{C.2}$$

and x_0 is the unit radiation length in g/cm^2. Collisional energy loss of the incoming and scattered electrons was determined using the ESTAR program for stopping power [210] and the known thicknesses of the target and spectrometer materials. It was found to be a small correction about 1-2 MeV.

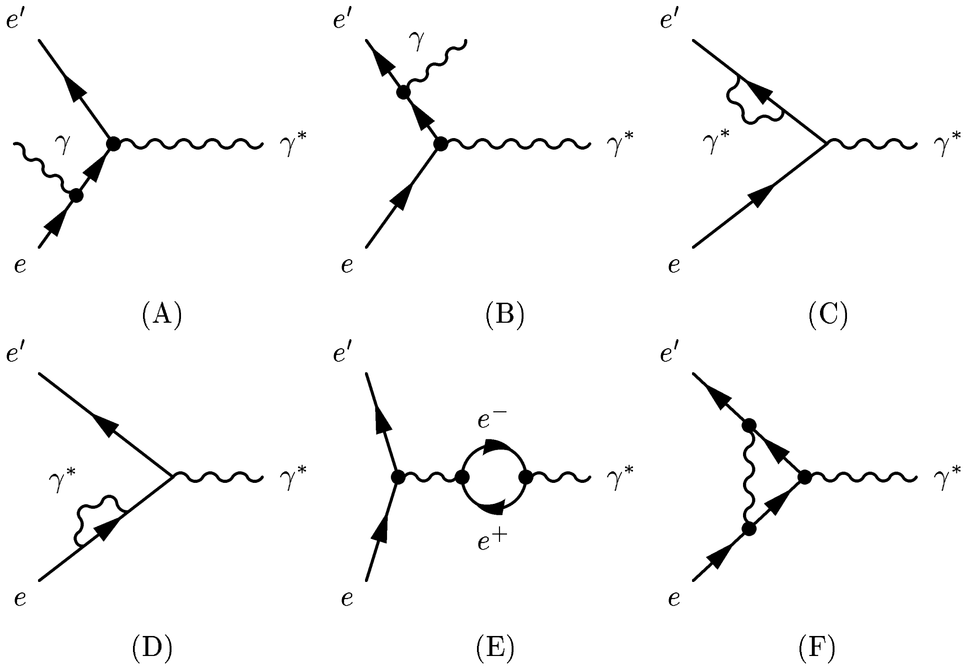

Figure C.1: Next to leading order internal radiative corrections. **A-B:** Bremsstrahlung before&after scattering. **C-D:** Self-energy. **E:** Vacuum polarization. **F:** Vertex correction.

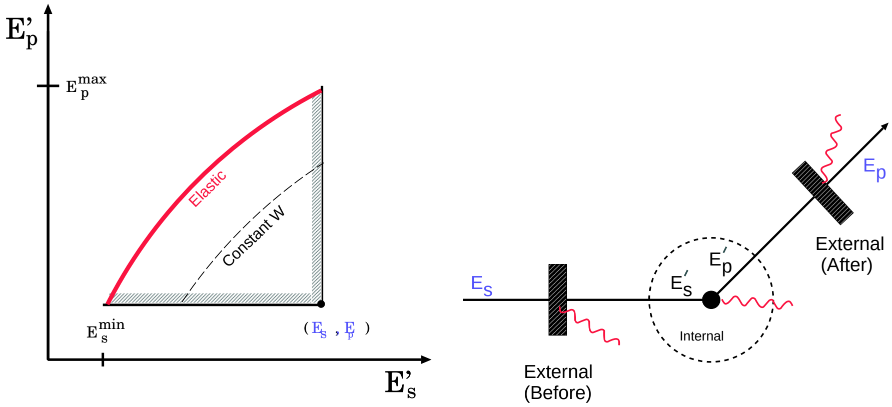

Figure C.2: Left: Kinematic region that contributes to the radiative corrections. **Right:** External and Internal radiation.

C.2 Virtual Photon One Loop Diagrams

Figure C.1 shows the next to leading order Feynman diagrams. Graphs (C) and (D) represent the 'self energy' terms and contribute to the electron mass renormalization. These two graphs reflect the influence of the vacuum fluctuations on the ground state energy of the electron. Graph (E) is known as the 'vacuum polarization' and represents the spontaneous production of an e^-, e^+ pair, which results in a partial screening of the charge. Finally, the 'vertex correction' in graph (F) leads to a small deviation of the electron magnetic moment from the value predicted for a Dirac particle. That is, this diagram is the lowest order contribution to the anomalous part of the electron magnetic moment. Since these four diagrams contribute to the cross section at $\mathcal{O}(\alpha^4)$ they are relatively small corrections compared to the bremsstrahlung. Diagrams of even higher order are generally ignored.

C.3 Bremsstrahlung

Electron scattering involves the acceleration of charged particles and as such we can expect bremsstrahlung to be produced during the collision.* In fact, the Bloch-Nordsieck [211] theorem states that it is impossible for an electron to scatter from a charged particle without emitting an infinite number of soft photons. However, the most likely scenario involves a single photon taking up most of the radiated energy with the remainder spread amongst the infinity of soft photons. Graphs (A) and (B) of figure C.1 illustrate the emission of real photons during the interaction with the nucleus. These graphs are known as the internal bremsstrahlung. There will also be external radiation produced as the particle passes through the materials surrounding the target. The second panel of figure C.2 illustrates the internal/external distinction. An incident electron of energy E_s loses some fraction of its energy as it passes through the materials before and after the target nucleus (external radiation), as well as during the interaction itself (internal radiation), before being detected in the spectrometer. Hence, the actual incident energy E'_s will be less than E_s, and the actual scattered electron energy E'_p will be greater than the detected energy of E_p. The physically accessible kinematic region is the quasi-triangular area bounded by elastic scattering in the left panel of fig. C.2. A state with lighter invariant mass W can effect the states at larger invariant mass, but not vice versa. The elastic peak has

---

*The radiation of the target system is suppressed by the much larger mass and is ignored here.

the lowest possible invariant mass and can therefore effect the entire spectra. The radiated tail from elastic scattering must therefore be subtracted from all other spectra first.

The external bremsstrahlung and ionization are sometimes collectively known as the straggling and are spin-independent. However, there can be a spin-flip when the incident electron interacts with the target nucleus, so the internal corrections to the polarized cross sections necessarily take polarization effects into account.

For the unpolarized cross section, we sum over all polarization states and evaluate the internal corrections with the Method of Equivalent Radiators; the internal bremsstrahlung is approximated by introducing two effective radiators into the external bremsstrahlung analysis, one before and one after the scattering, each of thickness:

$$t_r = \frac{1}{b}\frac{\alpha}{\pi}\left[\ln\frac{Q^2}{m_e^2} - 1\right] \tag{C.3}$$

Here, $b(z) \simeq \frac{4}{3}$ and varies only logarithmically with the target charge z.

For the polarized internal radiative corrections, we used the approach described in [134] and developed in [135] as implemented in the program POLRAD [136]. It is interesting to note that at our kinematics, the full spin-dependent approach to the radiative corrections of ref [135] is only marginally different from the classic approach of Mo and Tsai [131, 132] which ignores spin-dependent effects. This is demonstrated in figure C.4.

C.3.1 Formalism

In discussing the radiative corrections it is convenient to introduce three cross sections following the notation of [132]:

- σ_{exp} : The experimentally measured cross section.
- σ_{born} : The Born cross section depicted in the 1^{st}-order diagram of fig. 2.1.
- σ_r A hypothetical quantity containing only internal radiative effects.

The relationship between these three quantities is shown in fig. C.3. It is the goal of the radiative corrections to extract σ_{born} from σ_{exp}.

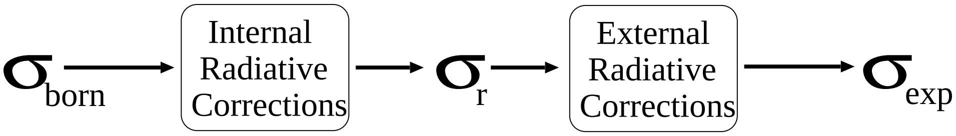

Figure C.3: Schematic of radiative corrections.

The experimentally measured cross section σ_{exp} is related to the internally radiated cross section σ_r by:

$$\begin{aligned}\sigma_{exp}(E_s, E_p) &= \int \frac{dt}{T} \\ &\int_{E_s^{min}}^{E_s} dE'_s \int_{E_p}^{E_p^{max}} dE'_p I(E_s, E'_s, t)\sigma_r(E'_s, E'_p) I(E_p, E'_p, t')\end{aligned} \tag{C.4}$$

where $I(E_0, E, t)$ is the probability of finding an electron that has undergone bremsstrahlung with energy E at a depth t within a material when the incident energy of the electron is E_0. The thicknesses satisfy $t + t' = T$, where T is the total material thickness. The two dimensional integration over $dE'_s dE'_p$ covers the triangular region of figure C.2. The integration over dt is simplified by assuming that the scattering takes place at one half the target thickness. The error on this approximation is less than 1% if T is less than 0.1.

Tsai [132] showed that the probability function I(E_0,E,t) can be expressed as:

$$I(E_0, E, t) = \frac{bt}{\Gamma(1+bt)} \left(\frac{E_0 - E}{E_0}\right)^{bt} \left(\frac{1}{E_0 - E}\right) \phi\left(\frac{E_0 - E}{E_0}\right) \tag{C.5}$$

where $\Gamma(t)$ is the gamma function and $\phi(v)$ is the shape of the bremsstrahlung spectrum and is approximated as $\phi(v) = 1 - v + \frac{3}{4}v^2$.

The 'Energy Peaking Approximation' takes advantage of the fact that the integrand of equation C.4 is strongly peaked in the grey region near the axes in fig. C.2 so that the two dimensional integration can be approximated with two one dimensional line integrals. We present the peaking approximation result as formulated in Stein *et al.* [133]:

$$\left(\frac{d^2\sigma}{d\Omega dE_p}\right)_{exp} = \left(\frac{R\Delta}{E_s}\right)^{bt'_b} \left(\frac{\Delta}{E_p}\right)^{bt'_a} \left[1 - \frac{\xi/\Delta}{1 - b(t'_b + t'_a)}\right] \tilde{\sigma}(E_s, E_p)$$

$$
\begin{aligned}
&+ \int_{E_{Smin}}^{E_S - R\Delta} \tilde{\sigma}(E'_s, E_p) \left(\frac{E_s - E'_s}{E_p R}\right)^{bt'_a} \left(\frac{E_s - E'_s}{E_s}\right)^{bt'_b} \\
&\quad \times \left[\frac{bt'_b}{E_s - E'_s}\phi\left(\frac{E_s - E'_s}{E_s}\right) + \frac{\xi}{2(E_s - E'_s)^2}\right] dE'_s \\
&+ \int_{E_P+\Delta}^{E_{Pmax}} \tilde{\sigma}(E_s, E'_p) \left(\frac{E'_p - E_p}{E'_p}\right)^{bt'_a} \left(\frac{(E'_p - E_p)R}{E_s}\right)^{bt'_b} \\
&\quad \times \left[\frac{bt'_a}{E'_p - E_p}\phi\left(\frac{E'_p - E_p}{E'_p}\right) + \frac{\xi}{2(E'_p - E_p)^2}\right] dE'_p
\end{aligned}
\tag{C.6}
$$

where:

$$
\tilde{\sigma}(E_s, E_p) = \tilde{F}(q^2)\sigma_{born}(E_s, E_p) \tag{C.7}
$$

and

$$
\begin{aligned}
\tilde{F}(q^2) &= (1 + 0.5772 \cdot bT) + \frac{2\alpha}{\pi}\left[\frac{-14}{9} + \frac{13}{12}\ln\frac{Q^2}{m^2}\right] \\
&\quad -\frac{\alpha}{2\pi}\ln^2\left(\frac{E_s}{E_p}\right) + \frac{\alpha}{\pi}\left[\frac{1}{6}\pi^2 - \Phi(\cos^2\frac{\theta}{2})\right]
\end{aligned}
\tag{C.8}
$$

The first term on the right hand side of equation C.8 is a normalization factor that arises in the expression for bremsstrahlung . The second term is the sum of the vacuum polarization and vertex corrections, while the third term represents a small correction to the peaking approximation. The final small term from Schwinger [212] is maximum for $\theta = \pi$ where it is still less than a half-percent correction.

Δ represents the detector resolution and must be chosen small enough that the spectra does not vary appreciably over this range. In principle, the final results are independent of Δ. For this analysis, we used $\Delta = 10MeV$.

The integration is bounded by the elastic scattering so

$$
\begin{aligned}
E_P^{max} &= \frac{E_s}{1 + \frac{E_s}{M}(1 - \cos\theta)} \\
E_S^{min} &= \frac{E_p}{1 - \frac{E_p}{M}(1 - \cos\theta)}
\end{aligned}
\tag{C.9}
$$

In the case of unpolarized spectra, the internal radiative corrections are included in equation C.6 by use of the equivalent radiator t_r so that the thickness before and after scattering t_b and t_a become:

$$\begin{aligned} t'_b &= t_b + t_r \\ t'_a &= t_a + t_r \end{aligned} \tag{C.10}$$

with t_r given by equation C.3.

The remaining factors in equation C.6 are:

$$R = \frac{M_T + 2E_s \sin^2(\theta/2)}{M_T - 2E_p \sin^2(\theta/2)} \tag{C.11}$$

$$\xi = \frac{\pi m}{2\alpha} \frac{t_b + t_a}{(Z+\eta)\ln(183/Z^{1/3})} \tag{C.12}$$

$$\eta = \ln(1440Z^{-2/3})/\ln(183Z^{-1/3}) \tag{C.13}$$

and the spence function is defined as:

$$\Phi(x) = \int_0^x \frac{-\ln|1-y|}{y} dy \tag{C.14}$$

Regarding the validity of the peaking approximation, we quote Tsai [132]:

> "...the tail from the elastic peak is large and long and its effect is felt all the way to the end of the spectrum, but the tails from the inelastic events are small and short and its effect is felt only by their neighbors. From the numerical examples given in MT [131] all versions of the peaking approximations give excellent results when the energy loss due to radiation is smaller than 10% of the electron energy. Hence the peaking approximation can be safely used when calculating the tail from the inelastic events."

C.3.2 Iterative procedure

In equation C.6, the experimentally measured, radiated cross section is given as a function of the unradiated Born cross sections at all possible values of E'_s and E'_p. It's not possible to directly invert this equation or 'unfold' the born cross sections but we can use an iterative procedure to access them. On the first pass, the measured cross sections themselves are used to create a model for the unfolded born cross sections. This initial model is inserted into the integrals of equation C.6 and radiated. The result is then compared to the actual experimentally measured cross section. Any difference is subtracted from the initial model and the new model is inserted in equation C.6. We repeat this up to ten times, but the results converge after only a few iterations.

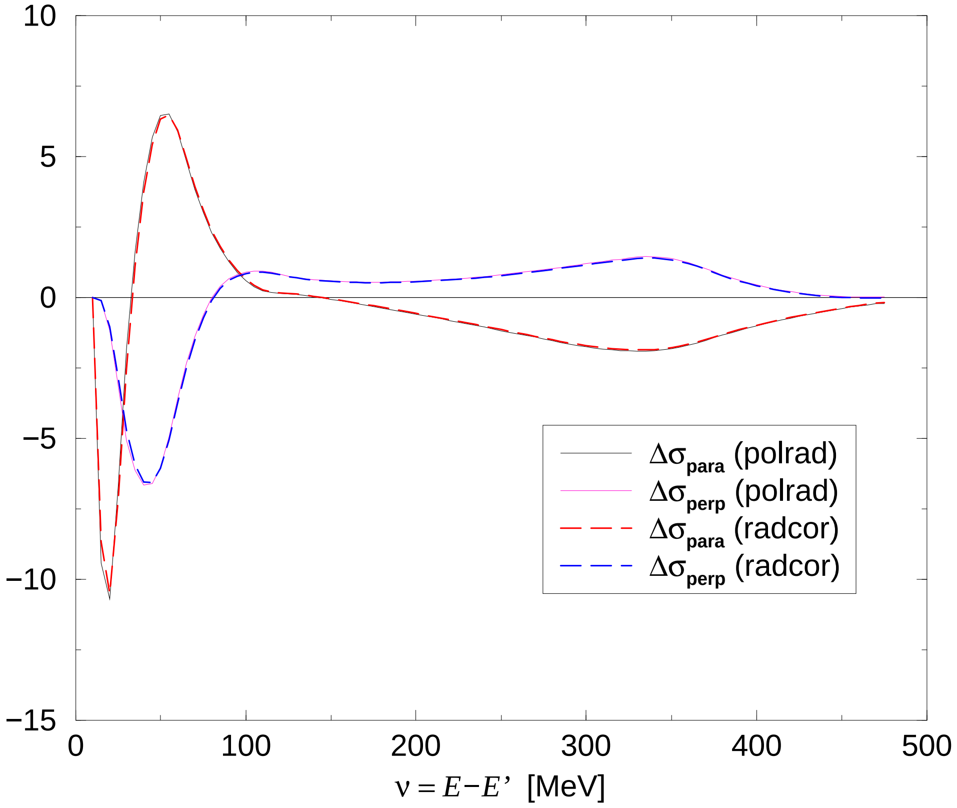

Figure C.4: $E_0 = 862$ MeV. Polarized cross section difference for parallel and perpendicular configuration. Solid lines are result of full treatment of Akushevich and Shumeiko [135] which explicitly treat spin-dependent effects as implemented in code POLRAD [136]. Dashed lines are approximate results based on the approach of Mo and Tsai [131, 132] as implemented in code RADCOR [164].

APPENDIX D

RADIATION LENGTHS

The radiative corrections depend upon the thickness of material before and after scattering. In this appendix, we list the material thicknesses encountered by electrons and estimate the uncertainty associated with the inferred radiation lengths. The location of each material is illustrated in figure D.1.

D.1 Non-Target Material

The electrons first encounter a thin beryllium window* as they exit the beamline vacuum. The aluminum window at the entrance to the helium bag has been measured with a micrometer. One mil uncertainty is used to account for the noticeable distortion of the window. The length of ^{4}He before and after scattering depends on the radius of the scattering chamber which is actually ellipsoidal. The quoted uncertainty corresponds to one half of the chamber wall thickness.

The aluminum exit windows used for E94-010 have been discarded. Ed Folts recalls using 15 mil aluminum exit windows. Caliper/micrometer measurement of the stock aluminum provided by Ed indicate that it is actually 16 mils. The thickness of air after scattering is determined from the survey results, the radius of the target can, and the location of the sieve slit within the collimator box. The latter two each contribute to the uncertainty of 5.5 cm. A caliper was used to measure a sample kapton window. The error represents the standard deviation. There is a titanium window located after the magnetic (momentum analyzing) section of the spectrometer. As such, it should not be included in the radiative corrections†.

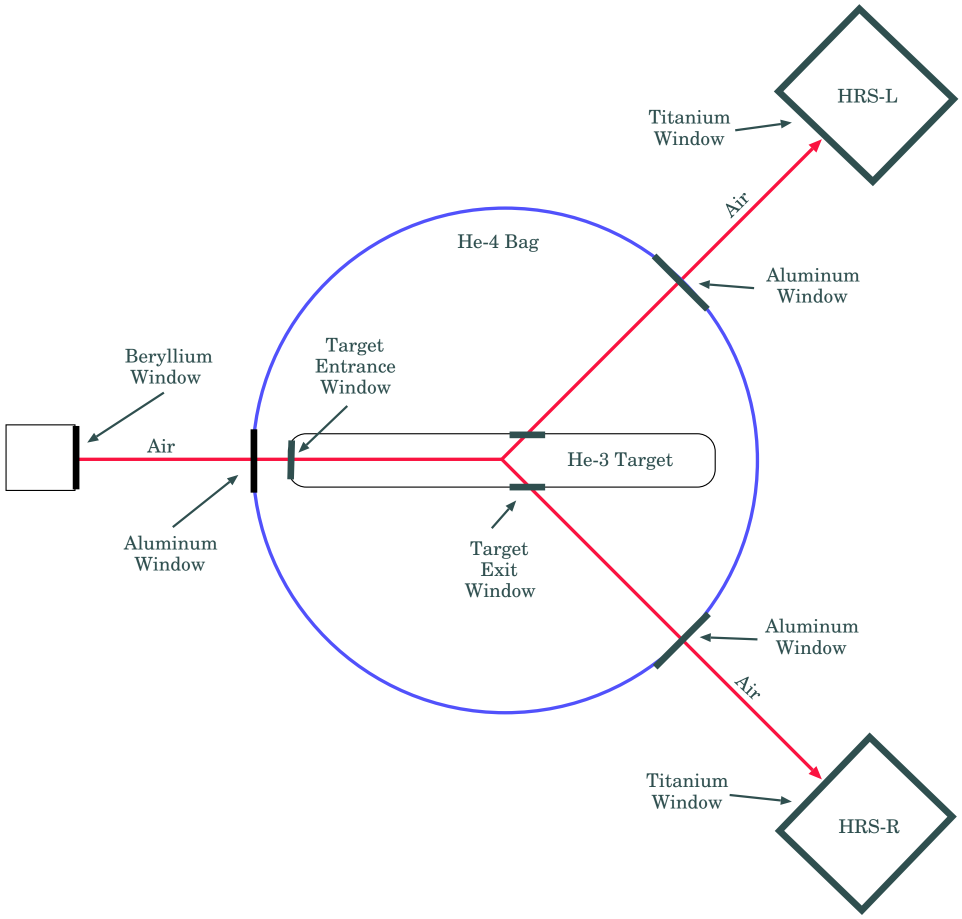

Figure D.1: Schematic of material thicknesses encountered by incoming and scattered electrons.

Material	thickness (cm.)	error (%)	Rad. Length	% of Tot. thickness
Be 15±1.5mil	0.0381	10	10.80×10^{-4}	19.3
Air 1±0.5in	2.54	50	8.349×10^{-5}	1.5
Al 15.4±1mil	0.0391	6.5	4.397×10^{-3}	78.4
^{4}He	25.7	10	4.534×10^{-5}	0.8
Total		5.5	5.606×10^{-3}	100

Table D.1: All material encountered prior to the target cell. *% of Tot. thickness* refers to percentage of total pre-target thickness.

Material	thickness (cm.)	error (%)	Rad. Length	% of Tot. thickness
^{4}He	42	6.0	7.410×10^{-5}	0.7
Al 16±1mil	0.0406	6.3	4.566×10^{-3}	44.8
Air	62.6	8.8	2.058×10^{-3}	20.2
Kapton 7.2±0.2mil	0.0183	2.7	6.407×10^{-4}	6.3
Total		4.6	7.338×10^{-3}	100

Table D.2: All material encountered after the target cell. *% of Tot. thickness* refers to percentage of total post-target thickness.

Target	Material	In(μm)	error	R.L.
Don't Worry	C1720	135.9± 0.6	0.4%	1.282×10^{-3}
Be Happy	C1720	131.8± 8.7	6.6%	1.226×10^{-3}
Armegeddon	GE180	130.5± 8.7	6.6%	1.854×10^{-3}
Nepheli	C1720	133.2±13.2	10.0%	1.256×10^{-3}
Sysiphos	C1720	127.6± 7.6	7.6%	1.203×10^{-3}
Jin	C1720	135.5± 1.6	1.2%	1.278×10^{-3}

Table D.3: Target cell entrance window thickness.

Target	Material	Out(mm)	error	R.L.
Don't Worry	C1720	0.977±0.038	3.9%	9.213×10^{-3}
Be Happy	C1720	0.960±0.1	10.4%	9.053×10^{-3}
Armegeddon	GE180	1.270±0.1	7.8%	18.040×10^{-3}
Nepheli	C1720	0.956±0.1	10.0%	9.015×10^{-3}
Sysiphos	C1720	0.971±0.020	2.1%	9.156×10^{-3}
Jin	C1720	0.850±0.021	2.4%	8.015×10^{-3}

Table D.4: Exit window, HRS-L side. The values assume 90° scattering.

D.2 Target Cell Entrance Window

The values in table D.3 are from Jensen's [123] interferometric measurement. Only *Don't Worry* has records describing which window is upstream and which is downstream. For the other cells, I have averaged the two windows together and the difference between average and measured value is taken as the error. For *Nepheli*, the windows were unfortunately not measured at all. An average over the other ten measured windows is used, with twice the standard deviation as the error.

D.3 Target Cell Exit Window

D.3.1 HRS-L Side

The sidewalls of *Don't Worry*, *Sysiphos* and *Jin* were measured using optical interferometry [214]. Each cell was measured at four points along the length of the glass. The values in table D.4 represents the average and standard deviation of the measurements.

Deur [215] provided estimates for the cells *Be Happy* and *Armegeddon* from the elastic cross section with an error estimate of ±0.1 mm. He also estimates a wall thickness of 0.92 mm for *Jin* which is in reasonable agreement with the interferometry analysis.

There is no direct measurement of *Nepheli*. Jensen [214] makes an estimate for the thickness by comparing the resizing prediction to the interferometry results quoting an error of 9%. To be cautious, we increase the

---

[*] The thickness of the beryllium window comes from Ed Folts [213]. Prior to the 2003 set of polarized ^{3}He experiments, the beryllium window was always 15 mils due to safety requirements.

[†] Thanks to Todd Averett for pointing this out.

Target	Material	Out(mm)	error	R.L.
Don't Worry	C1720	1.019±0.010	1.0%	9.609×10^{-3}
Be Happy	C1720	0.960±0.100	10.4%	9.053×10^{-3}
Armegeddon	GE180	1.460±0.240	16.4%	20.746×10^{-3}
Nepheli	C1720	0.956±0.100	10.4%	9.015×10^{-3}
Sysiphos	C1720	1.001±0.015	1.5%	9.440×10^{-3}
Jin	C1720	0.896±0.021	2.4%	8.449×10^{-3}

Table D.5: Exit window, HRS-R side. The values assume 90° scattering.

error to ±0.1 mm since it is most likely not more accurate than the elastic analysis estimate.

D.3.2 HRS-R Side

The value for the HRS-R exit thickness of *Armegeddon* is estimated by Deur [216] to be 15% thicker than the HRS-L. This estimate has unknown error. The physical limit for the window thickness is 1.7 mm [215] so we use this upper limit to establish an error of ±0.24mm. For all other cells see the discussion in section D.3.1

D.4 ^{3}He Contribution

The contribution of the ^{3}He gas within the target cell to the total radiation length is listed in tables D.6 and D.7. The values shown in table D.6 are deduced from the cell diagrams in the GDH logbook [217] and the cell densities. A conservative 1 cm. uncertainty on the cell length leads to the 5% error.

The values shown in table D.7 for the ^{3}He contribution after scattering were determined by averaging the four or five outer diameter measurements (also from the GDH logbook [217]) to determine a radius and subtracting the glass thickness. The values determined in this way have a standard deviation corresponding to 11 to 12% uncertainty.

D.5 Summary

All contributions to the total radiation length before scattering are summarized in table D.8. The total radiation lengths for scattering to HRS-L are

Target	cm	error	R.L.
Don't Worry	19.3	5.0%	4.501×10^{-4}
Be Happy	20.0	5.0%	4.390×10^{-4}
Armegeddon	19.7	5.0%	4.621×10^{-4}
Nepheli	18.4	5.0%	5.190×10^{-4}
Sysiphos	19.8	5.0%	3.746×10^{-4}
Jin	19.75	5.0%	3.846×10^{-4}

Table D.6: The thickness of the ^{3}He gas before scattering.

Target	cm	error	R.L.
Don't Worry	0.84	12%	1.960×10^{-5}
Be Happy	0.83	12%	1.820×10^{-5}
Armegeddon	0.94	11%	1.979×10^{-5}
Nepheli	0.85	12%	2.228×10^{-5}
Sysiphos	0.89	11%	1.684×10^{-5}
Jin	0.85	12%	1.655×10^{-5}

Table D.7: The thickness of the ^{3}He gas after scattering.

listed in table D.9. The total radiation lengths for scattering to HRS-R are listed in table D.10.

D.6 Conclusion

The thicknesses before scattering are known to about 5%. The thicknesses after scattering are known to better than 10%.

We have found significant differences from the radiation lengths used in the previous analysis [218]. In particular, we were using incorrect thicknesses for beamline beryllium and aluminum windows, and the target exit aluminum windows. Also, we were incorrectly including the spectrometer titanium window, which in fact does not affect the momentum determination. Tables D.11 to D.13 quantify the change.

Finally, we note here that the analysis of the HRS-R inelastic cross sections indicate that the new Armegeddon values are not quite right.

	Pre Target	err (%)	Glass before	err (%)	^{3}He before	err %	Total Rad. L.	err %
D.W.	.	.	1.282×10^{-3}	0.4	4.501×10^{-4}	5	7.338×10^{-3}	4.2
B.H.	.	.	1.226×10^{-3}	6.6	4.390×10^{-4}	5	7.271×10^{-3}	4.4
Arm.	5.606×10^{-3}	5.5	1.854×10^{-3}	6.6	4.621×10^{-4}	5	7.922×10^{-3}	4.2
Nep.	.	.	1.256×10^{-3}	10.0	5.190×10^{-4}	5	7.381×10^{-3}	4.5
Sys.	.	.	1.203×10^{-3}	7.6	3.746×10^{-4}	5	7.184×10^{-3}	4.5
Jin	.	.	1.278×10^{-3}	1.2	3.846×10^{-4}	5	7.269×10^{-3}	4.3

Table D.8: Total thickness before scattering.

	^{3}He After	err (%)	Glass after	err (%)	Post Target	err (%)	Total Rad. L.	err (%)
D.W.	1.960×10^{-5}	12	9.213×10^{-3}	3.9	.	.	4.189×10^{-2}	3.3
B.H.	1.822×10^{-5}	12	9.053×10^{-3}	10.4	.	.	4.128×10^{-2}	8.6
Arm.	2.205×10^{-5}	11	18.04×10^{-3}	7.8	7.338×10^{-3}	4.6	7.492×10^{-2}	7.0
Nep.	2.228×10^{-5}	12	9.015×10^{-3}	9.0	.	.	4.116×10^{-2}	7.4
Sys.	1.684×10^{-5}	11	9.156×10^{-3}	2.1	.	.	4.166×10^{-2}	1.9
Jin	1.655×10^{-5}	12	8.015×10^{-3}	2.4	.	.	3.739×10^{-2}	2.1

Table D.9: Total thickness after scattering (HRS-L side). ^{3}He and glass thicknesses assume 90° scattering. Total assumes 15.5° scattering.

	^{3}He After	err (%)	Glass after	err (%)	Post Target	err (%)	Total Rad. L.	err (%)
D.W.	1.960×10^{-5}	12	9.609×10^{-3}	0.9	.	.	4.337×10^{-2}	1.1
B.H.	1.822×10^{-5}	12	9.053×10^{-3}	10.4	.	.	4.128×10^{-2}	8.6
Arm.	2.205×10^{-5}	11	20.75×10^{-3}	10.0	7.338×10^{-3}	4.6	8.505×10^{-2}	9.1
Nep.	2.228×10^{-5}	12	9.015×10^{-3}	9.0	.	.	4.116×10^{-2}	7.4
Sys.	1.684×10^{-5}	11	9.440×10^{-3}	1.5	.	.	4.273×10^{-2}	1.5
Jin	1.655×10^{-5}	12	8.449×10^{-3}	2.4	.	.	3.902×10^{-2}	2.1

Table D.10: Total thickness after scattering (HRS-R side). ^{3}He and glass thicknesses assume 90° scattering. Total assumes 15.5° scattering.

	Old	New	Diff(%)
BH	5.370×10^{-3}	7.271×10^{-3}	+35.4
AR	6.021×10^{-3}	7.922×10^{-3}	+31.6
NE	5.455×10^{-3}	7.381×10^{-3}	+35.3
SY	5.309×10^{-3}	7.184×10^{-3}	+35.3
JN	5.415×10^{-3}	7.269×10^{-3}	+34.2

Table D.11: Comparison to previous analysis. Thickness before scattering.

	Old	New	Diff(%)
BH	4.389×10^{-2}	4.128×10^{-2}	-5.9
AR	7.611×10^{-2}	7.492×10^{-2}	-1.6
NE	4.390×10^{-2}	4.116×10^{-2}	-6.3
SY	4.389×10^{-2}	4.166×10^{-2}	-5.1
JN	3.965×10^{-2}	3.739×10^{-2}	-5.7

Table D.12: Comparison to previous analysis. (HRS-L) Thickness after scattering.

	Old	New	Diff(%)
BH	4.389×10^{-2}	4.128×10^{-2}	-5.9
AR	7.611×10^{-2}	8.505×10^{-2}	-11.7
NE	4.390×10^{-2}	4.116×10^{-2}	-6.3
SY	4.389×10^{-2}	4.273×10^{-2}	-2.7
JN	3.965×10^{-2}	3.902×10^{-2}	-1.6

Table D.13: Comparison to previous analysis. (HRS-R) Thickness after scattering.

APPENDIX E

INTEGRAL RELATIONS

E.1 Integral properties of g_2^{WW}

We consider here some properties under integration of g_2^{WW}. In general, we will be interested in integrals of the type [219]:

$$\int_0^{x_0} x^n g_2^{WW}(x)dx \tag{E.1}$$

We can evaluate this integral with a partial integration to obtain a very useful general relation:

$$\int_0^{x_0} x^n g_2^{WW}(x)dx = -\frac{n}{n+1}\int_0^{x_0} x^n g_1(x) + \frac{x_0^{n+1}}{n+1}\int_{x_0}^1 \frac{g_1(y)}{y}dy \tag{E.2}$$

Some specific applications of equation E.2 will be useful when we evaluate the unmeasured DIS contributions to the moments of g_2.

$\underline{n = 0}$:

$$\int_0^{x_0} g_2^{WW}(x)dx = x_0\int_{x_0}^1 \frac{g_1(y)}{y}dy \tag{E.3}$$

$\underline{x_0 = 1}$

$$\int_0^1 x^n g_2^{WW}(x)dx = -\frac{n}{n+1}\int_0^1 x^n g_1(x)dx \tag{E.4}$$

$\underline{x_0 = 1, n = 0}$

$$\int_0^1 g_2^{WW}(x)dx = 0 \tag{E.5}$$

$\underline{x_0 = 1, n = 1}$

$$\int_0^1 x g_2^{WW}(x)dx = -\frac{1}{2}\int_0^1 x g_1(x)dx \tag{E.6}$$

$\underline{x_0 = 1, n = 2}$

$$\int_0^1 x^2 g_2^{WW}(x)dx = -\frac{2}{3}\int_0^1 x^2 g_1(x)dx \tag{E.7}$$

E.2 Elastic Contribution to the Moments

The elastic contribution to the spin structure moments at $x = 1$ can be evaluated with the following two relations [220]:

$$\begin{aligned} g_1^{el}(x,Q^2) &= \frac{1}{2}G_M(Q^2)\frac{G_E(Q^2)+\tau G_M(Q^2)}{1+\tau}\delta(x-1) \\ g_2^{el}(x,Q^2) &= \frac{\tau}{2}G_M(Q^2)\frac{G_E(Q^2)-G_M(Q^2)}{1+\tau}\delta(x-1) \end{aligned} \tag{E.8}$$

So we have:

$$\begin{aligned} \Gamma_1^{el}(Q^2) &= \frac{1}{2}G_M(Q^2)\frac{G_E(Q^2)+\tau G_M(Q^2)}{1+\tau} \\ \Gamma_2^{el}(Q^2) &= \frac{\tau}{2}G_M(Q^2)\frac{G_E(Q^2)-G_M(Q^2)}{1+\tau} \end{aligned} \tag{E.9}$$

All higher moments of the structure functions will have identical elastic contributions since the delta function picks out only the contribution at $x = 1$ From Eq. 4.8 we can see that the elastic contribution to the extended GDH sum is:

$$\begin{aligned} I_A^{el}(Q^2) &= \frac{16\pi^2\alpha}{Q^2}\left[\Gamma_1^{el}(Q^2) - \frac{1}{\tau}\Gamma_2^{el}(Q^2)\right] \\ &= \frac{16\pi^2\alpha}{Q^2}\frac{G_M^2}{2} \end{aligned} \tag{E.10}$$

and finally, the elastic contribution to the d_2 matrix element is

$$d_2^{el}(Q^2) = 2\Gamma_1^{el}(Q^2) + 3\Gamma_2^{el}(Q^2) \tag{E.11}$$

E.2.1 Estimate of Q.E. Contribution

We can make a first order estimate of the ^{3}He quasielastic reaction portion of the moments using the impulse approximation. We assume that the quasielastic contribution is the incoherent sum of elastic contributions of the proton and neutron as given in section E.2. These elastic portions are then combined using the effective polarization formulae of equation A.9. Although admittedly crude, this method reproduces the trend of our data surprisingly well. See for example figure E.1.

The MAID model calculates only nucleon response in the resonance region. In order to compare this phenomenological model directly to our ^{3}He data, we have added an estimate of the quasielastic region following the above procedure.

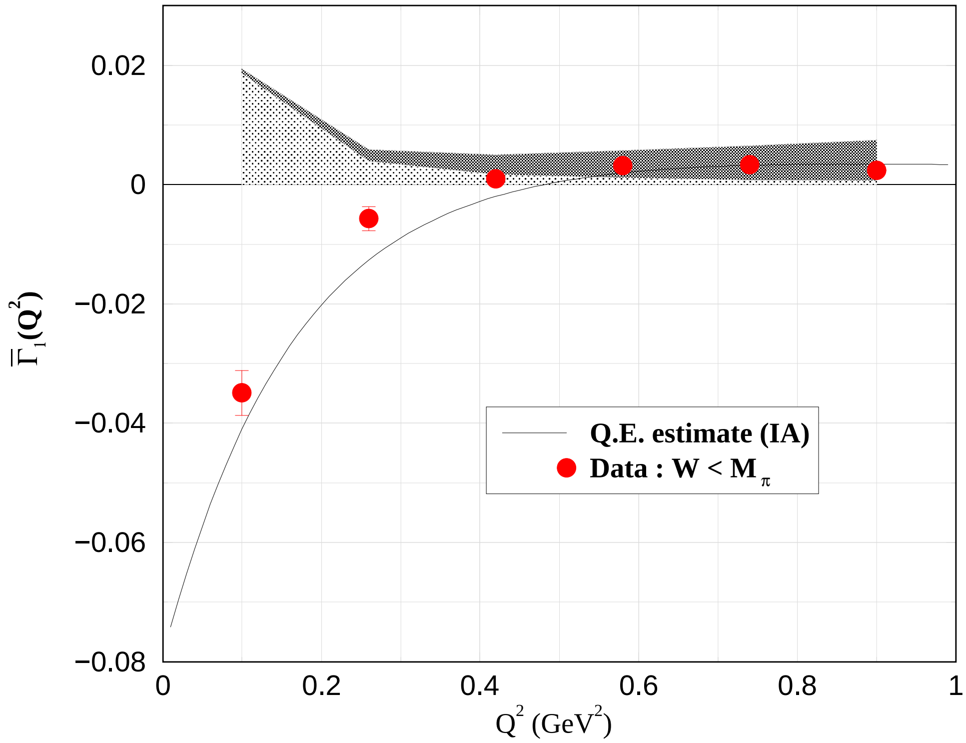

Figure E.1: $\overline{\Gamma}_1^{^3\mathrm{He}}$ for $W < M_\pi$. Curve is the incoherent sum of the nucleonic elastic contributions to Γ_1.

APPENDIX F

ADDITIONAL PROCESSING OF CROSS SECTIONS

Several of the raw cross section spectra required extra individual treatment to address difficulties encountered during the experimental run. We list the difficulties and extra processing steps here.

1. The 862 MeV data contains three spectrometer settings at large energy loss ($\nu > 450$ MeV) for which the HRS-L dipole momentum was not matched to the quadrupoles' magnetic setting. The NMR probe that is normally used to monitor the dipole magnetic field failed at these low field settings and the dipole gaussmeter was used instead. Later, using a combination of the recorded dipole magnet currents and the energy measurement capabilities of the HRS-L calorimeter, it was found that there was a sizable offset in the gaussmeter readout which lead to the mismatch. For full details, see [153].

   To limit the effect of the mismatch, we cut aggressively on the central acceptance region in order to minimize the need for the focusing that is normally provided by the quadrupoles. Although apparently effective, this method is admittedly crude and casts doubt on the validity of these three kinematics. One of the recovered kinematics overlaps with a normal kinematic and the data disagrees by 8% (See fig. F.1). The highest two kinematics (in ν) however seem to match up reasonably with the normal data. Therefore the overlapping data was discarded and no renormalization was applied to the remaining data.

   The special circumstances associated with these tail kinematics casts doubt on their accuracy. Accordingly, the unfolding was performed both including these kinematics and excluding them to gauge their effect on the radiative corrections. It was found that even excluding all the $E_s = 862$ MeV data above $\nu = 200$ MeV had negligible effect on the radiative corrections to the higher energy spectra. They were therefore retained in the final analysis.

2. We observed unexpected rapidly rising tails (see, for example, fig 8.18) for the two lowest E94-010 incident energies which can not be explained

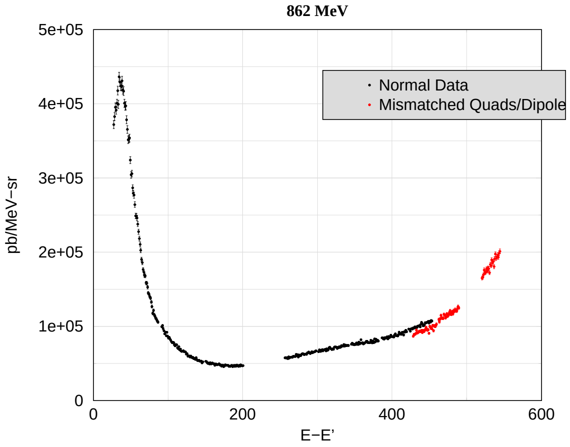

Figure F.1: HRS-L raw cross section for E_0 = 862 MeV. Black: normal data. Red: Spectrometer dipole and quadrupoles mismatched.

in terms of elastic ^{3}He or N_2 tails. The problem has been studied in detail by A. Deur [160] who concluded this was due to multiple scattering that did not originate in the target gas. Since these must originate from unpolarized material they are expected to have no effect on the polarized cross sections.

3. Replay of the data for $E_0 = 862$ MeV indicates a blockage of the acceptance for HRS-R. See figure F.2. This casts doubt on the validity of the HRS-R cross section data for this entire energy setting. Attempts at isolating and removing the problem data with cuts were unsuccessful.

4. The 4.2 GeV data contains contributions from two target cells: *Nepheli* and *Sysiphos* (See fig. 8.10). The kinematic coverage overlaps in the quasielastic region, but the *Nepheli* data is systematically lower than the *Sysiphos* data by 5% even though they agree within error. Accordingly, we normalize both sets of data to the average and leave the total error unmodified.

5. The 5.1 GeV data covers the range 1950 MeV $\leq \nu \leq$ 3050 MeV. Data at lower ν is needed for the radiative corrections. nQFS [162], normalized to the data, is used to generate the needed spectra.

6. As shown in figure F.1, there is a significant gap in the energy loss

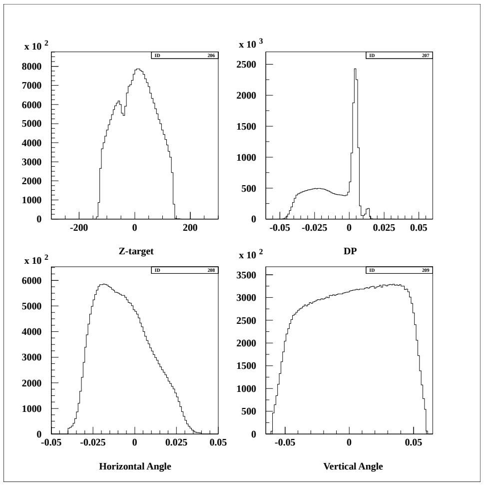

Figure F.2: Target variables for HRS-R. $E_0 = 862$ MeV, run 2749. Notice obstruction for upstream z-target.

coverage at around $\nu = 250$ MeV for the $E_0 = 862$ MeV data set. We were forced to interpolate over this region which represents the onset of the Δ excitation region.

APPENDIX G

CROSS SECTION TABLES

The quantities listed in the table below are all defined in chapter 8.

Table G.1: E94-010 Unpolarized ^{3}He cross sections. Energies given in MeV, cross sections in pb/MeV-sr. $\Theta = 15.5°$

E$_0$	ν	σ_{exp}	σ_{born}	dσ_{stat}	dσ_{syst}
862.0	15.5	0.2168E+05	0.1873E+06	0.6582E+04	0.3537E+05
862.0	16.5	0.5123E+05	0.2457E+06	0.7646E+04	0.3676E+05
862.0	17.5	0.6840E+05	0.2779E+06	0.8115E+04	0.3721E+05
862.0	18.5	0.1295E+06	0.2898E+06	0.8135E+04	0.3678E+05
862.0	19.5	0.1580E+06	0.2896E+06	0.8029E+04	0.3584E+05
862.0	20.5	0.1776E+06	0.3178E+06	0.8547E+04	0.3718E+05
862.0	21.5	0.1817E+06	0.3432E+06	0.9049E+04	0.3842E+05
862.0	22.5	0.1836E+06	0.3507E+06	0.9095E+04	0.3848E+05
862.0	23.5	0.2040E+06	0.3951E+06	0.1004E+05	0.4125E+05
862.0	24.5	0.2168E+06	0.4250E+06	0.1046E+05	0.4308E+05
862.0	25.5	0.2234E+06	0.4272E+06	0.1043E+05	0.4304E+05
862.0	26.5	0.2548E+06	0.4407E+06	0.1056E+05	0.4368E+05
862.0	27.5	0.2692E+06	0.4722E+06	0.1118E+05	0.4550E+05
862.0	28.5	0.2715E+06	0.4862E+06	0.1134E+05	0.4611E+05
862.0	29.5	0.2850E+06	0.5010E+06	0.1152E+05	0.4692E+05
862.0	30.5	0.3064E+06	0.5078E+06	0.1158E+05	0.4725E+05
862.0	31.5	0.3155E+06	0.5208E+06	0.1192E+05	0.4796E+05
862.0	32.5	0.3271E+06	0.5163E+06	0.1175E+05	0.4732E+05
862.0	33.5	0.3329E+06	0.5009E+06	0.1134E+05	0.4607E+05
862.0	34.5	0.3431E+06	0.4883E+06	0.1107E+05	0.4492E+05
862.0	35.5	0.3395E+06	0.5004E+06	0.1149E+05	0.4545E+05
862.0	36.5	0.3320E+06	0.4753E+06	0.1093E+05	0.4335E+05
862.0	37.5	0.3291E+06	0.4698E+06	0.1088E+05	0.4274E+05
862.0	38.5	0.3382E+06	0.4518E+06	0.1042E+05	0.4125E+05
862.0	39.5	0.3220E+06	0.4466E+06	0.1037E+05	0.4064E+05
862.0	40.5	0.3238E+06	0.4412E+06	0.1032E+05	0.4008E+05

continued on next page

Table G.1: *Unpolarized cross sections continued*

E_0	ν	σ_{exp}	σ_{born}	dσ_{stat}	dσ_{syst}
862.0	41.5	0.3130E+06	0.4166E+06	0.9717E+04	0.3808E+05
862.0	42.5	0.3149E+06	0.3971E+06	0.9238E+04	0.3629E+05
862.0	43.5	0.3112E+06	0.3707E+06	0.8622E+04	0.3428E+05
862.0	44.5	0.2975E+06	0.3876E+06	0.9150E+04	0.3531E+05
862.0	45.5	0.2875E+06	0.3585E+06	0.8504E+04	0.3302E+05
862.0	46.5	0.2755E+06	0.3210E+06	0.7720E+04	0.3035E+05
862.0	47.5	0.2891E+06	0.2899E+06	0.6571E+04	0.2812E+05
862.0	48.5	0.2658E+06	0.2939E+06	0.6642E+04	0.2818E+05
862.0	49.5	0.2460E+06	0.2727E+06	0.6179E+04	0.2663E+05
862.0	50.5	0.2303E+06	0.2488E+06	0.5544E+04	0.2484E+05
862.0	51.5	0.2357E+06	0.2580E+06	0.5808E+04	0.2516E+05
862.0	52.5	0.2191E+06	0.2351E+06	0.5276E+04	0.2354E+05
862.0	53.5	0.2094E+06	0.2050E+06	0.4614E+04	0.2147E+05
862.0	54.5	0.2161E+06	0.1992E+06	0.4525E+04	0.2097E+05
862.0	55.5	0.1977E+06	0.1905E+06	0.4377E+04	0.2025E+05
862.0	56.5	0.1823E+06	0.1904E+06	0.4420E+04	0.2008E+05
862.0	57.5	0.1805E+06	0.1688E+06	0.3906E+04	0.1848E+05
862.0	58.5	0.1754E+06	0.1707E+06	0.4008E+04	0.1849E+05
862.0	59.5	0.1748E+06	0.1592E+06	0.3743E+04	0.1757E+05
862.0	60.5	0.1605E+06	0.1449E+06	0.3419E+04	0.1648E+05
862.0	61.5	0.1638E+06	0.1199E+06	0.2861E+04	0.1474E+05
862.0	62.5	0.1536E+06	0.1149E+06	0.2779E+04	0.1434E+05
862.0	63.5	0.1443E+06	0.1046E+06	0.2531E+04	0.1347E+05
862.0	64.5	0.1284E+06	0.1047E+06	0.2589E+04	0.1335E+05
862.0	65.5	0.1268E+06	0.9083E+05	0.2243E+04	0.1231E+05
862.0	66.5	0.1191E+06	0.9967E+05	0.2472E+04	0.1273E+05
862.0	67.5	0.1191E+06	0.8496E+05	0.2105E+04	0.1167E+05
862.0	68.5	0.1097E+06	0.8338E+05	0.2093E+04	0.1141E+05
862.0	69.5	0.1158E+06	0.8118E+05	0.2047E+04	0.1113E+05
862.0	70.5	0.1034E+06	0.7309E+05	0.1839E+04	0.1045E+05
862.0	71.5	0.1047E+06	0.7068E+05	0.1796E+04	0.1016E+05
862.0	72.5	0.1009E+06	0.6595E+05	0.1670E+04	0.9730E+04
862.0	73.5	0.9567E+05	0.6517E+05	0.1658E+04	0.9534E+04
862.0	74.5	0.9361E+05	0.5823E+05	0.1492E+04	0.8959E+04
862.0	75.5	0.8973E+05	0.5231E+05	0.1342E+04	0.8450E+04
862.0	76.5	0.8850E+05	0.4270E+05	0.1111E+04	0.7774E+04

continued on next page

Table G.1: *Unpolarized cross sections continued*

E_0	ν	σ_{exp}	σ_{born}	$d\sigma_{stat}$	$d\sigma_{syst}$
862.0	77.5	0.8267E+05	0.4780E+05	0.1253E+04	0.7915E+04
862.0	78.5	0.7820E+05	0.4608E+05	0.1218E+04	0.7687E+04
862.0	79.5	0.7202E+05	0.4778E+05	0.1268E+04	0.7646E+04
862.0	80.5	0.7558E+05	0.4036E+05	0.1068E+04	0.7132E+04
862.0	81.5	0.7277E+05	0.4374E+05	0.1169E+04	0.7177E+04
862.0	82.5	0.7333E+05	0.4340E+05	0.1156E+04	0.7033E+04
862.0	83.5	0.6748E+05	0.3946E+05	0.1047E+04	0.6716E+04
862.0	84.5	0.7031E+05	0.4222E+05	0.1130E+04	0.6729E+04
862.0	85.5	0.6801E+05	0.3931E+05	0.1050E+04	0.6473E+04
862.0	86.5	0.6560E+05	0.4131E+05	0.1118E+04	0.6445E+04
862.0	87.5	0.6671E+05	0.4216E+05	0.9804E+03	0.6384E+04
862.0	88.5	0.6382E+05	0.4086E+05	0.7293E+03	0.6236E+04
862.0	89.5	0.6516E+05	0.4562E+05	0.7830E+03	0.6324E+04
862.0	90.5	0.6432E+05	0.4280E+05	0.7425E+03	0.6073E+04
862.0	91.5	0.6349E+05	0.3947E+05	0.6829E+03	0.5822E+04
862.0	92.5	0.6590E+05	0.3387E+05	0.5854E+03	0.5500E+04
862.0	93.5	0.6257E+05	0.3823E+05	0.6675E+03	0.5580E+04
862.0	94.5	0.6006E+05	0.3303E+05	0.5707E+03	0.5285E+04
862.0	95.5	0.5651E+05	0.4044E+05	0.6998E+03	0.5497E+04
862.0	96.5	0.5897E+05	0.3687E+05	0.6351E+03	0.5264E+04
862.0	97.5	0.5487E+05	0.3186E+05	0.5492E+03	0.4995E+04
862.0	98.5	0.6012E+05	0.3451E+05	0.5988E+03	0.5016E+04
862.0	99.5	0.5543E+05	0.3394E+05	0.5884E+03	0.4922E+04
862.0	100.5	0.5316E+05	0.3236E+05	0.5622E+03	0.4801E+04
862.0	101.5	0.5458E+05	0.3010E+05	0.5246E+03	0.4663E+04
862.0	102.5	0.5334E+05	0.2852E+05	0.4963E+03	0.4550E+04
862.0	103.5	0.5210E+05	0.3032E+05	0.5304E+03	0.4538E+04
862.0	104.5	0.5018E+05	0.3136E+05	0.5495E+03	0.4509E+04
862.0	105.5	0.4915E+05	0.2831E+05	0.4956E+03	0.4368E+04
862.0	106.5	0.5017E+05	0.2621E+05	0.4615E+03	0.4257E+04
862.0	107.5	0.5004E+05	0.2962E+05	0.5188E+03	0.4290E+04
862.0	108.5	0.4753E+05	0.3112E+05	0.5614E+03	0.4278E+04
862.0	109.5	0.4647E+05	0.2632E+05	0.4892E+03	0.4107E+04
862.0	110.5	0.4862E+05	0.2387E+05	0.4403E+03	0.4001E+04
862.0	111.5	0.4843E+05	0.2910E+05	0.5292E+03	0.4081E+04
862.0	112.5	0.4475E+05	0.2433E+05	0.4337E+03	0.3924E+04

continued on next page

Table G.1: *Unpolarized cross sections continued*

E_0	ν	σ_{exp}	σ_{born}	$d\sigma_{stat}$	$d\sigma_{syst}$
862.0	113.5	0.4400E+05	0.2577E+05	0.4556E+03	0.3904E+04
862.0	114.5	0.4676E+05	0.2366E+05	0.4176E+03	0.3825E+04
862.0	115.5	0.4272E+05	0.2270E+05	0.4008E+03	0.3761E+04
862.0	116.5	0.4416E+05	0.2400E+05	0.4220E+03	0.3745E+04
862.0	117.5	0.4180E+05	0.2583E+05	0.4565E+03	0.3748E+04
862.0	118.5	0.4153E+05	0.2473E+05	0.4412E+03	0.3687E+04
862.0	119.5	0.4217E+05	0.2507E+05	0.4455E+03	0.3660E+04
862.0	120.5	0.4293E+05	0.2593E+05	0.4605E+03	0.3642E+04
862.0	121.5	0.4176E+05	0.2188E+05	0.3934E+03	0.3531E+04
862.0	122.5	0.4213E+05	0.2325E+05	0.4282E+03	0.3518E+04
862.0	123.5	0.4189E+05	0.1940E+05	0.3644E+03	0.3435E+04
862.0	124.5	0.3913E+05	0.1950E+05	0.3699E+03	0.3399E+04
862.0	125.5	0.4002E+05	0.2071E+05	0.3946E+03	0.3383E+04
862.0	126.5	0.3685E+05	0.1877E+05	0.3599E+03	0.3326E+04
862.0	127.5	0.3750E+05	0.2095E+05	0.4035E+03	0.3329E+04
862.0	128.5	0.3753E+05	0.1964E+05	0.3729E+03	0.3286E+04
862.0	129.5	0.3622E+05	0.1843E+05	0.3509E+03	0.3241E+04
862.0	130.5	0.3762E+05	0.2008E+05	0.3811E+03	0.3235E+04
862.0	131.5	0.3605E+05	0.1848E+05	0.3479E+03	0.3191E+04
862.0	132.5	0.3556E+05	0.1904E+05	0.3606E+03	0.3169E+04
862.0	133.5	0.3630E+05	0.1755E+05	0.3332E+03	0.3123E+04
862.0	134.5	0.3494E+05	0.2113E+05	0.4023E+03	0.3155E+04
862.0	135.5	0.3520E+05	0.1953E+05	0.3771E+03	0.3099E+04
862.0	136.5	0.3411E+05	0.1673E+05	0.3316E+03	0.3040E+04
862.0	137.5	0.3650E+05	0.1711E+05	0.3468E+03	0.3028E+04
862.0	138.5	0.3433E+05	0.1821E+05	0.3698E+03	0.3018E+04
862.0	139.5	0.3281E+05	0.1717E+05	0.3508E+03	0.2988E+04
862.0	140.5	0.3314E+05	0.1646E+05	0.3368E+03	0.2961E+04
862.0	141.5	0.3346E+05	0.1827E+05	0.3726E+03	0.2959E+04
862.0	142.5	0.3248E+05	0.1502E+05	0.3054E+03	0.2903E+04
862.0	143.5	0.3222E+05	0.1637E+05	0.3338E+03	0.2906E+04
862.0	144.5	0.3289E+05	0.1766E+05	0.3493E+03	0.2904E+04
862.0	145.5	0.3047E+05	0.1821E+05	0.3464E+03	0.2894E+04
862.0	146.5	0.3190E+05	0.1883E+05	0.3456E+03	0.2891E+04
862.0	147.5	0.3217E+05	0.1954E+05	0.3438E+03	0.2888E+04
862.0	148.5	0.3243E+05	0.1956E+05	0.3418E+03	0.2871E+04

continued on next page

Table G.1: *Unpolarized cross sections continued*

E_0	ν	σ_{exp}	σ_{born}	$d\sigma_{stat}$	$d\sigma_{syst}$
862.0	149.5	0.3270E+05	0.1825E+05	0.3184E+03	0.2825E+04
862.0	150.5	0.3297E+05	0.1614E+05	0.2820E+03	0.2773E+04
862.0	151.5	0.3265E+05	0.1751E+05	0.3084E+03	0.2779E+04
862.0	152.5	0.3145E+05	0.1569E+05	0.2765E+03	0.2731E+04
862.0	153.5	0.3026E+05	0.1838E+05	0.3206E+03	0.2771E+04
862.0	154.5	0.3099E+05	0.1727E+05	0.2982E+03	0.2727E+04
862.0	155.5	0.2965E+05	0.1743E+05	0.3012E+03	0.2716E+04
862.0	156.5	0.3157E+05	0.1922E+05	0.3352E+03	0.2746E+04
862.0	157.5	0.3012E+05	0.1795E+05	0.3105E+03	0.2706E+04
862.0	158.5	0.3066E+05	0.1860E+05	0.3214E+03	0.2705E+04
862.0	159.5	0.3141E+05	0.1543E+05	0.2682E+03	0.2633E+04
862.0	160.5	0.3044E+05	0.1731E+05	0.3009E+03	0.2661E+04
862.0	161.5	0.3068E+05	0.1862E+05	0.3250E+03	0.2672E+04
862.0	162.5	0.2846E+05	0.1727E+05	0.3010E+03	0.2627E+04
862.0	163.5	0.3027E+05	0.1784E+05	0.3144E+03	0.2632E+04
862.0	164.5	0.3033E+05	0.1851E+05	0.3240E+03	0.2640E+04
862.0	165.5	0.2940E+05	0.2055E+05	0.3654E+03	0.2686E+04
862.0	166.5	0.2991E+05	0.1782E+05	0.3311E+03	0.2602E+04
862.0	167.5	0.3031E+05	0.1862E+05	0.3510E+03	0.2611E+04
862.0	168.5	0.3125E+05	0.1684E+05	0.3067E+03	0.2552E+04
862.0	169.5	0.2923E+05	0.1612E+05	0.2863E+03	0.2530E+04
862.0	170.5	0.2995E+05	0.1847E+05	0.3257E+03	0.2592E+04
862.0	171.5	0.2822E+05	0.1618E+05	0.2815E+03	0.2515E+04
862.0	172.5	0.2824E+05	0.1644E+05	0.2835E+03	0.2505E+04
862.0	173.5	0.2947E+05	0.1968E+05	0.3400E+03	0.2596E+04
862.0	174.5	0.2760E+05	0.2002E+05	0.3457E+03	0.2553E+04
862.0	175.5	0.2842E+05	0.1902E+05	0.3301E+03	0.2547E+04
862.0	176.5	0.3025E+05	0.1949E+05	0.3355E+03	0.2564E+04
862.0	177.5	0.2998E+05	0.1978E+05	0.3466E+03	0.2565E+04
862.0	178.5	0.2941E+05	0.1775E+05	0.3182E+03	0.2488E+04
862.0	179.5	0.2977E+05	0.1844E+05	0.3389E+03	0.2500E+04
862.0	180.5	0.2960E+05	0.1807E+05	0.3370E+03	0.2485E+04
862.0	181.5	0.2814E+05	0.1933E+05	0.3637E+03	0.2519E+04
862.0	182.5	0.2874E+05	0.2087E+05	0.3917E+03	0.2566E+04
862.0	183.5	0.2832E+05	0.1864E+05	0.3462E+03	0.2487E+04
862.0	184.5	0.2941E+05	0.1892E+05	0.3509E+03	0.2489E+04

continued on next page

Table G.1: *Unpolarized cross sections continued*

E_0	ν	σ_{exp}	σ_{born}	dσ_{stat}	dσ_{syst}
862.0	185.5	0.2992E+05	0.2117E+05	0.3907E+03	0.2564E+04
862.0	186.5	0.2830E+05	0.1918E+05	0.3519E+03	0.2487E+04
862.0	187.5	0.2902E+05	0.2110E+05	0.3849E+03	0.2551E+04
862.0	188.5	0.3005E+05	0.2026E+05	0.3672E+03	0.2488E+04
862.0	189.5	0.2861E+05	0.2211E+05	0.4029E+03	0.2578E+04
862.0	190.5	0.3003E+05	0.2198E+05	0.4079E+03	0.2573E+04
862.0	191.5	0.2918E+05	0.1993E+05	0.3776E+03	0.2489E+04
862.0	192.5	0.3074E+05	0.2228E+05	0.4297E+03	0.2577E+04
862.0	193.5	0.3002E+05	0.2083E+05	0.4062E+03	0.2511E+04
862.0	194.5	0.2906E+05	0.2300E+05	0.4495E+03	0.2598E+04
862.0	195.5	0.3052E+05	0.2287E+05	0.4453E+03	0.2588E+04
862.0	196.5	0.2931E+05	0.2187E+05	0.4212E+03	0.2543E+04
862.0	197.5	0.3113E+05	0.2215E+05	0.4239E+03	0.2551E+04
862.0	198.5	0.3039E+05	0.2263E+05	0.4312E+03	0.2566E+04
862.0	199.5	0.2992E+05	0.2298E+05	0.4359E+03	0.2580E+04
862.0	200.5	0.3020E+05	0.2343E+05	0.4426E+03	0.2596E+04
862.0	201.5	0.3041E+05	0.2388E+05	0.4492E+03	0.2613E+04
862.0	202.5	0.3062E+05	0.2407E+05	0.4509E+03	0.2623E+04
862.0	203.5	0.3083E+05	0.2455E+05	0.4580E+03	0.2642E+04
862.0	204.5	0.3104E+05	0.2487E+05	0.4622E+03	0.2655E+04
862.0	205.5	0.3125E+05	0.2528E+05	0.4677E+03	0.2672E+04
862.0	206.5	0.3146E+05	0.2561E+05	0.4721E+03	0.2687E+04
862.0	207.5	0.3167E+05	0.2591E+05	0.4755E+03	0.2700E+04
862.0	208.5	0.3188E+05	0.2634E+05	0.4816E+03	0.2719E+04
862.0	209.5	0.3209E+05	0.2673E+05	0.4869E+03	0.2736E+04
862.0	210.5	0.3229E+05	0.2711E+05	0.4918E+03	0.2754E+04
862.0	211.5	0.3250E+05	0.2741E+05	0.4953E+03	0.2767E+04
862.0	212.5	0.3271E+05	0.2787E+05	0.5016E+03	0.2789E+04
862.0	213.5	0.3292E+05	0.2824E+05	0.5064E+03	0.2806E+04
862.0	214.5	0.3313E+05	0.2846E+05	0.5085E+03	0.2816E+04
862.0	215.5	0.3334E+05	0.2888E+05	0.5140E+03	0.2837E+04
862.0	216.5	0.3355E+05	0.2916E+05	0.5170E+03	0.2849E+04
862.0	217.5	0.3376E+05	0.2939E+05	0.5193E+03	0.2860E+04
862.0	218.5	0.3397E+05	0.2974E+05	0.5236E+03	0.2877E+04
862.0	219.5	0.3418E+05	0.2998E+05	0.5260E+03	0.2889E+04
862.0	220.5	0.3439E+05	0.3028E+05	0.5293E+03	0.2903E+04

continued on next page

Table G.1: *Unpolarized cross sections continued*

E_0	ν	σ_{exp}	σ_{born}	dσ_{stat}	dσ_{syst}
862.0	221.5	0.3460E+05	0.3065E+05	0.5339E+03	0.2921E+04
862.0	222.5	0.3481E+05	0.3095E+05	0.5372E+03	0.2935E+04
862.0	223.5	0.3501E+05	0.3134E+05	0.5419E+03	0.2955E+04
862.0	224.5	0.3522E+05	0.3168E+05	0.5461E+03	0.2972E+04
862.0	225.5	0.3543E+05	0.3195E+05	0.5487E+03	0.2984E+04
862.0	226.5	0.3564E+05	0.3228E+05	0.5525E+03	0.3001E+04
862.0	227.5	0.3585E+05	0.3251E+05	0.5547E+03	0.3012E+04
862.0	228.5	0.3606E+05	0.3276E+05	0.5570E+03	0.3023E+04
862.0	229.5	0.3627E+05	0.3310E+05	0.5610E+03	0.3040E+04
862.0	230.5	0.3648E+05	0.3337E+05	0.5637E+03	0.3053E+04
862.0	231.5	0.3669E+05	0.3362E+05	0.5660E+03	0.3064E+04
862.0	232.5	0.3690E+05	0.3399E+05	0.5703E+03	0.3083E+04
862.0	233.5	0.3711E+05	0.3431E+05	0.5739E+03	0.3099E+04
862.0	234.5	0.3732E+05	0.3461E+05	0.5771E+03	0.3114E+04
862.0	235.5	0.3753E+05	0.3495E+05	0.5809E+03	0.3132E+04
862.0	236.5	0.3773E+05	0.3525E+05	0.5840E+03	0.3146E+04
862.0	237.5	0.3794E+05	0.3550E+05	0.5863E+03	0.3158E+04
862.0	238.5	0.3815E+05	0.3583E+05	0.5901E+03	0.3175E+04
862.0	239.5	0.3836E+05	0.3614E+05	0.5932E+03	0.3190E+04
862.0	240.5	0.3857E+05	0.3644E+05	0.5964E+03	0.3205E+04
862.0	241.5	0.3878E+05	0.3672E+05	0.5992E+03	0.3219E+04
862.0	242.5	0.3899E+05	0.3699E+05	0.6018E+03	0.3232E+04
862.0	243.5	0.3920E+05	0.3729E+05	0.6048E+03	0.3247E+04
862.0	244.5	0.3941E+05	0.3748E+05	0.6061E+03	0.3255E+04
862.0	245.5	0.3962E+05	0.3772E+05	0.6082E+03	0.3265E+04
862.0	246.5	0.3983E+05	0.3801E+05	0.6112E+03	0.3280E+04
862.0	247.5	0.4004E+05	0.3828E+05	0.6137E+03	0.3293E+04
862.0	248.5	0.4025E+05	0.3855E+05	0.6162E+03	0.3305E+04
862.0	249.5	0.4045E+05	0.3885E+05	0.6193E+03	0.3321E+04
862.0	250.5	0.4066E+05	0.3914E+05	0.6222E+03	0.3335E+04
862.0	251.5	0.4087E+05	0.3940E+05	0.6246E+03	0.3347E+04
862.0	252.5	0.4108E+05	0.3969E+05	0.6272E+03	0.3361E+04
862.0	253.5	0.4129E+05	0.3987E+05	0.6292E+03	0.3369E+04
862.0	254.5	0.4150E+05	0.4062E+05	0.6324E+03	0.3410E+04
862.0	255.5	0.4171E+05	0.3919E+05	0.6095E+03	0.3328E+04
862.0	256.5	0.4192E+05	0.4038E+05	0.6337E+03	0.3393E+04

continued on next page

Table G.1: *Unpolarized cross sections continued*

E_0	ν	σ_{exp}	σ_{born}	$d\sigma_{stat}$	$d\sigma_{syst}$
862.0	257.5	0.4228E+05	0.3807E+05	0.5852E+03	0.3263E+04
862.0	258.5	0.4142E+05	0.4131E+05	0.6326E+03	0.3444E+04
862.0	259.5	0.4227E+05	0.3950E+05	0.5972E+03	0.3339E+04
862.0	260.5	0.4082E+05	0.4000E+05	0.6046E+03	0.3365E+04
862.0	261.5	0.4330E+05	0.4026E+05	0.6078E+03	0.3378E+04
862.0	262.5	0.4157E+05	0.4087E+05	0.6177E+03	0.3411E+04
862.0	263.5	0.4254E+05	0.4007E+05	0.6140E+03	0.3365E+04
862.0	264.5	0.4248E+05	0.4191E+05	0.6364E+03	0.3468E+04
862.0	265.5	0.4294E+05	0.4258E+05	0.6491E+03	0.3505E+04
862.0	266.5	0.4247E+05	0.4210E+05	0.6386E+03	0.3478E+04
862.0	267.5	0.4393E+05	0.4142E+05	0.6292E+03	0.3437E+04
862.0	268.5	0.4404E+05	0.4591E+05	0.7450E+03	0.3696E+04
862.0	269.5	0.4369E+05	0.4391E+05	0.7422E+03	0.3579E+04
862.0	270.5	0.4370E+05	0.4572E+05	0.7439E+03	0.3682E+04
862.0	271.5	0.4661E+05	0.4126E+05	0.6412E+03	0.3426E+04
862.0	272.5	0.4487E+05	0.4401E+05	0.6694E+03	0.3581E+04
862.0	273.5	0.4627E+05	0.4375E+05	0.6581E+03	0.3566E+04
862.0	274.5	0.4307E+05	0.4292E+05	0.6353E+03	0.3516E+04
862.0	275.5	0.4575E+05	0.4465E+05	0.6631E+03	0.3613E+04
862.0	276.5	0.4472E+05	0.4648E+05	0.6914E+03	0.3724E+04
862.0	277.5	0.4479E+05	0.4727E+05	0.7049E+03	0.3769E+04
862.0	278.5	0.4607E+05	0.4637E+05	0.7128E+03	0.3713E+04
862.0	279.5	0.4714E+05	0.4480E+05	0.7126E+03	0.3621E+04
862.0	280.5	0.4756E+05	0.4559E+05	0.7583E+03	0.3666E+04
862.0	281.5	0.4689E+05	0.4603E+05	0.7719E+03	0.3690E+04
862.0	282.5	0.4606E+05	0.4504E+05	0.7544E+03	0.3630E+04
862.0	283.5	0.4682E+05	0.4787E+05	0.7984E+03	0.3796E+04
862.0	284.5	0.4686E+05	0.4823E+05	0.7948E+03	0.3814E+04
862.0	285.5	0.4657E+05	0.4989E+05	0.8244E+03	0.3910E+04
862.0	286.5	0.4855E+05	0.4836E+05	0.7874E+03	0.3817E+04
862.0	287.5	0.4863E+05	0.4651E+05	0.7477E+03	0.3709E+04
862.0	288.5	0.4986E+05	0.4786E+05	0.7807E+03	0.3786E+04
862.0	289.5	0.4845E+05	0.5040E+05	0.8411E+03	0.3938E+04
862.0	290.5	0.4767E+05	0.4817E+05	0.8290E+03	0.3807E+04
862.0	291.5	0.4894E+05	0.4875E+05	0.8523E+03	0.3840E+04
862.0	292.5	0.5028E+05	0.4959E+05	0.8897E+03	0.3887E+04

continued on next page

Table G.1: *Unpolarized cross sections continued*

E_0	ν	σ_{exp}	σ_{born}	$d\sigma_{stat}$	$d\sigma_{syst}$
862.0	293.5	0.4862E+05	0.4955E+05	0.8893E+03	0.3884E+04
862.0	294.5	0.4950E+05	0.5123E+05	0.9073E+03	0.3981E+04
862.0	295.5	0.4988E+05	0.5137E+05	0.8989E+03	0.3989E+04
862.0	296.5	0.5003E+05	0.5077E+05	0.8511E+03	0.3936E+04
862.0	297.5	0.5126E+05	0.5030E+05	0.8019E+03	0.3886E+04
862.0	298.5	0.5109E+05	0.4935E+05	0.7408E+03	0.3801E+04
862.0	299.5	0.5080E+05	0.5270E+05	0.7954E+03	0.4050E+04
862.0	300.5	0.5050E+05	0.5340E+05	0.8007E+03	0.4106E+04
862.0	301.5	0.5021E+05	0.4981E+05	0.7354E+03	0.3890E+04
862.0	302.5	0.5275E+05	0.5176E+05	0.7827E+03	0.4007E+04
862.0	303.5	0.5235E+05	0.5352E+05	0.7897E+03	0.4108E+04
862.0	304.5	0.5028E+05	0.5052E+05	0.7285E+03	0.3931E+04
862.0	305.5	0.5232E+05	0.5205E+05	0.7514E+03	0.4018E+04
862.0	306.5	0.5287E+05	0.5240E+05	0.7593E+03	0.4038E+04
862.0	307.5	0.5100E+05	0.5363E+05	0.7791E+03	0.4109E+04
862.0	308.5	0.5255E+05	0.5015E+05	0.7181E+03	0.3905E+04
862.0	309.5	0.5256E+05	0.5362E+05	0.7821E+03	0.4104E+04
862.0	310.5	0.5326E+05	0.5136E+05	0.7436E+03	0.3972E+04
862.0	311.5	0.5112E+05	0.5097E+05	0.7457E+03	0.3947E+04
862.0	312.5	0.5392E+05	0.5518E+05	0.8116E+03	0.4192E+04
862.0	313.5	0.5163E+05	0.5694E+05	0.8694E+03	0.4293E+04
862.0	314.5	0.5244E+05	0.5446E+05	0.8927E+03	0.4148E+04
862.0	315.5	0.5528E+05	0.5357E+05	0.8475E+03	0.4096E+04
862.0	316.5	0.5592E+05	0.5197E+05	0.7771E+03	0.4005E+04
862.0	317.5	0.5410E+05	0.5301E+05	0.7692E+03	0.4065E+04
862.0	318.5	0.5370E+05	0.5234E+05	0.7430E+03	0.4028E+04
862.0	319.5	0.5289E+05	0.5544E+05	0.7912E+03	0.4206E+04
862.0	320.5	0.5370E+05	0.5691E+05	0.8181E+03	0.4291E+04
862.0	321.5	0.5323E+05	0.5654E+05	0.8128E+03	0.4267E+04
862.0	322.5	0.5579E+05	0.5680E+05	0.8243E+03	0.4284E+04
862.0	323.5	0.5626E+05	0.5370E+05	0.8197E+03	0.4102E+04
862.0	324.5	0.5626E+05	0.5493E+05	0.8866E+03	0.4172E+04
862.0	325.5	0.5606E+05	0.5487E+05	0.8973E+03	0.4169E+04
862.0	326.5	0.5418E+05	0.5678E+05	0.9279E+03	0.4278E+04
862.0	327.5	0.5546E+05	0.5517E+05	0.9011E+03	0.4183E+04
862.0	328.5	0.5525E+05	0.5553E+05	0.8958E+03	0.4203E+04

continued on next page

Table G.1: *Unpolarized cross sections continued*

E_0	ν	σ_{exp}	σ_{born}	$d\sigma_{stat}$	$d\sigma_{syst}$
862.0	329.5	0.5669E+05	0.5823E+05	0.9459E+03	0.4359E+04
862.0	330.5	0.5534E+05	0.5848E+05	0.9370E+03	0.4375E+04
862.0	331.5	0.5627E+05	0.5683E+05	0.9069E+03	0.4276E+04
862.0	332.5	0.5800E+05	0.6063E+05	0.9860E+03	0.4503E+04
862.0	333.5	0.5769E+05	0.5741E+05	0.9636E+03	0.4310E+04
862.0	334.5	0.5711E+05	0.5861E+05	0.1022E+04	0.4376E+04
862.0	335.5	0.5954E+05	0.5797E+05	0.1028E+04	0.4354E+04
862.0	336.5	0.5705E+05	0.5750E+05	0.1020E+04	0.4331E+04
862.0	337.5	0.5859E+05	0.5821E+05	0.1024E+04	0.4371E+04
862.0	338.5	0.5770E+05	0.5773E+05	0.1012E+04	0.4342E+04
862.0	339.5	0.5778E+05	0.5799E+05	0.9842E+03	0.4355E+04
862.0	340.5	0.5817E+05	0.5860E+05	0.9546E+03	0.4390E+04
862.0	341.5	0.5792E+05	0.5921E+05	0.9279E+03	0.4424E+04
862.0	342.5	0.5831E+05	0.5932E+05	0.8878E+03	0.4429E+04
862.0	343.5	0.5871E+05	0.6173E+05	0.9230E+03	0.4550E+04
862.0	344.5	0.5911E+05	0.5964E+05	0.8759E+03	0.4424E+04
862.0	345.5	0.5950E+05	0.5982E+05	0.8957E+03	0.4437E+04
862.0	346.5	0.6110E+05	0.5838E+05	0.8512E+03	0.4351E+04
862.0	347.5	0.5937E+05	0.5906E+05	0.8429E+03	0.4392E+04
862.0	348.5	0.5976E+05	0.5853E+05	0.8355E+03	0.4359E+04
862.0	349.5	0.5879E+05	0.6100E+05	0.8686E+03	0.4504E+04
862.0	350.5	0.5947E+05	0.6159E+05	0.8679E+03	0.4538E+04
862.0	351.5	0.5922E+05	0.5804E+05	0.8297E+03	0.4331E+04
862.0	352.5	0.6113E+05	0.6249E+05	0.9040E+03	0.4588E+04
862.0	353.5	0.6080E+05	0.5978E+05	0.8716E+03	0.4428E+04
862.0	354.5	0.5910E+05	0.5975E+05	0.8681E+03	0.4423E+04
862.0	355.5	0.6236E+05	0.6708E+05	0.1012E+04	0.4855E+04
862.0	356.5	0.5965E+05	0.6147E+05	0.1015E+04	0.4526E+04
862.0	357.5	0.6113E+05	0.6105E+05	0.9749E+03	0.4497E+04
862.0	358.5	0.6534E+05	0.5925E+05	0.8897E+03	0.4396E+04
862.0	359.5	0.6070E+05	0.5886E+05	0.8396E+03	0.4373E+04
862.0	360.5	0.6159E+05	0.6021E+05	0.8505E+03	0.4446E+04
862.0	361.5	0.5980E+05	0.6085E+05	0.8479E+03	0.4481E+04
862.0	362.5	0.6025E+05	0.6307E+05	0.8917E+03	0.4612E+04
862.0	363.5	0.6104E+05	0.6381E+05	0.9183E+03	0.4654E+04
862.0	364.5	0.6164E+05	0.6062E+05	0.8840E+03	0.4468E+04

continued on next page

Table G.1: *Unpolarized cross sections continued*

E_0	ν	σ_{exp}	σ_{born}	$d\sigma_{stat}$	$d\sigma_{syst}$
862.0	365.5	0.6318E+05	0.6013E+05	0.9526E+03	0.4443E+04
862.0	366.5	0.6325E+05	0.6049E+05	0.1010E+04	0.4458E+04
862.0	367.5	0.6121E+05	0.5983E+05	0.1002E+04	0.4420E+04
862.0	368.5	0.6127E+05	0.6423E+05	0.1074E+04	0.4675E+04
862.0	369.5	0.6146E+05	0.6295E+05	0.1037E+04	0.4596E+04
862.0	370.5	0.6135E+05	0.5891E+05	0.9452E+03	0.4368E+04
862.0	371.5	0.6447E+05	0.6274E+05	0.1008E+04	0.4586E+04
862.0	372.5	0.6279E+05	0.5952E+05	0.9517E+03	0.4400E+04
862.0	373.5	0.6094E+05	0.6628E+05	0.1096E+04	0.4791E+04
862.0	374.5	0.6351E+05	0.6151E+05	0.1064E+04	0.4514E+04
862.0	375.5	0.6129E+05	0.6508E+05	0.1178E+04	0.4723E+04
862.0	376.5	0.6618E+05	0.6280E+05	0.1153E+04	0.4594E+04
862.0	377.5	0.6214E+05	0.6344E+05	0.1153E+04	0.4629E+04
862.0	378.5	0.6560E+05	0.6260E+05	0.1128E+04	0.4576E+04
862.0	379.5	0.6307E+05	0.6307E+05	0.1093E+04	0.4600E+04
862.0	380.5	0.6440E+05	0.6434E+05	0.1065E+04	0.4673E+04
862.0	381.5	0.6332E+05	0.6539E+05	0.1034E+04	0.4732E+04
862.0	382.5	0.6415E+05	0.6650E+05	0.1004E+04	0.4795E+04
862.0	383.5	0.6498E+05	0.6758E+05	0.9695E+03	0.4855E+04
862.0	384.5	0.6580E+05	0.6812E+05	0.9651E+03	0.4889E+04
862.0	385.5	0.6663E+05	0.6608E+05	0.9383E+03	0.4767E+04
862.0	386.5	0.6746E+05	0.6459E+05	0.8989E+03	0.4681E+04
862.0	387.5	0.6747E+05	0.6750E+05	0.9254E+03	0.4848E+04
862.0	388.5	0.6604E+05	0.6666E+05	0.9091E+03	0.4798E+04
862.0	389.5	0.6563E+05	0.6737E+05	0.9165E+03	0.4840E+04
862.0	390.5	0.6771E+05	0.6910E+05	0.9441E+03	0.4937E+04
862.0	391.5	0.6690E+05	0.6493E+05	0.8873E+03	0.4700E+04
862.0	392.5	0.6774E+05	0.6813E+05	0.9417E+03	0.4881E+04
862.0	393.5	0.6850E+05	0.6731E+05	0.9413E+03	0.4832E+04
862.0	394.5	0.6580E+05	0.6754E+05	0.9217E+03	0.4847E+04
862.0	395.5	0.6879E+05	0.7114E+05	0.1117E+04	0.5054E+04
862.0	396.5	0.6740E+05	0.6934E+05	0.1058E+04	0.4947E+04
862.0	397.5	0.6833E+05	0.6794E+05	0.9774E+03	0.4864E+04
862.0	398.5	0.7062E+05	0.6820E+05	0.9380E+03	0.4878E+04
862.0	399.5	0.6883E+05	0.6680E+05	0.8984E+03	0.4803E+04
862.0	400.5	0.6862E+05	0.7043E+05	0.9557E+03	0.5008E+04

continued on next page

Table G.1: *Unpolarized cross sections continued*

E_0	ν	σ_{exp}	σ_{born}	$d\sigma_{stat}$	$d\sigma_{syst}$
862.0	401.5	0.6869E+05	0.7351E+05	0.1007E+04	0.5189E+04
862.0	402.5	0.6790E+05	0.6979E+05	0.9594E+03	0.4971E+04
862.0	403.5	0.7101E+05	0.6910E+05	0.1019E+04	0.4927E+04
862.0	404.5	0.7218E+05	0.6874E+05	0.1063E+04	0.4908E+04
862.0	405.5	0.6968E+05	0.6972E+05	0.1122E+04	0.4962E+04
862.0	406.5	0.6979E+05	0.7558E+05	0.1209E+04	0.5307E+04
862.0	407.5	0.6948E+05	0.7234E+05	0.1129E+04	0.5113E+04
862.0	408.5	0.7098E+05	0.7214E+05	0.1118E+04	0.5100E+04
862.0	409.5	0.7445E+05	0.7082E+05	0.1088E+04	0.5025E+04
862.0	410.5	0.7170E+05	0.7360E+05	0.1121E+04	0.5188E+04
862.0	411.5	0.7221E+05	0.7538E+05	0.1182E+04	0.5288E+04
862.0	412.5	0.7133E+05	0.6919E+05	0.1146E+04	0.4931E+04
862.0	413.5	0.7383E+05	0.7469E+05	0.1282E+04	0.5252E+04
862.0	414.5	0.7395E+05	0.7473E+05	0.1291E+04	0.5248E+04
862.0	415.5	0.7036E+05	0.7723E+05	0.1328E+04	0.5393E+04
862.0	416.5	0.7489E+05	0.7527E+05	0.1270E+04	0.5278E+04
862.0	417.5	0.7420E+05	0.8292E+05	0.1438E+04	0.5728E+04
1716.9	50.0	0.1767E+04	0.6065E+04	0.1094E+03	0.4851E+03
1716.9	55.0	0.3209E+04	0.1061E+05	0.1573E+03	0.7177E+03
1716.9	60.0	0.5179E+04	0.1421E+05	0.1878E+03	0.9163E+03
1716.9	65.0	0.6930E+04	0.1713E+05	0.2123E+03	0.1073E+04
1716.9	70.0	0.8595E+04	0.2088E+05	0.2402E+03	0.1267E+04
1716.9	75.0	0.1089E+05	0.2626E+05	0.2876E+03	0.1563E+04
1716.9	80.0	0.1377E+05	0.3068E+05	0.3250E+03	0.1809E+04
1716.9	85.0	0.1626E+05	0.3685E+05	0.3805E+03	0.2137E+04
1716.9	90.0	0.1979E+05	0.4261E+05	0.4290E+03	0.2447E+04
1716.9	95.0	0.2310E+05	0.5052E+05	0.5087E+03	0.2876E+04
1716.9	100.0	0.2746E+05	0.5477E+05	0.5579E+03	0.3086E+04
1716.9	105.0	0.2975E+05	0.5665E+05	0.5575E+03	0.3180E+04
1716.9	110.0	0.3149E+05	0.5656E+05	0.5369E+03	0.3151E+04
1716.9	115.0	0.3256E+05	0.5890E+05	0.5663E+03	0.3267E+04
1716.9	120.0	0.3458E+05	0.5640E+05	0.5413E+03	0.3106E+04
1716.9	125.0	0.3359E+05	0.5056E+05	0.4937E+03	0.2762E+04
1716.9	130.0	0.3176E+05	0.4471E+05	0.4539E+03	0.2427E+04
1716.9	135.0	0.2984E+05	0.3960E+05	0.4107E+03	0.2141E+04
1716.9	140.0	0.2808E+05	0.3558E+05	0.3723E+03	0.1915E+04

continued on next page

Table G.1: *Unpolarized cross sections continued*

E_0	ν	σ_{exp}	σ_{born}	$d\sigma_{stat}$	$d\sigma_{syst}$
1716.9	145.0	0.2631E+05	0.2936E+05	0.3066E+03	0.1576E+04
1716.9	150.0	0.2344E+05	0.2531E+05	0.2692E+03	0.1357E+04
1716.9	155.0	0.2178E+05	0.2128E+05	0.2321E+03	0.1143E+04
1716.9	160.0	0.1960E+05	0.1767E+05	0.2043E+03	0.9588E+03
1716.9	165.0	0.1787E+05	0.1581E+05	0.1799E+03	0.8637E+03
1716.9	170.0	0.1669E+05	0.1303E+05	0.1910E+03	0.7246E+03
1716.9	175.0	0.1494E+05	0.1085E+05	0.1720E+03	0.6190E+03
1716.9	180.0	0.1375E+05	0.9793E+04	0.1202E+03	0.5676E+03
1716.9	185.0	0.1291E+05	0.8474E+04	0.8366E+02	0.5073E+03
1716.9	190.0	0.1186E+05	0.6990E+04	0.6748E+02	0.4430E+03
1716.9	195.0	0.1088E+05	0.6266E+04	0.6136E+02	0.4106E+03
1716.9	200.0	0.1030E+05	0.5792E+04	0.5677E+02	0.3863E+03
1716.9	205.0	0.9717E+04	0.4937E+04	0.4879E+02	0.3521E+03
1716.9	210.0	0.9028E+04	0.4465E+04	0.4465E+02	0.3312E+03
1716.9	215.0	0.8594E+04	0.4211E+04	0.4213E+02	0.3169E+03
1716.9	220.0	0.8228E+04	0.4159E+04	0.4447E+02	0.3069E+03
1716.9	225.0	0.7964E+04	0.3848E+04	0.4209E+02	0.2919E+03
1716.9	230.0	0.7569E+04	0.3471E+04	0.3604E+02	0.2764E+03
1716.9	235.0	0.7222E+04	0.3252E+04	0.3289E+02	0.2651E+03
1716.9	240.0	0.6986E+04	0.3561E+04	0.3623E+02	0.2663E+03
1716.9	245.0	0.6978E+04	0.3625E+04	0.3804E+02	0.2622E+03
1716.9	250.0	0.6785E+04	0.3354E+04	0.3790E+02	0.2508E+03
1716.9	255.0	0.6548E+04	0.3546E+04	0.4207E+02	0.2520E+03
1716.9	260.0	0.6550E+04	0.3590E+04	0.4228E+02	0.2498E+03
1716.9	265.0	0.6419E+04	0.3626E+04	0.4185E+02	0.2478E+03
1716.9	270.0	0.6375E+04	0.4050E+04	0.4665E+02	0.2600E+03
1716.9	275.0	0.6488E+04	0.4276E+04	0.5125E+02	0.2664E+03
1716.9	280.0	0.6483E+04	0.4494E+04	0.5916E+02	0.2738E+03
1716.9	285.0	0.6525E+04	0.4586E+04	0.5010E+02	0.2768E+03
1716.9	290.0	0.6532E+04	0.5191E+04	0.9778E+02	0.3011E+03
1716.9	295.0	0.6830E+04	0.5970E+04	0.1142E+03	0.3359E+03
1716.9	300.0	0.7116E+04	0.6320E+04	0.7683E+02	0.3531E+03
1716.9	305.0	0.7182E+04	0.5966E+04	0.6139E+02	0.3362E+03
1716.9	310.0	0.7009E+04	0.5944E+04	0.6197E+02	0.3364E+03
1716.9	315.0	0.7110E+04	0.6547E+04	0.6602E+02	0.3652E+03
1716.9	320.0	0.7354E+04	0.6470E+04	0.6460E+02	0.3615E+03

continued on next page

Table G.1: *Unpolarized cross sections continued*

E_0	ν	σ_{exp}	σ_{born}	dσ_{stat}	dσ_{syst}
1716.9	325.0	0.7303E+04	0.7315E+04	0.7523E+02	0.4037E+03
1716.9	330.0	0.7747E+04	0.7355E+04	0.7396E+02	0.4055E+03
1716.9	335.0	0.7718E+04	0.8287E+04	0.8878E+02	0.4536E+03
1716.9	340.0	0.8253E+04	0.8388E+04	0.9237E+02	0.4589E+03
1716.9	345.0	0.8179E+04	0.8209E+04	0.8329E+02	0.4501E+03
1716.9	350.0	0.8236E+04	0.8805E+04	0.8624E+02	0.4820E+03
1716.9	355.0	0.8625E+04	0.9655E+04	0.9466E+02	0.5257E+03
1716.9	360.0	0.8986E+04	0.9597E+04	0.9834E+02	0.5219E+03
1716.9	365.0	0.8930E+04	0.9574E+04	0.1070E+03	0.5227E+03
1716.9	370.0	0.9070E+04	0.1006E+05	0.1142E+03	0.5469E+03
1716.9	375.0	0.9352E+04	0.1023E+05	0.1135E+03	0.5551E+03
1716.9	380.0	0.9461E+04	0.1061E+05	0.1155E+03	0.5764E+03
1716.9	385.0	0.9688E+04	0.1043E+05	0.1131E+03	0.5660E+03
1716.9	390.0	0.9633E+04	0.1070E+05	0.1264E+03	0.5795E+03
1716.9	395.0	0.9881E+04	0.1078E+05	0.1132E+03	0.5838E+03
1716.9	400.0	0.9889E+04	0.1043E+05	0.1777E+03	0.5650E+03
1716.9	405.0	0.9802E+04	0.1070E+05	0.2326E+03	0.5787E+03
1716.9	410.0	0.1009E+05	0.1164E+05	0.1678E+03	0.6277E+03
1716.9	415.0	0.1051E+05	0.1149E+05	0.1327E+03	0.6216E+03
1716.9	420.0	0.1037E+05	0.1123E+05	0.1321E+03	0.6074E+03
1716.9	425.0	0.1037E+05	0.1109E+05	0.1278E+03	0.5981E+03
1716.9	430.0	0.1036E+05	0.1073E+05	0.1245E+03	0.5793E+03
1716.9	435.0	0.1015E+05	0.9662E+04	0.1069E+03	0.5250E+03
1716.9	440.0	0.9776E+04	0.1048E+05	0.1286E+03	0.5645E+03
1716.9	445.0	0.1023E+05	0.9601E+04	0.1219E+03	0.5197E+03
1716.9	450.0	0.9605E+04	0.9148E+04	0.1105E+03	0.4981E+03
1716.9	455.0	0.9574E+04	0.9163E+04	0.1041E+03	0.4983E+03
1716.9	460.0	0.9597E+04	0.9645E+04	0.1106E+03	0.5216E+03
1716.9	465.0	0.9696E+04	0.8148E+04	0.1033E+03	0.4486E+03
1716.9	470.0	0.8928E+04	0.8482E+04	0.1309E+03	0.4639E+03
1716.9	475.0	0.9307E+04	0.8520E+04	0.1281E+03	0.4659E+03
1716.9	480.0	0.9094E+04	0.7898E+04	0.1174E+03	0.4338E+03
1716.9	485.0	0.8770E+04	0.7091E+04	0.1013E+03	0.3983E+03
1716.9	490.0	0.8440E+04	0.7578E+04	0.1272E+03	0.4202E+03
1716.9	495.0	0.8670E+04	0.6915E+04	0.1029E+03	0.3881E+03
1716.9	500.0	0.8219E+04	0.7390E+04	0.1839E+03	0.4088E+03

continued on next page

Table G.1: *Unpolarized cross sections continued*

E_0	ν	σ_{exp}	σ_{born}	dσ_{stat}	dσ_{syst}
1716.9	505.0	0.8570E+04	0.7387E+04	0.1668E+03	0.4073E+03
1716.9	510.0	0.8315E+04	0.6233E+04	0.7185E+02	0.3545E+03
1716.9	515.0	0.7771E+04	0.5798E+04	0.5165E+02	0.3352E+03
1716.9	520.0	0.7645E+04	0.5733E+04	0.5418E+02	0.3313E+03
1716.9	525.0	0.7538E+04	0.5443E+04	0.5056E+02	0.3179E+03
1716.9	530.0	0.7298E+04	0.5028E+04	0.4737E+02	0.3001E+03
1716.9	535.0	0.7104E+04	0.5308E+04	0.5037E+02	0.3109E+03
1716.9	540.0	0.7228E+04	0.5480E+04	0.5849E+02	0.3172E+03
1716.9	545.0	0.7153E+04	0.4828E+04	0.4835E+02	0.2903E+03
1716.9	550.0	0.6776E+04	0.4524E+04	0.4197E+02	0.2776E+03
1716.9	555.0	0.6701E+04	0.4885E+04	0.4557E+02	0.2908E+03
1716.9	560.0	0.6808E+04	0.4664E+04	0.4781E+02	0.2804E+03
1716.9	565.0	0.6605E+04	0.4688E+04	0.5290E+02	0.2807E+03
1716.9	570.0	0.6614E+04	0.4567E+04	0.5170E+02	0.2752E+03
1716.9	575.0	0.6486E+04	0.4433E+04	0.4838E+02	0.2695E+03
1716.9	580.0	0.6413E+04	0.4314E+04	0.4794E+02	0.2640E+03
1716.9	585.0	0.6290E+04	0.3929E+04	0.4664E+02	0.2491E+03
1716.9	590.0	0.6101E+04	0.4099E+04	0.4963E+02	0.2546E+03
1716.9	595.0	0.6207E+04	0.4621E+04	0.5445E+02	0.2752E+03
1716.9	600.0	0.6396E+04	0.4756E+04	0.5274E+02	0.2805E+03
1716.9	605.0	0.6344E+04	0.3980E+04	0.3874E+02	0.2491E+03
1716.9	610.0	0.5942E+04	0.3738E+04	0.3444E+02	0.2394E+03
1716.9	615.0	0.5918E+04	0.3860E+04	0.3547E+02	0.2434E+03
1716.9	620.0	0.5931E+04	0.3883E+04	0.3620E+02	0.2436E+03
1716.9	625.0	0.5892E+04	0.3919E+04	0.3648E+02	0.2445E+03
1716.9	630.0	0.5897E+04	0.4178E+04	0.4412E+02	0.2543E+03
1716.9	635.0	0.5967E+04	0.3719E+04	0.3684E+02	0.2363E+03
1716.9	640.0	0.5688E+04	0.3540E+04	0.3264E+02	0.2295E+03
1716.9	645.0	0.5676E+04	0.3787E+04	0.3453E+02	0.2384E+03
1716.9	650.0	0.5749E+04	0.3679E+04	0.3837E+02	0.2336E+03
1716.9	655.0	0.5629E+04	0.3509E+04	0.3895E+02	0.2273E+03
1716.9	660.0	0.5561E+04	0.3668E+04	0.4052E+02	0.2329E+03
1716.9	665.0	0.5626E+04	0.3618E+04	0.3755E+02	0.2308E+03
1716.9	670.0	0.5569E+04	0.3773E+04	0.4767E+02	0.2370E+03
1716.9	675.0	0.5636E+04	0.3820E+04	0.3235E+02	0.2384E+03
1716.9	680.0	0.5648E+04	0.4119E+04	0.1073E+03	0.2508E+03

continued on next page

Table G.1: *Unpolarized cross sections continued*

E_0	ν	σ_{exp}	σ_{born}	$d\sigma_{stat}$	$d\sigma_{syst}$
1716.9	685.0	0.5828E+04	0.4276E+04	0.8427E+02	0.2579E+03
1716.9	690.0	0.5812E+04	0.3806E+04	0.4604E+02	0.2386E+03
1716.9	695.0	0.5586E+04	0.3737E+04	0.4347E+02	0.2359E+03
1716.9	700.0	0.5623E+04	0.3705E+04	0.4187E+02	0.2345E+03
1716.9	705.0	0.5560E+04	0.3495E+04	0.4147E+02	0.2262E+03
1716.9	710.0	0.5507E+04	0.4041E+04	0.4974E+02	0.2484E+03
1716.9	715.0	0.5749E+04	0.3757E+04	0.4965E+02	0.2378E+03
1716.9	720.0	0.5504E+04	0.3488E+04	0.4255E+02	0.2265E+03
1716.9	725.0	0.5494E+04	0.4160E+04	0.4624E+02	0.2535E+03
1716.9	730.0	0.5770E+04	0.3818E+04	0.4695E+02	0.2398E+03
1716.9	735.0	0.5550E+04	0.3884E+04	0.5941E+02	0.2427E+03
1716.9	740.0	0.5645E+04	0.3787E+04	0.5584E+02	0.2383E+03
1716.9	745.0	0.5539E+04	0.3877E+04	0.5359E+02	0.2423E+03
1716.9	750.0	0.5622E+04	0.3500E+04	0.5990E+02	0.2289E+03
1716.9	755.0	0.5374E+04	0.3525E+04	0.3772E+02	0.2288E+03
1716.9	760.0	0.5528E+04	0.4396E+04	0.1667E+03	0.2657E+03
1716.9	765.0	0.5885E+04	0.4193E+04	0.9677E+02	0.2568E+03
1716.9	770.0	0.5688E+04	0.3775E+04	0.3142E+02	0.2390E+03
1716.9	775.0	0.5541E+04	0.3649E+04	0.3456E+02	0.2340E+03
1716.9	780.0	0.5505E+04	0.3607E+04	0.3329E+02	0.2334E+03
1716.9	785.0	0.5521E+04	0.3725E+04	0.3392E+02	0.2381E+03
1716.9	790.0	0.5594E+04	0.3997E+04	0.4143E+02	0.2492E+03
1716.9	795.0	0.5656E+04	0.3475E+04	0.3396E+02	0.2285E+03
1716.9	800.0	0.5380E+04	0.3551E+04	0.3221E+02	0.2317E+03
1716.9	805.0	0.5544E+04	0.3841E+04	0.3834E+02	0.2432E+03
1716.9	810.0	0.5581E+04	0.3447E+04	0.3873E+02	0.2278E+03
1716.9	815.0	0.5380E+04	0.3569E+04	0.4094E+02	0.2327E+03
1716.9	820.0	0.5491E+04	0.3663E+04	0.4090E+02	0.2368E+03
1716.9	825.0	0.5503E+04	0.3639E+04	0.4409E+02	0.2362E+03
1716.9	830.0	0.5495E+04	0.3472E+04	0.4422E+02	0.2296E+03
1716.9	835.0	0.5419E+04	0.3713E+04	0.6347E+02	0.2400E+03
1716.9	840.0	0.5561E+04	0.3541E+04	0.4550E+02	0.2335E+03
1716.9	845.0	0.5415E+04	0.3301E+04	0.3355E+02	0.2242E+03
1716.9	850.0	0.5353E+04	0.3327E+04	0.3441E+02	0.2251E+03
1716.9	855.0	0.5340E+04	0.3166E+04	0.3299E+02	0.2195E+03
1716.9	860.0	0.5286E+04	0.3456E+04	0.4089E+02	0.2309E+03

continued on next page

Table G.1: *Unpolarized cross sections continued*

E_0	ν	σ_{exp}	σ_{born}	$d\sigma_{stat}$	$d\sigma_{syst}$
1716.9	865.0	0.5401E+04	0.2874E+04	0.3231E+02	0.2096E+03
1716.9	870.0	0.5076E+04	0.3111E+04	0.3181E+02	0.2184E+03
1716.9	875.0	0.5288E+04	0.3122E+04	0.3578E+02	0.2181E+03
1716.9	880.0	0.5193E+04	0.3175E+04	0.4299E+02	0.2213E+03
1716.9	885.0	0.5278E+04	0.3048E+04	0.3900E+02	0.2165E+03
1716.9	890.0	0.5160E+04	0.3149E+04	0.4608E+02	0.2208E+03
1716.9	895.0	0.5256E+04	0.2958E+04	0.2966E+02	0.2149E+03
1716.9	900.0	0.5102E+04	0.2905E+04	0.9078E+02	0.2122E+03
1716.9	905.0	0.5152E+04	0.3125E+04	0.6040E+02	0.2202E+03
1716.9	910.0	0.5214E+04	0.3004E+04	0.2656E+02	0.2169E+03
1716.9	915.0	0.5159E+04	0.2941E+04	0.2786E+02	0.2146E+03
1716.9	920.0	0.5109E+04	0.2627E+04	0.2384E+02	0.2040E+03
1716.9	925.0	0.4978E+04	0.2933E+04	0.2948E+02	0.2155E+03
1716.9	930.0	0.5146E+04	0.2587E+04	0.2581E+02	0.2033E+03
1716.9	935.0	0.4919E+04	0.2845E+04	0.2559E+02	0.2129E+03
1716.9	940.0	0.5105E+04	0.2566E+04	0.2569E+02	0.2032E+03
1716.9	945.0	0.4863E+04	0.2538E+04	0.2896E+02	0.2027E+03
1716.9	950.0	0.4978E+04	0.2856E+04	0.3208E+02	0.2142E+03
1716.9	955.0	0.5046E+04	0.2614E+04	0.2984E+02	0.2062E+03
1716.9	960.0	0.4929E+04	0.2594E+04	0.3480E+02	0.2056E+03
2580.5	95.0	0.4124E+02	0.8785E+02	0.2455E+01	0.1194E+02
2580.5	105.0	0.1029E+03	0.2177E+03	0.5032E+01	0.1947E+02
2580.5	115.0	0.1768E+03	0.3408E+03	0.7301E+01	0.2681E+02
2580.5	125.0	0.2850E+03	0.5267E+03	0.9375E+01	0.3809E+02
2580.5	135.0	0.4242E+03	0.7636E+03	0.1117E+02	0.5261E+02
2580.5	145.0	0.6217E+03	0.1109E+04	0.1465E+02	0.7274E+02
2580.5	155.0	0.9066E+03	0.1606E+04	0.2052E+02	0.1009E+03
2580.5	165.0	0.1295E+04	0.2265E+04	0.2844E+02	0.1375E+03
2580.5	175.0	0.1808E+04	0.3163E+04	0.3253E+02	0.1869E+03
2580.5	185.0	0.2515E+04	0.4327E+04	0.3336E+02	0.2502E+03
2580.5	195.0	0.3330E+04	0.5677E+04	0.4459E+02	0.3231E+03
2580.5	205.0	0.4325E+04	0.7168E+04	0.5649E+02	0.4030E+03
2580.5	215.0	0.5161E+04	0.8225E+04	0.6526E+02	0.4587E+03
2580.5	225.0	0.5814E+04	0.8952E+04	0.6797E+02	0.4960E+03
2580.5	235.0	0.6364E+04	0.9566E+04	0.7252E+02	0.5270E+03
2580.5	245.0	0.6721E+04	0.9503E+04	0.7282E+02	0.5213E+03

continued on next page

Table G.1: *Unpolarized cross sections continued*

E_0	ν	σ_{exp}	σ_{born}	$d\sigma_{stat}$	$d\sigma_{syst}$
2580.5	255.0	0.6355E+04	0.8492E+04	0.6606E+02	0.4644E+03
2580.5	265.0	0.6107E+04	0.7792E+04	0.6188E+02	0.4255E+03
2580.5	275.0	0.5560E+04	0.6615E+04	0.5234E+02	0.3617E+03
2580.5	285.0	0.4936E+04	0.5502E+04	0.4376E+02	0.3018E+03
2580.5	295.0	0.4366E+04	0.4564E+04	0.3769E+02	0.2528E+03
2580.5	305.0	0.3833E+04	0.3744E+04	0.3253E+02	0.2117E+03
2580.5	315.0	0.3366E+04	0.3082E+04	0.2694E+02	0.1780E+03
2580.5	325.0	0.2985E+04	0.2584E+04	0.2203E+02	0.1526E+03
2580.5	335.0	0.2682E+04	0.2221E+04	0.1822E+02	0.1340E+03
2580.5	345.0	0.2447E+04	0.1964E+04	0.1579E+02	0.1205E+03
2580.5	355.0	0.2268E+04	0.1788E+04	0.1438E+02	0.1110E+03
2580.5	365.0	0.2139E+04	0.1690E+04	0.1360E+02	0.1055E+03
2580.5	375.0	0.2051E+04	0.1620E+04	0.1312E+02	0.1014E+03
2580.5	385.0	0.1986E+04	0.1659E+04	0.1374E+02	0.1029E+03
2580.5	395.0	0.2061E+04	0.1810E+04	0.1572E+02	0.1098E+03
2580.5	405.0	0.1993E+04	0.1727E+04	0.1418E+02	0.1051E+03
2580.5	415.0	0.2041E+04	0.1922E+04	0.1525E+02	0.1148E+03
2580.5	425.0	0.2167E+04	0.2111E+04	0.1703E+02	0.1244E+03
2580.5	435.0	0.2178E+04	0.2174E+04	0.1848E+02	0.1275E+03
2580.5	445.0	0.2333E+04	0.2448E+04	0.2113E+02	0.1417E+03
2580.5	455.0	0.2429E+04	0.2594E+04	0.2171E+02	0.1492E+03
2580.5	465.0	0.2559E+04	0.2811E+04	0.2366E+02	0.1604E+03
2580.5	475.0	0.2690E+04	0.2981E+04	0.2608E+02	0.1694E+03
2580.5	485.0	0.2771E+04	0.3075E+04	0.2726E+02	0.1742E+03
2580.5	495.0	0.2866E+04	0.3210E+04	0.2801E+02	0.1812E+03
2580.5	505.0	0.2978E+04	0.3368E+04	0.2844E+02	0.1894E+03
2580.5	515.0	0.3088E+04	0.3509E+04	0.2853E+02	0.1968E+03
2580.5	525.0	0.3179E+04	0.3600E+04	0.2834E+02	0.2015E+03
2580.5	535.0	0.3232E+04	0.3621E+04	0.2823E+02	0.2023E+03
2580.5	545.0	0.3237E+04	0.3552E+04	0.2763E+02	0.1983E+03
2580.5	555.0	0.3228E+04	0.3563E+04	0.2896E+02	0.1987E+03
2580.5	565.0	0.3297E+04	0.3548E+04	0.3063E+02	0.1977E+03
2580.5	575.0	0.3132E+04	0.3269E+04	0.2561E+02	0.1829E+03
2580.5	585.0	0.3152E+04	0.3295E+04	0.2586E+02	0.1840E+03
2580.5	595.0	0.3059E+04	0.3088E+04	0.2564E+02	0.1732E+03
2580.5	605.0	0.2967E+04	0.2963E+04	0.2676E+02	0.1665E+03

continued on next page

Table G.1: *Unpolarized cross sections continued*

E_0	ν	σ_{exp}	σ_{born}	$d\sigma_{stat}$	$d\sigma_{syst}$
2580.5	615.0	0.2923E+04	0.2861E+04	0.2541E+02	0.1611E+03
2580.5	625.0	0.2806E+04	0.2692E+04	0.2399E+02	0.1522E+03
2580.5	635.0	0.2762E+04	0.2610E+04	0.2506E+02	0.1479E+03
2580.5	645.0	0.2648E+04	0.2450E+04	0.2493E+02	0.1396E+03
2580.5	655.0	0.2624E+04	0.2447E+04	0.2441E+02	0.1394E+03
2580.5	665.0	0.2579E+04	0.2363E+04	0.2321E+02	0.1351E+03
2580.5	675.0	0.2497E+04	0.2229E+04	0.2154E+02	0.1283E+03
2580.5	685.0	0.2418E+04	0.2124E+04	0.1984E+02	0.1229E+03
2580.5	695.0	0.2371E+04	0.2082E+04	0.1932E+02	0.1207E+03
2580.5	705.0	0.2352E+04	0.2084E+04	0.2098E+02	0.1208E+03
2580.5	715.0	0.2335E+04	0.2043E+04	0.2242E+02	0.1188E+03
2580.5	725.0	0.2274E+04	0.1980E+04	0.2137E+02	0.1156E+03
2580.5	735.0	0.2294E+04	0.2035E+04	0.1911E+02	0.1183E+03
2580.5	745.0	0.2259E+04	0.1940E+04	0.1990E+02	0.1137E+03
2580.5	755.0	0.2178E+04	0.1841E+04	0.2287E+02	0.1088E+03
2580.5	765.0	0.2186E+04	0.1885E+04	0.2265E+02	0.1111E+03
2580.5	775.0	0.2188E+04	0.1919E+04	0.2313E+02	0.1129E+03
2580.5	785.0	0.2228E+04	0.1980E+04	0.2743E+02	0.1159E+03
2580.5	795.0	0.2211E+04	0.1937E+04	0.2804E+02	0.1138E+03
2580.5	805.0	0.2200E+04	0.1933E+04	0.2464E+02	0.1137E+03
2580.5	815.0	0.2212E+04	0.1965E+04	0.2005E+02	0.1154E+03
2580.5	825.0	0.2234E+04	0.2004E+04	0.1724E+02	0.1175E+03
2580.5	835.0	0.2247E+04	0.2006E+04	0.1685E+02	0.1178E+03
2580.5	845.0	0.2236E+04	0.2003E+04	0.1664E+02	0.1176E+03
2580.5	855.0	0.2288E+04	0.2109E+04	0.1911E+02	0.1229E+03
2580.5	865.0	0.2317E+04	0.2096E+04	0.2049E+02	0.1223E+03
2580.5	875.0	0.2273E+04	0.2068E+04	0.1679E+02	0.1211E+03
2580.5	885.0	0.2352E+04	0.2146E+04	0.1879E+02	0.1250E+03
2580.5	895.0	0.2277E+04	0.2047E+04	0.2092E+02	0.1200E+03
2580.5	905.0	0.2353E+04	0.2156E+04	0.2173E+02	0.1255E+03
2580.5	915.0	0.2319E+04	0.2101E+04	0.2139E+02	0.1227E+03
2580.5	925.0	0.2361E+04	0.2154E+04	0.2486E+02	0.1254E+03
2580.5	935.0	0.2329E+04	0.2073E+04	0.2415E+02	0.1213E+03
2580.5	945.0	0.2301E+04	0.2030E+04	0.2143E+02	0.1191E+03
2580.5	955.0	0.2293E+04	0.2020E+04	0.1845E+02	0.1186E+03
2580.5	965.0	0.2274E+04	0.1972E+04	0.1630E+02	0.1163E+03

continued on next page

Table G.1: *Unpolarized cross sections continued*

E_0	ν	σ_{exp}	σ_{born}	$d\sigma_{stat}$	$d\sigma_{syst}$
2580.5	975.0	0.2234E+04	0.1913E+04	0.1549E+02	0.1133E+03
2580.5	985.0	0.2227E+04	0.1930E+04	0.1691E+02	0.1140E+03
2580.5	995.0	0.2241E+04	0.1917E+04	0.1812E+02	0.1135E+03
2580.5	1005.0	0.2183E+04	0.1857E+04	0.1509E+02	0.1105E+03
2580.5	1015.0	0.2222E+04	0.1895E+04	0.1645E+02	0.1124E+03
2580.5	1025.0	0.2144E+04	0.1772E+04	0.1820E+02	0.1064E+03
2580.5	1035.0	0.2155E+04	0.1818E+04	0.1816E+02	0.1086E+03
2580.5	1045.0	0.2147E+04	0.1779E+04	0.1828E+02	0.1066E+03
2580.5	1055.0	0.2109E+04	0.1752E+04	0.2080E+02	0.1053E+03
2580.5	1065.0	0.2158E+04	0.1843E+04	0.2144E+02	0.1098E+03
2580.5	1075.0	0.2156E+04	0.1805E+04	0.1827E+02	0.1079E+03
2580.5	1085.0	0.2115E+04	0.1732E+04	0.1520E+02	0.1044E+03
2580.5	1095.0	0.2079E+04	0.1664E+04	0.1387E+02	0.1011E+03
2580.5	1105.0	0.2036E+04	0.1636E+04	0.1477E+02	0.9959E+02
2580.5	1115.0	0.2071E+04	0.1692E+04	0.1663E+02	0.1023E+03
2580.5	1125.0	0.2053E+04	0.1676E+04	0.1419E+02	0.1016E+03
2580.5	1135.0	0.2079E+04	0.1696E+04	0.1522E+02	0.1026E+03
2580.5	1145.0	0.2040E+04	0.1650E+04	0.1813E+02	0.1003E+03
2580.5	1155.0	0.2068E+04	0.1672E+04	0.1796E+02	0.1014E+03
2580.5	1165.0	0.2012E+04	0.1583E+04	0.1813E+02	0.9715E+02
2580.5	1175.0	0.2019E+04	0.1628E+04	0.2133E+02	0.9933E+02
2580.5	1185.0	0.2054E+04	0.1678E+04	0.2036E+02	0.1017E+03
2580.5	1195.0	0.2042E+04	0.1623E+04	0.1617E+02	0.9908E+02
2580.5	1205.0	0.1977E+04	0.1489E+04	0.1254E+02	0.9271E+02
2580.5	1215.0	0.1926E+04	0.1495E+04	0.1346E+02	0.9302E+02
2580.5	1225.0	0.2022E+04	0.1619E+04	0.1627E+02	0.9893E+02
2580.5	1235.0	0.1953E+04	0.1492E+04	0.1370E+02	0.9286E+02
2580.5	1245.0	0.1954E+04	0.1496E+04	0.1308E+02	0.9305E+02
2580.5	1255.0	0.1912E+04	0.1432E+04	0.1354E+02	0.9019E+02
2580.5	1265.0	0.1901E+04	0.1422E+04	0.1261E+02	0.9029E+02
2580.5	1275.0	0.1880E+04	0.1402E+04	0.1346E+02	0.8913E+02
2580.5	1285.0	0.1885E+04	0.1414E+04	0.1437E+02	0.8910E+02
2580.5	1295.0	0.1872E+04	0.1386E+04	0.1348E+02	0.8767E+02
2580.5	1305.0	0.1844E+04	0.1340E+04	0.1188E+02	0.8569E+02
2580.5	1315.0	0.1823E+04	0.1322E+04	0.1111E+02	0.8500E+02
2580.5	1325.0	0.1826E+04	0.1342E+04	0.1250E+02	0.8591E+02

continued on next page

Table G.1: *Unpolarized cross sections continued*

E_0	ν	σ_{exp}	σ_{born}	$d\sigma_{stat}$	$d\sigma_{syst}$
2580.5	1335.0	0.1834E+04	0.1345E+04	0.1304E+02	0.8611E+02
2580.5	1345.0	0.1809E+04	0.1297E+04	0.1079E+02	0.8394E+02
2580.5	1355.0	0.1789E+04	0.1282E+04	0.1143E+02	0.8325E+02
2580.5	1365.0	0.1794E+04	0.1298E+04	0.1081E+02	0.8402E+02
2580.5	1375.0	0.1791E+04	0.1289E+04	0.1114E+02	0.8369E+02
2580.5	1385.0	0.1778E+04	0.1256E+04	0.1136E+02	0.8219E+02
2580.5	1395.0	0.1740E+04	0.1191E+04	0.1014E+02	0.7927E+02
2580.5	1405.0	0.1702E+04	0.1148E+04	0.9120E+01	0.7734E+02
2580.5	1415.0	0.1704E+04	0.1190E+04	0.1019E+02	0.7933E+02
2580.5	1425.0	0.1731E+04	0.1198E+04	0.1105E+02	0.7974E+02
2580.5	1435.0	0.1675E+04	0.1141E+04	0.9489E+01	0.7722E+02
2580.5	1445.0	0.1737E+04	0.1251E+04	0.1038E+02	0.8241E+02
2580.5	1455.0	0.1740E+04	0.1225E+04	0.1014E+02	0.8130E+02
2580.5	1465.0	0.1719E+04	0.1176E+04	0.9217E+01	0.7917E+02
2580.5	1475.0	0.1689E+04	0.1127E+04	0.8148E+01	0.7702E+02
2580.5	1485.0	0.1659E+04	0.1085E+04	0.7473E+01	0.7523E+02
2580.5	1495.0	0.1645E+04	0.1078E+04	0.7852E+01	0.7505E+02
2580.5	1505.0	0.1659E+04	0.1124E+04	0.9914E+01	0.7723E+02
2580.5	1515.0	0.1688E+04	0.1143E+04	0.1067E+02	0.7829E+02
2580.5	1525.0	0.1663E+04	0.1102E+04	0.8836E+01	0.7659E+02
2580.5	1535.0	0.1682E+04	0.1137E+04	0.9642E+01	0.7840E+02
2580.5	1545.0	0.1680E+04	0.1111E+04	0.8905E+01	0.7736E+02
2580.5	1555.0	0.1642E+04	0.1033E+04	0.8513E+01	0.7402E+02
2580.5	1565.0	0.1597E+04	0.9612E+03	0.7706E+01	0.7102E+02
2580.5	1575.0	0.1566E+04	0.9269E+03	0.7223E+01	0.6967E+02
2580.5	1585.0	0.1568E+04	0.9478E+03	0.7847E+01	0.7079E+02
2580.5	1595.0	0.1595E+04	0.9817E+03	0.8643E+01	0.7251E+02
2580.5	1605.0	0.1588E+04	0.9743E+03	0.8156E+01	0.7241E+02
2580.5	1615.0	0.1605E+04	0.9976E+03	0.8065E+01	0.7375E+02
2580.5	1625.0	0.1612E+04	0.1001E+04	0.7945E+01	0.7420E+02
2580.5	1635.0	0.1612E+04	0.9817E+03	0.8193E+01	0.7364E+02
2580.5	1645.0	0.1587E+04	0.9302E+03	0.7886E+01	0.7161E+02
2580.5	1655.0	0.1563E+04	0.9023E+03	0.8056E+01	0.7065E+02
2580.5	1665.0	0.1577E+04	0.9494E+03	0.9902E+01	0.7311E+02
2580.5	1675.0	0.1620E+04	0.9806E+03	0.1045E+02	0.7494E+02
2580.5	1685.0	0.1583E+04	0.9015E+03	0.8001E+01	0.7174E+02

continued on next page

Table G.1: *Unpolarized cross sections continued*

E_0	ν	σ_{exp}	σ_{born}	$d\sigma_{stat}$	$d\sigma_{syst}$
2580.5	1695.0	0.1586E+04	0.9249E+03	0.8608E+01	0.7320E+02
2580.5	1705.0	0.1607E+04	0.9120E+03	0.9343E+01	0.7313E+02
2580.5	1715.0	0.1571E+04	0.9029E+03	0.1222E+02	0.7287E+02
2580.5	1725.0	0.1676E+04	0.1020E+04	0.1310E+02	0.7819E+02
2580.5	1735.0	0.1627E+04	0.9337E+03	0.1218E+02	0.7573E+02
2580.5	1745.0	0.1669E+04	0.9737E+03	0.1244E+02	0.7802E+02
2580.5	1755.0	0.1630E+04	0.9058E+03	0.1215E+02	0.7533E+02
2580.5	1765.0	0.1653E+04	0.9396E+03	0.1213E+02	0.7786E+02
2580.5	1775.0	0.1657E+04	0.9285E+03	0.8922E+01	0.7878E+02
2580.5	1785.0	0.1664E+04	0.9239E+03	0.9318E+01	0.7857E+02
2580.5	1795.0	0.1670E+04	0.9195E+03	0.9172E+01	0.7858E+02
2580.5	1805.0	0.1678E+04	0.9198E+03	0.9225E+01	0.7874E+02
2580.5	1815.0	0.1685E+04	0.9195E+03	0.9211E+01	0.7894E+02
2580.5	1825.0	0.1693E+04	0.9156E+03	0.9136E+01	0.7897E+02
2580.5	1835.0	0.1702E+04	0.9162E+03	0.9161E+01	0.7918E+02
2580.5	1845.0	0.1710E+04	0.9136E+03	0.9120E+01	0.7940E+02
2580.5	1855.0	0.1720E+04	0.9195E+03	0.9252E+01	0.7956E+02
2580.5	1865.0	0.1730E+04	0.9043E+03	0.8827E+01	0.8044E+02
2580.5	1875.0	0.1725E+04	0.8994E+03	0.8057E+01	0.8474E+02
2580.5	1885.0	0.1781E+04	0.9777E+03	0.9216E+01	0.8955E+02
3381.8	260.0	0.1129E+03	0.2859E+03	0.1974E+01	0.1899E+02
3381.8	280.0	0.1766E+03	0.4220E+03	0.2789E+01	0.2893E+02
3381.8	300.0	0.2904E+03	0.6383E+03	0.4043E+01	0.4099E+02
3381.8	320.0	0.4577E+03	0.9957E+03	0.6233E+01	0.6154E+02
3381.8	340.0	0.6980E+03	0.1445E+04	0.9000E+01	0.8671E+02
3381.8	360.0	0.9257E+03	0.1821E+04	0.1095E+02	0.1070E+03
3381.8	380.0	0.1171E+04	0.2173E+04	0.1320E+02	0.1255E+03
3381.8	400.0	0.1279E+04	0.2148E+04	0.1305E+02	0.1224E+03
3381.8	420.0	0.1277E+04	0.1947E+04	0.1186E+02	0.1100E+03
3381.8	440.0	0.1186E+04	0.1621E+04	0.9786E+01	0.9202E+02
3381.8	460.0	0.1057E+04	0.1295E+04	0.8557E+01	0.7390E+02
3381.8	480.0	0.9221E+03	0.1005E+04	0.9055E+01	0.5802E+02
3381.8	500.0	0.7923E+03	0.7731E+03	0.4895E+01	0.4611E+02
3381.8	520.0	0.7142E+03	0.6834E+03	0.4681E+01	0.4163E+02
3381.8	540.0	0.6764E+03	0.6671E+03	0.4461E+01	0.4103E+02
3381.8	560.0	0.6734E+03	0.7050E+03	0.4854E+01	0.4332E+02

continued on next page

Table G.1: *Unpolarized cross sections continued*

E_0	ν	σ_{exp}	σ_{born}	$d\sigma_{stat}$	$d\sigma_{syst}$
3381.8	580.0	0.6880E+03	0.7612E+03	0.5392E+01	0.4655E+02
3381.8	600.0	0.7236E+03	0.8508E+03	0.5637E+01	0.5159E+02
3381.8	620.0	0.7747E+03	0.9566E+03	0.6692E+01	0.5734E+02
3381.8	640.0	0.8352E+03	0.1067E+04	0.7711E+01	0.6330E+02
3381.8	660.0	0.8982E+03	0.1164E+04	0.8037E+01	0.6854E+02
3381.8	680.0	0.9461E+03	0.1214E+04	0.9610E+01	0.7090E+02
3381.8	700.0	0.9769E+03	0.1232E+04	0.1380E+02	0.7186E+02
3381.8	720.0	0.9930E+03	0.1204E+04	0.1148E+02	0.7010E+02
3381.8	740.0	0.9637E+03	0.1107E+04	0.6814E+01	0.6397E+02
3381.8	760.0	0.9609E+03	0.1095E+04	0.7204E+01	0.6338E+02
3381.8	780.0	0.9365E+03	0.1013E+04	0.6760E+01	0.5884E+02
3381.8	800.0	0.9040E+03	0.9515E+03	0.6399E+01	0.5558E+02
3381.8	820.0	0.9015E+03	0.9518E+03	0.6278E+01	0.5573E+02
3381.8	840.0	0.8776E+03	0.8924E+03	0.6637E+01	0.5259E+02
3381.8	860.0	0.8674E+03	0.8795E+03	0.6511E+01	0.5214E+02
3381.8	880.0	0.8577E+03	0.8626E+03	0.6408E+01	0.5144E+02
3381.8	900.0	0.8647E+03	0.8940E+03	0.7352E+01	0.5344E+02
3381.8	920.0	0.8842E+03	0.9176E+03	0.8533E+01	0.5513E+02
3381.8	940.0	0.8683E+03	0.8686E+03	0.5300E+01	0.5237E+02
3381.8	960.0	0.8839E+03	0.9191E+03	0.5887E+01	0.5543E+02
3381.8	980.0	0.9066E+03	0.9435E+03	0.6145E+01	0.5695E+02
3381.8	1000.0	0.9123E+03	0.9487E+03	0.6219E+01	0.5732E+02
3381.8	1020.0	0.9487E+03	0.1007E+04	0.6457E+01	0.6066E+02
3381.8	1040.0	0.9463E+03	0.9716E+03	0.6964E+01	0.5874E+02
3381.8	1060.0	0.9703E+03	0.1024E+04	0.7054E+01	0.6173E+02
3381.8	1080.0	0.9911E+03	0.1036E+04	0.8331E+01	0.6236E+02
3381.8	1100.0	0.9865E+03	0.9921E+03	0.9904E+01	0.6001E+02
3381.8	1120.0	0.9724E+03	0.9572E+03	0.5704E+01	0.5824E+02
3381.8	1140.0	0.9740E+03	0.9523E+03	0.6082E+01	0.5809E+02
3381.8	1160.0	0.9580E+03	0.9092E+03	0.5799E+01	0.5587E+02
3381.8	1180.0	0.9603E+03	0.9219E+03	0.6097E+01	0.5672E+02
3381.8	1200.0	0.9674E+03	0.9297E+03	0.5959E+01	0.5723E+02
3381.8	1220.0	0.9718E+03	0.9266E+03	0.6928E+01	0.5717E+02
3381.8	1240.0	0.9711E+03	0.9164E+03	0.6462E+01	0.5660E+02
3381.8	1260.0	0.9787E+03	0.9346E+03	0.7809E+01	0.5767E+02
3381.8	1280.0	0.9964E+03	0.9554E+03	0.9796E+01	0.5888E+02

continued on next page

Table G.1: *Unpolarized cross sections continued*

E_0	ν	σ_{exp}	σ_{born}	$d\sigma_{stat}$	$d\sigma_{syst}$
3381.8	1300.0	0.9967E+03	0.9460E+03	0.6173E+01	0.5830E+02
3381.8	1320.0	0.1017E+04	0.9746E+03	0.6985E+01	0.5986E+02
3381.8	1340.0	0.1006E+04	0.9249E+03	0.6954E+01	0.5721E+02
3381.8	1360.0	0.9988E+03	0.9117E+03	0.6375E+01	0.5653E+02
3381.8	1380.0	0.9978E+03	0.9057E+03	0.7537E+01	0.5629E+02
3381.8	1400.0	0.9957E+03	0.8945E+03	0.7578E+01	0.5570E+02
3381.8	1420.0	0.9875E+03	0.8643E+03	0.8790E+01	0.5445E+02
3381.8	1440.0	0.9621E+03	0.8020E+03	0.1027E+02	0.5240E+02
3381.8	1460.0	0.9367E+03	0.7635E+03	0.4674E+01	0.4914E+02
3381.8	1480.0	0.9317E+03	0.7665E+03	0.5345E+01	0.4934E+02
3381.8	1500.0	0.9259E+03	0.7551E+03	0.5347E+01	0.4875E+02
3381.8	1520.0	0.9198E+03	0.7403E+03	0.4999E+01	0.4809E+02
3381.8	1540.0	0.9069E+03	0.7164E+03	0.5889E+01	0.4691E+02
3381.8	1560.0	0.9096E+03	0.7357E+03	0.6017E+01	0.4789E+02
3381.8	1580.0	0.9203E+03	0.7468E+03	0.6773E+01	0.4864E+02
3381.8	1600.0	0.9075E+03	0.7098E+03	0.7075E+01	0.4760E+02
3381.8	1620.0	0.9040E+03	0.7080E+03	0.7317E+01	0.4792E+02
3381.8	1640.0	0.9008E+03	0.6993E+03	0.7245E+01	0.4780E+02
3381.8	1660.0	0.8978E+03	0.6920E+03	0.6967E+01	0.4760E+02
3381.8	1680.0	0.8949E+03	0.6853E+03	0.6513E+01	0.4726E+02
3381.8	1700.0	0.8923E+03	0.6757E+03	0.5908E+01	0.4663E+02
3381.8	1720.0	0.8898E+03	0.6785E+03	0.5256E+01	0.4623E+02
3381.8	1740.0	0.9047E+03	0.6935E+03	0.4593E+01	0.4597E+02
3381.8	1760.0	0.8827E+03	0.6350E+03	0.4092E+01	0.4319E+02
3381.8	1780.0	0.8847E+03	0.6486E+03	0.4545E+01	0.4403E+02
3381.8	1800.0	0.8778E+03	0.6268E+03	0.4312E+01	0.4349E+02
3381.8	1820.0	0.8811E+03	0.6414E+03	0.5313E+01	0.4359E+02
3381.8	1840.0	0.8900E+03	0.6469E+03	0.5707E+01	0.4410E+02
3381.8	1860.0	0.8780E+03	0.6136E+03	0.6059E+01	0.4320E+02
3381.8	1880.0	0.8771E+03	0.6155E+03	0.6807E+01	0.4343E+02
3381.8	1900.0	0.8763E+03	0.6084E+03	0.7416E+01	0.4314E+02
3381.8	1920.0	0.8758E+03	0.6033E+03	0.7757E+01	0.4282E+02
3381.8	1940.0	0.8755E+03	0.5982E+03	0.7608E+01	0.4244E+02
3381.8	1960.0	0.8753E+03	0.5939E+03	0.6787E+01	0.4208E+02
3381.8	1980.0	0.8757E+03	0.5872E+03	0.5012E+01	0.4164E+02
3381.8	2000.0	0.8698E+03	0.5669E+03	0.3171E+01	0.4080E+02

continued on next page

Table G.1: *Unpolarized cross sections continued*

E_0	ν	σ_{exp}	σ_{born}	$d\sigma_{stat}$	$d\sigma_{syst}$
3381.8	2020.0	0.8657E+03	0.5616E+03	0.3553E+01	0.4065E+02
3381.8	2040.0	0.8747E+03	0.5739E+03	0.3802E+01	0.4131E+02
3381.8	2060.0	0.8728E+03	0.5645E+03	0.4568E+01	0.4103E+02
3381.8	2080.0	0.8852E+03	0.5788E+03	0.7464E+01	0.4197E+02
3381.8	2100.0	0.8796E+03	0.5563E+03	0.8337E+01	0.4155E+02
3381.8	2120.0	0.8809E+03	0.5604E+03	0.8153E+01	0.4198E+02
3381.8	2140.0	0.8825E+03	0.5534E+03	0.6960E+01	0.4181E+02
3381.8	2160.0	0.8843E+03	0.5498E+03	0.5481E+01	0.4170E+02
3381.8	2180.0	0.8862E+03	0.5539E+03	0.4200E+01	0.4180E+02
3381.8	2200.0	0.8926E+03	0.5495E+03	0.3482E+01	0.4149E+02
3381.8	2220.0	0.8809E+03	0.5196E+03	0.3488E+01	0.4039E+02
3381.8	2240.0	0.8902E+03	0.5471E+03	0.4224E+01	0.4166E+02
3381.8	2260.0	0.9033E+03	0.5507E+03	0.4967E+01	0.4242E+02
3381.8	2280.0	0.8988E+03	0.5253E+03	0.5655E+01	0.4191E+02
3381.8	2300.0	0.9019E+03	0.5259E+03	0.6397E+01	0.4212E+02
3381.8	2320.0	0.9052E+03	0.5204E+03	0.6653E+01	0.4203E+02
3381.8	2340.0	0.9087E+03	0.5146E+03	0.6199E+01	0.4197E+02
3381.8	2360.0	0.9167E+03	0.5188E+03	0.4805E+01	0.4248E+02
3381.8	2380.0	0.9230E+03	0.4990E+03	0.3039E+01	0.4212E+02
3381.8	2400.0	0.9103E+03	0.4631E+03	0.3335E+01	0.4108E+02
4238.6	495.0	0.1116E+03	0.2208E+03	0.1838E+01	0.1476E+02
4238.6	525.0	0.1750E+03	0.3092E+03	0.2123E+01	0.1969E+02
4238.6	555.0	0.2520E+03	0.4158E+03	0.2701E+01	0.2585E+02
4238.6	585.0	0.3206E+03	0.4957E+03	0.3299E+01	0.3034E+02
4238.6	615.0	0.3394E+03	0.4825E+03	0.2982E+01	0.2932E+02
4238.6	645.0	0.3355E+03	0.4462E+03	0.2933E+01	0.2717E+02
4238.6	675.0	0.3021E+03	0.3659E+03	0.2726E+01	0.2255E+02
4238.6	705.0	0.2683E+03	0.3059E+03	0.2330E+01	0.1907E+02
4238.6	735.0	0.2490E+03	0.2783E+03	0.2452E+01	0.1759E+02
4238.6	765.0	0.2453E+03	0.2766E+03	0.2197E+01	0.1759E+02
4238.6	795.0	0.2538E+03	0.2936E+03	0.1505E+01	0.1868E+02
4238.6	825.0	0.2721E+03	0.3248E+03	0.1707E+01	0.2055E+02
4238.6	855.0	0.3000E+03	0.3658E+03	0.1922E+01	0.2299E+02
4238.6	885.0	0.3161E+03	0.3807E+03	0.1991E+01	0.2373E+02
4238.6	915.0	0.3344E+03	0.4008E+03	0.2085E+01	0.2490E+02
4238.6	945.0	0.3390E+03	0.3943E+03	0.2104E+01	0.2447E+02

continued on next page

Table G.1: *Unpolarized cross sections continued*

E_0	ν	σ_{exp}	σ_{born}	$d\sigma_{stat}$	$d\sigma_{syst}$
4238.6	975.0	0.3422E+03	0.3914E+03	0.2074E+01	0.2436E+02
4238.6	1005.0	0.3410E+03	0.3803E+03	0.2091E+01	0.2364E+02
4238.6	1035.0	0.3383E+03	0.3701E+03	0.2256E+01	0.2190E+02
4238.6	1065.0	0.3357E+03	0.3615E+03	0.2200E+01	0.2161E+02
4238.6	1095.0	0.3369E+03	0.3632E+03	0.2150E+01	0.2185E+02
4238.6	1125.0	0.3506E+03	0.3835E+03	0.2352E+01	0.2318E+02
4238.6	1155.0	0.3573E+03	0.3880E+03	0.2347E+01	0.2351E+02
4238.6	1185.0	0.3776E+03	0.4189E+03	0.2594E+01	0.2539E+02
4238.6	1215.0	0.3924E+03	0.4320E+03	0.2862E+01	0.2621E+02
4238.6	1245.0	0.4045E+03	0.4434E+03	0.3082E+01	0.2695E+02
4238.6	1275.0	0.4182E+03	0.4562E+03	0.3951E+01	0.2773E+02
4238.6	1305.0	0.4211E+03	0.4492E+03	0.2739E+01	0.2745E+02
4238.6	1335.0	0.4255E+03	0.4502E+03	0.2780E+01	0.2760E+02
4238.6	1365.0	0.4299E+03	0.4509E+03	0.2929E+01	0.2776E+02
4238.6	1395.0	0.4376E+03	0.4579E+03	0.2787E+01	0.2821E+02
4238.6	1425.0	0.4433E+03	0.4601E+03	0.3214E+01	0.2845E+02
4238.6	1455.0	0.4505E+03	0.4656E+03	0.3235E+01	0.2880E+02
4238.6	1485.0	0.4552E+03	0.4662E+03	0.3888E+01	0.2890E+02
4238.6	1515.0	0.4600E+03	0.4678E+03	0.5689E+01	0.2905E+02
4238.6	1545.0	0.4632E+03	0.4665E+03	0.2879E+01	0.2902E+02
4238.6	1575.0	0.4663E+03	0.4651E+03	0.3267E+01	0.2902E+02
4238.6	1605.0	0.4614E+03	0.4487E+03	0.3146E+01	0.2816E+02
4238.6	1635.0	0.4553E+03	0.4370E+03	0.3171E+01	0.2752E+02
4238.6	1665.0	0.4625E+03	0.4471E+03	0.3632E+01	0.2816E+02
4238.6	1695.0	0.4587E+03	0.4349E+03	0.4198E+01	0.2751E+02
4238.6	1725.0	0.4661E+03	0.4441E+03	0.5434E+01	0.2807E+02
4238.6	1755.0	0.4553E+03	0.4183E+03	0.2542E+01	0.2668E+02
4238.6	1785.0	0.4583E+03	0.4243E+03	0.2960E+01	0.2711E+02
4238.6	1815.0	0.4554E+03	0.4136E+03	0.2746E+01	0.2649E+02
4238.6	1845.0	0.4561E+03	0.4120E+03	0.3168E+01	0.2647E+02
4238.6	1875.0	0.4568E+03	0.4084E+03	0.3365E+01	0.2623E+02
4238.6	1905.0	0.4570E+03	0.4035E+03	0.4765E+01	0.2601E+02
4238.6	1935.0	0.4535E+03	0.3934E+03	0.5391E+01	0.2556E+02
4238.6	1965.0	0.4529E+03	0.3904E+03	0.5326E+01	0.2528E+02
4238.6	1995.0	0.4524E+03	0.3862E+03	0.4748E+01	0.2493E+02
4238.6	2025.0	0.4521E+03	0.3825E+03	0.3926E+01	0.2462E+02

continued on next page

Table G.1: *Unpolarized cross sections continued*

E_0	ν	σ_{exp}	σ_{born}	dσ_{stat}	dσ_{syst}
4238.6	2055.0	0.4518E+03	0.3790E+03	0.3097E+01	0.2441E+02
4238.6	2085.0	0.4517E+03	0.3751E+03	0.2490E+01	0.2430E+02
4238.6	2115.0	0.4502E+03	0.3706E+03	0.2328E+01	0.2436E+02
4238.6	2145.0	0.4566E+03	0.3782E+03	0.2484E+01	0.2476E+02
4238.6	2175.0	0.4521E+03	0.3642E+03	0.2351E+01	0.2401E+02
4238.6	2205.0	0.4523E+03	0.3644E+03	0.2882E+01	0.2406E+02
4238.6	2235.0	0.4565E+03	0.3675E+03	0.3151E+01	0.2427E+02
4238.6	2265.0	0.4535E+03	0.3576E+03	0.3354E+01	0.2401E+02
4238.6	2295.0	0.4542E+03	0.3569E+03	0.3639E+01	0.2403E+02
4238.6	2325.0	0.4550E+03	0.3552E+03	0.3877E+01	0.2388E+02
4238.6	2355.0	0.4582E+03	0.3559E+03	0.4032E+01	0.2368E+02
4238.6	2385.0	0.4539E+03	0.3447E+03	0.3929E+01	0.2313E+02
4238.6	2415.0	0.4596E+03	0.3523E+03	0.4070E+01	0.2356E+02
4238.6	2445.0	0.4612E+03	0.3498E+03	0.4339E+01	0.2347E+02
4238.6	2475.0	0.4643E+03	0.3481E+03	0.2976E+01	0.2339E+02
4238.6	2505.0	0.4533E+03	0.3270E+03	0.2090E+01	0.2241E+02
4238.6	2535.0	0.4681E+03	0.3522E+03	0.2833E+01	0.2371E+02
4238.6	2565.0	0.4648E+03	0.3355E+03	0.4491E+01	0.2290E+02
4238.6	2595.0	0.4635E+03	0.3309E+03	0.4669E+01	0.2272E+02
4238.6	2625.0	0.4698E+03	0.3352E+03	0.4644E+01	0.2282E+02
4238.6	2655.0	0.4719E+03	0.3316E+03	0.4552E+01	0.2268E+02
4238.6	2685.0	0.4741E+03	0.3297E+03	0.4441E+01	0.2261E+02
4238.6	2715.0	0.4765E+03	0.3278E+03	0.4254E+01	0.2257E+02
4238.6	2745.0	0.4789E+03	0.3259E+03	0.3951E+01	0.2256E+02
4238.6	2775.0	0.4815E+03	0.3222E+03	0.3487E+01	0.2254E+02
4238.6	2805.0	0.4772E+03	0.3092E+03	0.2789E+01	0.2233E+02
4238.6	2835.0	0.4841E+03	0.3165E+03	0.2238E+01	0.2278E+02
4238.6	2865.0	0.4897E+03	0.3181E+03	0.2359E+01	0.2302E+02
5058.2	1900.0	0.2539E+03	0.2681E+03	0.2644E+01	0.1742E+02
5058.2	1950.0	0.2611E+03	0.2746E+03	0.1563E+01	0.1752E+02
5058.2	2000.0	0.2664E+03	0.2754E+03	0.1379E+01	0.1766E+02
5058.2	2050.0	0.2628E+03	0.2623E+03	0.2268E+01	0.1689E+02
5058.2	2100.0	0.2644E+03	0.2620E+03	0.2361E+01	0.1663E+02
5058.2	2150.0	0.2661E+03	0.2607E+03	0.1936E+01	0.1676E+02
5058.2	2200.0	0.2747E+03	0.2708E+03	0.1973E+01	0.1758E+02
5058.2	2250.0	0.2719E+03	0.2591E+03	0.1465E+01	0.1676E+02

continued on next page

Table G.1: *Unpolarized cross sections continued*

E_0	ν	σ_{exp}	σ_{born}	dσ_{stat}	dσ_{syst}
5058.2	2300.0	0.2768E+03	0.2650E+03	0.4636E+01	0.1721E+02
5058.2	2350.0	0.2774E+03	0.2602E+03	0.3618E+01	0.1697E+02
5058.2	2400.0	0.2786E+03	0.2590E+03	0.1594E+01	0.1682E+02
5058.2	2450.0	0.2814E+03	0.2592E+03	0.1306E+01	0.1692E+02
5058.2	2500.0	0.2770E+03	0.2476E+03	0.2237E+01	0.1624E+02
5058.2	2550.0	0.2848E+03	0.2596E+03	0.3404E+01	0.1679E+02
5058.2	2600.0	0.2917E+03	0.2644E+03	0.1957E+01	0.1714E+02
5058.2	2650.0	0.2945E+03	0.2625E+03	0.9998E+00	0.1699E+02
5058.2	2700.0	0.2994E+03	0.2637E+03	0.2103E+01	0.1706E+02
5058.2	2750.0	0.2967E+03	0.2518E+03	0.2516E+01	0.1651E+02
5058.2	2800.0	0.2932E+03	0.2429E+03	0.1734E+01	0.1594E+02
5058.2	2850.0	0.2963E+03	0.2449E+03	0.1086E+01	0.1610E+02
5058.2	2900.0	0.2967E+03	0.2398E+03	0.3261E+01	0.1583E+02
5058.2	2950.0	0.2954E+03	0.2336E+03	0.1806E+01	0.1551E+02
5058.2	3000.0	0.2972E+03	0.2328E+03	0.9485E+00	0.1555E+02
5058.2	3050.0	0.2990E+03	0.2316E+03	0.1530E+01	0.1553E+02

REFERENCES

[1] D. Drechsel, in *Proceedings of the Symposium on the GDH Sum Rule and the Nucleon Spin Structure in the Resonance Region*, 1st ed., edited by D. Drechsel and L. Tiator (World Scientific, Singapore, 2001).

[2] A. W. Thomas and W. Weise, *The Structure of the Nucleon* (Wiley-Vch, Berlin, 2001).

[3] B. Povh, K. Rith, C. Scholz, and F. Zetsche, *Particles and Nuclei, An Introduction to the Physical Concepts.* (Springer, Berlin, 1995).

[4] M. N. Rosenbluth, Phys. Rev. **79**, 615 (1950).

[5] M. K. Jones *et al.*, Phys. Rev. Lett. **84**, 1398 (2000).

[6] O. Gayou *et al.*, Phys. Rev. Lett. **88**, 092301 (2002).

[7] V. Burkert and Zhu-jun Li, Phys. Rev. **D47**, 46 (1993).

[8] V. D. Burkert, Int. J. Mod. Phys. **E1**, 421 (1992).

[9] J. Callan, Curtis G. and D. J. Gross, Phys. Rev. Lett. **22**, 156 (1969).

[10] V. Bernard, T. R. Hemmert, and U.-G. Meissner, Phys. Rev. **D67**, 076008 (2003).

[11] R. P. Feynman, Phys. Rev. Lett. **23**, 1415 (1969).

[12] J. D. Bjorken and E. A. Paschos, Phys. Rev. **185**, 1975 (1969).

[13] D. Drechsel and L. Tiator, J. Phys. **G18**, 449 (1992).

[14] D. Drechsel, S. S. Kamalov, and L. Tiator, Phys. Rev. **D63**, 114010 (2001).

[15] F. J. Gilman, Phys. Rev. **167**, 1365 (1968).

[16] L. N. Hand, Phys. Rev. **129**, 1834 (1963).

[17] V. Bernard, N. Kaiser, and U.-G. Meissner, Int. J. Mod. Phys. **E4**, 193 (1995).

[18] D. Dolgov, R. Brower, J. W. Negele, and A. Pochinsky, Nucl. Phys. Proc. Suppl. **73**, 300 (1999).

[19] K. G. Wilson, Phys. Rev. **179**, 1499 (1969).

[20] A. V. Manohar, (1992), hep-ph/9204208.

[21] R. L. Jaffe, Comments Nucl. Part. Phys. **19**, 239 (1990).

[22] S. Wandzura and F. Wilczek, Phys. Lett. **B72**, 195 (1977).

[23] X.-D. Ji and W. Melnitchouk, Phys. Rev. **D56**, 1 (1997).

[24] Z.-E. Meziani *et al.*, (2004), hep-ph/0404066.

[25] S. A. Larin, T. van Ritbergen, and J. A. M. Vermaseren, Phys. Lett. **B404**, 153 (1997).

[26] S. A. Larin, Phys. Lett. **B334**, 192 (1994).

[27] E. Stein, P. Gornicki, L. Mankiewicz, and A. Schafer, Phys. Lett. **B353**, 107 (1995).

[28] X.-D. Ji, (1995), hep-ph/9510362.

[29] M. Gluck, E. Reya, and A. Vogt, Z. Phys. **C67**, 433 (1995).

[30] M. I. Niculescu, Ph.D. thesis, Hampton University, 1999.

[31] E. D. Bloom and F. J. Gilman, Phys. Rev. Lett. **25**, 1140 (1970).

[32] E. D. Bloom and F. J. Gilman, Phys. Rev. D **4**, 2901 (1971).

[33] H. Georgi and H. D. Politzer, Phys. Rev. Lett. **36**, 1281 (1976).

[34] A. De Rujula, H. Georgi, and H. D. Politzer, Phys. Lett. **B64**, 428 (1977).

[35] A. De Rujula, H. Georgi, and H. D. Politzer, Ann. Phys. **103**, 315 (1977).

[36] C. E. Carlson and N. C. Mukhopadhyay, Phys. Rev. **D58**, 094029 (1998).

[37] F. E. Close and W. Melnitchouk, Phys. Rev. **C68**, 035210 (2003).

[38] F. E. Close and N. Isgur, Phys. Lett. **B509**, 81 (2001).

[39] N. Liyanage, J.-P. Chen, and S. Choi, JLab experiment E01-012, http://hallaweb.jlab.org/experiment/E01-012/.

[40] D. Drechsel, O. Hanstein, S. S. Kamalov, and L. Tiator, Nucl. Phys. **A645**, 145 (1999).

[41] M. Anselmino, B. L. Ioffe, and E. Leader, Sov. J. Nucl. Phys. **49**, 136 (1989).

[42] J. Sakurai, *Currents and Mesons* (University of Chicago Press, Chicago, 1969).

[43] R. P. Feynman, *Photon-Hadron Interactions* (Benjamin, Reading, 1972).

[44] V. D. Burkert and B. L. Ioffe, Phys. Lett. **B296**, 223 (1992).

[45] V. D. Burkert and B. L. Ioffe, J. Exp. Theor. Phys. **78**, 619 (1994).

[46] J. Soffer and O. V. Teryaev, Phys. Lett. **B545**, 323 (2002).

[47] H. Burkhardt and W. N. Cottingham, Annals Phys. **56**, 453 (1970).

[48] J. S. Schwinger, Proc. Nat. Acad. Sci. **72**, 1559 (1975).

[49] Wu-yang Tsai, J. DeRaad, Lester L., and K. A. Milton, Phys. Rev. **D11**, 3537 (1975).

[50] F. E. Low, Phys. Rev. **96**, 1428 (1954).

[51] M. Gell-Mann and M. L. Goldberger, Phys. Rev. **96**, 1433 (1954).

[52] M. Gell-Mann, M. L. Goldberger, and W. E. Thirring, Phys. Rev. **95**, 1612 (1954).

[53] S. D. Drell and A. C. Hearn, Phys. Rev. Lett. **16**, 908 (1966).

[54] S. Gerasimov, Yad. Fiz. **2**, 598 (1965).

[55] S. Gerasimov, Sov. J. Nucl. Phys. **2**, 430 (1966).

[56] M. Hosoda and K. Yamamoto, Prog. Theor. Phys. (Kyoto) **30**, 425 (1966).

[57] J. Ahrens *et al.*, Phys. Rev. Lett. **87**, 22003 (2001).

[58] P. Grabmayr, in *Proceedings of the Second International Symposium on the GDH Sum Rule and the Spin Structure of the Nucleon*, 1st ed., edited by M. Anghinolfi, M. Battaglieri, and R. D. Vita (World Scientific, New Jersey, 2003).

[59] R. S. Canon *et al.*, Technical report, Triangle Universities Nuclear labs, (unpublished), http://www.tunl.duke.edu/Local/progrep/1999/.

[60] The GDH Collaboration, http://www.pit.physik.uni-tuebingen.de/grabmayr/GDH/gdh_text.html#links.

[61] J. L. Friar, Phys. Rev. **C16**, 1504 (1977).

[62] H. R. Weller, in *Proceedings of the Second International Symposium on the GDH Sum Rule and the Spin Structure of the Nucleon*, 1st ed., edited by M. Anghinolfi, M. Battaglieri, and R. D. Vita (World Scientific, New Jersey, 2003).

[63] H. Arenhovel, (2000), nucl-th/0006083.

[64] E. A. Wulf *et al.*, Phys. Rev. **C61**, 021601 (2000).

[65] R. Pantforder, (1998), hep-ph/9805434.

[66] X.-D. Ji and J. Osborne, J. Phys. **G27**, 127 (2001).

[67] D. Drechsel, B. Pasquini, and M. Vanderhaeghen, Phys. Rept. **378**, 99 (2003).

[68] V. Bernard, N. Kaiser, and U. G. Meissner, Phys. Rev. **D48**, 3062 (1993).

[69] J. D. Bjorken, Phys. Rev. **148**, 1467 (1966).

[70] X.-D. Ji and P. Unrau, Phys. Lett. **B333**, 228 (1994).

[71] B. Lampe and E. Reya, Phys. Rept. **332**, 1 (2000).

[72] K. Abe *et al.*, Phys. Rev. Lett. **79**, 26 (1997).

[73] P. L. Anthony *et al.*, Phys. Lett. **B493**, 19 (2000).

[74] A. Deur *et al.*, (2004), hep-ex/0407007.

[75] L. Frankfurt, V. Guzey, and M. Strikman, Phys. Lett. **B381**, 379 (1996).

[76] A. W. Thomas, Nucl. Phys. Proc. Suppl. **105**, 80 (2002).

[77] F. Bissey, V. Guzey, M. Strikman, and A. W. Thomas, Phys. Rev. **C65**, 064317 (2002).

[78] J. Ashman *et al.*, Nucl. Phys. **B328**, 1 (1989).

[79] G. Baum *et al.*, Phys. Rev. Lett. **51**, 1135 (1983).

[80] J. R. Ellis and R. L. Jaffe, Phys. Rev. **D9**, 1444 (1974).

[81] S. D. Bass and A. W. Thomas, Prog. Part. Nucl. Phys. **33**, 449 (1994).

[82] R. Fatemi *et al.*, Phys. Rev. Lett. **91**, 222002 (2003).

[83] C. Ciofi degli Atti and S. Scopetta, Phys. Lett. **B404**, 223 (1997).

[84] V. D. Burkert, Phys. Rev. **D63**, 097904 (2001).

[85] R. L. Jaffe and X.-D. Ji, Phys. Rev. **D43**, 724 (1991).

[86] G. Altarelli, B. Lampe, P. Nason, and G. Ridolfi, Phys. Lett. **B334**, 187 (1994).

[87] T. B. Humensky *et al.*, Nucl. Instrum. Meth. **A521**, 261 (2004).

[88] T. Maruyama *et al.*, Nucl. Instrum. Meth. **A492**, 199 (2002).

[89] J. Alcorn *et al.*, Nucl. Inst. Meth. **A522**, 294 (2004).

[90] G. Laveissiere, Hall A Charge and Current Monitor Home Page, http://www.jlab.org/~geraud/current.html.

[91] J.-C. Denard, A. Saha, and G. Lavessire, Technical report, JLab Hall A, (unpublished), JLAB-ACT-01-12.

[92] K. Unser, IEEE Transactions on Nuclear Science **NS-28**, 3 (1981).

[93] P. E. Ulmer, Technical report, JLab Hall A E89-003 (unpublished).

[94] A. Deur, Technical report, E94010 Collaboration, (unpublished), http://www.jlab.org/e94010/, TN-E94010-30.

[95] Jlab Hall A Moller Polarimeter Group, http://www.jlab.org/~moller.

[96] A. V. Glamazdin *et al.*, (1999), hep-ex/9912063.

[97] H. R. Band, G. Mitchell, R. Prepost, and T. Wright, Nucl. Instrum. Meth. **A400**, 24 (1997).

[98] Jlab Hall A Beam and Polarimeter webpage, http://hallaweb.jlab.org/equipment/beam.html.

[99] P. Ulmer *et al.*, Technical report, JLab, (unpublished), JLab technical note 94-001.

[100] A. Deur, Technical report, E94010 Collaboration, (unpublished), http://www.jlab.org/e94010/, TN-E94010-35.

[101] A. Deur, Ph.D. thesis, Universite Blaise Pascal, 2000, http://www.jlab.org/e94010/.

[102] N. Liyanage, Technical report, Jefferson Lab, (unpublished), technical Note JLAB-TN-01-049.

[103] K. Slifer, Technical report, E94010 Collaboration, (unpublished), http://www.jlab.org/∼slifer/tn/technote.html.

[104] M. Liang, Technical report, E89-003,E89-033 Collaboration (unpublished).

[105] Nilanga Liyanage, University of Virginia, nilanga@jlab.org, private communication.

[106] W. R. Leo, *Techniques for Nuclear and Particle Physics Experiments, A How-to Approach*, 1st ed. (Springer Verlag, Berlin, 1987).

[107] K. G. Fissum *et al.*, Nucl. Instrum. Meth. **A474**, 108 (2001).

[108] M. Iodice *et al.*, Nucl. Instrum. Meth. **A411**, 223 (1998).

[109] A. Keitikyan *et al.*, Technical report, (unpublished), http://www.jlab.org/∼armen/sh_web_page/welcome.html.

[110] J. R. Johnson *et al.*, Nucl. Instrum. Meth. **A356**, 148 (1995).

[111] P. L. Anthony *et al.*, Phys. Rev. **D54**, 6620 (1996).

[112] R. Herman, Phys. Rev. A **137**, 1062 (1965).

[113] K. P. Coulter, Ph.D. thesis, Princeton University, 1989.

[114] T. J. Killian, Phys. Rev. **27**, 578 (1926).

[115] M. E. Wagshul, Ph.D. thesis, Harvard University, 1991.

[116] N. R. Newbury *et al.*, Phys. Rev. A **48**, 4411 (1993).

[117] R. E. Jacob, S. W. Morgan, B. Saam, and J. C. Leawoods, Phys. Rev. Lett. **87**, 143004 (2001).

[118] T. Chupp *et al.*, Phys. Rev. C **36**, 2244 (1987).

[119] A. Deur, Technical report, E94010 Collaboration, (unpublished), http://www.jlab.org/e94010/, TN-E94010-21.

[120] K. D. Bonin, T. G. Walker, and W. Happer, Phys. Rev. A **37**, 3270 (1988).

[121] K. D. Bonin, D. P. Saltzberg, and W. Happer, Phys. Rev. A **38**, 4481 (1988).

[122] M. Romalis and G. Cates, Phys. Rev. A **58**, 4 (1998).

[123] J. S. Jensen, Ph.D. thesis, California Institute of Technology, 2000, http://www.jlab.org/e94010/.

[124] I. Kominis, Ph.D. thesis, Princeton University, 2001, http://www.jlab.org/e94010/.

[125] JLab E94010 Collaboration homepage, http://www.jlab.org/e94010.

[126] I. Kominis, private communication.

[127] The Jlab Hall A Collaboration, Technical report, Jlab, (unpublished), *Hall A Experimental Equipment Operations Manual and Safety Assessment.*

[128] M. M. Rvachev, Ph.D. thesis, MIT, 2003.

[129] The Jlab HallA Collaboration, Technical report, JLab, (unpublished), *Espace User's Guide*, http://hallaweb.jlab.org/espace/.

[130] Cern Program Library, Technical report, CERN, (unpublished), *The Zebra System.*

[131] L. W. Mo and Y.-S. Tsai, Rev. Mod. Phys. **41**, 205 (1969).

[132] Yung-Su Tsai, (1970), Lectures given at Nato Advanced Institute on Electron Scattering and Nuclear Structure at Cagliari, Italy, SLAC-PUB-848.

[133] S. Stein *et al.*, Phys. Rev. **D12**, 1884 (1975).

[134] T. V. Kukhto and N. M. Shumeiko, Nucl. Phys. **B219**, 412 (1983).

[135] I. V. Akushevich and N. M. Shumeiko, J. Phys. **G20**, 513 (1994).

[136] I. Akushevich *et al.*, Comput. Phys. Commun. **104**, 201 (1997).

[137] S. Choi, choi@jlab.org, private communication.

[138] R. Altulmus and J. Wise., **ROSETAIL.F**, fortran analysis code.

[139] A. Deur, Technical report, E94010 Collaboration, (unpublished), http://www.jlab.org/e94010/, TN-E94010-29.

[140] K. Slifer, Technical report, E94010 Collaboration, (unpublished), http://www.jlab.org/e94010/, TN-E94010-32.

[141] L. Todor, Technical report, Jefferson Lab VCS Collaboration, (unpublished), *Hall A Detector Database Calibration.*

[142] K. Slifer, Technical report, E94010 Collaboration, (unpublished), http://www.jlab.org/e94010/, TN-E94010-31.

[143] Particle Data Group, *Review of Particle Physics* (Springer, Berkely, CA, 1998), table 25.4.

[144] N. Liyanage, Technical report, Jefferson Lab, (unpublished), TN02-012.

[145] X. Jiang, Technical report, E94010 Collaboration, (unpublished), *Acceptance Function of Hall-A E94010 Experiment.*

[146] K. Slifer, Technical report, E94010 Collaboration, (unpublished), http://www.jlab.org/e94010/, TN-E94010-37.

[147] K. Slifer, Technical report, E94010 Collaboration, (unpublished), http://www.jlab.org/~slifer/collab/short_rep.html.

[148] N. Liyanage, Technical report, Jefferson Lab, (unpublished), www.jlab.org/~nilanga/physics/94010/cross_section.ps.

[149] Arun Saha, JLab Hall A staff, saha@jlab.org, private communication.

[150] I. Kominis, Technical report, E94010 Collaboration, (unpublished), http://www.jlab.org/e94010/, TN-E94010-25.

[151] K. Slifer, Technical report, E94010 Collaboration, (unpublished), http://www.jlab.org/~slifer/collab/short_rep.html.

[152] G. Cates and A. Deur, private communication.

[153] K. Slifer, Technical report, E94010 Collaboration, (unpublished), http://www.jlab.org/e94010/, TN-E94010-38.

[154] K. Slifer, Technical report, E94010 Collaboration, (unpublished), http://www.jlab.org/e94010/, TN-E94010-43.

[155] K. Slifer, Technical report, E94010 Collaboration, (unpublished), http://www.jlab.org/~slifer/tn/technote.html.

[156] John Steffen Jensen, steffen@jlab.org, private communication.

[157] E. B. Dally, M. G. Croissiaux, and B. Schweitz, Phys. Rev. **C2**, 2057 (1970).

[158] A. Amroun *et al.*, Phys. Rev. Lett. **69**, 253 (1992).

[159] A. Amroun *et al.*, Nucl. Phys. **A579**, 596 (1994).

[160] A. Deur, *Single Arm Monte Carlo*, 2002, Hall A data analysis workshop. http://hallaweb.jlab.org/data_reduc/AnaWork2002/.

[161] J.W. Lightbody Jr. and J. O'Connell, Computers in Physics **May/June**, 57 (1988).

[162] K. Slifer, Technical report, E94010 Collaboration, (unpublished), http://www.jlab.org/e94010/, TN-E94010-44.

[163] J. S. Mccarthy, I. Sick, and R. R. Whitney, Phys. Rev. **C15**, 1396 (1977).

[164] R. Whitney, **RADCOR.F**, fortran analysis code.

[165] G. Miller, Ph.D. thesis, Stanford University, 1971, SLAC-R-0129.

[166] C. Marchand *et al.*, Phys. Lett. **B153**, 29 (1985).

[167] T.-S. Ueng, Ph.D. thesis, University of Virginia, 1988.

[168] K. A. Dow, Ph.D. thesis, Massachusetts Institute of Technology, 1987.

[169] A. Kievsky, E. Pace, G. Salme, and M. Viviani, Phys. Rev. **C56**, 64 (1997).

[170] S. Scopetta, private communication.

[171] C. Ciofi degli Atti, E. Pace, and G. Salmè, Phys. Rev. **C46**, 1591 (1992).

[172] R.-W. Schulze and P. U. Sauer, Phys. Rev. **C48**, 38 (1993).

[173] O. Benhar, E. Pace, and G. Salme, Phys. Lett. **B195**, 13 (1987).

[174] H. Meier-Hajduk, U. Olfke, and P. U. Sauer, Nucl. Phys. **A499**, 637 (1989).

[175] J. Golak, private communication.

[176] J. Golak *et al.*, Nucl. Phys. **A707**, 365 (2002).

[177] H. W. Hammer, U.-G. Meissner, and D. Drechsel, Phys. Lett. **B385**, 343 (1996).

[178] R. B. Wiringa, V. G. J. Stoks, and R. Schiavilla, Phys. Rev. **C51**, 38 (1995).

[179] R. B. Wiringa, Phys. Rev. **C43**, 1585 (1991).

[180] B. S. Pudliner *et al.*, Phys. Rev. **C56**, 1720 (1997).

[181] A. Nogga *et al.*, Phys. Rev. **C67**, 034004 (2003).

[182] H. Witała, W. Glockle, and T. Cornelius, Phys. Rev. **C39**, 384 (1989).

[183] R. Schiavilla, V. R. Pandharipande, and D. O. Riska, Phys. Rev. **C40**, 2294 (1989).

[184] R. Schiavilla, V. R. Pandharipande, and D. O. Riska, Phys. Rev. **C**, 309 (1990).

[185] P. L. Anthony *et al.*, Phys. Rev. Lett. **71**, 959 (1993).

[186] K. Abe *et al.*, Phys. Rev. **D58**, 112003 (1998).

[187] K. Abe *et al.*, Phys. Lett. **B364**, 61 (1995).

[188] E. Thomas and N. Bianchi, Nucl. Phys. Proc. Suppl. **82**, 256 (2000).

[189] X.-D. Ji, C.-W. Kao, and J. Osborne, Phys. Lett. **B472**, 1 (2000).

[190] V. Bernard, T. R. Hemmert, and U.-G. Meissner, Phys. Lett. **B545**, 105 (2002).

[191] U.-G. Meissner, private communication.

[192] J. Chen, A. Deur, and F. Garibaldi, JLab experiment E97-110, http://hallaweb.jlab.org/experiment/E97-110/.

[193] P. L. Anthony *et al.*, Phys. Lett. **B553**, 18 (2003).

[194] M. Amarian *et al.*, Phys. Rev. Lett. **92**, 022301 (2004).

[195] M. Amarian *et al.*, Phys. Rev. Lett. **89**, 242301 (2002).

[196] M. Amarian *et al.*, (2004).

[197] J. Yun *et al.*, Phys. Rev. **C67**, 055204 (2003).

[198] H. Arenhovel, D. Drechsel, and H. J. Weber, Nucl. Phys. **A305**, 485 (1978).

[199] D. Adams *et al.*, Phys. Lett. **B329**, 399 (1994).

[200] B. Adeva *et al.*, Phys. Lett. **B320**, 400 (1994).

[201] K. Ackerstaff *et al.*, Phys. Lett. **B444**, 531 (1998).

[202] C. Ciofi degli Atti, S. Scopetta, E. Pace, and G. Salme, Phys. Rev. **C48**, 968 (1993).

[203] J. L. Friar *et al.*, Phys. Rev. **C42**, 2310 (1990).

[204] Wally Melnitchouk, JLab staff theorist, wmelnitc@jlab.org, private communication.

[205] S. A. Kulagin, W. Melnitchouk, G. Piller, and W. Weise, Phys. Rev. **C52**, 932 (1995).

[206] M. M. Giannini, in *Proceedings of the Second International Symposium on the GDH Sum Rule and the Spin Structure of the Nucleon*, 1st ed., edited by M. Anghinolfi, M. Battaglieri, and R. D. Vita (World Scientific, New Jersey, 2003).

[207] G. B. Arfken and H. J. Weber, *Mathematical Methods for Physicists*, fourth ed. (Academic Press, San Diego, California, 1995).

[208] E. C. Titchmarsh, *Introduction to the Theory of Fourier Integrals*, 2nd ed. (Oxford University Press, New York, NY, 1937).

[209] L. Landau, J.Phys. **8**, 201 (1944).

[210] M. Berger, J. Coursey, and M. Zucker, *Stopping-Power and Range Tables for Electrons, Protons, and Helium Ions*, http://physics.nist.gov/PhysRefData/Star/Text/.

[211] F. Bloch and A. Nordsieck, Phys. Rev. **52**, 54 (1937).

[212] J. S. Schwinger, Phys. Rev. **76**, 790 (1949).

[213] Ed Folts, JLab Hall A staff, private communication.

[214] J. S. Jensen, Technical report, E94010 Collaboration (unpublished).

[215] A. Deur, Technical report, E94010 Collaboration, (unpublished), http://www.jlab.org/e94010/, TN-E94010-39.

[216] A. Deur, deurpam@jlab.org, private communication.

[217] E94-010 ^{3}He Target Cell Specifications, http://www.jlab.org/e94010/cells.html.

[218] F. Xiong, Ph.D. thesis, Massachusetts Institute of Technology, 2002.

[219] S. Choi, Technical report, E94010 Collaboration (unpublished).

[220] W. Melnitchouk, (1999), hep-ph/0006170.